

CONSEJO SUPERIOR DE INVESTIGACIONES CIENTIFICAS
INSTITUTO DE CIENCIA DE MATERIALES DE MADRID



Theoretical methods for surface structure analysis by Low-Energy Electron Diffraction

Tesis Doctoral

María Blanco Rey

Abril, 2006

UNIVERSIDAD AUTONOMA DE MADRID



CONSEJO SUPERIOR DE INVESTIGACIONES CIENTIFICAS
INSTITUTO DE CIENCIA DE MATERIALES DE MADRID

Theoretical methods for surface structure analysis by Low-Energy Electron Diffraction

Memoria de Tesis Doctoral presentada ante la Facultad de Ciencias,
Sección de Ciencias Físicas, de la Universidad Autónoma de Madrid
por **María Blanco Rey**.

Trabajo dirigido por el Dr. Pedro L. de Andrés Rodríguez
y tutelado por el Prof. Fernando Flores Sintas.

Madrid, Abril 2006

A mi familia

Contents

Abbreviations	v
1 Introducción / Introduction	1
2 Surface Structure by LEED	13
2.1 Introduction	13
2.2 LEED experiments	14
2.3 Single atom scattering: the muffin tin approach	15
2.4 Information from IV visualization	17
2.5 General MS theory	19
2.6 Full-dynamical LEED theory	21
2.6.1 Scattering by an atomic plane	21
2.6.2 Scattering by a stack of planes: layer doubling	24
2.6.3 Temperature effects	25
2.7 The LEED90 program	28
2.7.1 Technical remarks about LEED90	29
2.8 R-factors	31
2.9 Diffuse LEED (DLEED)	33
2.10 Tensor LEED (TLEED)	34
3 The structure of TiO_2 (110)-1×2 surface	37
3.1 Introduction	37
3.2 The rutile TiO_2 bulk structure	38
3.3 The rutile TiO_2 (110) face	38
3.3.1 The rutile TiO_2 (110)- 1×1 surface	38
3.3.2 The rutile TiO_2 (110)- 1×2 reconstruction	39
3.4 Experiments	41
3.4.1 Sample preparation and measurements	41
3.4.2 STM interpretation	42
3.5 Theory	42
3.5.1 LEED calculations	42
3.5.2 DFT calculations	51
3.6 Discussion on the atomic structure	52
3.6.1 Geometry	52
3.6.2 Thermal vibrations	54
3.7 Discussion on the electronic structure	60
3.8 Conclusions	61

4	Molecular t-matrix	63
4.1	Introduction and motivation	63
4.2	Molecular T-matrix construction	64
4.3	Applications and properties	65
4.3.1	Matrix translation using Green's propagators	65
4.3.2	Matrix rotation using Wigner's matrices	65
4.3.3	Molecular vibrations	66
4.3.4	$l_{T,\max}$ determination	66
4.3.5	The molecular T-matrix symmetries and the S-matrix	67
4.4	The TMOL (v1.1) program	68
4.5	Model calculations	69
4.5.1	Test of key non-geometrical parameters	69
4.5.2	Strong Scatterers	74
4.5.3	Larger molecules: benzene on Ni(111)	77
4.6	Conclusions	77
5	Perturbative approximations with TMOL	81
5.1	Introduction	81
5.2	Molecular distortions	82
5.2.1	Formalism	82
5.2.2	Example: the CO/Cu(100)-c(2×2) surface	83
5.2.3	Description of molecular normal modes of vibration	85
5.3	Use of TMOL in a TLEED program	88
5.4	Conclusions	92
6	Structure from Simultaneous Optimization	97
6.1	Introduction	97
6.2	R-factor topography	99
6.3	Previous work overview	100
6.3.1	Local methods	101
6.3.2	Global methods	102
6.4	The SO strategy	105
6.4.1	The partial problem	106
6.4.2	The global problem	108
6.5	Electronic parameter retrieval	110
6.5.1	Results for phase shifts retrieval	112
6.5.2	Data-base size effect	113
6.5.3	Noise effect	115
6.6	Structure determination from LEED simulated data	115
6.6.1	Topography of the $N = 2$ case	118
6.6.2	Statistical interpretation	118
6.6.3	Scale law	122
6.6.4	Fitting V_{0r}	122
6.7	Structure determination from LEED experiments	126
6.8	Conclusions	130

7	Structure from tomography and ER	133
7.1	Introduction	133
7.2	Overview of previous work on direct methods	137
7.2.1	Holography	137
7.2.2	Patterson Function	139
7.2.3	Maximum entropy method	140
7.3	Phase retrieval methods	141
7.4	Diffraction Tomography	143
7.5	Structure and phase retrieval from clusters	144
7.5.1	The algorithm	146
7.5.2	Reconstruction from two-dimensional scans	148
7.5.3	Position retrieval from measured amplitudes: results for a flat molecule	150
7.5.4	Position retrieval from measured intensities: results for localized clusters	154
7.6	Approach for MS in clusters	156
7.6.1	Results	161
7.7	Error reduction at ordered surfaces	162
7.8	Conclusions	166
8	Conclusiones / Conclusions	171
A	Green propagators in spherical wave basis	179
B	Gaunt coefficients	181
C	Poisson probability distribution derivation	183
	References	185
	Agradecimientos / Acknowledgements	195

Abbreviations

AES - Auger Electron Spectroscopy
AFM - Atomic Force Microscopy
BPP - Backpropagation
CG - Conjugate Gradients
DFT - Density Functional Theory
DLEED - Diffuse LEED
DOS - Density of States
DT - Diffraction tomography
DW - Debye-Waller
EELS - Electron Energy Loss Spectroscopy
ER - Error-Reduction
ESDIAD - Electron Stimulated Desorption Ion Angular Distribution
FFT - Fast Fourier Transform
GA - Genetic Algorithm
GGA - Generalized Gradient Approximation
HEIS - High-Energy Ion Scattering
HF - Hartree-Fock
HIO - Hybrid Input-Output
HLEED - Holographic LEED
ICISS - Impact Collision Ion-scattering Spectroscopy
IRAS - Infra-red Absorption Spectroscopy
KKR - Korring-Kohn-Rostoker
LDA - Local Density Approximation
LDOS - Local Density of States
LEED - Low-Energy Electron Diffraction
MEED - Medium-Energy Electron Diffraction
MEIS - Medium-Energy Ion Scattering
MS - Multiple Scattering
NEXAFS or XANES - Near-Edge X-Ray Absorption Fine Structure
PBE - Perdew-Burke-Ernzerhof
PD - PhotoElectron Diffraction
PDF - Probability Distribution Function
PDOS - Projected Density of States
PHS - Phase Shift
RFS - Renormalised Forward Scattering
RHEED - Reflection High-Energy Electron Diffraction
RSA - Random Sampling Algorithm

SA - Simulated Annealing
SEXAFS - Surface Extended X-Ray Absorption Fine Structure
SO - Simultaneous Optimization
STM - Scanning Tunneling Microscopy
SXRD - Surface X-Rays Diffraction
TDS - Thermal Diffuse Scattering
TLEED - Tensor LEED
UFR - Unified Frequency Domain Interpolation
UHV - Ultra-High Vacuum
UPS - UV Phototelectron Spectroscopy
XPD - X-Ray Phototelectron Diffraction
XPS - X-Ray Phototelectron Spectroscopy

Chapter 1

Introducción / Introduction

Dentro del cristal, los átomos adoptan la configuración de mínima energía. La existencia de una superficie implica una ruptura de la simetría de traslación en dirección perpendicular a la superficie, lo que provoca un incremento en la energía total. Los átomos de la región de la superficie adoptan posiciones distorsionadas respecto a las del sólido, creando un término elástico para compensar la pérdida de simetría. Por tanto, en la superficie del sólido aparecen estructuras complejas, algunas por creación de nuevos enlaces y otras por destrucción de enlaces existentes. La simetría de red en dirección paralela puede cambiar eventualmente, dando lugar a las llamadas *reconstrucciones de superficie*. El grupo de simetría de la superficie reconstruida será un subgrupo del grupo de simetría del sustrato. Estas reconstrucciones pueden aparecer también como consecuencia de la adsorción de átomos o moléculas sobre la superficie. Esta es la respuesta del cristal a la aparición de un término en la energía total asociado al enlace sustrato/adsorbato. La disposición geométrica de los átomos de la superficie determina las propiedades tanto electrónicas como vibracionales de la superficie, que serán, en general, diferentes de las propiedades del sólido. Un conocimiento detallado de la geometría de adsorción es crucial, por ejemplo, para comprender procesos químicos sobre la superficie, como la catálisis heterogénea. De hecho, la diferencia entre fisisorción y quimisorción determina las longitudes de enlace entre los átomos del sustrato y los del adsorbato, y los caminos de reacción dependen fuertemente del sitio de adsorción y de la orientación del adsorbato. Otro ejemplo se encuentra en el diseño de dispositivos electrónicos, que depende del conocimiento de las propiedades electrónicas y magnéticas de la superficie.

Durante las últimas décadas se han desarrollado un gran número de técnicas de caracterización de superficies. Se pueden dividir en dos categorías: espectroscopías de superficie para el análisis químico y electrónico (por ejemplo, AES, XPS, EELS, NEXAFS y SEXAFS) por un lado, y difracción (por ejemplo, LEED, MEED, RHEED, MEIS, HEIS, XPD y SXRD) y microscopías con resolución atómica (por ejemplo, STM y AFM) para el análisis estructural por otro lado, algunas de ellas incluyendo también sensibilidad química [1, 2, 3, 4]. Además de estas técnicas experimentales, debemos mencionar la importancia de los métodos DFT en la actualidad, como apoyo para experimentos y como técnica de predicción de propiedades estructurales y electrónicas. La Fig. 1.1 muestra la clasificación de estructuras resueltas en función de varias técnicas experimentales elaborada por *NIST Surface Structure*

Database. Entre ellas, la Difracción de Electrones de Baja Energía (*Low-Energy Electron Diffraction*, LEED) parece ser la más exitosa hasta la fecha.

LEED fue uno de los primeros temas en el estudio de las superficies. Los primeros experimentos fueron llevados a cabo por Davisson y Germer en 1927 sobre la superficie Ni(111) [5]. Estos primeros experimentos de LEED fueron la demostración práctica de la naturaleza ondulatoria de los electrones, postulada en la misma época por Thompson y Reid [6]. Thompson y Davisson compartieron un premio Nobel en 1937 por estas investigaciones. Van Hove *et al* dan una buena descripción histórica de la evolución de LEED en la Ref. [1]. Resulta interesante destacar que el desarrollo de LEED se mantuvo estancado hasta la década de los sesenta, en parte por la falta de una teoría adecuada para describirlo. El trabajo teórico sobre la dispersión múltiple y la fabricación de las cámaras de ultra-alto vacío (UHV) impulsaron LEED. Han contribuido significativamente en la teoría para LEED investigadores como McRae (dispersión múltiple y matriz de transferencia [7]), Marcus y Jona (transformadas de Fourier de las ondas [8]) o Beeby (funciones de Green [9]). Pendry incluyó el formalismo de matriz- t atómico y cayó en la cuenta de que los efectos inelásticos, que dan lugar a ondas evanescentes, deben ser considerados [10]. También introdujo dos métodos eficientes para describir la dispersión múltiple entre capas atómicas: RFS (perturbativo) [11] y el doblado de capas o *layer doubling* (exacto) en colaboración con Van Hove [12]. Tong desarrolló el método *composite layer*, que combina bases de ondas planas y ondas parciales [13].

Aprovechando los recursos computacionales que acababan de surgir, Pendry, Van Hove y colaboradores dieron el paso adelante definitivo escribiendo los primeros códigos para calcular espectros de LEED en los años setenta [14, 15]. En los setenta se progresó también en experimentación, en laboratorios como IBM (grupo de Marcus y Jona), Berkeley (grupo de Van Hove), Cambridge (grupo de King) o Erlangen (grupo de Heinz). Se redujo el flujo de electrones en los equipos experimentales y se desarrollaron técnicas de adquisición rápida de datos. Uno de los principales avances en monitorización fue Video LEED, desarrollado por Heinz y colaboradores [16]. Desde entonces, LEED se ha establecido como una de las técnicas más relevantes de caracterización de superficies.

Como se ha mencionado anteriormente, una descripción completa de LEED requiere un formalismo de dispersión múltiple, ya que los electrones lentos interactúan fuertemente con los átomos de la superficie, haciendo los cálculos mucho más complicados que en cualquier otra técnica de difracción, como la difracción de rayos-X, donde los rayos-X interactúan débilmente con la materia permitiendo una descripción simple con factores de dispersión. Sin embargo, los procesos de dispersión múltiple producen una estructura mucho más rica en los espectros de difracción (la evolución de las intensidades difractadas con la energía de los electrones incidentes, llamadas curvas IV), que incrementa la sensibilidad de LEED a las posiciones atómicas hasta una precisión de centésimas de Å. Existen otras muchas técnicas para superficies que comparten la propiedad de la dispersión múltiple con LEED y que, por lo tanto, podrían beneficiarse de desarrollos en la teoría para LEED. Por ejemplo, este es el caso de la difracción de fotoelectrones (PD) [17], *Near-Edge X-ray Absorption Fine Structure* (NEXAFS) [18] e incluso la microscopía de efecto túnel (STM) [19].

Como en cualquier otro experimento de difracción, sólo se pueden medir las intensidades. Además, los procesos de dispersión múltiple convierten las intensidades en una función con una dependencia compleja de la estructura. Por tanto, para obtener la estructura de la superficie a partir de un espectro experimental, debemos enfrentarnos a un problema no directamente invertible. El procedimiento habitual para abordarlo es un método de prueba y error, que consiste en proponer superficies modelo y calcular las curvas IV correspondientes, hasta encontrar el modelo que mejor ajusta los datos experimentales. Cuando el número de parámetros de superficie a ajustar es grande, se pueden utilizar algoritmos que hacen esta búsqueda más eficiente [20]. Esta Tesis trata los aspectos teóricos de LEED. En esta memoria se discutirán varios métodos de análisis de LEED, incluyendo implementaciones de cálculo de espectros, técnicas de prueba y error y, desde otro punto de vista, la extracción de información estructural directamente de los datos experimentales, es decir, los llamados métodos directos.

Avances recientes en teoría de LEED

Las teorías de dispersión múltiple para el cálculo de curvas IV desarrolladas en los sesenta son muy precisas, y las rutinas elaboradas por Pendry y Van Hove se siguen utilizando dentro de códigos modernos de LEED. Algunos códigos de LEED publicados recientemente consisten en versiones modernas de los paquetes de rutinas antiguos. Estos cálculos incluyen también efectos de vibración térmica, que los convierten en herramientas efectivas incluso hoy en día. Este es caso de códigos como DLLEED (FORTRAN90) [21] y CLEED (C++) [22] más recientemente, que incluye anisotropía en las vibraciones.

Desde entonces, los desafíos teóricos en LEED tienen que ver con la forma de hacer más eficientes los cálculos de intensidades y los procesos de búsqueda para poder dar cuenta de superficies cada vez más complejas. Tensor LEED (TLEED) [23, 24] y Linear LEED (LLEED) [25] fueron los primeros intentos de acelerar los cálculos de las curvas IV. Con estos dos métodos, dadas las amplitudes difractadas por una cierta estructura, es posible calcular eficientemente las amplitudes difractadas por una estructura ligeramente distorsionada respecto a la primera, utilizando una aproximación perturbativa.

El interés de las estructuras desordenadas, como los adsorbatos en forma de “red gaseosa” presentes en algunos procesos catalíticos, ha motivado la implementación de cálculos de dispersión múltiple en *clusters* de átomos para explicar los patrones de LEED difuso (DLEED) [26], haciendo uso de formalismos que han sido probados con éxito en otras técnicas como NEXAFS o PD.

Hoy en día, los esfuerzos están orientados hacia los métodos directos, es decir, recuperación directa de información a partir de los datos de difracción, sin emplear métodos de prueba y error [27]. Muchos de ellos guardan similitud con métodos implementados para otras técnicas de difracción, ya que todas estas técnicas están conectadas por la falta de información acerca de la fase. Por tanto, los métodos directos son, intrínsecamente, métodos de recuperación de fase a partir de datos incompletos. Este es un problema clásico en teoría de difracción, sobre el que se puede encontrar mucha literatura del campo de óptica. Por ejemplo, la idea de considerar el espectro de difracción difuso como un holograma se propuso en el ámbito de PD,

primero con dispersión simple [28], después para doble dispersión [29] y más tarde en LEED [30], donde existe dispersión múltiple en el sustrato. Los métodos holográficos modernos en difracción de electrones consideran términos de corrección (*kernels*) y superposición de hologramas recogidos bajo distintas condiciones [31, 32].

Importada de la cristalografía de rayos-X, la función de Patterson [33] se ha aplicado a LEED en estructuras ordenadas. Para minimizar el efecto de la dispersión múltiple, que produce reconstrucciones borrosas y artefactos, se pueden superponer datos recogidos a diferentes incidencias [34, 35]. Los métodos bayesianos [36] son otro típico ejemplo de método directo en cristalografía que se ha transferido recientemente a LEED [37].

Experimentos y cálculos se comparan a través de un factor de calidad (factor-R). El factor-R, como función de los parámetros que describen la superficie, es una hipersuperficie de topografía compleja. La estructura modelo que produce el mínimo absoluto en el factor-R se considera la estructura más probable, ya que produce el mejor acuerdo con los datos disponibles, es decir, la máxima correlación entre teoría y experimento. Se han desarrollado métodos de búsqueda direccional que disminuyen el número de estructuras modelo visitadas durante la búsqueda. Estos métodos no son más que algoritmos eficientes de minimización del factor-R. Los esfuerzos en esta área de la teoría de LEED están focalizados en el desarrollo de métodos globales, que permiten explorar regiones más grandes del espacio de parámetros. Los códigos de LEED disponibles suelen combinar procedimientos de cálculo de espectros con algoritmos de búsqueda eficientes, que varían los parámetros de acuerdo con el algoritmo de minimización para explorar el mínimo número de estructuras posible.

En realidad, estos métodos de minimización del factor-R no deberían considerarse como “directos”. Efectúan un proceso de prueba y error optimizado, en contraposición a métodos directos importados de óptica, que incluyen síntesis de Fourier, como la holografía y la función de Patterson. Dentro de este último tipo de métodos, los vectores interatómicos y/o las posiciones atómicas se extraen directamente de un análisis espectral de las intensidades medidas. En el marco de esta discusión, los métodos de tipo Bayesiano se encontrarían en una posición intermedia, ya que tienen la capacidad de combinar síntesis de Fourier con un proceso iterativo que proporciona una estructura modelo que minimiza una cierta función de costo.

Motivación, objetivos y logros de esta Tesis

El objetivo de esta Tesis es contribuir en la reparación de las deficiencias actuales de la teoría de LEED. A pesar de las mejoras significativas en otras técnicas que las están haciendo más populares, creemos que LEED todavía puede proporcionar buenos recursos a los laboratorios de ciencia de superficies si se efectúan algunas actualizaciones desde el punto de vista teórico.

Se ha escrito un código de LEED-IV moderno en FORTRAN-90/95, llamado LEED90, con el propósito de probar en él los nuevos métodos propuestos en esta Tesis. Este código ha sido el primero en funcionar con matrices-t no diagonales, lo que es necesario para nuestro trabajo. Aunque la descripción ya existente de la dispersión múltiple es satisfactoria, nuestro primer objetivo ha sido elaborar una descripción útil de los adsorbatos moleculares ordenados, debido al interés de estas

estructuras en química de superficies. Este trabajo se ha basado en un formalismo propuesto por Andersson y Pendry [38], y manteniendo cierto paralelismo con otros códigos desarrollados para *clusters* de átomos en otras técnicas y en DLEED. El resultado ha sido un código FORTRAN-90/95, TMOL, que calcula la matriz-t de una molécula, y que puede emplearse en combinación con códigos de LEED típicos. La funcionalidad de este método se ha chequeado en varias superficies modelo. Esta parte del trabajo ha dado lugar a tres publicaciones:

- M. Blanco-Rey, P. de Andres, G. Held and D.A. King, “TMOL v1.1: Molecular t-matrices for Low-Energy Electron Diffraction”, *Comp. Phys. Commun.* **161** (2004) 166-178
- M. Blanco-Rey, P. de Andres, G. Held and D.A. King, “A FORTRAN-90 Low-Energy Electron Diffraction program (LEED90 v1.1)”, *Comp. Phys. Commun.* **161** (2004) 151-165
- M. Blanco-Rey, P. de Andres, G. Held and D.A. King, “A molecular t-matrix approach to calculating Low-Energy Electron Diffraction intensities for ordered molecular adsorbates”, *Surf. Sci.* **579** (2005) 89-99

El trabajo anterior se ha prolongado combinando las matrices moleculares y el formalismo TLEED, en colaboración con el Prof. K. Heinz de la Universidad de Erlangen-Nuremberg. Los resultados correspondientes han sido el objeto de una comunicación en el congreso ICSOS-8, celebrado en Munich en julio de 2005, titulada “Molecular T-matrix formalism for LEED”.

Se ha propuesto un nuevo algoritmo global de búsqueda direccionada. Este algoritmo utiliza una combinación de ideas sobre bases de datos reducidas y métodos ergódicos. Se llama algoritmo de “Optimización Simultánea” (SO), y se ha chequeado en dos situaciones modelo: en la recuperación de desfases en dispersión por un átomo y en el ajuste de parámetros estructurales en datos simulados de LEED. Un estudio exhaustivo sobre su comportamiento a nivel estadístico ha probado que SO es altamente competitivo en comparación con otros métodos similares. Los resultados relativos a este trabajo han sido publicados en la siguiente referencia:

- M. Blanco-Rey P. de Andres, “Surface Diffraction Structure Determination from Combinatorial Simultaneous Optimization”, *Surf. Sci.* **600** (2006) L91-L95.

Otro artículo sobre el comportamiento de SO sobre datos experimentales se encuentra en preparación.

El problema de la fase en LEED se ha investigado utilizando métodos típicos de recuperación de fase a partir de medidas de intensidad importados de Óptica, en lugar de la interpretación holográfica de las intensidades. Se ha estudiado su aplicación a pequeños *clusters* de átomos, ya que suponen un modelo simplificado de los experimentos de LEED difuso. En particular, se han utilizado bases de datos recogidas a partir de diferentes direcciones de incidencia (tomografía). Este método se ha extendido también a superficies ordenadas. Los resultados de esta parte de la Tesis aún no se han publicado.

Paralelamente al desarrollo de nuevos métodos de LEED, se ha trabajado en la caracterización estructural de las superficies del rutilo TiO_2 . En particular, se ha realizado un estudio cuantitativo de datos LEED-IV experimentales de la superficie reconstruida $\text{TiO}_2(110)-1 \times 2$. Esta superficie ha sido objeto de controversia recientemente, debido a que diferentes observaciones experimentales han conducido a distintas interpretaciones y modelos para esta superficie [39]. Además de estos cálculos de LEED, el trabajo experimental (STM) y teórico (DFT) de otros miembros del grupo ha determinado la estructura relajada de esta superficie, junto a algunos hallazgos interesantes acerca de su estructura electrónica, que pueden encontrarse en:

- M. Blanco-Rey, J. Abad, C. Rogero, J. Mendez, M.F. Lopez, J.A. Martin-Gago, P. de Andres, "Structure of rutile $\text{TiO}_2(110)-1 \times 2$: formation of quasi-1D metallic chains", *Phys. Rev. Lett.* **96** (2006) 055502

Actualmente, se está preparando un artículo más completo donde se dan todos los detalles de la estructura.

Contenidos de la memoria

En el Capítulo 2 se hace una introducción a LEED, destacando el formalismo de tipo Dyson para la descripción de la dispersión múltiple y el concepto del operador matriz-t. Se realiza una descripción detallada de un cálculo IV completo típico en varios pasos, desde la dispersión por un sólo átomo hasta la dispersión por un bloque de varios planos atómicos, incluyendo vibraciones térmicas. Esta descripción es necesaria para introducir el código LEED90. Finalmente, se discuten brevemente otros aspectos de la teoría de LEED que aparecerán a lo largo de la memoria.

El Capítulo 3 muestra una descripción completa del análisis de la superficie $\text{TiO}_2(110)-1 \times 2$. En el contexto de una Tesis metodológica como esta, el Capítulo 3 puede considerarse como un ejemplo típico de búsqueda de una estructura por LEED. Esta estructura es altamente no trivial, y sobre ella se pueden discutir muchas características interesantes del análisis cuantitativo de LEED, como pueden ser la utilización de varias bases de datos experimentales, el efecto de las vibraciones térmicas, la topografía de los factores-R, etc.

El trabajo acerca de los adsorbatos moleculares se recoge en el Capítulo 4. De nuevo, se presenta el formalismo de Dyson para la dispersión múltiple, pero esta vez aplicado al caso particular de una molécula, en lugar de una superficie. Después, se presentan una serie de ejemplos de utilización de la matriz-t molecular en diferentes estructuras modelo. En el Capítulo 5 se muestra la prolongación de este trabajo, donde se presentan dos aplicaciones perturbativas del formalismo de matriz-t molecular.

El método SO se presenta en el Capítulo 6. Se analiza su rendimiento en varios sistemas modelo y se compara con otras técnicas de optimización para LEED existentes en la literatura.

El último Capítulo, 7, se ocupa de los métodos directos empleando técnicas convencionales de recuperación de fase y tomografía. Para chequear la efectividad del algoritmo propuesto, se emplean varios *clusters* de átomos, variando las direcciones

de incidencia y las energías. Se estudian también diversas formas de evitar las reconstrucciones borrosas, que son consecuencia de la dispersión múltiple en algunos casos. Finalmente, se discute la transferabilidad de estas técnicas a superficies ordenadas.

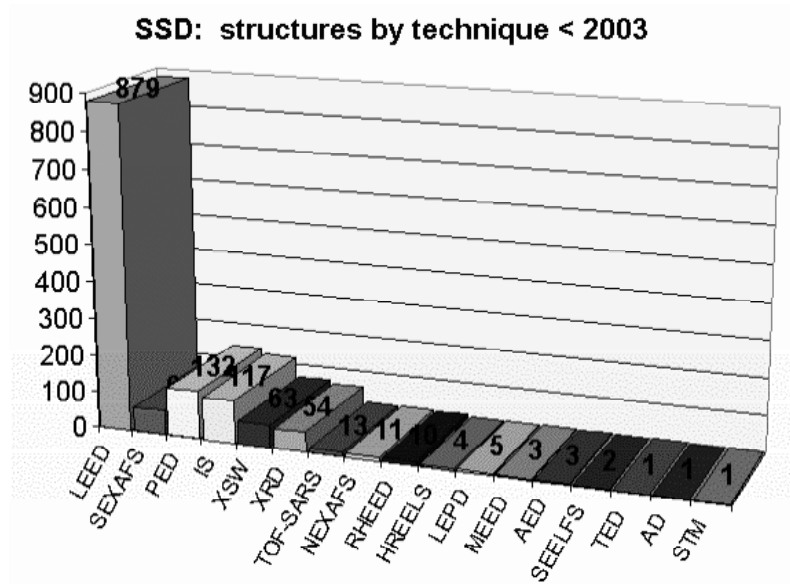


Figure 1.1: Number of resolved surface structures contained in NIST Surface Structure Database classified by the techniques used to determine them. The picture is taken from Ref. [40].

Inside the crystal in equilibrium, atoms adopt the minimum energy configuration. The existence of a surface implies a breaking of the translational lattice symmetry in the direction perpendicular to the surface, which provokes an increase in the total energy. Atoms in the surface region will adopt distorted positions w.r.t. bulk positions, creating an elastic term to compensate the symmetry loss. Thus, complex structures appear at the solid surface, some of them creating new bonds or destroying existing ones. In-plane lattice symmetry can eventually change, arising the so-called *surface reconstructions*. The symmetry group of the reconstructed surface will be a subgroup of the substrate symmetry group. Such reconstructions may appear, too, as a consequence of atom or molecule adsorption on the surface. It is the crystal's response to the appearance of a substrate/adsorbate bond term in the total energy. The geometrical arrangement of surface atoms determines both electronic and vibrational properties of the surface, that will be, in general, different from the bulk properties. A detailed knowledge of adsorption geometry is crucial, for example, to understand chemistry processes at the surface, such as heterogeneous catalysis. In

fact, the difference between physisorption and chemisorption determines the bond lengths between adsorbate and substrate atoms, and reaction paths are strongly dependent on the adsorption site and adsorbate orientation. Another example can be found at electronic device design, which relies in the knowledge of surface electronic and magnetic properties.

A number of surface characterization techniques have been developed in the last decades. They can be roughly divided into two categories: surface spectroscopies for chemical and electronic analysis (e.g. AES, XPS, EELS, NEXAFS and SEXAFS) on one hand, and diffraction (e.g. LEED, MEED, RHEED, MEIS, HEIS, XPD and SXRD) and microscopies with atomic resolution (e.g. STM and AFM) for structural analysis on the other hand, some of them including chemical selectivity, too [1, 2, 3, 4]. Apart from these experimental techniques, we must mention the importance of DFT methods in the present, as a support method for experiments and as a predictive tool of surface structural and electronic properties. Fig. 1.1 shows the NIST Surface Structure Database classification of the number of resolved structures by experimental techniques. Among them, Low-Energy Electron Diffraction (LEED) seems to be the most successful one to date.

LEED was one of the first subjects of surface study. Early experiments were carried out by Davisson and Germer in 1927 on a Ni(111) surface [5]. These first LEED experiments were the practical demonstration of the wave nature of electrons, postulated by Thompson and Reid [6]. For these investigations, Thompson and Davisson shared a Nobel prize in 1937. Van Hove *et al* give a nice historical description of LEED evolution in Ref. [1]. It is interesting to highlight that LEED development was stagnated until the sixties decade, in part because of the lack of an adequate theory to describe it. The theoretical work on multiple scattering theory and the fabrication of Ultra-High Vacuum (UHV) chambers gave a boost to LEED. Significant contributions to LEED theory were made by McRae (multiple scattering and transfer matrix [7]), Marcus and Jona (Fourier transforming of the wavefield [8]) or Beeby (Green functions [9]). Pendry included the atomic t-matrix formalism and realized inelastic damping effects must be considered, which produce evanescent waves [10]. He also introduced two efficient methods to account for interlayer multiple scattering: RFS (perturbative) [11] and layer doubling (exact), the latter in collaboration with Van Hove [12]. Tong developed composite layer method, that combines plane wave and partial wave basis sets [13].

Taking advantage of newly born computational resources, Pendry, Van Hove and collaborators gave the definitive step forward writing the first codes for LEED spectra calculation in the seventies [14, 15]. Experimental progress was done in the seventies, too, at laboratories such as IBM (Marcus and Jona group), Berkeley (Van Hove group), Cambridge (King group) or Erlangen (Heinz group). Electron dose was reduced in experimental setups and fast data acquisition techniques were developed. One of the main advances in monitorization was Video LEED, developed by Heinz *et al* [16]. Since then, LEED has established as one of the most relevant surface characterization technique.

As mentioned above, a complete description of LEED requires a multiple scattering formalism, since slow electrons interact strongly with surface atoms, making calculations much more complicated than in other diffraction techniques, like X-ray

diffraction, where X-rays interact weakly with the matter allowing a single scattering description with simple atomic scattering factors. However, multiple scattering processes produce a rich structure at diffracted spectra (the evolution of diffracted intensity spots with the incident electron energy, the so-called IV curves), which enhances sensitivity of LEED to atomic positions within a precision of hundredths of Å. There exist many other surface techniques that share the property of multiple scattering with LEED, and therefore, that could obtain some profit from theory developments in LEED. This is the case, for example, of Photoelectron Diffraction (PD) [17], Near-Edge X-ray Absorption Fine Structure (NEXAFS) [18] and even Scanning Tunneling Microscopy (STM) [19].

As in any other diffraction experiment, only intensities can be measured. In addition to this, multiple scattering processes convert the intensities in a function of complex dependence on the structure. Thus, to obtain the surface structure from a given experimental spectra, we must face a non-directly invertible problem. The usual procedure is a trial and error method, consisting of proposing model surfaces and computing the corresponding IV curves, until finding the model that best fits the experimental data. When the number of surface parameters to fit is high, algorithms can be used to make the search efficient [20]. The present Thesis deals with the theoretical aspects of LEED. In this dissertation, several methods of LEED analysis will be discussed, including implementations of spectra calculations, trial and error techniques and, from the opposite point of view, extraction of structural information directly from experimental spectra, i.e. the so-called direct methods.

Recent progress in LEED theory

The multiple scattering theory for IV curves calculation built in the sixties is very accurate, and the routines developed by Pendry and Van Hove are still widely used by other modern LEED codes.

Some LEED codes have been recently published that consist of modern version of those old sets of routines. These calculations include also thermal vibrations effects, which make them powerful tools even nowadays. This is the case of codes such as DL-LEED (FORTRAN90) [21] and CLEED (C++) [22] more recently including anisotropic vibrations.

Since then, theoretical challenges in LEED concern the way of making intensity calculations and structure search procedures more efficient in order to account for more complicated surfaces. Tensor LEED (TLEED) [23, 24] and Linear LEED (LLEED) [25] were the first attempts to accelerate IV calculations. With these two methods, given the diffracted amplitudes by a certain structure, it is possible to efficiently compute the amplitudes diffracted by a slightly different structure using a perturbative approach.

The interest in disordered structures, like lattice gas adsorbates present at some catalysis processes, motivated the implementations of multiple scattering calculations in clusters of atoms to account for diffuse LEED (DLEED) patterns [26], making use of formalisms that had been previously benchmarked at other techniques such as NEXAFS and PD.

Nowadays, efforts are oriented towards direct methods, i.e. direct retrieval of information from diffraction data with no trial and error methods [27]. Many of them

bear similarities with methods implemented for other diffraction techniques, since all diffraction methods are connected by lack of experimental information on the phase. Thus, direct methods are inherently phase retrieval methods from incomplete data. This is a classical problem in diffraction theory, and much literature can be found about this topic in general optics. For example, the idea of considering the diffuse diffracted spectra as a hologram was first put forward in the context of PD, first for single scattering [28], then for double scattering [29], and afterwards in LEED [30], where multiple scattering exists at the substrate. Modern implementations of holographic methods at electron diffraction techniques consider correction terms (*kernels*) and superposition of holograms recorded under different conditions [31, 32].

Imported from X-ray crystallography, the Patterson function [33] method has been applied to LEED in ordered surfaces, too. To overcome the blurring effect of multiple scattering and artifacts on the Patterson function, superposition of data taken at different incidences is lately used [34, 35]. Bayesian methods [36] are another type of X-ray crystallography typical direct methods that have been transferred to LEED recently [37].

Comparison between experiment and calculation is done by means of a reliability factor (R-factor). The R-factor, as a function of the surface parameters, is a hypersurface of complex topography. The model structure that produces the absolute minimum of the R-factor is regarded as the most likely structure, since it produces the best agreement with the available data, i.e. maximum correlation between theory and experiment. Directed search methods have also been developed to diminish the number of tried structures when doing searches. These methods are nothing but efficient minimum finding algorithms for the R-factor. Efforts in this area of LEED theory are focused in the development of global methods, which allow exploring larger areas in the parameter space. Available LEED codes usually combine the spectra calculation procedure with an efficient search code, that varies the parameters according to a minimum finder algorithm in order to try the least number of structures.

Actually, these methods of R-factor minimization should not be regarded as "direct" by themselves. They perform a trial and error procedure, though rather optimized, in contrast to the methods directly imported from optics, which involve a Fourier synthesis, such as holography and Patterson function. In the latter kind of methods, interatomic vectors and/or atomic positions are directly inferred from a spectral analysis of the intensity data. In the framework of this discussion, Bayesian-like methods would be in-between, since they have the ability of combining a Fourier synthesis with an iterative procedure that achieves a structure model that minimizes a certain cost function.

Motivation, objectives and achievements of this Thesis

The aim of the present Thesis is to make progress on current shortcomings of LEED theory. Despite significative improvements in other techniques that are making them more popular, we think that LEED can still provide surface science laboratories with good resources if some updates from the theory point of view are made.

A LEED-IV modern code has been written from scratch in FORTRAN-90/95, called LEED90, with the purpose of using it to benchmark any new method proposed

in the Thesis. This code has been the first one to work with non-diagonal t-matrices, necessary for our work. Although the existing description of multiple scattering is satisfactory, we have taken as the first objective a handy description of ordered molecular adsorbates, due to the interest of these structures in chemistry at surfaces. This work has been based in the formalism put forward by Andersson and Pendry [38] and keeping an eye in the already developed codes for atomic clusters in other techniques and DLEED. The result has been a FORTRAN-90/95 code, TMOL, that computes a molecular t-matrix that can be used in combination to typical LEED codes. Functionality of this method has been tested in a number of model surfaces. This part of the work has produced three publications:

- M. Blanco-Rey, P. de Andres, G. Held and D.A. King, “TMOL v1.1: Molecular t-matrices for Low-Energy Electron Diffraction”, *Comp. Phys. Commun.* **161** (2004) 166-178
- M. Blanco-Rey, P. de Andres, G. Held and D.A. King, “A FORTRAN-90 Low-Energy Electron Diffraction program (LEED90 v1.1)”, *Comp. Phys. Commun.* **161** (2004) 151-165
- M. Blanco-Rey, P. de Andres, G. Held and D.A. King, “A molecular t-matrix approach to calculating Low-Energy Electron Diffraction intensities for ordered molecular adsorbates”, *Surf. Sci.* **579** (2005) 89-99

A prolongation to this work combining molecular t-matrices and TLEED formalism has been carried out in collaboration with Prof. K. Heinz of the University of Erlangen-Nürnberg. The corresponding results have been the subject of a communication to the ICSOS-8 conference, held in Munich in July, 2005, and entitled “Molecular T-matrix formalism for LEED”.

A new global directed search algorithm has been proposed. It uses a combination of ideas about reduced databases and ergodic methods. Its name is Simultaneous Optimization algorithm (SO), and has been tested on two model situations: phase shifts retrieval in scattering by a single atoms and structural parameter fit in LEED simulated data. A thorough study on its statistical behaviour has proved that SO is highly competitive when compared to other similar global methods. The results concerning this work have been published in the following reference:

- M. Blanco-Rey P. de Andres, “Surface Diffraction Structure Determination from Combinatorial Simultaneous Optimization”, *Surf. Sci.* **600** (2006) L91-L95.

A paper about SO performance on real experimental data is under preparation.

The phase problem in LEED has been investigated using typical phase retrieval methods from intensity measurements imported from optics, rather than the holographic interpretation of diffracted intensities. The ability of the proposed algorithm to determine structures has been applied to small clusters of atoms, since they can be considered as simplified models of DLEED experiments. In particular, databases from multiple incidence (tomography) have been used. An extension of this method to ordered surfaces has been made, too. The results of this part of the Thesis are still unpublished.

In parallel to new LEED methods development, work has been carried out on the topic of the rutile TiO_2 surface structure characterization. Particularly, a quantitative study of the experimental LEED-IV data from the reconstructed face $\text{TiO}_2(110)-1 \times 2$ has been done. This surface has been a subject of controversy lately, since different experimental observations lead to different interpretations and models for this surface [39]. In addition to these LEED calculations, the experimental (STM) and theoretical (DFT) work of other group members yielded the relaxed structure of this surface, together with some interesting findings in the electronic structure, which can be found at:

- M. Blanco-Rey, J. Abad, C. Rogero, J. Mendez, M.F. Lopez, J.A. Martin-Gago, P. de Andres, “Structure of rutile $\text{TiO}_2(110)-1 \times 2$: formation of quasi-1D metallic chains”, *Phys. Rev. Lett.* **96** (2006) 055502

A more comprehensive paper, based on the structure details found by LEED-IV, is being prepared.

Outline of the dissertation

In Chapter 2 an introduction to LEED is made, emphasizing the Dyson-like multiple scattering formalism derivation and the concept of the t-matrix operator. A detailed description of a complete typical IV calculation for an ordered surface is done in several steps, from scattering by a single atom to scattering by a stack of planes, including thermal vibrations. The description of these methods is necessary to introduce the LEED90 code. Finally, other LEED aspects that will appear during the dissertation are briefly discussed.

Chapter 3 shows a comprehensive description of the $\text{TiO}_2(110)-1 \times 2$ surface analysis. In the context of a methodological Thesis like this, Chapter 3 can be seen as an example of how a typical structure search by LEED is done. This structure is highly non-trivial and many interesting features of LEED quantitative analysis can be discussed on it, such as the use of several experimental databases, thermal vibrations effect, the R-factor topography, etc.

The work regarding the study of molecular adsorbates is shown in Chapter 4. Again, the Dyson formalism for multiple scattering is presented, but applied to the particular case of a molecule, rather than to a surface. Afterwards, a series of examples of the molecular t-matrix performance on different model structures is presented. A prolongation to this work is shown in Chapter 5, where two perturbative usages of the molecular t-matrix formalism are presented.

The SO method is presented at Chapter 6. Its performance on model systems will be analyzed and compared with other optimization techniques previously reported for LEED.

The last Chapter, 7, deals with the approach to direct method using conventional phase retrieval methods and tomography. Small clusters of atoms are used to benchmark the efficiency of the proposed algorithm, varying incidence directions and energies. Ways to overcome the multiple scattering blurring effect are investigated, too. Finally, the transferability of these techniques to ordered surfaces is discussed.

Chapter 2

Surface Structure by LEED

2.1 Introduction

In a LEED experiment, electrons elastically backscattered from a surface are analyzed. The incident electrons in a LEED experiment, similarly to other diffraction techniques, have a De Broglie wavelength of the order of the interatomic spacings inside the crystal (for $E = 150$ eV, wavelength is ~ 1 Å). On the other hand, we are looking for structural sensitivity at the ~ 5 atomic layers closer to the vacuum. Inelastic mean free path in solids, λ , takes its lowest values for a range of energies 20-500 eV, $\lambda = 5 - 10$ Å, which is adequate to explore the surface region.

If the surface has translational ordering, electrons will exchange parallel momentum with the lattice in discrete quantities, namely the surface reciprocal lattice vectors following Bloch theorem, while electron perpendicular momentum takes its value from energy conservation condition. Thus, reflected electron wavevectors are written as ¹:

$$\vec{k}_{\vec{g},||} = \vec{k}_{0||} + \vec{g} \quad k_{\vec{g},z} = -\sqrt{2E - |\vec{k}_{0||} + \vec{g}|^2} \quad (2.1)$$

Here, E is the incident electron energy and \vec{g} labels reciprocal lattice vectors,

$$\vec{g} = h\vec{A} + k\vec{B} \quad (2.2)$$

where (h, k) are the Miller indices describing \vec{g} and (\vec{A}, \vec{B}) are the surface reciprocal lattice unit cell vectors. Notice that the 0Z axis points inwards the solid. We will use this convention through all the dissertation. The condition for backscattered waves to propagate in the vacuum is $|\vec{k}_{0||} + \vec{g}|^2 > 2E$. These non-evanescent diffracted beams are collected in the detector as a set of sharp bright spots. The diffraction pattern will contain the symmetry elements of the surface symmetry group. Lack of ordering, due to surface defects or disordered adsorbates, appears as a continuous background superimposed to the spot pattern. For its simplicity, LEED is widely used in surface science laboratories as an additional instrument for determination of symmetries and/or sample quality by simple visual inspection.

However, the power of LEED is revealed when studying quantitatively the diffracted intensity evolution with both the incident electron energy and direction. Normally,

¹These formulas are correct if atomic units are to be used, i.e. $\hbar = m = e = 1$, energies in Hartrees (1 H = 27.2 eV) and distances in Bohr or atomic units (1 a.u. = 0.529 Å). Otherwise, $|\vec{k}_{\vec{g}}|^2 = \frac{2mE}{\hbar^2}$ must be used.

plots of the intensity vs. energy for each diffraction spot, the so-called IV curves, show a rich structure. A thorough study of these curves allows to solve surface structures with a higher precision than that given by the electron De Broglie wavelength, $\sim 1 \text{ \AA}$. The reason for this is that backscattered wavefield interference conditions, which appear as a complex profile in the spectra, are intimately related to the surface structure due to multiple scattering (MS) paths undergone by the electrons. Moreover, it can provide information about non-structural parameters, such as atomic thermal vibration amplitudes and/or chemical species concentration at the lattice sites.

The main problem concerning LEED-IV analysis is that the relationship between structure and spectra is not directly invertible, due to MS and the impossibility of measuring the diffracted wave phase. As the theory for computing the LEED-IV spectra caused by a given surface has been already developed and is very accurate [14, 1], the structure is solved by surface models trial and comparison of their IV's with the experimental ones. Most popular IV calculation methods are summarized in the present Chapter. Comparison of theory and experiment is made by means of a correlation quality factor or R-factor. Many R-factors have been proposed in the literature, being Pendry's R_P [41], the most widely used. The trial and error procedure mentioned above may result unprofitable if done by hand, since IV calculation is usually a computationally demanding task and since, in many cases, a number of surface parameters are to be fitted. To overcome this drawback much effort has been developed in several fronts:

- Methods for efficient computation of diffracted intensities, some of them based on perturbative approaches, such as Tensor LEED [23] (to be seen at section 2.10) and Linear LEED [25, 42].
- In the present Thesis a method for handy dealing with molecular adsorbates when computing IV curves is discussed in Chapter 4.
- Directed search methods have been developed. These are, roughly speaking, methods for minimizing the R-factor, which can be seen as a hypersurface of several variables. These variables can be both structural or nonstructural parameters. As a function of them, the R-factor is a complex hypersurface, generally showing several minima. Thus, its minimization is one of the main actual subjects of LEED theory. In Chapter 6 a review of existing search methods is done and a new algorithm is proposed.
- Other techniques for directly extracting surface parameters from intensity measurements exist, such as holographic and bayesian methods. They will be discussed in Chapter 7.

2.2 LEED experiments

The LEED experimental setup must be kept under UHV conditions ($< 10 \text{ Torr}$) to avoid sample deterioration by impurity adsorption during the measurement process. Deterioration can be due to damaging of the sample by the incident electron beam,

too. Despite low dose methods have been developed to overcome this, accurate intensity measurements should be as fast as possible. Auger Electron Spectroscopy (AES) is commonly used during the measurements to monitor impurity concentration. Fig. 2.1 shows a scheme of a typical LEED equipment.

The electron gun provides a low current ($10^{-4} - 10^{-8}$ A) electron beam emitted from a heated tungsten filament. Electron energy is selected by varying the potential across anode and cathode, and noise is eliminated by several filters. The incident beam is focused by a magnetic lensing system. The sample is mounted on a precision manipulator and connected to earth. A system of energy suppressor grids is used for filtering out non-elastically backscattered electrons. The energy spread of these filters depends on the bias potential applied to the filtering grids, which are connected to the gun anodes. The proportion of backscattered electrons is small, about $\lesssim 1\%$ of the incident intensity, and decrease when incident energy increases. The area coherently illuminated by incident electrons is ~ 500 Å.

Electrons backscattered from the surface are collected on a fluorescent screen. Long ago, a Faraday-cup collector was used on individual beams for intensity recording, following the beam being drift by energy variation. This method had the drawback of being time consuming, with the subsequent risk for the sample integrity. Nowadays, the spectra is video recorded, like in the AUTOLEED system developed at Erlangen [26], and intensities are measured afterwards from integration and background filtering out of the recorded image by using a specific software. An alternative novel recording method that uses fiber optic and very low beam current (~ 1 nA) is being tested in Cambridge [43].

Low current and fast data acquisition contribute positively to diminish the experimental error at intensity measurements. However, other sources of error may exist, such as misalignment of the sample. Known symmetry conditions in the spots can be used to adjust incidence conditions, by moving the manipulator and comparing IV curves by a R-factor until finding the desired symmetry among them. It is a widely used task to take averages of equally symmetric curves to reduce the signal-to-noise ratio. Residual noise in the curves can be further reduced by application of smoothing algorithms [1, 44].

2.3 Single atom scattering: the muffin tin approach

The whole all-electron Schrödinger equation for elastic scattering of a electron inside the surface must account for all interactions among the incident electron, the crystal electrons and nuclei. As in many solid state problems, the Hartree-Fock (HF) approximation is introduced to make the Schrödinger equation tractable. It consists in taking the crystal electron wavefunction to be a product (a Slater determinant) of individual electron functions, $\psi_i(\vec{r}_i)$. Calling $\phi(\vec{r})$ to the incident electron wavefunction, the one-electron HF equation for the LEED problem is:

$$\left[-\frac{1}{2} \vec{\nabla}_n^2 + V_H(\vec{r}_n) \right] \phi(\vec{r}_n) + \int d^3\vec{r}_i V_{ex}(\vec{r}_i; \vec{r}_n) \phi(\vec{r}_i) = E \phi(\vec{r}_n) \quad (2.3)$$

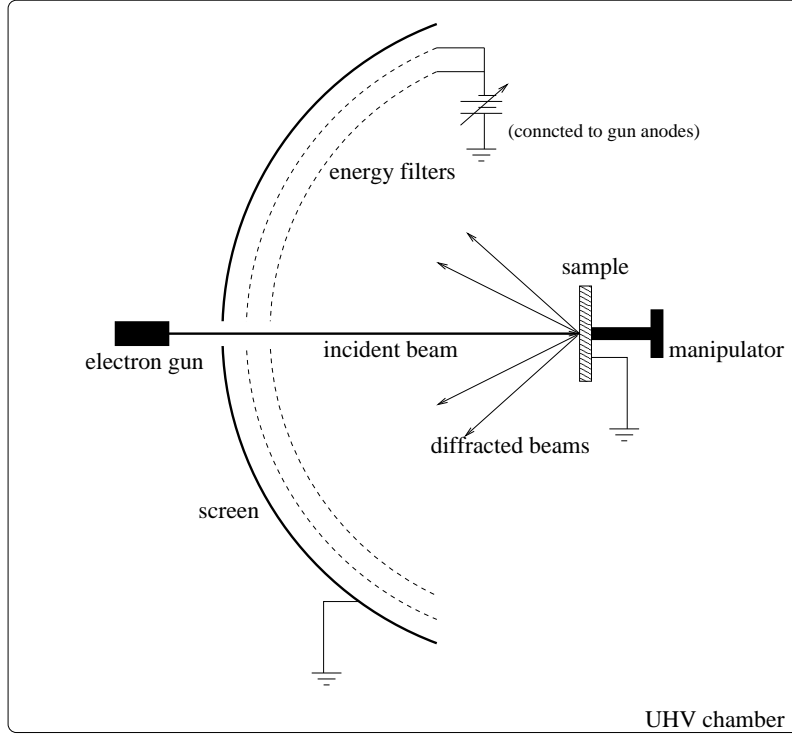


Figure 2.1: Schematic LEED experimental setup

where

$$V_H(\vec{r}_n) = -\frac{Z_n}{r_n} + V_{sc}(\vec{r}_n) + \sum_i^{\text{electrons}} \int d^3\vec{r}_i \frac{|\psi_i(\vec{r}_i)|^2}{|\vec{r}_n - \vec{r}_i|} \quad (2.4)$$

and

$$V_{ex}(\vec{r}_i; \vec{r}_n) = - \sum_i^{\text{electrons}} \frac{\psi_i^*(\vec{r}_i)\psi(\vec{r}_n)}{|\vec{r}_n - \vec{r}_i|} \quad (2.5)$$

Here, i labels crystal electrons, n labels atoms and Z_n are the atomic numbers. V_{sc} is the screened potential, that is weak in general. V_{ex} is the exchange term, that is taken to be local in the so-called Slater approximation, to yield a separable HF equation.

Even if the HF equation is separable and can be solved self-consistently, the so-called *muffin tin* further approximation is taken to further simplify the problem. It assumes that, around an ion core, the electric charge stays inside a sphere, centred at each atomic position, in such a way that neighbouring spheres do not overlap. Thus, the potential inside the spheres has spherical symmetry and the potential outside the spheres is constant. This approximation has been proved to be accurate in close packed metals. Fig. 2.2 shows a transversal slice of the surface potential after taking the muffin tin approximation. The muffin tin constant, V_{0r} , is defined as the interstitial potential value. This is not exactly the crystal inner potential, but this coarse description is enough to develop an accurate theory for LEED, because energies are not too close to the Fermi level. When referred to the vacuum level,

the muffin tin constant accounts for the kinetic energy change experimented by the incident electron entering or leaving the surface region. At the surface upper layers, the potential outside the spheres is no longer constant. Usually, its functional form is approximated by a square step to simplify LEED calculations. Spherical symmetry strongly simplifies the HF equation, because it allows to split it into radial and angular parts. In this situation, the most appropriate basis consists of a set of partial waves,

$$R_l(r)Y_{lm}(\theta, \phi) \quad (2.6)$$

where Y_{lm} are spherical harmonics for quantum numbers (l, m) and R_l is the solution to the radial equation:

$$-\frac{1}{r} \frac{d}{dr} \left(r^2 \frac{dR_l(r)}{dr} \right) + \frac{l(l+1)}{2r^2} R_l(r) + (V_H(r) + V_{ex}(r)) R_l(r) = E R_l(r) \quad (2.7)$$

Thus, the two main parameters in the LEED problem appear to be the incident electron momentum, κ , and the cutoff value of the partial wave expansion, l_{\max} . Summarizing, the problem has been split into ion core parts, each of which is further split into radial and angular parts. Outside the potential range, with V_H and V_{ex} set to zero, solutions to Eq. (2.7) are

$$R_l(r) \propto j_l(r) + \frac{1}{2}(e^{2i\delta_l} - 1)h_l^{(1)}(r) \quad (2.8)$$

where j_l are Bessel spherical functions and $h_l^{(1)}$ are first kind spherical Hankel functions. The aim of phase shifts δ_l is to keep flux conservation in scattering at the ion core. The actual phase shift values are calculated from matching conditions at the muffin tin surface. The scattering by the ion core can be described matricially by the so-called t-matrix, whose elements in the partial wave basis set are

$$t_l(E) = \frac{1}{2}(e^{2i\delta_l(E)} - 1) \quad (2.9)$$

In this case, the t-matrix is diagonal, since we have used spherical muffin tins. A more general solution can be found for a single ion core Schrödinger equation that do not impose spherical symmetry to the potential [45]. The wavefunction is written as an expansion of plane waves, too, the difference being that different (l, m) components are not separable into single- l equations. As a result to that, a generalized non-diagonal t-matrix can be defined. We will find this case for atom anisotropic vibrations.

As the core region is not very polarisable, the scattering by the core does not change much from an atomic to a crystalline environment, even at the surface region. This fact can be observed in the practice. Furthermore, LEED has chemical sensitivity via the phase shifts, but it is less accurate than in the case of PD, where the incident photon energies determines which chemical species contribute to the diffraction pattern.

2.4 Information from IV curves visualization

Some valuable information can be retrieved from LEED spectra prior to MS calculations. This information concerns symmetry (achievable from direct visualization

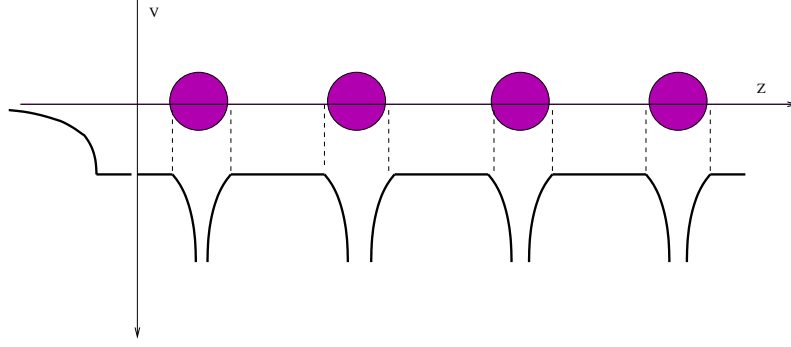


Figure 2.2: Transversal slice of the crystal potential near the surface within the muffin tin approximation. Positive z axis points inwards the solid.

of the spots symmetry), electronic parameters, such as V_{0r} and V_{0i} , and even some structural parameters can be accessed by a kinematic theory, less demanding than MS.

Symmetry

Commonly, the overlayer has a larger unit cell than that of the clean surface. If their basis vectors are simply related, fractional order spots appear in the diffraction pattern. If $\{\vec{a}_B, \vec{b}_B\}$ and $\{\vec{a}_C, \vec{b}_C\}$ are the vectors defining the bulk and overlayer unit cells respectively, then the superstructure matrix $\{m_{ij}\}$ is defined by

$$\begin{pmatrix} \vec{a}_C \\ \vec{b}_C \end{pmatrix} = \begin{pmatrix} m_{11} & m_{12} \\ m_{21} & m_{22} \end{pmatrix} \begin{pmatrix} \vec{a}_B \\ \vec{b}_B \end{pmatrix} \quad (2.10)$$

This information about the superstructure is directly available from simple spot pattern visualization. Since the diffraction pattern must contain all the crystal symmetry elements, the symmetry group can be determined sometimes. However, this must be carefully done, since several domains with different orientations can coexist in the surface. In this case, the total diffraction pattern is a superposition of the patterns generated by the independent domains, weighted by their respective extent area. As mentioned above, lack of ordering will appear as a continuous background diffraction pattern overimposed to the spots generated by lattice periodicity (i.e. Diffuse LEED, to be discussed at section 2.9).

Peak position: Bragg conditions

A kind of Bragg condition for atomic planes can be established for LEED reflections, in a similar way to X-ray diffraction, being the main difference the deeper penetration of the latter. When using X-rays, the diffraction pattern can be interpreted (in a very simplified picture) as the product

$$f_1(\vec{q})S(\vec{q}) \quad (2.11)$$

where \vec{q} are the diffraction vectors, $f_1(\vec{q})$ is a single atom scattering factor and $S(\vec{q})$ is the crystal structure factor. This formula appears as the result of Fourier transforming the whole crystal potential, which can be seen as the convolution product of individual single atomic potentials and a Dirac delta function with peaks at the atomic positions. This interpretation is valid when MS events are not present. Actually, spot positions in the diffraction pattern are kinematic. Taking this kinematic approach in LEED formalism, some peaks of the IV curves can be identified as interlayer distances. However, for the majority of surfaces, this approach does not provide trustworthy information about real interatomic distances.

Besides, in all cases, a shift in the peak position appears which is related to V_{0r} . In general, V_{0r} is treated as an additional parameter to fit during the refinement procedure. Values usually range between 5 – 15 eV. For fine structure fitting, an energy-dependent inner potential must be used [46] to take into account the energy dependence of the self-energy, due to the readjustment of solid's electrons to the incoming electron as described by the exchange-correlation potential term [47].

Peak width: electron damping

Inelastic scattering events contribute a damping in the electron penetration depth. Therefore, the electron mean free path reduces the number of contributing ion cores. This behaviour can be modelled by adding an imaginary part to the incident electron energy inside the solid (optical potential):

$$V_0 = V_{0r} - iV_{0i} \quad (2.12)$$

with $V_{0i} \sim k/\lambda$. As long as energies are kept inside the 20 – 250 eV range mentioned before, this approximation will be useful. A relationship can be established between peak width and V_{0i} . If only a finite number of scatterers (atomic planes within the penetration region in our case), is taken, from simple optics diffraction theory in Fraunhofer conditions, peak width is $\Delta = \frac{\pi k}{2\lambda} \sim V_{0i}$ [15]. Some refinement can be introduced by letting V_{0i} be dependent on the depth.

2.5 General MS theory

Before focusing in the LEED problem, we shall discuss MS theory in general [45]. In the presence of a generic scatterer described by a central potential $V(\vec{r})$, the electron wavefunction must hold the time-independent Schrödinger equation (in atomic units, i.e. Bohr and Hartrees):

$$\left(-\frac{1}{2}\vec{\nabla}^2 + V(\vec{r}) \right) \psi(\vec{r}) = E\psi(\vec{r}) \quad (2.13)$$

The solutions to this equation can be written formally as the integral Lippman-Schwinger equation:

$$\psi(\vec{r}) = \phi(\vec{r}) + \int G_0(k; \vec{r} - \vec{r}') V(\vec{r}') \psi(\vec{r}') d^3\vec{r}' \quad (2.14)$$

where $\phi(\vec{r}) = e^{i\vec{k}\cdot\vec{r}}$ is the incident plane wave, $k = \sqrt{2E}$ and $G_0(k; \vec{r} - \vec{r}')$ is the free space Green propagator:

$$G_0(k; \vec{r} - \vec{r}') = -\frac{1}{4\pi} \frac{e^{ik|\vec{r}-\vec{r}'|}}{|\vec{r} - \vec{r}'|} \quad (2.15)$$

The meaning of Eq. (2.14) is clear: the total scattered wavefield $\psi(\vec{r})$ is formed by the superposition of the wavefield not affected by the potential and the scattered wavefield, which depends on $\psi(\vec{r})$ itself.

We can introduce the T -operator to rewrite Eq. (2.14):

$$\begin{aligned} \psi(\vec{r}) &= \phi(\vec{r}) + \int G_0(k; \vec{r} - \vec{r}') T(\vec{r}', \vec{r}'') \phi(\vec{r}'') d^3\vec{r}' d^3\vec{r}'' \\ T(\vec{r}', \vec{r}'') &= V(\vec{r}') \left[\delta(\vec{r}' - \vec{r}'') + \int G_0(k; \vec{r} - \vec{r}') T(\vec{r}', \vec{r}'') d^3\vec{r}'' \right] \end{aligned} \quad (2.16)$$

We can change the coordinate representation above to a description in terms of operators, converting the integral spatial equations into matrix equations:

$$T = V + VG_0T = V + VG_0V + VG_0VG_0V + \dots \quad (2.17)$$

If this series is convergent, this equation can be solved by doing

$$T = (1 - VG_0)^{-1}V \quad (2.18)$$

which is known as the Dyson equation.

We are interested in the particular case of a potential formed by the superposition of individual scatterers, i.e. $V(\vec{r}) = \sum_i V^i(\vec{r} - \vec{r}_i)$, or formally $V = \sum_i V^i$. In this case, the Eq. (2.17) is

$$T = \sum_i V_i + \sum_{ij} V_i G_0 V_j + \sum_{ijk} V_i G_0 V_j G_0 V_k + \dots \quad (2.19)$$

Here, the G_0 propagators connect scatterer sites. For example, in the term $V_i G_0 V_j$, G_0 is connecting sites j -th and i -th. We can define the t^i -matrix as the sum of products over the same i -th scatterer, $t^i = V_i + V_i G_0 V_i + V_i G_0 V_i G_0 V_i + \dots$, so that Eq. (2.19) is written as

$$T = \sum_i t^i + \sum_{i,j \neq i} t^i G_0 t^j + \dots \quad (2.20)$$

In this equation, reading from right to left, we can distinguish scattering paths described by terms T^{ij} beginning at the j -th and ending at the i -th scatterer. Grouping those terms, we obtain:

$$T^{ij} = t^i \delta_{ij} + t^i G_0 \sum_{k \neq i} T^{kj} \quad (2.21)$$

which is a fundamental equation to understand MS.

2.6 Full-dynamical LEED theory

The LEED backscattered intensity obtained by taking into account MS theory is the so-called “full-dynamical”, in contrast to the single scattering or “kinematic” theory. In this section, we will develop the usual full-dynamical LEED theory for surfaces from the lowest level, atomic scattering, to the highest, scattering by a stack of atomic planes forming a semi-infinite slab. The MS expression will be worked out for the particular case of Bravais atomic planes, for simplicity and since the program LEED90 developed during this Thesis works under that constraint.

Inside the solid, electrons are affected by the inner potential. Thus, their wavevector perpendicular component is a complex magnitude, that depends on E , V_{0r} , V_{0i} , $\vec{k}_{0||}$ and \vec{g} :

$$K_{\vec{g},z}^{\pm} = \pm \sqrt{2(E - V_{0r} + iV_{0i}) - |\vec{k}_{0||} + \vec{g}|^2} \quad (2.22)$$

resulting in a damping of the wavefunction as the electron travels through the solid. According to the convention used throughout this dissertation, the $(+/-)$ signs indicate if the wave propagates towards the bulk or towards the vacuum respectively.

2.6.1 Scattering by an atomic plane

The incident wavefield impinging on the (Bravais) atomic plane can be expressed as a superposition of plane waves:

$$\psi_{\text{inc}}(\vec{r}) = \sum_{\vec{g}} U_{\vec{g}}^+ e^{i\vec{K}_{\vec{g}}^+ \cdot \vec{r}} \quad (2.23)$$

where the electron momentum is conditioned by the Bloch theorem according to Eq. (2.1). We change to a partial wave basis, where phase shifts formalism is easy to apply. To do this, we chose an ion core, the k -th unit cell with position vector \vec{R}_k for example, and write the incident wavefield as an expansion of incoming partial waves centred about it:

$$\psi_{\text{inc}}(\vec{r}) = \sum_{lm} A_{lm,k}^{(0)} j_l(\kappa|\vec{r} - \vec{R}_k|) Y_{lm}(\Omega(\vec{r} - \vec{R}_k)) \quad (2.24)$$

where the expansion coefficients are:

$$A_{lm,k}^{(0)} = \sum_{\vec{g}} U_{\vec{g}}^+ e^{i\vec{K}_{\vec{g}}^+ \cdot \vec{R}_k} 4\pi i^l (-1)^m Y_{l-m}(\vec{K}_{\vec{g}}^+) \quad (2.25)$$

The wavefield scattered by the k -th ion core is

$$\psi_{\text{scat}}(\vec{r}) = \sum_{lm} A_{lm,k}^{(0)} t_l(k) h_l^{(1)}(\kappa|\vec{r} - \vec{R}_k|) Y_{lm}(\Omega(\vec{r} - \vec{R}_k)) \quad (2.26)$$

where $t_l(k)$ are the k -th ion core atomic t-matrix elements. Now, the total incident amplitude coefficients on k are the superposition of incident and scattered wavefields:

$$A_{lm,k} = A_{lm,k}^{(s)} + A_{lm,k}^{(0)} \quad (2.27)$$

where $A_{lm,k}^{(s)}$ represents the coefficients of the amplitude incident on k scattered by the other ion cores, which depends on $A_{lm,k}$ through MS. Thus, the $A_{lm,k}^{(s)}$ quantities must be determined *self-consistently*. This fact is the key to the LEED formalism.

In a similar way, the wavefield incident on the atom at the origin is contributed by scattering at the other ion cores of the plane. This wavefield is:

$$\sum_{lm} \sum_{k \neq 0} A_{lm,k} t_l(k) h_l^{(1)}(\kappa|\vec{r} - \vec{R}_k|) Y_{lm}(\Omega(\vec{r} - \vec{R}_k)) \quad (2.28)$$

Due to lattice periodicity, the wavefield incident at two sites k and k' of the plane differ by a phase factor $e^{i\vec{k}_{\parallel,0} \cdot (\vec{R}_k - \vec{R}_{k'})}$. Thus,

$$A_{lm,k} = A_{lm,0} e^{i\vec{k}_{\parallel,0} \cdot \vec{R}_k} \quad (2.29)$$

On the other hand, we want to compute $A_{lm,0}^{(s)}$ using partial waves centred at the origin. For this, we use Green free space propagators, $G_{lm,l''m''}$ (their explicit expression can be found in Appendix A), that have the following property:

$$h_l^{(1)}(\kappa|\vec{r} - \vec{R}_k|) Y_{lm}(\Omega(\vec{r} - \vec{R}_k)) = \sum_{l''m''} G_{lm,l''m''}(-\vec{R}_k) j_{l''}(kr) Y_{l''m''}(\Omega(\vec{r})) \quad (2.30)$$

Finally, we substitute Eqs. (2.29,2.30) in Eq. (2.28) to obtain the total wavefield incident at the origin:

$$\sum_{l''m''} \left(\sum_{lm} \sum_{k \neq 0} A_{lm,0} t_l(k) e^{i\vec{k}_{\parallel,0} \cdot \vec{R}_k} G_{lm,l''m''}(-\vec{R}_k) \right) j_{l''}(kr) Y_{l''m''}(\Omega(\vec{r})) \quad (2.31)$$

where some quantities have been grouped to allow writing the expansion coefficients in this way:

$$\begin{aligned} A_{l''m'',0}^{(s)} &= \sum_{lm} A_{lm,0} X_{lm,l''m''} \\ A_{lm,0} &= A_{lm,0}^{(s)} + A_{lm,0}^{(0)} \end{aligned} \quad (2.32)$$

where the \tilde{X} matrix elements are

$$X_{lm,l''m''} = \sum_{k \neq 0} t_l(k) e^{i\vec{k}_{\parallel,0} \cdot \vec{R}_k} G_{lm,l''m''} \quad (2.33)$$

and we obtain the MS self-consistency relationship:

$$A_{lm,0}^{(s)} = \sum_{l'm'} A_{l'm',0}^{(0)} (1 - X)_{lm,l'm'}^{-1} \quad (2.34)$$

Setting the \tilde{X} matrix to zero suppresses MS contributions inside a layer.

It is useful to use operator formulation to rewrite the formulas derived above, especially because we are expecting to work with general non-diagonal t-matrices for the individual scatterers, as it is the case of the present Thesis. We can write the \tilde{X} matrix as

$$\tilde{X} = \tilde{t} \cdot \tilde{g} \quad (2.35)$$

where $\tilde{\mathcal{G}}$ would be the plane's Green function, containing information about all scattering paths therein, and

$$\tilde{\mathcal{T}} = (1 - \tilde{X})^{-1} \cdot \tilde{t} \quad (2.36)$$

is the whole plane scattering matrix. Observing that all the t -matrices are equal, the self-consistency relationship this formula was derived from can be revised in terms of scattering operators in this way:

$$\begin{aligned} \tilde{\mathcal{T}} &= \tilde{t} + \tilde{t} \left(\sum_{k \neq 0} \mathcal{G}^{(k)} \right) \tilde{\mathcal{T}} \\ \tilde{\mathcal{G}} &= \sum_{k \neq 0} \mathcal{G}^{(k)} \\ \tilde{\mathcal{G}}_{lm, l'' m''}^{(k)} &= e^{i \vec{k}_{\parallel, 0} \cdot \vec{R}_k} G_{lm, l'' m''}(-\vec{R}_k) \end{aligned} \quad (2.37)$$

Substituting the expression of propagator elements (see Appendix A), and noticing that atoms are coplanar, the explicate expression for the operators above are:

$$\mathcal{G}_{lm, l'' m''} = \sum_{L'} C^{lm}(l' m', l'' m'') F_{l' m'} \quad (2.38)$$

$$\begin{aligned} C^{lm}(l' m', l'' m'') &= 4\pi (-1)^{\frac{1}{2}(l-l'-l'')} (-1)^{m'+m''} Y_{l'-m'}\left(\frac{\pi}{2}, 0\right) \\ &\times \int d\Omega Y_{lm}(\Omega) Y_{l' m'}(\Omega) Y_{l'' m''}(\Omega) \end{aligned} \quad (2.39)$$

$$F_{l' m'} = \sum_{k \neq 0} i h_{l'}^{(1)}(\kappa |\vec{R}_k|) e^{-i m' \phi(\vec{R}_k)} (-1)^{m'} e^{i \vec{k}_{0\parallel} \cdot \vec{R}_k} \quad (2.40)$$

where the $C^{lm}(l' m', l'' m'')$ are the Clebsch-Gordan coefficients and the three-spherical harmonics integrals are the so-called Gaunt coefficients. Some information about these coefficients is summarized in Appendix B. $\phi(\vec{R}_k)$ is the angle of the \vec{R}_k vector w.r.t. the plane axes. Lattice summations, $F_{l' m'}$, are done over a finite number of unit cells. Convergence of these sums is ensured as long as electron damping is strong enough. However, if damping is weak, an alternative method is required, such as Kambe's, based on a Madelung-like summation scheme, which we will not use.

The last step is straightforward and consists in a basis change of the $\tilde{\mathcal{T}}$ matrix from the partial waves back to the crystal plane waves, better suited to the plane symmetry. This change yields a set of four matrices for the plane: \tilde{M}^{++} and \tilde{M}^{--} for layer transmission in both incidence directions, and \tilde{M}^{+-} and \tilde{M}^{-+} for layer reflection. Symbolically, this change is

$$\langle k_{\parallel} + \vec{g}' | \mathcal{T} | k_{\parallel} + \vec{g} \rangle \quad (2.41)$$

and the matrix elements, as a function of $\tilde{\mathcal{T}}$ matrix elements, are [13, 14]:

$$M_{\vec{g}', \vec{g}}^{\pm\pm} = \frac{8\pi^2 i}{A \kappa K_{\vec{g}'z}^+} \sum_{L'L} i^l (-1)^m Y_{l-m}(\Omega(K_{\vec{g}}^{\pm})) \mathcal{T}_{LL'} i^{-l'} Y_{l' m'}(\Omega(K_{\vec{g}}^{\pm})) \quad (2.42)$$

If a superstructure is present at the surface, then any substrate vector can be written as

$$\vec{R}^B = N_1 \vec{a}_C + N_2 \vec{b}_C + n_1 \vec{a}_B + n_2 \vec{b}_B \quad (2.43)$$

where $N_{1,2}$ are integers that can take any value and $n_{1,2}$ are finite integers. Bulk lattice is thus split into sublattices, each of them labelled by a pair of indices (n_1, n_2) . The number of sublattices present in the system is $|\det M|$ with $|\det M| = (1 + nl_1) \cdot (1 + nl_2)$, where $0 \leq n_1 \leq nl_1$ and $0 \leq n_2 \leq nl_2$. In the same way, any vector of the reciprocal superlattice can be written as

$$\vec{g}^C = h \vec{A}_B + k \vec{B}_B + n_1 \vec{A}_C + n_2 \vec{A}_C \quad (2.44)$$

where $\{A_B, B_B\}$ and $\{A_C, B_C\}$ are sets of substrate and overlayer reciprocal lattice vectors, respectively. (h, k) are the integer Miller indices of the 1×1 structure and each subset of beams is described by a pair of indices (n_1, n_2) with $n_1 \vec{A}_C + n_2 \vec{A}_C$ being inside the first Brillouin zone of the 1×1 surface. Thus, the diffraction spots can be divided into $(nl_1 + 1) \cdot (nl_2 + 1)$ subsets, each of them belonging to a sublattice. The reciprocal lattice vectors belonging to the same subset differ by 1×1 reciprocal lattice vectors: $h \vec{A}_B + k \vec{B}_B$. As the substrate layers can scatter an incident plane wave only into plane waves with a momentum that differs from the incident one by a 1×1 reciprocal lattice vector, the waves arriving from the overlayer at the bulk will be scattered only within their own subsets. Therefore, if the beam list is ordered by subsets, substrate matrices (see Eq. (2.42)) are block diagonalized, each block corresponding to a beam subset [9]. This is particularly important for increasing efficiency at lattice sums evaluation and for constructing the total bulk diffraction matrix. If symmetry elements are present at the surface, such as mirror planes or rotation axes, greater savings can be achieved at the matrix expression.

2.6.2 Scattering by a stack of planes: layer doubling

In this section, we describe the most popular method for constructing the total diffraction matrix of a stack of atomic planes, called “layer doubling” [12, 14]. Incidentally, a similar approach to solve the dyson equation was later developed by Guinea *et al* in a tight binding basis [48]

The plane wave basis results appropriate for working with atomic planes. In this case, interlayer propagators are simply plane waves for each \vec{g} component. First, a stack of two planes is contracted adding all the MS contributions to the reflected / transmitted wavefield. This procedure is schematically described at the left hand panel of Fig. 2.3 for a pair of atomic planes labelled A and B , determined by $M_{A,B}^{++}$ and $M_{A,B}^{--}$ transmission matrices and $M_{A,B}^{+-}$ and $M_{A,B}^{-+}$ reflection matrices respectively. The figure shows all the possible scattering paths undergone by a plane wave incident on the left plane A . Propagation operators for the plane wave basis are:

$$P_{\vec{g}}^{\pm} = e^{\pm i \vec{K}_{\vec{g}}^{\pm} \cdot \vec{r}_{BA}} \quad (2.45)$$

taking the $(+)$ sign for $A \rightarrow B$ propagation and $(-)$ for $B \rightarrow A$. The vector \vec{r}_{BA} starts and ends at A and B plane origins, respectively. Adding all the contributions,

the stack reflection (R^{-+} and R^{+-}) and transmission matrices (T^{++} and T^{--}) for a pair of atomic planes are shown to have the expressions:

$$\begin{aligned}
R^{-+} &= M_A^{-+} + M_A^{--} P^- M_B^{-+} P^+ [1 - M_A^{+-} P^- M_B^{-+} P^+]^{-1} M_A^{++} \\
R^{+-} &= M_B^{-+} + M_B^{++} P^+ M_A^{+-} P^- [1 - M_B^{+-} P^+ M_A^{+-} P^-]^{-1} M_B^{--} \\
T^{++} &= M_B^{++} P^+ [1 - M_A^{+-} P^- M_B^{-+} P^+]^{-1} M_A^{++} \\
T^{--} &= M_A^{--} P^- [1 - M_B^{+-} P^+ M_A^{+-} P^-]^{-1} M_B^{--}
\end{aligned} \tag{2.46}$$

Once this has been done, it is easy to build a complete stack by feeding again the layer doubling expressions (2.46) with the double-plane matrices. In n steps, a stack of 2^n planes is grown, as it is shown schematically on the right hand panel of Fig. 2.3. This procedure converges fast and computation gains efficiency using the block diagonalized bulk layer matrices.

Finally, if overlayers are present, the whole surface reflection matrix is calculated by applying the first of Eqs. (2.46), substituting bulk matrices at B plane and the overlayer matrices at A plane. The amplitudes diffracted by the surface are proportional to one column of R^{-+} , namely that corresponding to $\vec{g} = 0$.

An alternative and popular method for plane stacking is “Renormalized Forward Scattering” (RFS) [11]. It describes interlayer scattering using perturbed plane waves, assuming that scattering by a layer is weak. Forward propagating plane waves suffer an amplitude loss when being transmitted through a plane. The wavefield between two planes is constructed by adding up plane waves that have undergone all order scattering paths. First order would consist in a plane wave that has been reflected once, but transmitted a number of times, and so on. This method fails if layers are too close ($\lesssim 1.1$ Å), since perturbative approach no longer applies. If this is the case, one must come back to the partial wave description of the scattering, and build a $\tilde{\tau}$ matrix for the stack of closely packed planes (the so-called “composite layer”), as it would be done if the layer was a non-Bravais lattice. Efficient methods exist for accomplishing a composite layer diffraction matrix, such as the “Combined-Space Method” described by Van Hove and Tong [13, 15].

Layer doubling, on the contrary, is an exact method, if n is big enough. interlayer spacing, as long as enough plane waves are taken at the basis set. The closer the planes, the more plane waves are needed. However, in practice, it results more efficient to apply composite layer at small spacings rather than taking a long basis set of plane waves.

2.6.3 Temperature effects

To describe lattice vibration, the adiabatic approach can be assumed, since vibration typical times are several orders of magnitude larger than electron scattering times (a factor 10^4 , neglecting energy loss to phonons). Waves outgoing from the atoms are in phase, but waves outgoing from a displaced atom are phase shifted. In the direction parallel to propagation, larger diffraction path differences are formed and coherence is thus reduced. This effect is larger for larger vibration amplitudes and smaller wavelengths, and is reflected in a reduction of the backscattered intensities. Similarly to X-rays theory of thermal diffuse scattering (TDS), temperature effects

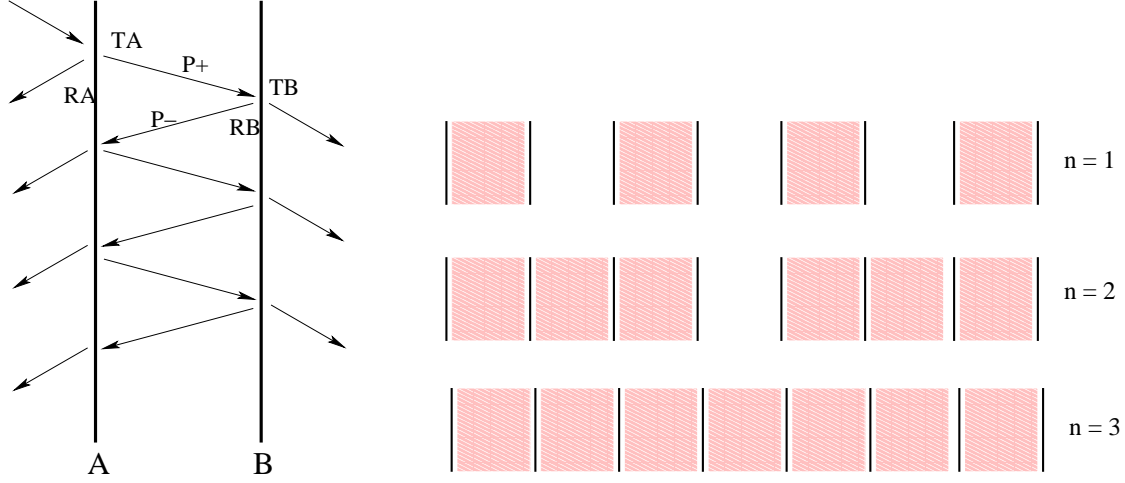


Figure 2.3: Schematic view of the construction of a stack of planes following the layer doubling method. The left hand panel shows the contributions to transmission and reflection of a pair of planes A and B for an incident plane wave incoming from the left. The right hand panel shows the $n = 1, 2, 3$ steps of the procedure to build a stack of 2^n planes.

can be quantified by a Debye-Waller (DW) factor added to scattering factors:

$$e^{-M} = e^{-|\vec{q}|^2 \langle (\Delta \vec{r})^2 \rangle_T} \quad (2.47)$$

where \vec{q} is the 3D electron momentum transfer at the considered beam and $\langle (\Delta \vec{r})^2 \rangle_T$ is the mean-square deviation. The DW factor is maximal at forward scattering, where $\vec{q} = 0$, and minimal at backscattering. Thus, it enhances forward scattering and diminishes backscattered intensities.

For the case of isotropic vibrations, it can be shown [14] that:

$$\begin{aligned} t_l(T) &= t_l(T=0)e^{-M} \\ &= \sum_{l'l''} i^{l'} e^{-2\alpha\kappa^2} j_{l'}(-2i\alpha\kappa^2) t_{l''}(T=0) \sqrt{\frac{4\pi(2l'+1)(2l''+1)}{2l+1}} \\ &\quad \times \int Y_{l0} Y_{l'0} Y_{l''0} \end{aligned} \quad (2.48)$$

where $\alpha = \frac{1}{6} \langle (\Delta r)^2 \rangle_T$. Using this t-matrix is equivalent to using phase shifts with an imaginary component, which is always positive and accounts for a kind of flux absorption at the ion core scattering, since we are ignoring incoherently scattered flux.

The mean square deviation can be derived from a Debye model using the following formulas:

$$\begin{aligned} T \gg \Theta_D &\quad \langle (\Delta \vec{r})^2 \rangle_T \simeq \frac{9}{mk_b \Theta_D} \frac{T}{\Theta_D} \\ T \ll \Theta_D &\quad \langle (\Delta \vec{r})^2 \rangle_T \simeq \frac{9}{mk_b \Theta_D} \left(\frac{1}{4} + 1.642 \left(\frac{T}{\Theta_D} \right)^2 \right) \end{aligned} \quad (2.49)$$

where T and Θ_D are given in degrees K, m is the atomic mass in electron mass units, and Boltzmann constant is $k_b = 3.16 \times 10^{-6}$ H/K. Following Van Hove and Tong, we can interpolate to obtain an approach for intermediate temperatures:

$$\begin{aligned} \langle (\Delta \vec{r})^2 \rangle_T &= \sqrt{(\langle (\Delta \vec{r})^2 \rangle_{T=0})^2 + (\langle (\Delta \vec{r})^2 \rangle_{T \rightarrow \infty})^2} \\ &= \frac{9}{mk_b \Theta_D} \sqrt{\frac{1}{16} + \left(\frac{T}{\Theta_D} \right)^2} \end{aligned} \quad (2.50)$$

Anisotropic vibrations

Atoms nearby the surface region are not likely to vibrate isotropically, due to the perpendicular symmetry breaking. Debye-Waller formalism assumes, too, that the atomic vibrations are constrained to a quadratic well. For these reasons, a more general description of vibrations would be desirable, in the sense of anisotropic and/or anharmonic vibrations. For atoms vibrating uncorrelated, i.e. independently w.r.t. other atoms, a formalism is already developed. It begins with a general definition of the DW factor:

$$e^{-M(\vec{k}' - \vec{k})} = \int P(\vec{r}) e^{i(\vec{k}' - \vec{k}) \cdot \vec{r}} d^3 \vec{r} \quad (2.51)$$

If the atom is oscillating harmonically, its PDF has gaussian shape, and a set of axes can be found for which the PDF can be written as:

$$P_{\vec{\sigma}}(\vec{r}) = \frac{1}{\sqrt{8\pi^3}} \frac{1}{\sigma_x \sigma_y \sigma_z} e^{-\frac{1}{2}(\frac{x^2}{\sigma_x^2} + \frac{y^2}{\sigma_y^2} + \frac{z^2}{\sigma_z^2})} \quad (2.52)$$

Neglecting correlation effects, it is possible to describe thermal vibration by simply correcting the atomic t-matrix with the generalized DW factor described above. Using the plane wave basis,

$$t(T, \vec{k}, \vec{k}') = t(0, \vec{k}, \vec{k}') e^{-M} \quad (2.53)$$

This expression must be changed to a partial waves basis set to be used by LEED codes, by doing:

$$t(T)_{l'm', lm} = \frac{1}{8\pi^2} \int d^2 \Omega_{\vec{k}} \int d^2 \Omega_{\vec{k}'} Y_{l'm'}(\Omega_{\vec{k}'} t(T, \vec{k}, \vec{k}') Y_{lm}^*(\Omega_{\vec{k}}) \quad (2.54)$$

The task of evaluating this integral is hard, but possible using several expansion formalisms [49, 50], such as multipoles [51] or cumulants [52]. Obviously, the final t-matrix will be non-diagonal.

Correlation effects (e.g. due to phonons), have not been incorporated yet to LEED. However, correlation terms are not expected to significantly affect diffraction. The correlation would be only important at paths involving atoms nearby, and the probability of such paths is strongly reduced by forward scattering being stronger.

Layer approach

Different vibrations in the direction perpendicular to the surface and in the parallel direction can be introduced by multiplying by e^{-M} each layer diffraction matrix element, $M_{\vec{g},\vec{g}'}^{\pm\pm}$. The DW factor for this case is

$$M = \frac{1}{6} \left[|\Delta \vec{k}_{\parallel}|^2 \langle (\Delta \vec{r}_{\parallel})^2 \rangle_T + |\Delta k_{\perp}|^2 \langle (\Delta \vec{r}_{\perp})^2 \rangle_T \right] \quad (2.55)$$

where $\langle (\Delta \vec{r}_{\parallel})^2 \rangle_T$ and $\langle (\Delta \vec{r}_{\perp})^2 \rangle_T$ are computed using

$$\langle (\Delta \vec{r})^2 \rangle_T = \frac{9}{mk_b \Theta_D} \sqrt{\frac{1}{16} + \left(\frac{fT}{\Theta_D} \right)^2} \quad (2.56)$$

with the corresponding enhancement factor f , which is used to give different thermal behaviour to bulk and overlayer. Actually, if one wished to include this option in the calculations, vibrations should be included also in the \tilde{X} matrix of each atomic layer. Following Van Hove, this is done isotropically, using an angle average vibration amplitude:

$$\sqrt{\frac{1}{3} [2 \langle (\Delta \vec{r}_{\parallel})^2 \rangle_T + \langle (\Delta r_{\perp})^2 \rangle_T]} \quad (2.57)$$

in the t-matrix entering \tilde{X} .

2.7 The LEED90 program

Self-consistent formalisms that can solve the MS problem have been available for a long time. Furthermore, computer codes implementing these algorithms have also been available [14, 15, 53, 21], enabling many groups not directly involved in theory to perform accurate calculations for their own experiments. These freely available codes have, without any doubt, contributed greatly to the fast and wide development of the LEED technique. Some of these programs, however, have evolved from the initial set of routines written in old flavours of FORTRAN (ranging from FORTRAN II and IV to 77) making difficult to adapt to the new standard of FORTRAN-90/95. Other programs have evolved to become more specialized by taking advantage of different saving features, like symmetries, different approximations, etc. These features make the structural search more efficient, but impose their own constraints (e.g., the use of symmetry).

As a part of this Thesis work, we have implemented a set of FORTRAN-90/95 routines for solving the LEED problem, that use the techniques explained in the sections above. Its name is LEED90, and can be obtained from the CPC Library [54]. They have been written from scratch, trying to emphasize simplicity, modularity, and general applicability, so they may be quickly and safely used for testing and/or teaching purposes. Due to FORTRAN-90 ability to allocate arrays dynamically, the program does not need to be recompiled when the problem parameters (such as l_{\max} , lattice superstructure or number of adsorbed layers) change. LEED90 has been written keeping an eye in parallelism, one of the strongest features of FORTRAN-90/95

when compared with other programming languages [44]. It should be straightforward to parallelize the program in energies and/or incidences. Besides, operations involving arrays would be parallelized when using a proper compilation.

In particular, the possibility of introducing adsorbates characterized by non-diagonal t-matrices has been included in LEED90. It has been done in order to study the MS problem on overlayers made of molecules that is based in the “a priori” calculation of a non-diagonal molecular t-matrix where all the intra-molecular scattering paths have been included. This will be the subject of study of Chapter 4. Other applications of the non-diagonal t-matrix implementations are the study of anisotropic vibrations or non-spherical muffin tins.

The code is clearly divided into routines that generate the operators identified in section 2.6, and intralayer MS can be easily enabled or disabled. Bulk diffraction matrices use block diagonalization property. The stack of planes is constructed following the layer doubling method. LEED90 has the ability to uncouple dynamical calculations of substrate and adsorbate layer, i.e., a different value for l_{\max} can be taken and intralayer MS can be switched independently. This feature is particularly useful when working with large superstructure unit cells and/or large molecular adsorbates. The later, when described by a molecular t-matrix, will require a higher l_{\max} than when treated as independent atoms, as we will see in Chapter 4. Unfortunately, LEED90 can only cope with Bravais layers and composite layer calculations are not yet implemented. To keep a transparent code, no optimizations that make use of surface symmetry elements have been done. Regarding temperature effects, LEED90 offers all the possibilities described at section 2.6.3, including different input options for vibrational parameters and layer matrix Debye-Waller anisotropic correction.

2.7.1 Technical remarks about LEED90

This subsection describes some features of LEED90 routines. Some of them, like the way Clebsch-Gordan coefficients are handled, are only found in LEED90.

Number of plane wave used

We use Van Hove and Tong criterion [15] and include all plane waves that do not decay from one layer to the next to less than a fraction t of their original amplitude:

$$e^{-\text{Im}(K_{gz}^{\pm})d_{\min}} > t \quad (2.58)$$

where d_{\min} is the smallest interlayer spacing present in the surface. $t = 0.002$ is usually enough for our purposes.

Spherical Harmonics

The so-called “natural ordering” of spherical harmonics is used throughout the code. It consists in ordering (l, m) pairs in a list $(0, 0)$, $(1, -1)$, $(1, 0)$, $(1, 1)$, $(2, -2)$, $(2, -1)$, $(2, 0)$, $(2, 1)$, $(2, 2)$, ... etc. A total number of $(l_{\max} + 1)^2$ pair elements is needed in the calculations. A routine that generates spherical harmonics recursively has been implemented. Notice that, since K_{gz}^{\pm} take complex values inside the solid, spherical

harmonic arguments in LEED calculations are complex, and one must be aware that complex conjugation is not an analytical operation [14]. The relationship

$$Y_{lm}^*(\theta, \phi) = (-1)^m Y_{l-m}(\theta, \phi) \quad (2.59)$$

is hold only for real arguments θ and ϕ .

Miller algorithm for Bessel j function.

In LEED90, Bessel and Hankel functions are built as routines that use recurrence relations. The series for $j_l(z)$ is not stable for increasing values of l . This effect is more noticeable for small values of the argument z , because functions with successive l values quickly become small. In this case, they are better calculated using a downward algorithm, such as Miller's[55]. This algorithm allows implementing a downward recurrence without any previous knowledge of the starting values. The steps are the following:

1. Assume tentative values $f_{N+1} = 0$ and $f_N = 1$ for a large N .
2. Compute $f_{N-1}, f_{N-2}, \dots, f_0$ using a recurrence relation for Bessel functions.
3. $p = \frac{j_0(z)}{f_0}$ is the proportionality factor between the true series $\{j_l(z)\}$ and the tentative series $\{f_l\}$.
4. Finally, $\{pf_l\}$ are the expected values for $\{j_l(z)\}$.

Clebsch-Gordan coefficients storage

Due to the triangular condition, two l_i indices of Gaunt coefficients (see Appendix B) will run up to l_{\max} and the third one up to $2l_{\max}$. Inside any LEED program, storing Clebsch-Gordan elements into arrays is a complex task. Unoptimized storage inside arrays is a memory waste, since many of them are zero, due to the conditions above. Traditional LEED programs, such as Pendry's or Van Hove's, use a complicated system of index ordering to store non-zero elements. Taking advantage of Fortran 90/95 new variable type definition facilities, LEED90 uses the method of linked lists [56] to store and handle efficiently these coefficients. This is advantageous from both the point of view of coefficient handling inside the code and memory saving. The linked list consists of a sequence of boxes with two compartments: one contains a data item and the other one is a pointer to the next box. During $X_{lm,l'm'}$ evaluation, Clebsch-Gordan coefficients are accessed one by one following the order established by the pointers.

Typical running time

A single IV curve for a fixed atomic configuration takes a few seconds/minutes depending on the two key parameters controlling the convergence: the maximum angular momentum quantum number, l_{\max} , and the number of beams, n_b . In principle, time should scale as $\mathcal{O}(N^3)$, where N is a typical matrix dimension inside the program, since MS calculations require matrix inversion. Thus, it is clear that

running time scales as n_b^3 at least. Running time scales as n_b^3 for a single energy, since MS calculations (at layer doubling) require matrix inversion. It must be considered that n_b increases with energy according to Eq. (2.58), and this affects the computation time spent at the basis change of Eq. (2.42). The inversion $(1 - \tilde{X})^{-1}$ makes the program time scale as l_{\max}^6 for a single energy. However, a faster l_{\max}^4 is found for typical calculations of complete IV curves, mainly due to optimization of other parameters connected to l_{\max} , such as $n_b(E)$. Typical values for energies up to 300 eV are 7 to 10 for l_{\max} for single atoms, and 10 to 15 for molecular adsorbates. n_b takes values of a few hundreds.

Program BEAMGEN

A short program called BEAMGEN is distributed together with LEED90, which generates the list of the superstructure diffraction pattern Miller indices (h', k') divided into sets with the correct order to apply block diagonalization at bulk matrices. Using these indices, the reciprocal superlattice vectors corresponding to the sublattice labelled by (n_1, n_2) are:

$$g_{(n_1, n_2)}^{(C)} = h' \vec{A}_C + k' \vec{B}_C = h \vec{A}_B + k \vec{B}_B + n_1 \vec{A}_C + n_2 \vec{B}_C \quad (2.60)$$

The relation between the (1×1) and the superstructure reciprocal lattice basis is:

$$\begin{pmatrix} \vec{A}_B \\ \vec{B}_B \end{pmatrix} = \frac{1}{|M|} \begin{pmatrix} m_{22} & -m_{21} \\ -m_{12} & m_{11} \end{pmatrix} \begin{pmatrix} \vec{A}_C \\ \vec{B}_C \end{pmatrix} \quad ; \quad |M| = m_{11}m_{22} - m_{21}m_{12} \quad (2.61)$$

therefore

$$\begin{aligned} h' &= h + \frac{n_1}{|M|}m_{22} - \frac{n_2}{|M|}m_{12} \\ k' &= k - \frac{n_1}{|M|}m_{21} + \frac{n_2}{|M|}m_{11} \end{aligned} \quad (2.62)$$

2.8 R-factors

As we have already mentioned, LEED-IV search method is non-direct, in the sense that we consider a proposed model to be good if its calculated spectra is similar to the experimental one. Thus, the whole fit is constrained to have a reliable merit function (R-factor) for the experiment-theory comparison. What features of the spectra should describe a proper R-factor? Depending on this choice, a great variety of R-factors can be defined [1].

Main geometry information is contained in intensity peak positions, that can be roughly related to interplanar distances as a consequence of Bragg law. However, peak positions can be affected, too, by non-structural parameters, such as atomic phase shifts, temperature effects or electron damping. These parameters have a nonlinear effect on the intensities, and should also be fitted during the search.

Structural information is also contained in relative peak heights and widths. As intensities are affected by a background contribution, it is preferable to use their derivatives, dI/dE .

The most widely used R-factor is Pendry's R_P [41], which gathers the properties describe above. R_P attempts to treat all peaks and minima with equal weight, as we will discuss below in detail, while other R-factors weight peaks with their height. Any peak, even if it is small, contains structural information, so it should be treated on the same footing as a big one. This is important at high energies, where intensities are smaller due to temperature effects. Of course, the experiment must be carefully analyzed in order to remove any noise peaks.

The use of the logarithmic derivatives allows this homogeneous treatment of the peaks, $L(E) = I'(E)/I(E)$. More precisely, R_P , makes use of the Y-function,

$$Y(E) = \frac{L(E)^{-1}}{L(E)^{-2} + V_{0i}^2} \quad (2.63)$$

where V_{0i} is the imaginary part of the crystal potential. $Y(E)$ is a strongly oscillating function of the energy, that is highly sensitive to closely spaced peaks and avoids problems caused by L at zeroes in the intensities. Then, R_P is constructed by comparing the calculated and experimental Y-functions (Y^{th} and Y^{exp} respectively) over all the experimental data set:

$$R_P = \frac{\int \sum_g (Y_g^{\text{th}}(E) - Y_g^{\text{exp}}(E))^2 dE}{\int \sum_g ((Y_g^{\text{th}}(E))^2 + (Y_g^{\text{exp}}(E))^2) dE} \quad (2.64)$$

where g is an index running over the beams. This factor takes values in the interval $[0 : 2]$, with $R_P \rightarrow 0$ for a perfect fit, $R_P \rightarrow 2$ for perfect anticorrelation between experiment and theory and $R_P = 1$ if experiment and theory are uncorrelated.

The R-factor exhibits a complex topography if represented as a function of structural parameters, with several local minima for different structures. Therefore, local search procedures will not produce reliable solutions in general. As we will see in Chapter 6, considering this features is determinant to design an optimum R-factor minimization strategy. Besides, it is possible to find several minima of similar depth, so we need to discriminate between the corresponding geometries. This is done by increasing the experimental data base, for example, by taking IV curves at other incidence directions. Another possibility is to observe that different R-factor types should strongly differ at the unphysical minima. Further comments about R-factor topography will be done at Chapter 6.

Fluctuations in the hypersurface, due to random correlations between datapoints, may produce spurious minima. Thus, an uncertainty will exist for the minimum R-factor structure. The quantity usually taken as the best estimate for the standard deviation of R_P is

$$R_{\min} \cdot RR = R_{\min} \cdot \sqrt{\frac{8V_{0i}}{\Delta E}} \quad (2.65)$$

where ΔE is the total energy overlap between experimental and calculated IV curves, and R_{\min} is the minimum R_P achieved in the search procedure ². Any point of the

²This expression arises from the following argument: the standard deviation of R_P is $\sqrt{\langle (R_P - \langle R_P \rangle)^2 \rangle} = \langle R_P \rangle \sqrt{2/N}$, where N is the number of distinguishable peaks at the IV curve, $N \simeq \Delta E / 4V_{0i}$, which are regarded as independent datapoints at this context. R_{\min} is used as an estimate of the expectation value $\langle R_P \rangle$. A short discussion about redundancy in the database will be given at section 6.3.1.

parameter search space that gives

$$R_P \leq R_{\min}(1 + RR) \quad (2.66)$$

should be regarded as a solution to the problem, in the sense that it is not likely to be a random fluctuation. Thus, such a quantity provides a measurement of the experimental uncertainty of the fitting procedure. Commonly, the error bars in the parameters are obtained from single parameter R-factor scans, that is, computing the R-factor for different values of a certain parameters with the rest of parameters kept fixed at their R_{\min} values. The range where the condition (2.66) is held defines the size of the error bar for that parameter. We must point out that this technique does not consider the existing correlations between parameters. The correct procedure should optimize the values of the rest of parameters. However, this involves a considerable computational effort, so it is only done in special situations. As an example, this technique is widely used when managing occupational and vibrational parameters simultaneously, since these magnitudes are correlated via the DW factor [57].

Possible chaotic nature of wavefunctions, due to the complexity introduced by MS, influences the R_P factor. It has been shown that, for typical experimental diffracted intensities, the parameter space region having $R_P \gtrsim 0.4$ is fully chaotic, so that structures belonging to that region should not be taken as reliable [58].

2.9 Diffuse LEED (DLEED)

Lack of ordering at surfaces appears as a fuzzy pattern superimposed to diffraction spots. The present section deals with the case of lattice-gas-like adsorbates, i.e. those randomly distributed over surfaces occupying equal adsorption sites. Such stems can be found at early stages of some catalytic processes involving gas molecules. The continuous diffraction pattern contains information about both long-range ordering of the molecules and short-range bonds of the molecule to its environment at the surface.

Similarities exist between this lattice-gas and overlayers made of large molecules (thus forming large unit cells) at saturation coverage [59]. Here, the chemical substrate-adsorbate interaction predominates, while interaction between molecules, which is responsible for the ordering is weak. In fact, a system like this, with a high density of fractional order spots per reciprocal 1×1 unit cell, can be interpreted as a DLEED pattern and individual cluster methods can be applied [60], since it has been found that a coarse grid can be used when measuring experimental DLEED data with negligible loss of accuracy [61]. Alternatively, there are some specific methods for large unit cell surfaces, such as the “beam-set-neglect” method, which was successfully experienced on a number of systems, like $C_6H_6/Rh(100)$ surface [62] applied to local adsorption cluster only.

From the point of view of chemistry, as in the case of ordered surface, it is valuable to have information about the structure of the local environment surrounding the molecule. In the case of this Thesis, our interest about DLEED is focused in the application and development of direct methods. It is well known that an interpretation of a DLEED pattern in terms of holography can be made (HLEED) [30],

as it has been done previously for PD patterns [29]. For this picture to be sensible, a low coverage limit is required. In HLEED, the adsorbate acts as a beam splitter. The wave recorded at the screen is formed by the superposition of two components:

- The wave diffracted by the adsorbate, called reference wave.
- The wave diffracted by the adsorbate first and the atoms at adsorbate surroundings afterwards, called object wave.

We will give further details about CLEED in section 7.2.1.

The development of DLEED theory follows closely the SEXAFS theory, the main difference being that a SEXAFS experiment uses X-rays to excite the inner shells of atoms bound to the surface. The environment of the excited atom modulates the signal. In these calculations it is assumed that the lattice-gas is very dilute. The simplest case would correspond to atomic adsorbates. For DLEED, the calculation is made in three steps [63] dividing all the scattering paths in three groups:

1. All scattering events preceding the first encounter with the adsorbate (molecule). This is done by conventional LEED theory for ordered surfaces.
2. All paths starting at the first encounter with the molecule and ending with the last. The molecule breaks the translational symmetry, so conventional LEED can not be used. Instead, a SEXAFS or NEXAFS cluster calculation is required [64, 60]. These kind of cluster formalisms divide the surroundings of the adsorbate into shells and the final diff rated amplitudes are computed in two steps: (1) first, intra-shell MS is computed resulting in a shell t-matrix, and (2) inter-shell MS is done to achieve the full cluster t-matrix. This procedure has points in common with the molecular t-matrix formalism described at Chapter 4.
3. Scattering paths beginning after the last encounter with the molecule and terminating at the detector. This part of the calculation uses a path reverse LEED wavefunction similar to photoemission theories [65].

The details of these calculations can be found at Ref. [66]. In SEXAFS, the environment of the excited atom modulates the wavefunction, and the structure of the diffraction pattern arising from a single energy as a function of the parallel momentum component, $\vec{k}'_{||}$, is fairly rich. In DLEED, steps 1 and 3 provide additional information about the molecule orientation. Finally, a generalized R-factor can be defined, in the same fashion as Pendry's R_P for beams, for DLEED maps [67, 68]:

$$R_{\text{DLEED}} = \frac{\sum_{\vec{k}'_{||}} (Y_{\text{th}}(\vec{k}'_{||}) - Y_{\text{exp}}(\vec{k}'_{||}))^2}{\sum_{\vec{k}'_{||}} (Y_{\text{th}}^2(\vec{k}'_{||}) + Y_{\text{exp}}^2(\vec{k}'_{||}))} \quad (2.67)$$

2.10 Tensor LEED (TLEED)

Tensor LEED is a perturbative approach that allows fast intensity calculations, and it is easy to embed in a search code. It was firstly proposed by Rous, Pendry, Heinz

and co-authors [23, 69]. The first step for a search using TLEED is to have a good guess, or “reference structure”, for the real surface structure. The basic principle of TLEED approach is that small distortions from the reference structure will only cause small changes in the diffracted amplitudes. The approach has three levels of sophistication:

1. Perturbative terms in the amplitudes can be written as linear terms in the atomic displacements.
2. Perturbative terms are linear in the matrix elements of the change in the atomic scattering matrices.
3. The third level would include also second order terms in the previous correction.

It is the second the level the one that is usually employed by available LEED codes, such as TensErLEED [70] and SATLEED [71]. For example, the change in the amplitude of beam \vec{g} due to a displacement \vec{R}_w of the w -th atom on the surface in second level TLEED approach is, symbolically,

$$\delta A_{\vec{g}w} = \langle \vec{k} + \vec{g}; \text{out} | \delta \tilde{t}^w(\delta \vec{R}_w) | \vec{k}; \text{in} \rangle = \tilde{M}_{\vec{g}w} f(\delta \vec{R}_w) \quad (2.68)$$

where $f(\delta \vec{R}_w)$ is a function of the displacement and $\tilde{M}_{\vec{g}w}$ is the *tensor*. The trick that makes TLEED so handy is that the tensor $\tilde{M}_{\vec{g}w}$ is independent of \vec{R}_w : they depend on the reference structure only. Therefore, they are calculated once and stored. Then, it is a straightforward and fast procedure to evaluate the diffracted intensities for a set of distortions $\{\vec{R}_w\}$. If more than one atom is varied, individual amplitude perturbation terms $\delta A_{\vec{g}w}$ are added.

One of the advantages of TLEED is that it can account for a number of magnitudes affecting the surface structure. It can describe not only geometrical distortions, but also changes in the thermal vibrations or even the chemical composition. Actually, at the second level approach, any modification applicable to a single atomic t-matrix is likely of being described by the TLEED formalism.

- Geometry changes: the change in the w -th atom t-matrix caused by a displacement \vec{r}_w on this atom is:

$$\delta \tilde{t}^w = \tilde{G}_{II}(\delta \vec{r}_w) \cdot \tilde{t}^w \cdot \tilde{G}_{II}(-\delta \vec{r}_w) - \tilde{t}^w \quad (2.69)$$

where \tilde{G}_{II} is a translation operator described at Appendix A. According to Rous *et al.* [23], this approximation remains correct up to a typical distance of $0.2 - 0.4$ Å. This threshold depends on other parameters, though, such as the chemical identity of the atom (in general, the heavier the element, the smaller the applicability range) or the other parameters being varied during a structure optimization (remember that usually the R-factor shows correlations for several surface parameters).

- Thermal vibrations: the change in w -th t-matrix due to a change in vibration amplitudes from \vec{u} to \vec{u}' is just

$$\delta \tilde{t}^w = \tilde{t}^w(\vec{u}') - \tilde{t}^w(\vec{u}) \quad (2.70)$$

Notice that, in principle, it is not necessary to assume any constraint about isotropy and general non-diagonal t-matrices can be used [72, 50].

- Chemical composition [73]: if the w -th site can be occupied by atomic species A and B with probabilities c_w and $1 - c_w$, and scattering t-matrices \tilde{t}_A and \tilde{t}_B respectively ³, then the variation on the w -th t-matrix caused by a change δ_{c_w} in the occupation will be given by:

$$\delta\tilde{t}^w = \delta_{c_w}(\tilde{t}_A - \tilde{t}_B) \quad (2.71)$$

The validity range for this technique is surprisingly large. There exist cases where even an element exchange can be done. This seems to be related to the lack of changes on the relevant propagators in the system, which in fact are the limiting factors in conventional TLEED. This approach has been successfully applied in investigations about segregation in alloy surfaces [75].

³in the “Average t-matrix Approximation” (ATA) sense [74]

Chapter 3

The structure of rutile TiO_2 (110)- 1×2 surface: Ti_2O_3 reconstruction

3.1 Introduction

For the last decades, the interest on understanding metal oxide surfaces has increased. This interest has been mainly motivated by their wide variety of technological application fields, such as heterogeneous catalysis, photocatalysis, gas sensing, corrosion coating, optical coating, pigments [76]. TiO_2 is probably the most popular metal oxide, not only for its applicability, but also because it is a handy benchmark for metal oxide modelling in both experiments and theory. This is proved by the huge number of relevant publications on TiO_2 . Ref. [39] is a superb comprehensive review of recent progress on TiO_2 surface science.

In the present Chapter, we show a complete study on the geometry and electronic structure of 1×2 reconstruction of the (110) face of rutile TiO_2 . A potential usage of this surface in heterogeneous catalysis is the motivation of this work. Recently, adsorption of NO has been studied on the (110) face, the most stable one of TiO_2 , [77] at room temperature. It has been found that the molecule dissociates, and that the N atom returns to the gas phase while the O atom occupies a vacancy at surface. However, the mechanism driving the reaction on the surface is unknown. In contrast, the unreconstructed 1×1 surface does not interact with the molecule. These works are examples of the properties of metal oxides surfaces as gas sensors.

Actually, most stable faces of TiO_2 are known to host interesting chemistry. Much literature exist about small molecule interaction with the rutile TiO_2 (110)- 1×1 surface (H_2 , NO, O_2 , CO, H_2O , etc.). Refs. [76, 78, 39] are some of the existing reviews regarding this topic. In general, it is observed that chemisorption takes place at defect sites of the surface, such as O vacancies or steps, depending on the case. In particular, much effort has been done in order to investigate the possibilities of water dissociation on this surface, but it is still a subject of controversy. While theory predicts dissociation even in absence of defects, experiments yield different and contradictory interpretations. A reconciliation between theory and experiment can be done by assuming coexistence of dissociated and non-dissociated molecules

[79].

Other usage of reducible metal surfaces in heterogeneous catalysis is as substrate for metal clusters with catalytic properties in reactions of interest to several industrial processes. As an example, disordered and diluted Au nanoclusters adsorbed on $\text{TiO}_2(110)$ have been found to help CO oxidation at low temperatures [80, 81]. Again, vacancy sites seem very active for Au adsorption.

The complete understanding of all the examples of TiO_2 surfaces applications explained above would require a previous thorough knowledge of the surface structural and electronic properties. In the case of the 1×1 surface, the atomic relaxed positions have already been studied by different methods. It would be highly desirable to do the same for the 1×2 reconstruction. Discrepancies could be found in the literature about the best atomic model to describe this surface, as we will see in the section 3.3.2. Even the stoichiometry has been under discussion. The work presented in this Chapter aims to find the best model (with relaxed positions) from three different techniques: LEED-IV, STM and DFT.

3.2 The rutile TiO_2 bulk structure

TiO_2 crystallizes in three main crystallographic phases: rutile, anatase and brookite. The first two structures, which have tetragonal symmetry, have the greatest technological interest. Brookite is rhombohedral.

The rutile structure space group is $P4_2/mnm$, with two TiO_2 units per unit cell. Lattice parameters are $a = 4.587 \text{ \AA}$ and $c = 2.954 \text{ \AA}$. Ti atoms relative positions inside the unit cell are $(0, 0, 0)$ and $(1/2, 1/2, 1/2)$. O positions are $(u, u, 0)$, $(-u, -u, 0)$, $(1/2 - u, 1/2 + u, 0)$ and $(1/2 + u, 1/2 - u, 0)$, where the parameter u takes the typical value 0.3 of rutile structures. In the bulk, each Ti cation is surrounded by six O anions, located at the corners of a slightly distorted octahedron. These octahedra form the basic building units of the rutile structure. The octahedra placed at $(0, 0, 0)$ and $(1/2, 1/2, 1/2)$ form 90° w.r.t. the c -axis. The rutile structure as a whole can be seen as an arrangement of chains of equally oriented octahedra running parallel to the $[001]$ crystallographic direction and alternatively oriented in the $[110]$ and $[\bar{1}10]$ directions. In an ionic picture, nominal charges are Ti^{4+} and O^{2-} .

3.3 The rutile TiO_2 (110) face

3.3.1 The rutile TiO_2 (110)- 1×1 surface

Rutile TiO_2 (110) surface is the most stable, while (001) has the highest energy, as reported from first-principles calculations of the Wulff construction for TiO_2 crystal [82]. We shall focus on the stoichiometric (110) surface, which is depicted without reconstruction on Fig. 3.1. Its construction from bulk truncation requires only breaking the longer Ti-O bond. The stability of (110)- 1×1 can be predicted also from electrostatic considerations [83] and the autocompensation principle [84]:

- Electrostatics: the dipole moment of a repeated unit perpendicular to the surface must be zero for the surface energy to converge.

- Autocompensation: all cation/anion-derived dangling bonds must be completely empty or fully occupied on stable surfaces. To form the 1×1 surface, the same number of Ti-O and O-Ti bonds are broken.

Slabs used in DFT calculations are constructed according to these principles.

The stoichiometric TiO_2 (110)- 1×1 surface alternates 6-fold coordinated Ti-atoms (as in the bulk) with 5-fold coordinated Ti-atoms (holding a dangling bond). There are two types of O atoms: 3-fold and 2-fold coordinated. The latter are the bridge oxygens forming the rows [85]. These oxygens are a subject of debate for their non-saturated coordination: it has been suggested that they are susceptible of leaving the surface and creating punctual defects [39].

The relaxed geometry of TiO_2 (110)- 1×1 surface has been a popular subject of publications recently. Experimentally, it has been examined by SXRD [86] and LEED [87]. Comparison of both studies do not show good agreement, though. However, Density Functional Theory (DFT) [88] and Hartree-Fock (HF) [89] calculations favour the LEED-IV study, which is one reason for us to choose LEED and DFT for a quantitative determination of the 1×2 reconstruction.

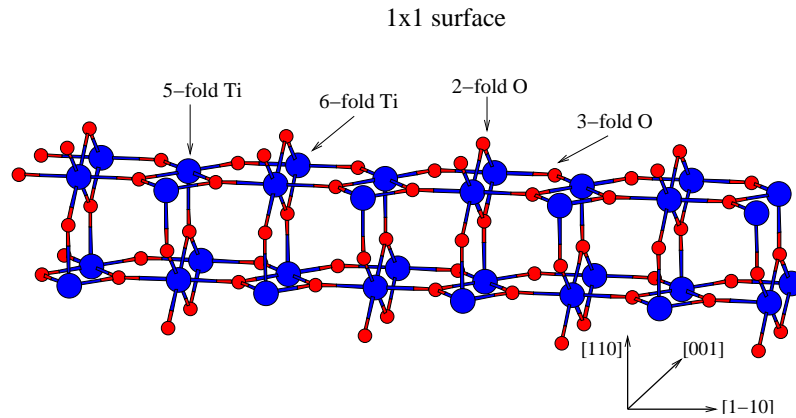


Figure 3.1: Ball and stick model for the undistorted surface TiO_2 (110)- 1×1 . Big spheres correspond to Ti atoms and small spheres to O atoms.

3.3.2 The rutile TiO_2 (110)- 1×2 reconstruction

The TiO_2 (110) surface undergoes a 1×2 reconstruction under annealing. However, there was no agreement about the geometry, neither about the stoichiometry of the surface. The most widely used experimental technique to study the structure of this surface has been STM [90, 91, 92, 93, 94, 95, 96, 97, 98], assisted by STM image simulations [99, 100, 101, 102]. Some qualitative LEED measurements have been done [103, 91, 104, 93, 94], but, to the author's knowledge, our work is the first quantitative LEED-IV analysis on the TiO_2 (110)- 1×2 reconstruction. To date, several models have been proposed in the literature. Fig. 3.2 shows ball and stick constructions of some of them, that will be discussed below.

- Missing row [103]: it was first intuitively proposed as a simple removal of bridging O rows from the stoichiometric 1×1 surface. This model is consistent with the presence of O vacancies, evidenced by photoemission [103]. Afterwards, the model was refined by introducing lateral relaxations on O and 5-fold coordinated Ti^{4+} atoms along $[1\bar{1}0]$ direction from STM images observation [90].
- Ti_3O_5 [92]: this model is based on high resolution STM images, which have been also simulated using first principles atomic orbital based calculations, where a simple match between surface LDOS and STM images is done. The proposed model consists of added rows on the 1×1 surface, with all bridging oxygens removed. In this structure, all the atoms reside on bulk terminated positions. It is also supported by photoemission and ESDIAD [104].
- Ti_3O_6 [94]: these authors report “cross links” on high temperature STM images, which are believed to stabilize the structure. Lower corrugation rows have Ti_2O_3 stoichiometry (this structure is described in detail in the next paragraph). Higher rows (cross linked) appear to have similarities with the added Ti_3O_5 model, the difference being an additional oxygen atom row upon Ti_3O_5 group, healing the bulk-like compensated structure.
- Ti_2O_3 [91, 105]: Onishi and co-workers proposed a model with added rows of Ti_2O_3 stoichiometry, centred above 5-fold Ti atoms. Double rows of Ti cations run in a string along $[001]$ direction located at octahedral sites, whereas the O atoms are placed at their original positions. The separation of Ti rows in the images is smaller than the 1×1 periodicity (about $\sim 4 \text{ \AA}$), and the heights of the ridges are smaller than a complete single step. In later observations, Onishi and co-workers assume that tunneling into vacant states of Ti^{3+} in the added row causes the double strand topography. The Ti^{3+} sites are 0.16 nm closer to the tip than the in-plane Ti^{4+} sites.

Those Ti sites would correspond to bulk interstitial defects, and consequently they can not be caused by simple removal of bridging oxygens, as considered for the missing row model. There exist two types of interstitial site, since the octahedra can take two possible orientations: aligned horizontally or vertically w.r.t. the (110) surface. First principles calculations show that it is the vertical orientation the one that is the energetically favoured [100].

The added-row Ti_2O_3 model is the one we favour [106], and it is supported by other theoretical and experimental techniques. This model has the lowest surface free energy [107, 102], and it holds the best agreement with simulated STM images [101, 102]. It is supported, too, by ESDIAD measurements [104, 108], AFM [97, 98, 109] and ICISS [110, 111], the last one adding O atoms upon exposed 5-fold Ti atom (i.e. heavily reduced surface).

Finally, it must be pointed out that the Ti_2O_3 units are not related to the alumina-like structure of bulk Ti_2O_3 oxide [112].

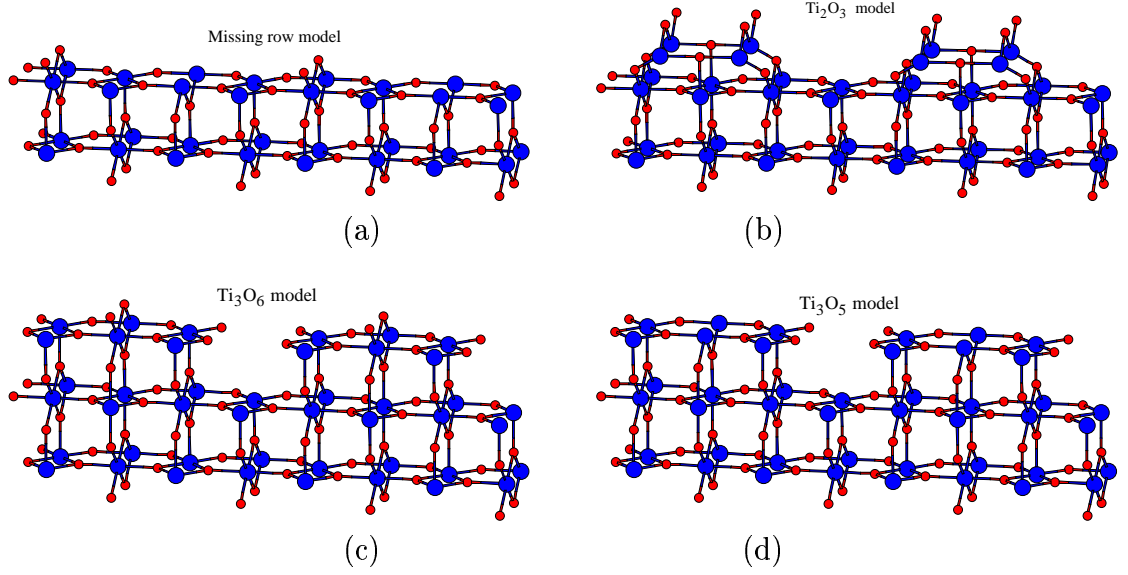


Figure 3.2: Ball and stick models for the undistorted surface $\text{TiO}_2(110)-1 \times 2$. There are four panels: (a) Missing row, (b) Added Ti_2O_3 row, (c) Added Ti_3O_6 row and (d) Added Ti_3O_5 row.

3.4 Experiments

3.4.1 Sample preparation and measurements

The experimental database to be analyzed has been obtained in the ICMM (ESISNA group [113]) and consists of STM images and LEED-IV curves. First, the optimum annealing conditions to obtain the 1×2 reconstruction are investigated. The sample, a both sides polished TiO_2 rutile single crystal of $10 \times 10 \times 1 \text{ mm}^3$ (PI-KEM Ltd. UK), has been treated by cycles for Ar^+ ion bombardment (1 keV, 10-30 min) and UHV annealing (1150 K, 60 min) until the surface was judged clean by AES. This procedure gives a very sharp 1×2 LEED pattern, with low background.

The surface, as checked by STM, displays mono-atomic steps ($\approx 3.2 \pm 0.2 \text{ \AA}$ height), and large areas of atomically flat terraces (more than 100 \AA wide). Color of the $\text{TiO}_2(110)$ sample turned from transparent to deep blue after the cycles (the blue colour becomes more intense as the bulk oxygen vacancy density increases). Experiments were performed in an ultra high vacuum system, with a base pressure of $2 \times 10^{-10} \text{ mbar}$. STM images were recorded in-situ at constant current mode and room temperature: scans were always recorded in the same direction. Tungsten tips were prepared by field emission. Best images have been found for bias voltages around 1.5 V (electrons tunneling from the tip into the sample). Fig. 3.3 shows two STM images, taken at different resolution ranges, of the 1×2 reconstructed surface. The existence of such a reconstruction is clear from the sharp features of the Fourier transform, shown at the bottom left panel of Fig. 3.3.

LEED IV curves were recorded using a 8-bits digital camera at room temperature. Prolonged electron beam exposure during the LEED IV measurements pro-

duces degradation of the LEED spots and increasing background intensity. To avoid these effects, the sample was displaced at short time intervals to expose fresh areas to the electron beam, and the sample was re-annealed (1150 K, 10-30 min.) to restore the 1×2 pattern to the initial quality. As an example, the bottom right hand panel of Fig. 3.3 shows the LEED pattern recorded at $E = 105$ eV. Finally, LEED IV curves have been measured at normal and off-normal incidence.

3.4.2 STM interpretation

The bright features appearing in the STM images are due to Ti atoms. This point has already been discussed in the literature [99, 107]: the contrast in positively sampled bias STM images is due to Ti (3d) electrons (electronic structure features) rather than bridging oxygens (2p) (geometry features). The LDOS in the vacuum region above the surface, calculated from pseudopotentials, shows that the charge density contours extend higher above the 5-fold Ti atoms, in spite of the physical protrusion of the bridging oxygens. This occurs near the conduction band minimum, where the states have a strong Ti-3d character [107].

Among the ball and stick models shown at Fig. 3.2, it is Onishi's Ti_2O_3 added row model, the one that holds the best agreement between the top view of Ti atoms and the bright features in the measured high resolution STM images. As shown in the top right hand panel of Fig. 3.3, the two brightest rows are separated by a distance of ~ 4 Å, which is Onishi's model main geometrical feature. More accurate theoretical support of this model has been reported using STM images simulated from first principles with Tersoff and Hamman approach [102]. In addition, a satisfactory visual agreement exists between that simulated image for Ti_2O_3 model and our experimental image of Fig. 3.3.

3.5 Theory

3.5.1 LEED calculations

To obtain qualitative detailed information about the stoichiometry and atomic positions a LEED-IV analysis has been performed. The Pendry R-factor, R_P [41], has been employed to compare experimental and calculated IV curves. Nineteen atoms have been included in the search, including both geometrical and vibrational variables. It should be taken into account that increasing the number of fit parameters may not always be a good strategy, since one structure could provide better results from the point of view of fit quality, despite being unphysical or "artifact-like" structure [114]. However, a large data base is known to provide better accuracy in the structural determination. Therefore, intensities measured at both normal and another off-normal incidence have been used in the analysis. The total size of the experimental data base is 2951 eV, 1424 eV on normal incidence and 1527 eV on off-normal incidence. Table 3.1 shows explicitly the list of the beams used in the analysis and the energy overlap corresponding to each one. Even if the two data sets have a similar size, the former is given greater confidence, since symmetry related beams have been averaged to decrease the signal-to-noise ratio. This allows us to

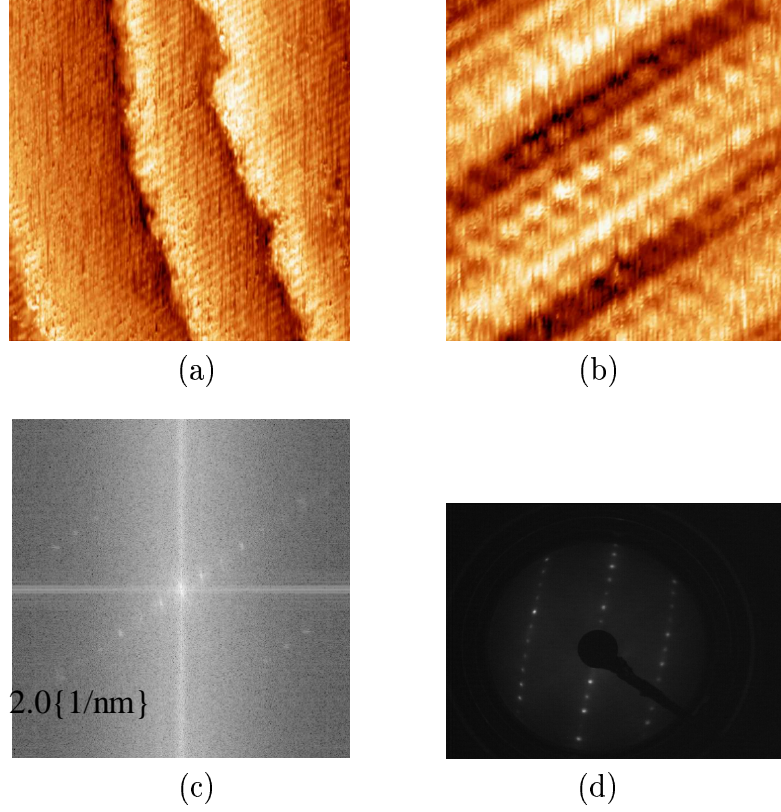


Figure 3.3: Constant current STM images of $\text{TiO}_2(110)\text{-}1 \times 2$, $V = +1.5$ V. Top left hand panel (a) shows monoatomic steps and large terraces on a $500 \times 500 \text{ \AA}^2$ area ($I = 0.146$ nA). Top right hand panel (b) shows a high-resolution image on a $30 \times 30 \text{ \AA}^2$ area on one of these terraces ($I = 0.178$ nA). Bottom left hand panel (c) shows the inverse Fourier transform of the STM high resolution image, which shows the existence of a 1×2 reconstruction. Bottom right hand panel (d) shows the sharp features of the LEED pattern taken at energy $E = 105$ eV.

define a global R-factor,

$$R_P = \frac{2}{3}R_{P,\text{normal}} + \frac{1}{3}R_{P,\text{off-normal}} \quad (3.1)$$

where the weights are inferred from the relative extent in energies of each non-averaged data base. The price to pay for using off-normal data is that the incidence polar (θ) and azimuthal (ϕ) angles must be fitted as independent parameters.

Estimates for angle values can be taken from the manipulator goniometer itself, or in a more advantageous way, from an iterative triangulation method [1]. The calibration of the manipulator in the experimental set up yields $6^\circ \pm 2^\circ$ as initial experimental value for the polar angle. Angle estimation using the iterative procedure given by Van Hove *et al* [1] yields $\theta = 4.5^\circ$. Azimuthal angle ϕ was not estimated from these methods. In any case, this is only to provide initial values and the angles must be fitted during the full-dynamical IV analysis. We have done this by analyzing the most promising structures derived from normal incidence data and minimizing the R_P around the initial guesses given by manipulator calibration and triangulation.

	normal-incidence	off-normal incidence
integer-beams	(01) 219 eV	(00) 220 eV
	(02) 115 eV	(0-1) 212 eV
	(10) 239 eV	(0-2) 75 eV
	(12) 139 eV	(02) 40 eV
	(03) 134 eV	(-10) 158 eV
		(10) 180 eV
		(-1 -1) 30 eV
total overlap	790 eV	915 eV
non-integer-beams	(0 3/2) 162 eV	(0 1/2) 83 eV
	(1 1/2) 138 eV	(0 -3/2) 105 eV
	(0 5/2) 167 eV	(1 -1/2) 160 eV
	(1 3/2) 167 eV	(1 1/2) 145 eV
		(-1 1/2) 79 eV
		(1 3/2) 40 eV
total overlap	634 eV	612 eV

Table 3.1: Beams forming the experimental database for the LEED-IV analysis and the energy overlap (in eV) corresponding to each of them.

Phase shifts

Phase shifts have been computed from MUF POT code [14] and Hartree-Fock solutions to the neutral and ionic species. The muffin tin radii for Ti and O influence the computed phase shifts, and it is not obvious how to choose their values. Self-consistent DFT calculations of the charge density distribution in a TiO_2 molecule using Gaussian code [115] show that a good choice is to give the same radius 0.95 Å to both ions, rather than values close to their atomic radii (1.45 Å for Ti and 0.65

Å for O) or to their covalent radii (1.32 Å for Ti and 0.73 Å for O). Charge transfer suggest that only Ti^{2+} and O^{1-} ions need to be considered, instead of the nominal charge values, Ti^{4+} and O^{2-} . For the Ti^{2+} ion, we take the minimum energy electronic configuration, which corresponds to $4s^1 3d^1$. We find only minor differences between using neutral or charged muffin tins. This is shown at Figs. 3.4 and 3.5, where the calculated phase shifts of both neutral and charged species of Ti and O atoms are compared, respectively. However, more significant changes in the phase shifts appear for different radii. As reported by Lindsay *et al.* [87], phase shifts have played an important role at the determination of the TiO_2 (110) - 1×1 relaxed structure. These authors did not find satisfactory agreement between their experimental and calculated IV curves when working with the usual Hartree-Fock and muffin tin approach. They suggest that charge transfer is strong enough to deviate the scattering potential from a simple atomic wavefunction superposition. Thus, they have developed a more sophisticated self-consistent procedure [116]. First, they produce an accurate ab-initio electron density, which is used to divide the crystal into regions according to Bader topological criterion [117]. The critical points positions of the electron density isosurfaces are used to assign a new radius to each ion, which is, in general, different from that of its gas phase. Lindsay *et al.* obtain radii of 1 Å, a similar result to ours. Finally, these muffin tins are used in a Korringa-Kohn-Rostoker (KKR) [45] calculation to generate the phase shifts.

We have introduced their self-consistent phase shifts in our calculations, and we have found that R-factors and geometries are little affected by using sets computed differently, although, as commented above, self-consistent DFT calculations are required to choose the right muffin tin radii. The set of self-consistent phase shifts is plotted in Figs. 3.4 and 3.5, too. We can observe that discrepancies with our MUF-POT calculations for charged muffin tins are almost negligible. The IV curves will be analyzed using this set of phase shifts from charged muffin tins. A more accurate representation of the atomic scatterers for LEED calculations would consist of using non-spherical muffin tins estimated from Bader division of the crystal.

A maximum angular momentum number $l_{\max} = 8$ is enough for convergence in IV calculations, and it has been tested by comparing for values $l_{\max} \pm 1$.

Search procedure

The used search code is TensErLEED [70]. First, reference structure calculations are full-dynamically done using a layer doubling and composite layer scheme for interlayer distances ≤ 1.2 Å. Then, a search is performed for small distortions (± 0.2 Å) of these reference models using the Tensor-LEED approach [23]. To reduce the number of search parameters, vibrations have been restricted to outer layers and constrained to the same value in each layer.

It is well known that LEED intensities are rather insensitive to lateral displacements in the atoms. Besides, as commented above, it is not convenient to enlarge the parameter set when fitting the IV curves. For these reasons, the lateral displacements provided by DFT calculations are fed in LEED calculations. In fact, it is observed that the changes in the parallel coordinates lead to non-significant changes in the R-factor. We have explored around those values to find, as anticipated, too big error bars to get significant conclusions.

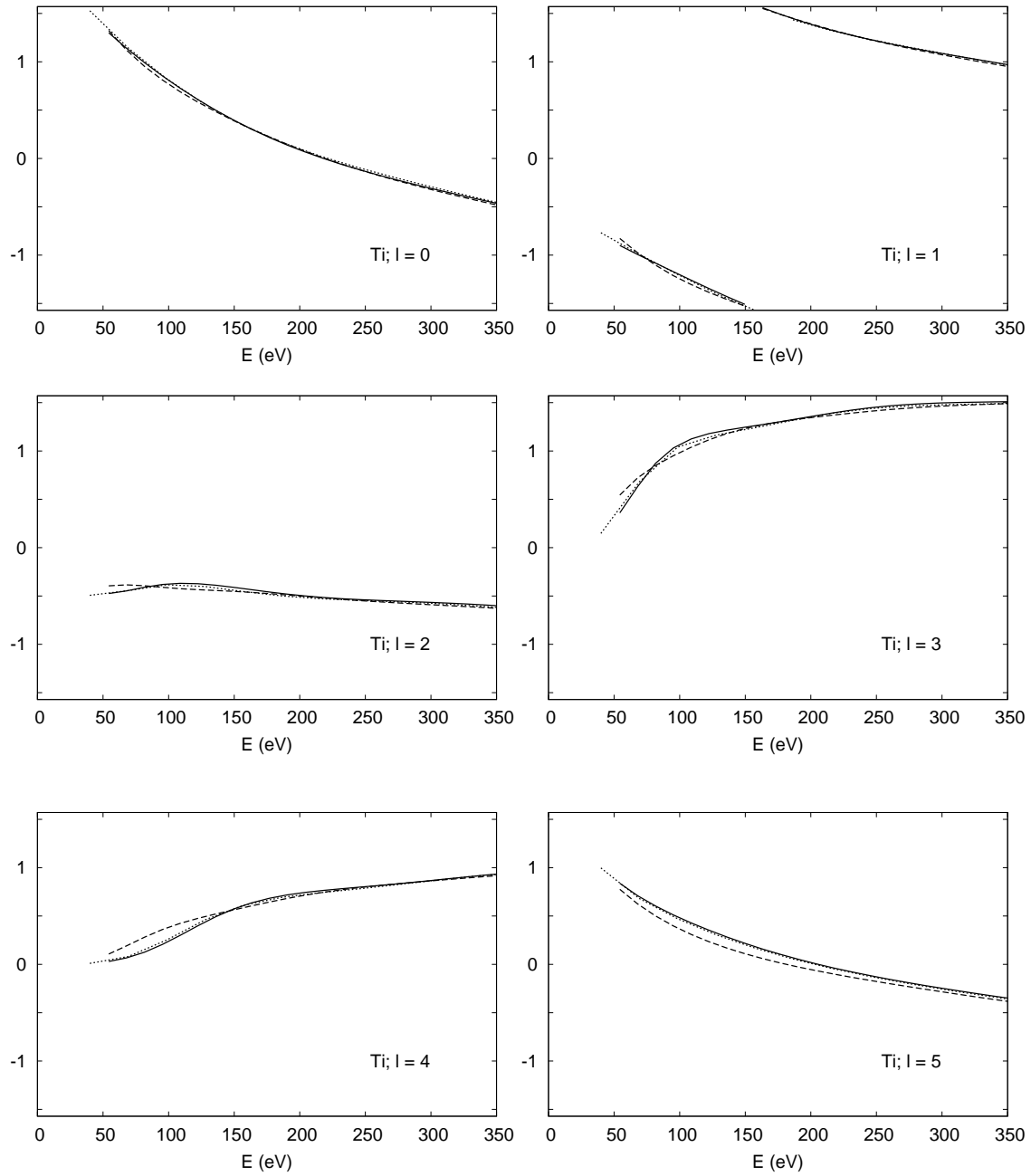


Figure 3.4: Titanium phase shifts for angular momentum numbers $l = 0, \dots, 5$. Solid line corresponds to the phase shifts used in the IV curve analysis of this work, calculated with MUFFPOT program for 0.9 Å muffin tin radius and charged ion cores, Ti^{2+} (at electronic configuration $4s^1 3d^1$, the one that has the minimum energy) and O^{1-} ; dashed line corresponds to the same calculation but made with neutral muffin tins, and dotted lines are the self-consistent phase shifts calculated by Lindsay *et al* [116].

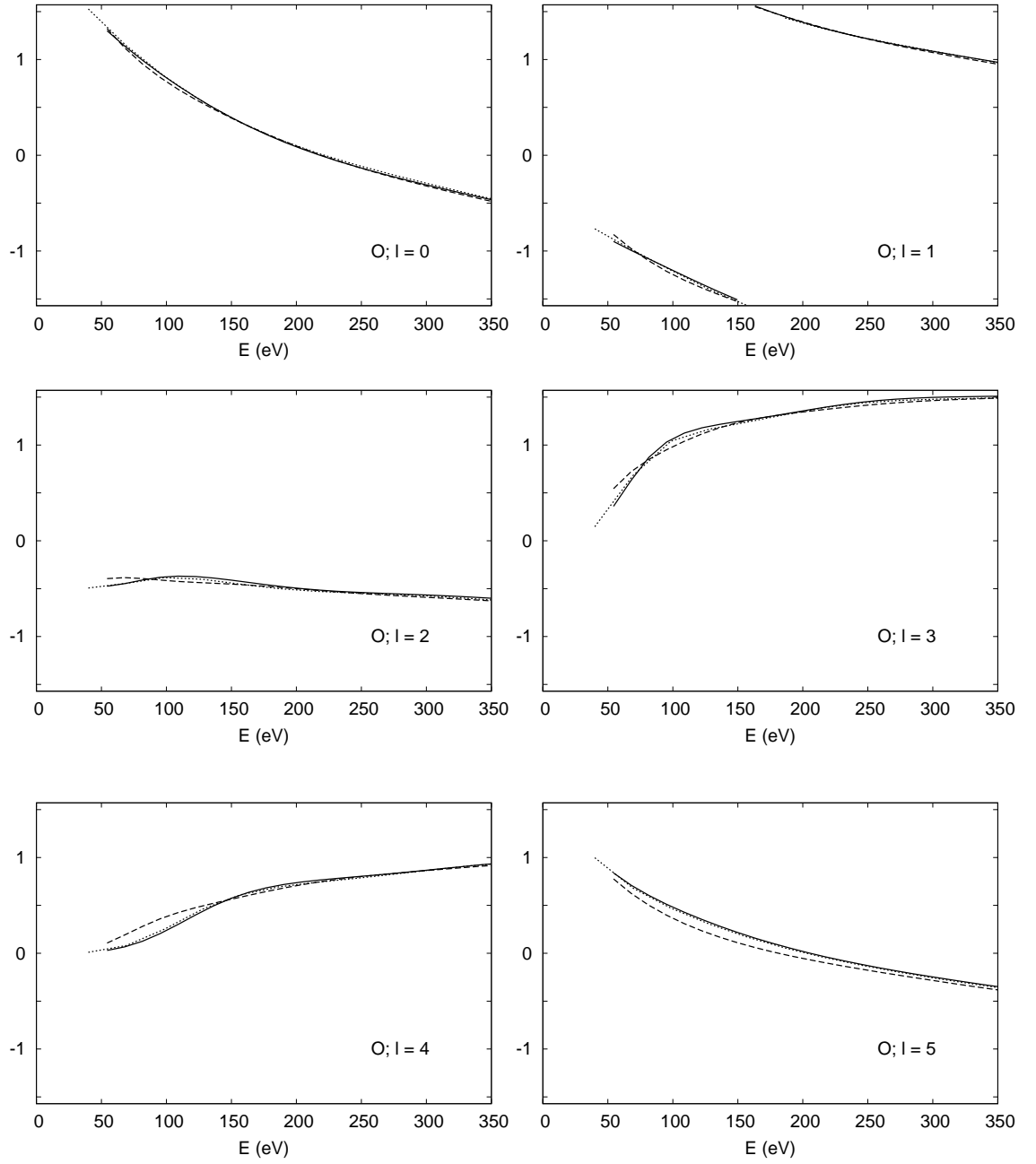


Figure 3.5: Oxygen phase shifts for angular momentum numbers $l = 0, \dots, 5$. Calculation parameter's and line types correspond to the same cases explained at the caption of Fig. 3.4.

Despite of these constraints, the number of search parameters is still high, and the R-factor hypersurface shows multiple local minima. TensErLEED uses the random sampling algorithm (RSA) [118] to explore efficiently the resulting huge parameter space. It is a global algorithm combined with a multiple launch strategy. More on this algorithm will be commented in Chapter 6.

Prior to working with the complete database, we have performed an initial screening for some model structures (Fig. 3.2) using only normal incidence data. It is well accepted that Pendry R-factors larger than 0.5 reflect such a poor correlation between theory and experiment that those models are very unlikely and can immediately be rejected. This is the case for most of the candidates shown on Fig. 3.2, which have been discarded from a preliminar analysis of the normal-incidence data only. In particular we find $R_P = 0.67$ for Ti_3O_6 groups, $R_P = 0.61$ for Ti_3O_5 groups and $R_P = 0.52$ for the missing row model. Another model, based on direct reconstruction of LEED data by Patterson methods, has been also investigated. It is a stoichiometric model, where the 1×2 symmetry is achieved by buckling alternate bridging oxygens in the $[1\bar{1}0]$ direction at the 1×1 surface [119]. The best fit for this model yielded $R_P = 0.50$, big enough to discard it. This model was constructed by comparison of experimental and model Patterson function maps from multiple incidences [120]. It is not very reliable, since the data base, consisting of just two incidences, is not large enough and the experimental map looks fairly blurred. The only model showing a reasonable agreement is Onishi's Ti_2O_3 added row model, with $R_P = 0.28$. This value is reasonably good if the previous LEED work on the 1×1 surface [87] is used as a reference. Different reasonable "deformations" of this model have been explored, too, particularly those concerning the interstitial position of the Ti(a) atom [100]. This possibility gives a best R-factor around 0.6. We should mention that another group working on the same reconstruction with LEED and SXRD has reported preliminar results favouring the same Ti_2O_3 stoichiometry [121].

After this initial screening of candidates, we proceed to optimize further atomic positions and discriminate between the most likely structures adding the off-normal incidence IV curves to our database. From direct visual inspection of the off-normal incidence database we can infer that ϕ does not correspond to any symmetry direction of the surface. After our full dynamical calculations, the pair of angles showing the best overall agreement is $\theta = 4^\circ \pm 1^\circ$ and $\phi = 25^\circ \pm 10^\circ$. The azimuthal angle is less precisely determined, since that movement in the manipulator produces a smaller symmetry breaking in the spot intensities than that produced by changing the polar angle. In Table 3.3 we analyze our results from the point of view of both data sets and the integer and non-integer beams respectively. The global value of $R_P = 0.28$ is very convincing, as it is the visual agreement between experimental and calculated beams, shown at Fig. 3.8. Furthermore, individual R-factors for the different data sets show a reassuring similar agreement.

Optimized values for the real and imaginary part of the self-energy are $V_{0r} = 8.0$ eV and $V_{0i} = 5.5$ eV, respectively. It must be pointed out the importance of using large vibrations at surface atoms. During the LEED fit of normal-incidence data, the R_P value dropped from 0.4 to 0.3 when introducing isotropic vibrations via a Debye-Waller model. First values for thermal vibration amplitudes were taken from

EXAFS measurements in the literature [122].

It can be observed that, when applying this strategy to normal incidence data, the independent launches fall in different minima, quite close to each other and of similar depth. Off-normal data are used afterwards to choose the structures that give the best overall agreement according to the global R_P defined above. We follow this procedure to increase our confidence on the final structure.

We have tried this procedure in the inverse direction, i.e. using RSA on off-normal data and checking these structures with normal data. Doing this, unsatisfactory results are achieved, with very low $R_{P,\text{off-normal}}$ and high $R_{P,\text{normal}}$. The reason for this is that signal-to-noise ratio is higher at off-normal data, since beams are not averaged. These curves will contain a number of small peaks that are likely to be fitted by many proposed structures. Some of these structures may eventually be revealed as non-physical. In fact, it can be checked that structures yielding $R_P \sim 0.2$ for off-normal data provide $R_P \sim 0.4$ for normal curves. We can illustrate this situation with the following example. When analyzing the off-normal data (varying incidence direction, vibrations and vertical displacements, but not lateral displacements for simplicity), we find a structure that provides a minimum $R_P = 0.32$, with $R_{P,\text{off-normal}} = 0.22$ but $R_{P,\text{normal}} = 0.36$. The details of this structure, that we denote “I”, are summarized at Table 3.2. To check if “I” is a reliable minimum, we study the R-factor behaviour when a perturbation is applied to the “I” structure by varying one parameter. As we will see in the next section, the z coordinate of the the topmost oxygen atom (the O(1) atom in the the ball and stick model of Fig. 3.6) is a relevant parameter of the surface. The R-factor dependence with $z(\text{O}(1))$ is plotted at Fig. 3.7. There, we can see that the “I” structure does not correspond to a minimum of the global R_P . Even if “I” lies in a clear well of $R_{P,\text{off-normal}}$, $R_{P,\text{normal}}$ does not vary significantly.

To calculate error bars of the fitted magnitudes, we use the techniques given in section 2.8. We will consider as valid all the structures holding the condition $R_P \leq R_{\min}(1 + RR)$. As the number of parameters to fit is considerably high, single parameter R-factor scans have been done freezing the other parameters at their optimum values, i.e. those values yielding R_{\min} .

The apparently different brightness at both sides of the Ti_2O_3 ridges in the $[1\bar{1}0]$ direction at the STM images suggests the possibility of certain symmetry breaking. As, for normal incidence, IV curves show a mirror plane σ_y perpendicular to that direction, we have examined the possibility of two co-existing domains, rotated 180° w.r.t. each other, with no σ_y symmetry. Parameter fitting using TensErLEED package demonstrates that this possibility should be dismissed. This procedure involves a considerable increase of the search space size, which is considered to be a drawback as we explained before. Thus, some sensible constraints must be applied, for example, maintaining the σ_y plane for deep layers. In any case, the drop in the R_P value is not significant enough to consider two domains. The apparent loss of symmetry in the STM images is probably an artifact due to sweeping effects of the tip.

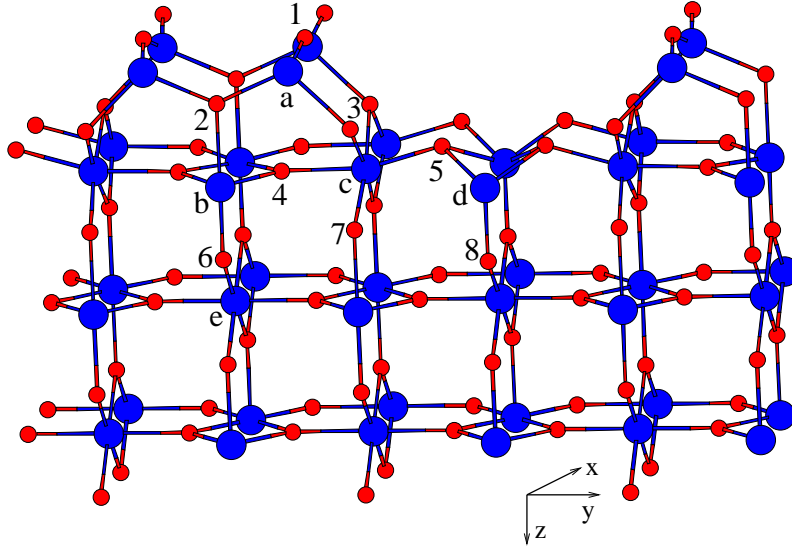


Figure 3.6: Schematic model for $\text{TiO}_2(110)-1 \times 2$ obtained from the best fit to LEED data ($R_P = 0.28$), denoted as “H” structure in the text. Large and small spheres arbitrarily correspond to Ti and O atoms respectively. O atoms have been labelled with numbers (1-8), while Ti atoms have been labelled with small letters (a-d). Atoms in the lowest layer have been frozen to their optimized bulk positions.

Atom	u	x	y	z
Ti(a)	0.22	0.0	1.77	-5.97
Ti(b)	0.14	0.0	0.0	-3.10
Ti(c)	0.14	1.48	3.28	-3.27
Ti(d)	0.14	0.0	6.49	-3.07
O(1)	0.30	1.48	1.99	-7.09
O(2)	0.14	0.0	0.0	-5.22
O(3)	0.10	0.0	3.07	-4.58
O(4)	0.10	1.48	1.25	-3.18
O(5)	0.10	1.48	5.22	-3.52
O(6)	0.10	0.0	0.0	-1.36
O(7)	0.10	0.0	3.28	-2.00
O(8)	0.10	0.0	6.49	-1.34

Table 3.2: Parameters determining the structure “I”, corresponding to the minimum R_P from analysis of the off-normal incidence data. Cartesian coordinates x, y, z and root mean square vibration amplitude, u , are given in Å. Other parameters of this calculation are $V_{0i} = 5.5$ eV, $V_{0r} = 7.0$ eV and incidence angles $\theta = 3^\circ$ and $\phi = 15^\circ$.

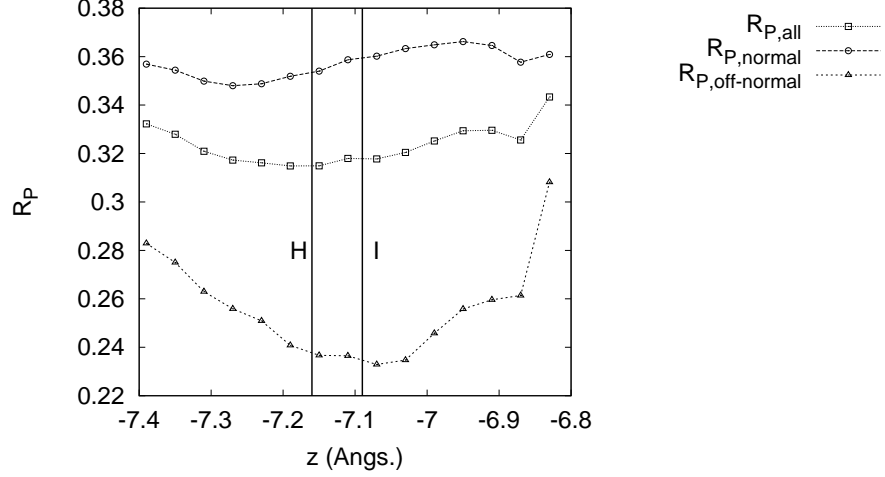


Figure 3.7: R_P as a function of the O(1) atom height, calculated with the other parameters fixed at the values of “I” structure (these values can be found at Table 3.2). Height is taken w.r.t. the origin at Ti(e) atom (see Fig. 3.6 for atom labels). The vertical line on the right indicates the $z(\text{O}(1))$ value corresponding to the “I” structure. The line on the left indicates the $z(\text{O}(1))$ value at the actual best fit structure, labelled “H”.

3.5.2 DFT calculations

The consistency of the structure can be tested further by computing its total energy and the forces on the different atoms. This allows us to understand different electronic and vibrational properties of the material that should be relevant to understand more general properties. Such calculations have been done with the help of Dr. P.L. de Andrés, using the Barcelona Supercomputer Center facilities [123]. Using a plane-waves basis, a pseudopotential approach can describe quite accurately the structural properties of the bulk TiO_2 .

We have minimized the total energy and the stress on the unit cell from calculations based on Density Functional Theory (DFT) [124]. Electronic states are expanded in a plane-wave basis [125] or gaussians [115], and appropriated pseudopotentials [126] have been used to describe the different atoms (O $2s^2 2p^4$, and Ti $3s^2 3p^6 3d^2 4s^2$). The Perdew-Burke-Ernzerhof (PBE) generalized gradient approximation to the exchange and correlation functional has been used [127] (the use of LDA instead of PBE, leads to differences of order $\lesssim 0.05 \text{ \AA}$ in the coordinates). An energy cutoff of 340 eV has been routinely used with finite basis corrections estimated at ± 5 eV increments. Converged equilibrium structures have been recomputed with a cutoff of 400 eV. The supercell for the 1×2 model included 41 atoms with the lowest layer kept fixed to optimized bulk positions (see Fig. 3.6). This makes an slab with three 1×1 layers and one 1×2 layer (approximately 13 \AA wide). To avoid interactions between different slabs, we have introduced a 24 \AA vacuum gap in the direction perpendicular to the surface. Calculations were performed with a $7 \times 13 \times 1$ Monkhorst and Pack k-points grid ($4 \times 7 \times 4$ for bulk calculations). Convergence on

the energy cutoff and the number of k-points have been monitored to make sure that the the maximum change in any atomic position is less than 0.02 Å. Phonons were only computed at the gamma point, constructing the dynamical matrix from small finite displacements of each atom in the unit cell. Other convergence thresholds have been chosen as follows: total energy change per ion less than 10^{-5} eV, maximum displacement of any ion less than 0.001 Å, maximum force on any ion less than 0.01 eV Å⁻¹, and maximum stress on the unit cell less than 0.02 GPa.

3.6 Discussion on the atomic structure

3.6.1 Geometry

Fig. 3.6 shows the relaxed Onishi's model after optimization (notice that Z axis points inwards). The corresponding atomic coordinates and thermal vibration amplitudes obtained from LEED analysis are shown on Table 3.6, and the position differences from the structure provided by DFT/GGA energy minimization are shown as well. Table 3.5 shows explicitly the structure obtained from DFT/GGA. Since DFT in the GGA approximation slightly overestimates lattice parameters, the fractional coordinates derived from this method have been rescaled to their experimental values for a proper comparison with LEED positions, i.e. errors in the unit cell size and in the internal positions are taken apart. Some of the experimental IV curves and their corresponding calculated ones for that structure are shown at Fig. 3.8. The R-factors of those calculations are summed up in Table 3.3, which shows the R-factors of separated beam sets. The final global R-factor value is $R_P = 0.28$, which we consider satisfactory either from its absolute value and from visual agreement in the IV curves.

Error bars have been systematically computed following the method explained above. O(1) atom z parameter appears to have a singular behaviour and we shall comment it in detail. The partial and global R-factor as a function of the O(1) atom height, keeping the other parameters of the search fixed at their values of Table 3.6, shows a clear double well taking values below the error bounds of R_P , as it is shown on the graph at Fig. 3.10. The minimum placed at $z = -7.16$ Å corresponds to the structure described above, that will be denoted by “H” (from “high”) in the following. A second minimum appears at $z = -6.55$ Å that yields $R_P = 0.27$ ($R_{P,\text{normal}} = 0.28$ and $R_{P,\text{off-normal}} = 0.26$). We must check that this second well really corresponds to another valid structure, and that it is not an artifact of error estimation as a consequence of parameter correlation effects. We will denote this structure by “L” (from “low”). Thus, we perform further refinements for structures close to the new minimum, including again both incidence data sets in the search, in the same fashion as it has been done for “H” structure. We find that the O(1) actual height in “L” structure is $z = -6.49$ Å. The R-factor and coordinate details for this “L” structure are given on Tables 3.7 and 3.4, respectively. The IV curve fitting achieved in this case, shown at Fig. 3.9, is visually correct, too.

In the “L” structure, O(1) atom seems to be too close to the underlying Ti(a) atomic plane, forming bonds of length $d = 1.57$ Å, in contrast to typical Ti–O distances, $d \sim 1.9$ Å. A similar feature has been observed at a different reconstructed

face of TiO_2 , the (011)- 2×1 , where double bond species $\text{Ti}=\text{O}$ of length $d = 1.62 \text{ \AA}$ appear [128]. However, in the (011) surface, the dangling oxygen occupies an atop site, whereas O(1) in (110) surface occupies a bridge position. We have found that atop position for that atom leads to $R_P > 0.5$.

Using LEED arguments only, we can not distinguish between “H” and “L” structures, so we use DFT results to discriminate between them. Direct comparison of xyz coordinates clearly favours “H” structure. Tables 3.7 and 3.4 contain a column showing the differences in the atomic coordinates yielded by LEED and DFT. As bond lengths are important from the point of view of surface chemistry, we have analyzed the nineteen most relevant interatomic distances, shown at Table 3.8. Again, the discrepancy with DFT is clearly lower for “H” structure.

Another reason for rejecting “L” structure might be the strong difference between the normal and the off-normal R-factors, 0.24 and 0.33 respectively, whereas the R-factors obtained for “H” structure are more homogeneous. This could be interpreted as an inconsistency that leads us to conclude that “L” gives a spurious agreement with the normal database.

It is interesting to notice that the total energy increases slowly as a function of the height of O(1). This explains why large amplitudes of vibration can be found, giving a rather delocalized picture of the atom, and a large uncertainty on the position derived from LEED. We find that a vertical displacement of the two oxygen atom in the unit cell towards the bulk by about 0.27 \AA brings an increase in the total energy of about 0.15 eV , while small displacements towards the vacuum region brings restoring forces four times bigger.

Schematically, the total energy, as a function of the O(1) atom height, has the shape depicted at the top panel of Fig. 3.11. A minimum exists for a set of coordinates closer to the “H” structure determined by LEED and further from the “L” structure. The growth in the energy is faster for increasing heights of O(1) and slower when O(1) moves towards the bulk. This situation is combined with the behaviour shown by LEED R_P as a function of O(1) height. R_P has a local minima at the “H” structure and another slightly deeper minimum at “L”. The scenario shown at Fig. 3.11, makes us to conclude that DFT favours the “H” structure.

Once the “H” model has been chosen as the most likely one, we shall comment briefly on the discrepancies with DFT results. Only O(2) and Ti(d) atoms show height differences outside the error bars. However, we must bear in mind that DFT calculations are done at $T = 0 \text{ K}$, so the differences can be explained by the extent of atomic thermal vibrations, which are crucial in the IV fit as explained above, and are of the same order of the discrepancy.

Regarding interatomic bond distances, Ti(a)-Ti(b) and Ti(a)-Ti(c) bond lengths are reduced w.r.t. the typical Ti-Ti bulk distance (3.56 \AA , 3.60 \AA for DFT) by 0.2 \AA , and 0.12 \AA respectively. The maximum discrepancy between LEED and DFT on these values is 0.04 \AA : both techniques show the existence of an increased interaction between these Ti atoms. Regarding the interaction between Ti and O, the highest reduction in bond length is observed between Ti(d) and O(8): 1.77 \AA (discrepancy with DFT is 0.04 \AA), making this 5-fold coordinated Ti interesting from the point of view of chemical reactivity. Other relevant distances are shown at Table 3.8. The average discrepancy between LEED and DFT is less than 0.001 \AA , with a standard

deviation of 0.05 Å. Only five of these lengths differ from DFT by an amount bigger than 0.05 Å.

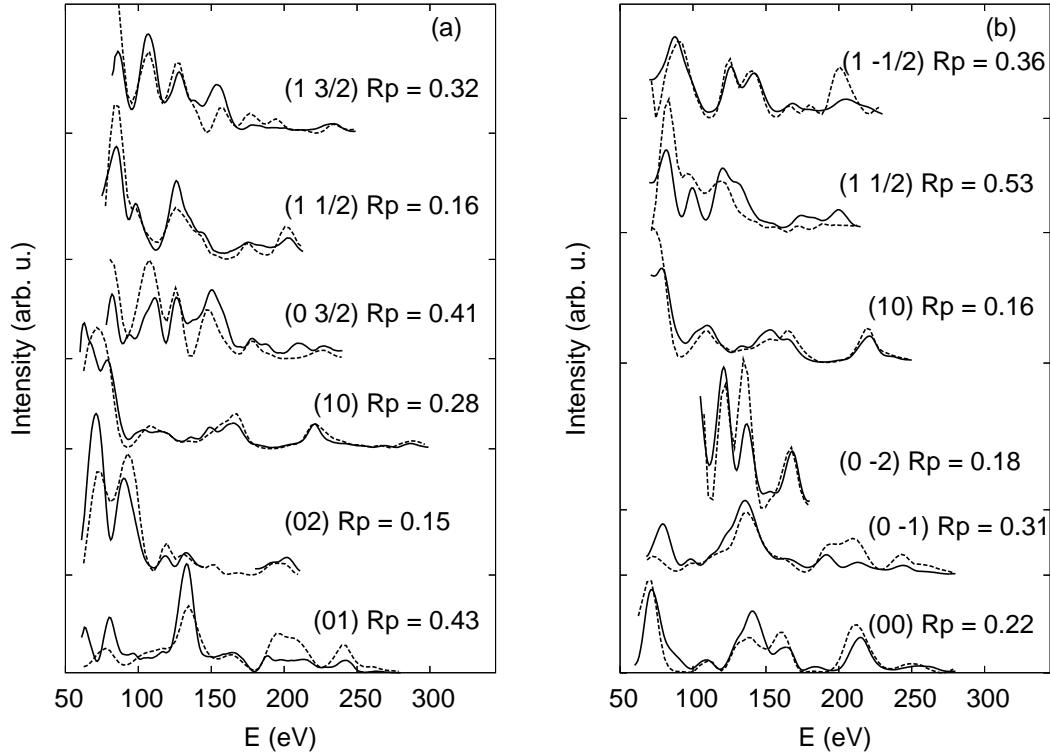


Figure 3.8: Experimental LEED $I_g(E)$ curves (full line) compared with theoretical calculations (dashed line) for the best-fit model “H”. A few representative integer and non-integer beams are given for normal incidence (a) and off-normal one (b).

	normal-incidence	off-normal incidence	all
integer-beams	0.27 (790 eV)	0.22 (915 eV)	0.25
non-integer-beams	0.30 (634 eV)	0.38 (612 eV)	0.33
all-beams	0.28 (1424 eV)	0.28 (1527 eV)	0.28

Table 3.3: Pendry R-factors for best fit Ti_2O_3 “added-row” structure, denoted “H” structure in the text, (overlap between experiment and theory is given in parenthesis in eV). Normal incidence (averaged over symmetry related beams) and off-normal ($\theta = 4^\circ$, $\phi = 25^\circ$) values are given.

3.6.2 Thermal vibrations

As mentioned above, top layers thermal vibration have a strong influence on the LEED spectra. The values determined for the Ti_2O_3 group show a considerable enhancement w.r.t. the bulk values, taking values in a range of $u = 0.20 \sim 0.30$ Å.

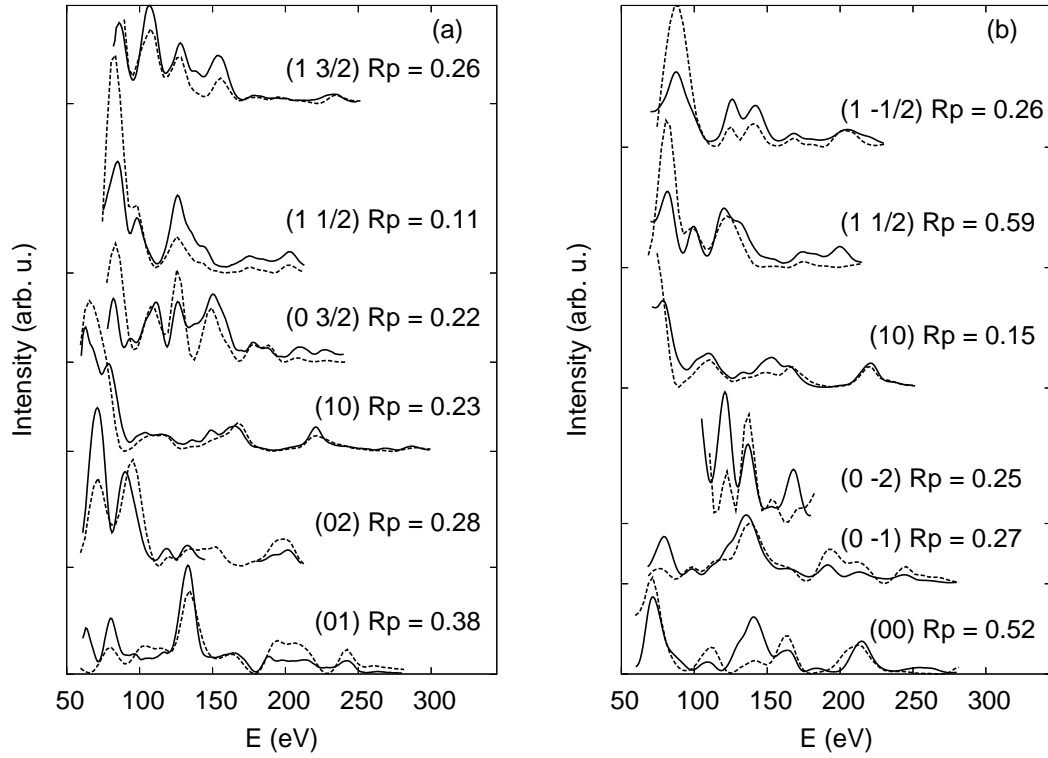


Figure 3.9: Experimental LEED $I_g(E)$ curves (full line) compared with theoretical calculations (dashed line) for the model “L”. A few representative integer and non-integer beams are given for normal incidence (a) and off-normal one (b).

	normal-incidence	off-normal incidence	all
integer-beams	0.27 (790 eV)	0.33 (915 eV)	0.29
non-integer-beams	0.21 (634 eV)	0.33 (612 eV)	0.25
all-beams	0.24 (1424 eV)	0.33 (1527 eV)	0.27

Table 3.4: Pendry R-factors for best fit Ti_2O_3 model (overlap between experiment and theory is given in eV) with “L” structure positions.

Atom	x	y	z
Ti(a)	0.0	1.77	-6.01
Ti(b)	0.0	0.0	-3.20
Ti(c)	1.48	3.29	-3.32
Ti(d)	0.0	6.49	-3.22
O(1)	1.48	1.99	-7.01
O(2)	0.0	0.0	-5.42
O(3)	0.0	3.07	-4.72
O(4)	1.48	1.27	-3.36
O(5)	1.48	5.24	-3.59
O(6)	0.0	0.0	-1.30
O(7)	0.0	3.32	-2.13
O(8)	0.0	6.49	-1.40

Table 3.5: Lower-energy structure found from DFT, in Å. Origin is at Ti(e). Fractional coordinates from DFT calculations have been rescaled with the experimental lattice parameters to obtain the position shown at the present table.

Atom	u	x	y	z	Δz	$\Delta \rho$	ΔQ
Ti(a)	0.22	0.0	1.77	-5.99 ± 0.03	-0.02	0.0	0.04
Ti(b)	0.14	0.0	0.0	-3.14 ± 0.07	-0.06	0.0	0.02
Ti(c)	0.14	1.48	3.28	-3.27 ± 0.06	-0.05	0.01	-0.03
Ti(d)	0.14	0.0	6.49	-3.08 ± 0.05	-0.14	0.0	-0.05
O(1)	0.36	1.48	1.99	-7.16 ± 0.24	0.15	0.0	0.0
O(2)	0.14	0.0	0.0	-5.23 ± 0.07	-0.19	0.0	-0.06
O(3)	0.12	0.0	3.07	-4.60 ± 0.11	-0.12	0.0	-0.05
O(4)	0.10	1.48	1.25	-3.21 ± 0.12	-0.15	0.01	-0.04
O(5)	0.10	1.48	5.22	-3.54 ± 0.06	-0.05	0.02	-0.06
O(6)	0.10	0.0	0.0	-1.30 ± 0.22	0.0	0.0	-0.02
O(7)	0.10	0.0	3.28	-2.03 ± 0.22	-0.10	0.04	-0.02
O(8)	0.10	0.0	6.49	-1.31 ± 0.12	-0.09	0.0	-0.01

Table 3.6: Atomic coordinates of the best-fit structure obtained from LEED ($R_P = 0.28$), i.e. “H” structure, and comparison with the lower-energy structure found from DFT. Origin is at Ti(e). Cartesian coordinates x , y , z , root mean square vibration amplitude, u , and DFT displacement respect the LEED value in the perpendicular, Δz , and parallel direction, $\Delta \rho$, are given in Å. Where appropriate, the error bars are given. The excess or defect of charges respect the bulk, ΔQ , are given in units of the electron charge. Error bar for atom O(1) is estimated from half-width of the well corresponding to “H” structure in R_P plot of Fig. 3.10.

Atom	u	x	y	z	Δz
Ti(a)	0.26	0.0	1.78	-5.96 ± 0.02	-0.05
Ti(b)	0.16	0.0	0.0	-3.15 ± 0.03	-0.05
Ti(c)	0.16	1.48	3.34	-3.20 ± 0.04	-0.12
Ti(d)	0.16	0.0	6.49	-3.06 ± 0.03	-0.15
O(1)	0.30	1.48	1.98	-6.49 ± 0.22	-0.52
O(2)	0.26	0.0	0.0	-5.19 ± 0.16	-0.23
O(3)	0.16	0.0	3.24	-4.57 ± 0.06	-0.15
O(4)	0.16	1.48	1.26	-3.18 ± 0.09	-0.18
O(5)	0.16	1.48	5.22	-3.49 ± 0.07	-0.09
O(6)	0.10	0.0	0.0	-1.20 ± 0.18	-0.10
O(7)	0.10	0.0	3.24	-2.03 ± 0.14	-0.10
O(8)	0.10	0.0	6.49	-1.30 ± 0.06	-0.10

Table 3.7: Fitted atomic coordinates in Å for “L” structure and their vertical discrepancy with DFT values. Error bar for atom O(1) is estimated from half-width of the well corresponding to “L” structure in R_P plot of Fig. 3.10.

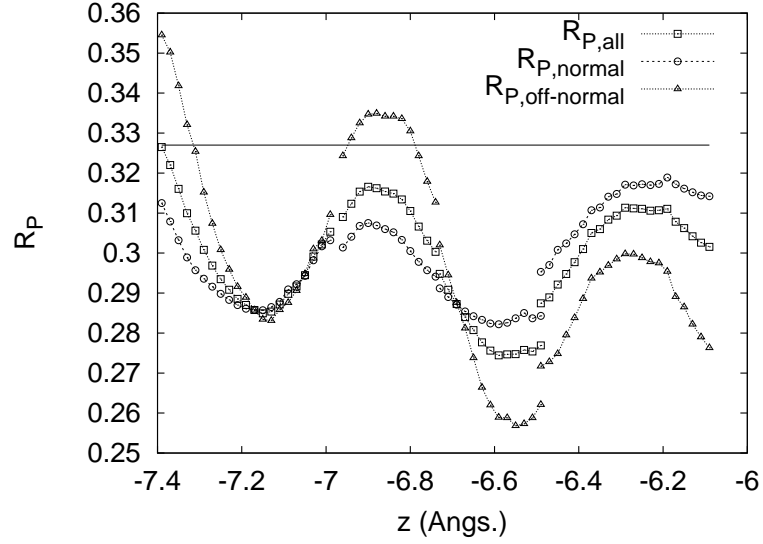


Figure 3.10: R_P as a function of the O(1) atom height, calculated with the rest of parameters frozen at the values of “H” structure (see Table 3.6). The horizontal line establishes the limits given by the standard deviation value, after Eq. (2.66).

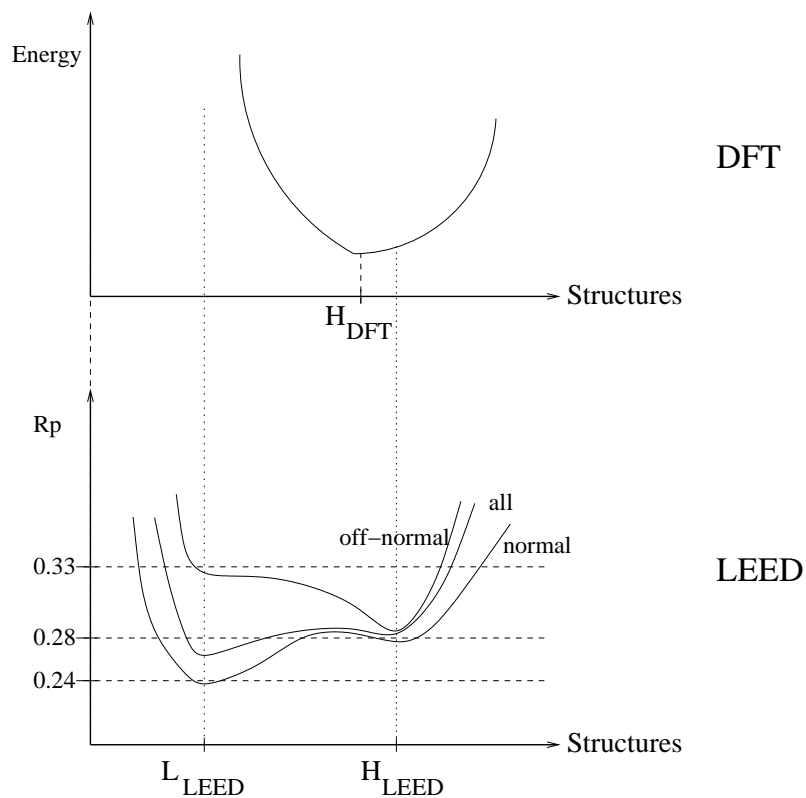


Figure 3.11: Schematic picture of the behaviour of the total energy and LEED R_P as a function of the two proposed candidate structures. R_P wells have comparable depths, but the total energy minimum supports the “H” structure.

Pair	$d(\text{DFT})$	$d(\text{L})$	$d(\text{H})$	$d(\text{DFT-L})$	$d(\text{DFT-H})$
Ti(a)-O(1)	1.80	1.58	1.90	-0.22	0.10
Ti(a)-O(2)	1.86	1.94	1.93	-0.08	-0.06
Ti(a)-O(3)	1.84	2.02	1.90	-0.19	-0.07
Ti(b)-O(2)	2.22	2.04	2.09	-0.18	-0.13
Ti(b)-O(4)	1.95	1.94	1.94	0.01	0.01
Ti(b)-O(6)	1.90	1.95	1.84	-0.05	0.06
Ti(c)-O(3)	2.05	2.01	2.00	-0.03	-0.05
Ti(c)-O(4)	2.02	2.08	2.03	0.06	0.01
Ti(c)-O(5)	1.97	1.90	1.96	0.07	0.01
Ti(c)-O(7)	1.90	1.89	1.93	0.01	-0.03
Ti(d)-O(5)	1.97	1.99	2.00	0.02	0.03
Ti(d)-O(8)	1.81	1.76	1.77	0.05	0.04
Ti(a)-Ti(b)	3.32	3.33	3.35	-0.01	-0.04
Ti(a)-Ti(c)	3.43	3.50	3.44	-0.07	-0.02
Ti(b)-Ti(c)	3.60	3.66	3.60	-0.05	0.01
Ti(c)-Ti(d)	3.53	3.48	3.54	0.05	-0.01
O(2)-O(4)	2.83	2.80	2.80	0.04	0.04
O(3)-O(4)	2.70	2.83	2.72	-0.13	-0.02
O(3)-O(5)	2.86	2.69	2.82	0.17	0.04

Table 3.8: Interatomic distances in Å for the different Ti_2O_3 structures found by DFT on one hand, and LEED “H” and “L” models on the other hand, appear at the left hand part of this table. On the right hand part, the discrepancies in the interatomic distances between different structures are show. The top part of the table corresponds to nearest neighbouring atom pairs and other pair distances appear below.

This might lead to think that the Ti_2O_3 group vibrates somehow detached from the surface. Calculations for Ti_2O_3 show vibrational modes on a band from 50 to 500 cm^{-1} . These soft modes (e.g., 50 cm^{-1}) correspond to semiclassical amplitudes of vibration of ≈ 0.35 Å, which is the order of magnitude we obtain from LEED.

We have tried to refine the LEED calculations by including anisotropic vibrations of the topmost O atoms. To do this, TMAT v1.1 code [50] was used to compute a set of t-matrices for the O(1) atom with a list of values of anisotropic vibration amplitudes, $\vec{u} = (u_x, u_y, u_z)$. A wide range of \vec{u} values, allowing enhancement of in-plane and/or perpendicular vibrations, was used. These t-matrices are non-diagonal, since the anisotropic vibrations break the muffin tin spherical symmetry. In the reference structure calculation, the parameters that had been already fitted were used, including a tentative isotropic u for the topmost oxygens. Then, amplitude changes were calculated in the TLEED approximation using the oxygen non-diagonal t-matrices as a perturbation of the isotropic t-matrix used at the reference structure. To do this, TensErLEED had to be modified. However the effort, the R-factor did not improve significantly. This result could be understood if several different modes in the Ti_2O_3 group are relevant at the same time, resulting in a fairly isotropic average of displacements.

3.7 Discussion on the electronic structure

Fig. 3.12 shows the density of states (DOS) for bulk rutile TiO_2 , 1×1 and 1×2 surfaces. In that figure, the shift due to the dipole appearing in the slabs calculations has been compensated by aligning the strongly bound atomic level peak near -27.7 eV, which results in good alignment of peaks near -51.5 eV and -11.0 eV. New peaks associated to the reconstruction appear in the gap, mainly related to Ti(a) 3d orbitals of the Ti_2O_3 groups. Due to the reduced character of the 1×2 reconstruction, the Fermi level is displaced 2 eV above the edge of the valence band, located upon a small peak. The Ti(a) atom is located at a local reduced environment, in a similar situation of reduced TiO_2 (110) surfaces, where the Ti^{3+} states give rise to gap states [129, 130]. The main difference with those surfaces is the strongly anisotropic character induced by the 1×2 reconstruction. This feature can be observed on the bands near the Fermi level, depicted on Fig. 3.13. The metallic character of Ti_2O_3 chains is reflected in the parabolic shape of the branches crossing the Fermi level in the $\Gamma - X$ direction while no dispersion is observed along the $\Gamma - Y$ direction. From an experimental point of view, it helps to explain why the surface is not appreciably charged during the LEED experiment, and might be related to a small peak observed in UPS and XPS [131].

It has been suggested in the literature that the gap states could be explained in terms of a spin-polarized ground state [129]. Although convincing experimental evidence in favour of spin-polarized states has been elusive [39], it is indeed interesting to analyze the role of spin. First, we notice that the TiO_2 group favours a spin-paired ground state by 3.36 eV, and the bulk rutile TiO_2 also prefers the non-magnetic state by about 3.0 eV. On the other hand, the ground state for the group Ti_2O_3 corresponds to a spin-polarized solution, better than the spin-paired one by 1.40 eV. Therefore, it is reasonable to investigate magnetic solutions related to the 1×2

Ti₂O₃ chains. To investigate the role of spin on this reconstructed surface we have allowed the system to fully relax its geometry starting from an initial condition with a net spin unbalance : $n_{\uparrow} - n_{\downarrow} = 2$. Our calculations favour the spin-paired scenario. Differences in energy between both cases are usually small, in the order of hundredths of eV, tenths of eV at most. These differences always were reduced by using more stringent convergence conditions: we notice that spin-polarized solutions become less favoured when moving from a three-layers slab to a four-layers one, or by increasing the number of special k-points. Therefore, we find that the energetic balance between the spin-paired and the spin-polarized solutions is delicate, but our best calculations drive us to conclude in favour of a spin-paired one.

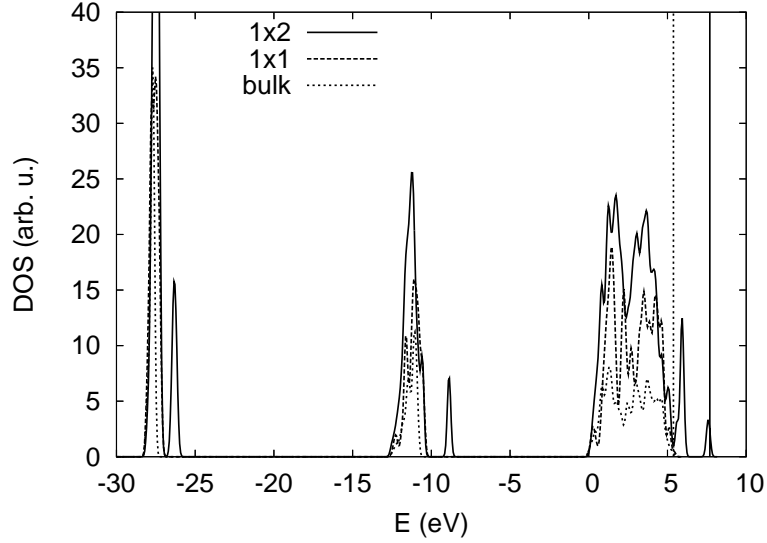


Figure 3.12: Density of states for the TiO₂(110)-1 × 2 (solid line) compared with TiO₂(110)-1 × 1 (dashed line), and bulk rutile TiO₂ (dotted line). Fermi energies are marked by vertical lines for bulk (5.4 eV, the edge of the valence band), and for the reduced surface (7.5 eV). A rigid shift due to the dipole appearing in the slabs calculations has been compensated by aligning the strongly bound atomic level peak near −27.7 eV, which results in good alignment of peaks near −51.5 eV and −11.0 eV. The conduction band is not shown.

3.8 Conclusions

In this Chapter, the relaxed geometry of the TiO₂(110)-1×2 surface has been unveiled using three different techniques coordinately: STM, LEED-IV and DFT. The main structural work has been performed with LEED while DFT has been useful to check and interpret the result. This surface is interesting for its technical applications, but its structure has been a subject of debate in the last years. A preliminar analysis of normal incidence IV curves allows us to chose Onishi's model as the most likely one. This model consists of added rows to the clean surface of Ti₂O₃ stoichiometry. Other models proposed in the literature, having different stoichiometries,

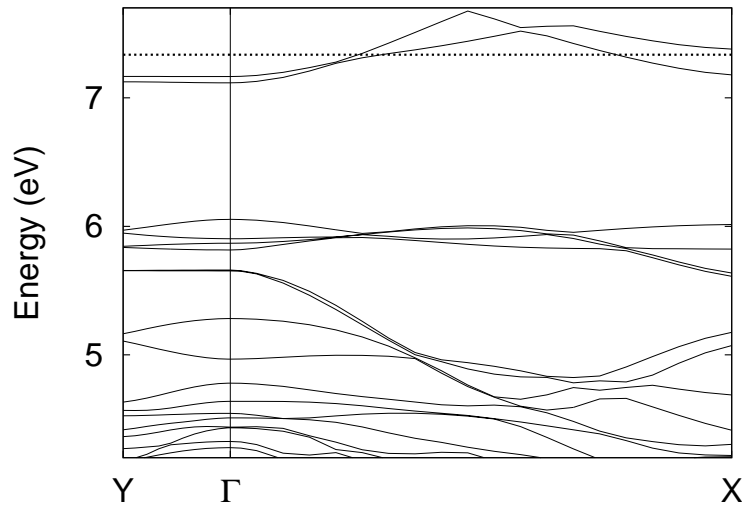


Figure 3.13: Band structure for $\text{TiO}_2(110)-1 \times 2$ along $\Gamma - X$ and $\Gamma - Y$. The dotted line indicates the Fermi level. The conduction band is not shown. Notice that the dispersion is parabolic at $\Gamma - X$ whereas branches are flat at $\Gamma - Y$.

can be discarded for having $R_P > 0.5$. Besides, STM high resolution images, where Ti atoms appear as bright features, agree with the Ti_2O_3 added row model.

A more detailed LEED-IV analysis has been performed to obtain the relaxed atomic positions of the geometry. A larger database containing the diffracted spectra for an off-normal incidence allows fitting a quite large number of parameters, both structural and vibrational. Regarding the structure, two equally admissible structures exist which produce two equally deep minima at the R_P , of value ~ 0.3 . These two minima appear when changing the height of the topmost O atoms. Regarding vibrations, we find that these are enhanced at the Ti_2O_3 added rows. In particular, topmost O atoms have vibrations amplitudes $> 0.30 \text{ \AA}$ which are suspected to be strongly anisotropic and related to the double minima at the R_P map. Unfortunately, R_P sensitivity was not enough to determine any anisotropic behaviour. One of these two structures can be discriminated by DFT. The structure provided by this technique agrees fairly well in both positions and bond lengths with one of the two LEED structures. Discrepancies can be explained by taking into account thermal effects.

The final geometry offers sites which can be interesting from the point of view of chemistry. The Ti atoms of Ti_2O_3 groups are attracted to the underlying Ti atoms, and the atomic positions at the trough in the unit cell are strongly buckled. This buckling is more intense near the 5-fold coordinated Ti atom, where the difference in vertical positions with the surrounding O atoms is $\sim 0.45 \text{ \AA}$.

DFT calculations find an electronic feature that can have interesting implications for future work: the Ti_2O_3 added rows are metallic, so that conductivity should be high in the $[001]$ crystallographic direction, but not in the $[1\bar{1}0]$ direction.

Chapter 4

Molecular t-matrix approach to LEED intensities for ordered molecular adsorbates

4.1 Introduction and motivation

Almost all problems related to surface chemistry involve adsorbed molecules. When using any of the above methods in this context, molecules are usually broken up into separate atoms, which are distributed over different layers according to their vertical positions. This does not appreciate the fact that adsorbed molecules are separate chemical units, whose internal structure does usually not deviate much from the gas phase. From a chemical, as well as from a search strategic point of view, it would be advantageous if an adsorbed molecule could actually be treated as a single scattering object, which can be translated and rotated with respect to the substrate surface.

In this Chapter we present and discuss the implementation of a method, where the intra-molecular multiple scattering (MS) is calculated first, leading to a non-diagonal scattering matrix ('T-matrix'), which represents the entire molecule. Using this T-matrix, the molecule is treated as a single scattering object within a conventional LEED code. A similar method has, in fact, been suggested more than two decades ago by Andersson and Pendry [38] for conventional LEED calculations of ordered structures, but to the best of our knowledge it has never been used or even theoretically demonstrated. However, the same idea was pursued for the diffuse LEED problem by Saldin and Pendry[132], and it was successfully used to analyze the structure of disordered $\text{CO}_2/\text{Ni}(110)$ [133].

The aim of the present work is to study the validity and accuracy of the T-matrix approach by a direct detailed comparison with well established standard theoretical approaches (e.g., layer doubling). By computing LEED IV curves for the same structures, we study the convergence as a function of the parameters governing the calculation, mainly the highest partial waves quantum number, $l_{T,\max}$ determining the size of T . This parameter must not be confused with $l_{A,\max}$, a similar quantity which is related to the scattering by atomic potentials.

4.2 Molecular T-matrix construction

In this section, molecular T-matrix construction is explained in detail, as suggested by [38]. Similar formalisms can be found in the literature for related techniques, such as SEXAFS, NEXAFS and DLEED [64, 134, 132]. The aim of the molecular T-matrix is to build an operator (in a partial wave basis for convenience) that gathers all intramolecular scattering paths and can be used as a black box, substituting all the molecule atomic positions in a subsequent LEED-IV calculations. Such an operator should be referred at a particular origin (the molecule centre is a good choice) and have dimensions $(l_{\max} + 1)^2 \times (l_{\max} + 1)^2$.

The main difference with other cluster calculations, such as those for NEXAFS, is that we will not divide the molecule into sub-units. We recall that those methods split the cluster into shells, computing intra-shell and inter-shell scattering in two steps.

Let the wavefield incident on the molecule be the following superposition of incoming partial waves:

$$\psi^{\text{inc}}(\vec{r}) = \sum_{lm} A_{lm}^{\text{inc}} j_l(\kappa|\vec{r} - \vec{r}_0|) Y_{lm}(\vec{r} - \vec{r}_0) \quad (4.1)$$

where \vec{r}_0 is the position of the molecule and κ is the electron wavevector. Y_{lm} is a spherical harmonic and j_l a spherical Bessel function. If the incoming wavefield is a plane wave, $e^{i\vec{k} \cdot (\vec{r} - \vec{r}_0)}$, the expansion coefficients are:

$$A_{lm}^{\text{inc}} = 4\pi i^l Y_{l-m}(\hat{k}) \quad (4.2)$$

The wavefield scattered by the molecule can be described as a superposition of outgoing partial waves:

$$\psi^{\text{scat}}(\vec{r}) = \sum_{lm} A_{lm}^{\text{scat}} h_l^{(1)}(\kappa|\vec{r} - \vec{r}_0|) Y_{lm}(\vec{r} - \vec{r}_0) \quad (4.3)$$

where $h_l^{(1)}$ is a spherical Hankel function. The molecular t-matrix, \tilde{T} , is defined as a matrix that relates the incident and scattered amplitudes:

$$A_{l''m''}^{\text{scat}} = \sum_{lm} A_{lm}^{\text{inc}} T_{lm, l''m''} \quad (4.4)$$

A muffin tin model (non-overlapping spheres) is taken for the electron potential inside the molecule. Between two consecutive scattering events, electrons move in a constant potential, $V = V_{0r} - iV_{0i}$, so that this process can be described by free space Green propagators (see Appendix A). The complex constant $V_{0i} > 0$ accounts for the electron wavefunction amplitude damping due to inelastic scattering processes. Thus, κ is a complex quantity in LEED theory. We use the propagators as matrix operators in a spherical wave basis ($lm, l'm'$ indices). The explicit expressions for these operators can be found in Appendix A.

For incident electrons of energy E , the atomic t-matrix \tilde{t}^v describing the single scattering event at the v -th atom of the molecule is written in terms of its phase shifts, $\delta_l^v(E)$:

$$t_{lm, l'm'}^v(E) = \frac{1}{2} (e^{2i\delta_l^v(E)} - 1) \delta_{ll'} \delta_{mm'} \quad (4.5)$$

Let us define $\tilde{\tau}^{vv''}$ as a renormalized t-matrix that accounts for all the possible scattering paths starting at the v'' -th atom and finishing at the v -th atom, i.e., it transforms a wave incident at the v'' -th atomic position into an outgoing wave at the v -th position. $\tilde{\tau}^{vv''}$ is calculated by adding up the contributions from all single and all-order MS events, which leads to the following self-consistent Dyson-like equation [9, 135, 45]:

$$\tilde{\tau}^{vv''} = \tilde{t}^v \delta_{vv''} + \tilde{t}^v \sum_{v'} \tilde{G}_{OI}^{vv'} \tau^{v'v''} \quad (4.6)$$

where the $\tilde{G}_{OI}^{vv'}$ operator propagates incoming partial waves at the v' -th atomic position into outgoing partial waves at the v -th position, and where

$$\delta_{vv'} = \begin{cases} 1 & \text{if } v' \neq v \\ 0 & \text{if } v' = v \end{cases} \quad (4.7)$$

Eq. (4.6) is solved by matrix inversion:

$$\tilde{\tau}^{vv''} = (1 - \tilde{X})_{vv''}^{-1} \tilde{t}^{v''} \quad ; \quad \tilde{X}^{vv''} = \tilde{t}^v \tilde{G}_{OI}^{vv''} \quad (4.8)$$

The \tilde{X} matrix is formed by blocks for each pair of atoms in the molecule, labelled by $\tilde{X}^{vv''}$. MS between a pair vv'' of atoms can be switched off by setting to zero their corresponding block at \tilde{X} .

4.3 Applications and properties

4.3.1 Matrix translation using Green's propagators

The t-matrix for the entire molecule, \tilde{T} , referring to a common origin \vec{r}_0 , is obtained by adding up all $\tau^{vv''}$ matrices.

$$\tilde{T} = \sum_{vv''} \tilde{G}_{II}^{0v} \tilde{\tau}^{vv''} \tilde{G}_{II}^{v''0} \quad (4.9)$$

The operators \tilde{G}_{II}^{0v} and $\tilde{G}_{II}^{v''0}$ are essentially phase factors accounting for the fact that the atoms are at positions different from \vec{r}_0 . \tilde{G}_{II}^{0v} propagates incoming spherical waves centered at the v' -th atom into incoming spherical waves centered at \vec{r}_0 , and $\tilde{G}_{II}^{v''0}$ propagates incoming waves centered at \vec{r}_0 into incoming spherical waves centered at the v -th atom. These propagators are computed with V_{0i} set to zero because the electrons do not really travel these paths between the origin and each atom in the molecule. It is only a translation of the $\tilde{\tau}^{vv''}$ operators to the position \vec{r}_0 , with no damping of the electron wavefunction. Using the same propagators, \tilde{T} can be translated from \vec{r}_0 to any other position.

4.3.2 Matrix rotation using Wigner's matrices

If we rotate the molecule through a set of Euler angles (α, β, γ) , the t-matrix for the rotated molecule, \tilde{T}^{rot} and the initial matrix, \tilde{T}^0 , are related by:

$$T_{lm,l'm'}^{\text{rot}} = \sum_{kk'} D_{mk}^{l*}(\alpha, \beta, \gamma) T_{lk,l'k'}^0 D_{k'm'}^{l'*}(\alpha', \beta', \gamma') \quad (4.10)$$

where $\tilde{D}^l(\alpha, \beta, \gamma)$ are Wigner rotation matrices [136]. $(\alpha', \beta', \gamma')$ is the set of angles that produce the inverse rotation to (α, β, γ) .

Rotations can be defined also using alternative, and sometimes more convenient, set of angles $(\omega; \theta, \phi)$ [136]. This set describes the rotation by an angle ω with respect to an axis

$$\hat{n} = (\sin \theta \cos \phi, \sin \theta \sin \phi, \cos \theta) \quad (4.11)$$

The rotation matrices in terms of these angles, \tilde{U}^l , are related to \tilde{D}^l by:

$$U_{mm'}^l(\omega; \theta, \phi) = \sum_{m''} D_{mm''}^l(\phi, \theta, -\phi) e^{-im''\omega} D_{m''m'}^l(\phi, -\theta, -\phi) \quad (4.12)$$

4.3.3 Molecular vibrations

One advantage of using the molecular T-matrix is that it can be used to describe vibrations of the entire molecule without intramolecular bond distortion. We can find a number of molecular adsorbates where this description can result interesting, e.g. (i) vibration of the CO upright molecule in the direction perpendicular to the substrate, at CO/Ni(100) and CO/Cu(100) surfaces [38], (ii) frustrated translation of CO/Ir(100) [137], (iii) frustrated rotation and perpendicular vibration of C₆H₆/Ru(0001) [138], etc.

Briefly, this correction uses the following formalism: with a plane wave basis description, the usual Debye-Waller (DW) thermal correction is applied to the matrix:

$$t(T; \vec{k}, \vec{k}') = t(T = 0; \vec{k}, \vec{k}') e^{-M(\vec{k}' - \vec{k})} \quad (4.13)$$

$$e^{-M(\vec{k}' - \vec{k})} = \int P(\vec{r}) e^{i(\vec{k}' - \vec{k}) \cdot \vec{r}} d^3\vec{r} \quad (4.14)$$

where $P(\vec{r})$ is the molecule position PDF, assumed to be gaussian (harmonic or anharmonic). A basis change is done, from plane to partial waves, to expand the DW factor in terms of spherical harmonics:

$$e^{-M(\vec{k}' - \vec{k})} = \sum_{LL'} W_{L'L} Y_L(\hat{k}) Y_{L'}^*(\hat{k}') \quad (4.15)$$

where $L \equiv (lm)$ and $L' \equiv (l'm')$. The $W_{L'L}$ coefficients are determined from expanding the PDF in terms of radial functions and spherical harmonics as:

$$P(\vec{r}) = \sum_n \sum_L R_n(r) Y_L(\hat{r}) \quad (4.16)$$

Multipole or cumulant expansions can be used for this task [50, 52]. In CLEED code this facility has been already implemented [22].

4.3.4 $l_{T,\max}$ determination

The quantum mechanical expectation value for the modulus of the angular momentum is $\hbar\sqrt{l \cdot (l+1)}$, which is equal to $\hbar(\vec{k} \times \vec{r})$ in the classical limit. This enables us to estimate the maximum angular momentum quantum number, $l_{T,\max}$, necessary

to describe the scattering of a given potential confined in space to a region of radius $\approx R$ [14]. For kinetic energies up to E_{\max} :

$$l_{T,\max} \approx \sqrt{2E_{\max}} \cdot R \quad (4.17)$$

From a quantum-mechanical point of view, $l_{T,\max}$ determines the size of the subspace used to construct \tilde{T} . Therefore, the accuracy of the molecular T-matrix method should be primarily determined by this parameter. Convergence of the IV curves for a given energy range with increasing $l_{T,\max}$ must, in general, be closely monitored to make sure that the semi-classical argument is adequate. It is interesting to notice how the crude semi-classical approximation can bring us closely to values of $l_{T,\max}$ where the calculation is converged. For CO, where $R \approx 1.3$ Å (atomic radii for O and C are taken as ≈ 0.7 Å), the above equation leads to a value of $l_{T,\max} \approx 9$, while nice convergence is already observed for $l_{T,\max} \geq 8$ (see Fig. 4.1). For benzene (C_6H_6), for $E_{\max} = 125$ eV and $R \approx 2.1$ Å, we expect $l_{T,\max} = 12$ which is seen to be enough to reach convergence (see Fig. 4.9).

4.3.5 The molecular T-matrix symmetries and the S-matrix

Scattering amplitudes must hold general principles like the optical theorem and the reciprocity theorem [139, 140], which are, respectively:

$$\begin{aligned} \frac{i}{2}(A^*(\vec{k}, \vec{k}') - A(\vec{k}', \vec{k})) &= \frac{\kappa}{4\pi} \int d\Omega_{\vec{k}_1} A^*(\vec{k}_1, \vec{k}') A(\vec{k}_1, \vec{k}) \\ A(\vec{k}', \vec{k}) &= A(-\vec{k}, -\vec{k}') \end{aligned} \quad (4.18)$$

where the amplitude is

$$A(\vec{k}', \vec{k}) = 4\pi \sum_{l'm', lm} Y_{l'm'}(\vec{k}') T_{l'm', lm} Y_{lm}^*(\vec{k}) \quad (4.19)$$

Reciprocity condition leads to the following symmetry conditions in the T-matrix elements:

$$T_{l'm', lm} = (-1)^{l+l'} (-1)^{m+m'} T_{l-m, l'-m'} \quad (4.20)$$

The S-matrix accounts for the change in the wavefunction during the scattering process. Substituting far field expressions of radial Bessel and Hankel functions at Eqs. (4.1), (4.3) and (4.4), we obtain the following final wavefield leaving a molecule at the origin:

$$\begin{aligned} \psi(\vec{r}) &= e^{i\vec{k} \cdot \vec{r}} + \psi^{\text{scat}}(\vec{r}) \rightarrow \\ &\sum_{lm} Y_{lm}(\hat{r}) \frac{i}{2\kappa r} \left[A_{lm}^{\text{inc}} e^{-i(\kappa r - \frac{\pi l}{2})} - e^{i(\kappa r - \frac{\pi l}{2})} \sum_{l'm'} A_{l'm'}^{\text{inc}} (1 + 2T_{l'm', lm}) \right] \end{aligned} \quad (4.21)$$

where we can identify the S-matrix as

$$\tilde{S} = 1 + 2\tilde{T} \quad (4.22)$$

In particular, the diagonal S-matrix terms for a single atom are $s_l = e^{2i\delta_l}$. In the absence of absorption in the scattering process, wavefield flux conservation conditions leads to the unitary property for the S-matrix, $\tilde{S}\tilde{S}^\dagger = 1$. This property can be numerically checked for the molecular T-matrices constructed following the Dyson formalism with $V_{0i} = 0$ and a sufficiently large $l_{T,\max}$. We notice that when $l_{T,\max}$ is not large enough to account for all intramolecular scattering paths, extradiagonal terms appear in the product $\tilde{S}\tilde{S}^\dagger$.

4.4 The TMOL (v1.1) program

TMOL (v1.1) [141] is a FORTRAN-90 program for the computation of non-diagonal scattering t-matrices for molecules or any other poly-atomic sub-unit of surface structures. It makes use of the Dyson formalism explained above. Making the necessary changes to existing LEED codes, this t-matrix can be fed into any standard LEED program [14, 15, 54, 22]. This method treats the molecule as whole, and introduces an efficient way of describing vibrations of the molecule. Furthermore, the molecule can be split into fragments behaving as rigid-units. For this reason, TMOL has been implemented to work with either spherical muffin tins or more general scatterers, described by a non-diagonal t-matrix. The latter would describe non-isotropic vibrations.

If one wishes to compute the molecular T-matrix of a large molecule, a less computational demanding calculation can be done by switching off the MS paths between distant atoms by simply setting to zero the corresponding \tilde{X} -matrix block. Further optimization can be achieved by using special routines for handling sparse matrix. The only drawback is that a high l_{\max} is still required.

This program is written in FORTRAN-90/95 from scratch. Priorities while writing the code have been to keep it clear, modular and keep close to the parallelism concept. Therefore, no particular effort to optimization has been made.

A program called WIGNER for rotating the resulting t-matrices using Wigner matrices [136] is provided together with TMOL.

TMOL computes the t-matrices of a molecule for a set of energies. As the program treats one-scatterer matrices, \tilde{t}^v , as general square matrices, the molecule can be thought to be formed by spherical muffin tins or by more general non-spherical scatterers with a non-diagonal t-matrix, which can be useful when dealing with non-isotropic vibrations. In the first case, a phase shift file must be provided. In the second, a file containing a non-diagonal t-matrix. The computed molecular t-matrix is arbitrarily referred to the geometrical center of the molecule: $\vec{r}_0 = \frac{1}{N} \sum_i^N \vec{r}_i$, where N is the number of scatterers.

Throughout the program, (l, m) pairs indexing t-matrix elements follow the natural ordering, as in the LEED90 program (see section 2.7).

Matrix dimensions are defined by the values of $l_{T,\max}$ and N . In the code, \tilde{X} and $\tilde{\tau}$ are matrices of size $N(1 + l_{T,\max})^2 \times N(1 + l_{T,\max})^2$, which are divided into blocks for each pair of individual scatterers. Propagators and the final t-matrix \tilde{T} are of size $(1 + l_{T,\max})^2 \times (1 + l_{T,\max})^2$. Matrices are allocated dynamically, so that the program does not need to be recompiled when dimensions change.

TMOL writes out the non-zero elements of the T-matrix, only. Thus, if a high

symmetry orientation of the molecule is chosen, storage space can be saved, since the T-matrix will be more sparse.

A comprehensive listing and description of the program routines is given in reference [141].

4.5 Model calculations

In this section the accuracy of the T-matrix approach is tested by comparing theoretical IV curves calculated with this method against calculations based on conventional LEED theory. Standard dynamical LEED theory has been proved very accurate describing metal surfaces with or without adsorbates. Experiment to theory $R_{P,\min}$ values for the best determinations are usually below 0.2, or even at the 0.1 level. The R_P values comparing IV curves from conventional and T-matrix approach methods are expected to be below that experimental threshold $R_{P,\min} \gtrsim 0.1$ given by data fitting. Therefore, the fact of introducing the T-matrix approximation should not affect the final structure resulting from a structural search with real experimental curves.

In all cases identical geometrical and non-geometrical program parameters are used for both types of calculations. Pendry's R_P factor [41] has been used to quantify the agreement between the two sets of theoretical IV curves. These theory-theory comparisons allow us to focus on the role of certain parameters in the calculation, mainly the maximum angular momentum value for partial waves expansions, $l_{T,\max}$. The influence of different geometrical and non-geometrical parameters is studied using a $c(2 \times 2)$ -CO overlayer on Cu(100), with CO hypothetically adsorbed on atop or hollow sites. As an example of strong scatterers a $p(1 \times 1)$ layer of hypothetical Cu₂ 'molecules' is used, which is equivalent to an extra double layer of copper terminating the surface. Finally, in order to study the applicability to larger molecular units, we use a $p(\sqrt{7} \times \sqrt{7})R19^\circ$ -(C₆H₆) layer on Ni(111) [142].

4.5.1 Test of key non-geometrical parameters: CO on Cu(100)

Normal incidence, c(2x2) upright CO adsorbed on top

The first set of calculations aims to characterizing the influence of the maximum angular momentum value for partial waves expansions in the calculation of the T-matrix, $l_{T,\max}$. This is done by using CO on atop positions on Cu(100) as test geometry. The molecule is oriented perpendicular to the surface with the C atom closer to the surface. The internal C-O distance is 1.20 Å, and the C-Cu distance is 1.83 Å. The copper surface is assumed to be ideally bulk terminated with a surface lattice parameter of 2.55 Å. An energy independent imaginary part of the optical potential, set to a typical value of $V_{0i} = -4$ eV, ensures the convergence of lattice sums and layer doubling for the distances involved. By restricting the calculations to normal incidence we can check that symmetry requirements are obeyed by our calculation. IV curves were computed between 54 eV and 190 eV, in energy steps of 1.36 eV (0.05 Hartree). For the whole conventional LEED calculation, and for the

metal substrate in the formalism using a molecular T-matrix, we use $l_{\max} = 7$. The number of plane-waves is determined by the criteria

$$e^{-Im(k_z, \vec{g})d_{min}} \geq 0.001 \quad (4.23)$$

and we use 8 layer doublings. These are enough to ensure convergence in this energy range. In addition, we notice that the molecular T-matrix elements can be linearly interpolated between different energies. In particular, in this work we have stored these matrices at 10 eV steps, which has been enough for the accuracy targeted in this work.

In Fig. 4.1 we show the behaviour of Pendry's R-factor between theoretical IV curves vs. the maximum angular momentum quantum number $l_{T,\max}$ used in the computation of the molecular T-matrix. This parameter defines the number of partial spherical waves included in the wave field expansion in this part of the calculation. The behaviour of each beam is plotted separately, to show their individual convergence. In addition, the R factor averaged over all beams is given. It can be appreciated how the T-matrix method converges towards the conventional calculation for large enough $l_{T,\max}$ values. The R-factor steadily drops to acceptable low values when $l_{T,\max}$ is increased, and we observe convergence with the conventional reference calculation for $l_{T,\max} \geq 8$. This value is in agreement with the semi-classical prediction provided by Eq. (4.17) for $R = 1.30 \text{ \AA}$. For $l_{T,\max} \geq 8$ the R factors of all beams are below 0.1, with an average value of < 0.03 . This low R_P value means that the shapes of the IV curves are essentially identical. For visual inspection the IV curves from both methods for $l_{T,\max} = 8$ (converged) and $l_{T,\max} = 4$ (not converged) are plotted in Fig. 4.2.

Different adsorption site, upright and tilted molecules forming a $p(2 \times 2)$ CO overlayer adsorbed on hollow

The set of IV curves shown in Fig. 4.4 has been calculated for a hypothetical $p(2 \times 2)$ -CO layer on Cu(100) with upright CO molecules on hollow sites, using the same parameters as before. The same T-matrix was used as for the IV curves shown in Fig. 4.2, which demonstrates the potential efficiency of the T-matrix approach to explore different adsorption sites: the intra-molecular MS does not form part of the new calculation. The scattering object was placed on a different position w.r.t. the substrate, namely the hollow site, and the periodicity of the overlayer has been changed too. The T-matrix approach shows again almost perfect agreement with the conventional LEED calculations. The somewhat lower intensities at low kinetic energies, especially for the fractional order beams, are due to the different treatment of the attenuation of the electron wave field inside the molecule in the two methods.

Normal incidence, $c(2 \times 2)$ tilted CO on top

Not only can the scattering object represented by the T-matrix be translated easily with respect to the substrate, but also rotations can be imposed very economically by applying Wigner's rotation matrices.

For the IV curves shown in Fig. 4.5, we use the same T-matrices, calculated for upright CO, and program parameters as for the $c(2 \times 2)$ -CO overlayer in Fig. 4.2,

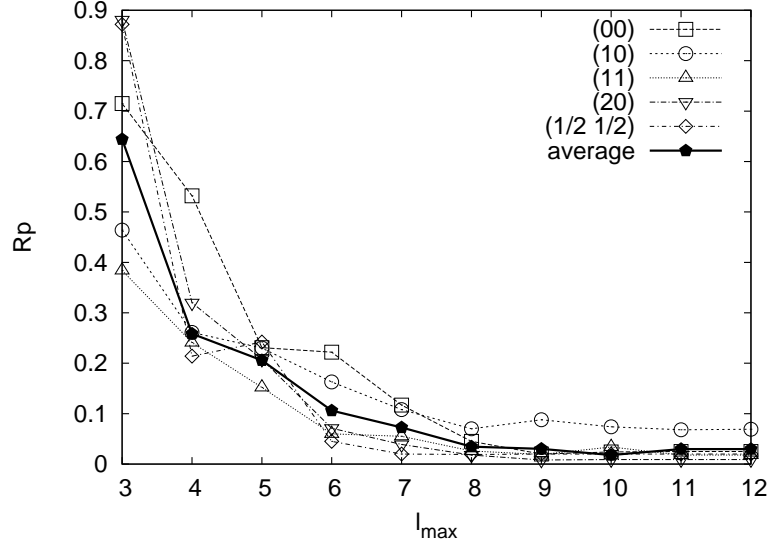


Figure 4.1: Pendry's R-factor (R_P) vs. the maximum angular component of partial waves expansion ($l_{T,\max}$). Individual beams, and an average value (thick line) are given for atop CO/Cu(100)-c(2 × 2). The molecule is assumed to be upright, the C-O distance is fixed at 1.2 Å, and the C-Cu distance is fixed at 1.83 Å.

with the same periodicity and adsorption site. However, now the molecules are tilted by $\theta = 30^\circ$ and $\phi = 60^\circ$ in the polar and azimuthal directions, respectively. The tilting of the molecule in the T-matrix approach is achieved by applying Wigner's rotation matrices to the scattering matrix for the upright molecule. This transformation makes the T-matrix less sparse than in the highly symmetric case of an upright molecule. The loss of accuracy is, however, negligible. Tests with different values of $l_{T,\max}$ show that for light atoms like C and O, good convergence is achieved with $l_{T,\max} = 8$. Both, the visual comparison and the low R_P values of the two sets of IV curves plotted in Fig. 4.5 show excellent agreement between the T-matrix approach and the conventional LEED calculation. The ability to rotate the molecule without the need of recalculating the scattering matrix is probably one of the greatest advantages of this approach, since it can save significant amounts of computer time with a negligible loss of accuracy for large molecules, particularly in the initial stages of a geometry search when many different orientations need to be tested.

$I(\theta)$ for c(2x2) upright CO adsorbed on top

Finally, we consider the agreement between the T-matrix approach and the conventional LEED approach upon variation of the incidence angle of the electron beam, which again imposes changes in the symmetry of the system as the incidence angle deviates from the surface normal. The variation of LEED intensities with the incidence angle, $I(\theta)$ at a fixed energy E is as useful for structural analysis as IV curves at a fixed angle of incidence. In particular, it can be used to increase the

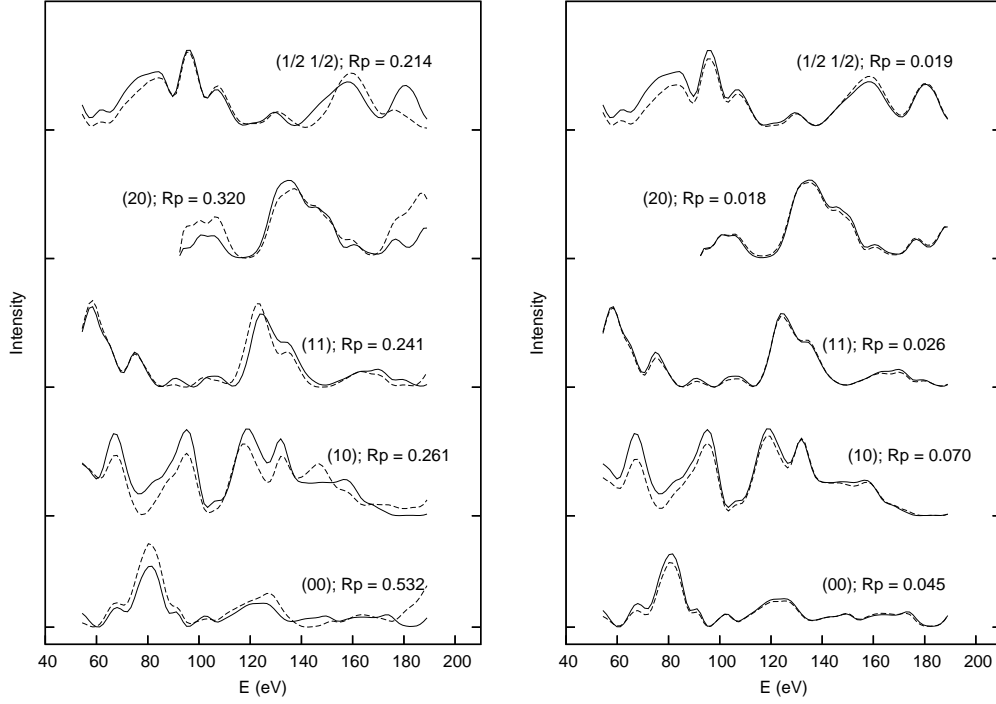


Figure 4.2: IV curves for atop CO/Cu(100)-c(2×2) calculated using the T-matrix approach (dashed lines) with $l_{T,\max} = 4$ (left) and $l_{T,\max} = 8$ (right) are compared to a reference calculation (solid line); for $l_{T,\max} = 8$ convergence is achieved within the whole energy range.

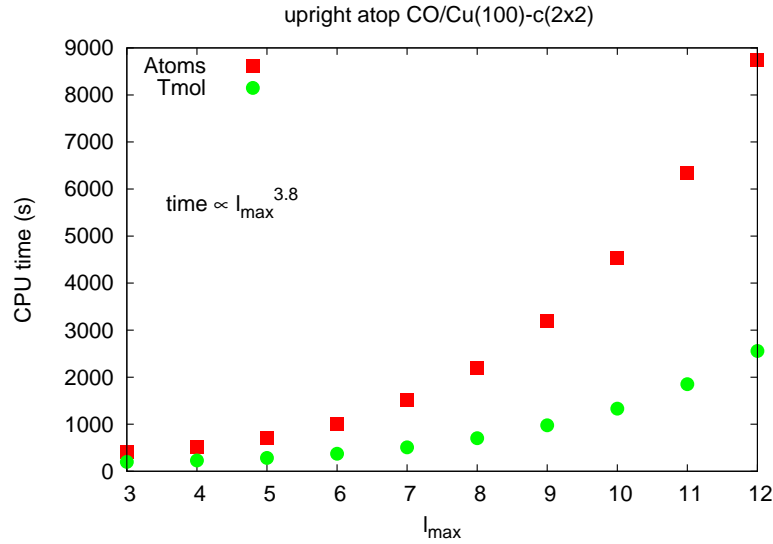


Figure 4.3: CPU time for atop CO/Cu(100)-c(2×2) normal incidence IV calculations as a function of overlayer l_{\max} value in both approaches, conventional calculation (squares) and T-matrix (circles).

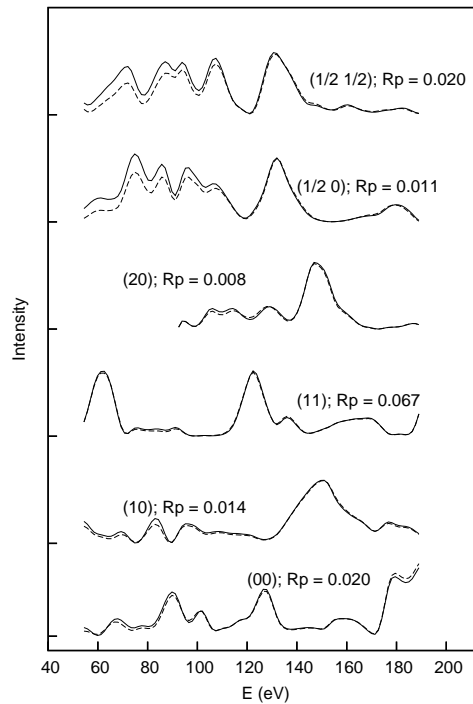


Figure 4.4: IV curves for integer and non-integer beams corresponding to a hypothetical hollow CO/Cu(100)- $p(2 \times 2)$. In the standard layer-type LEED calculation the molecule has been formed from two different atomic planes (solid line). By using a non-diagonal molecular T-matrix, an alternative approach is used where a single molecular plane is formed (dashed line). Layer doubling has been used to assemble planes into a surface. Other parameters have been kept to the same values as in the previous example.

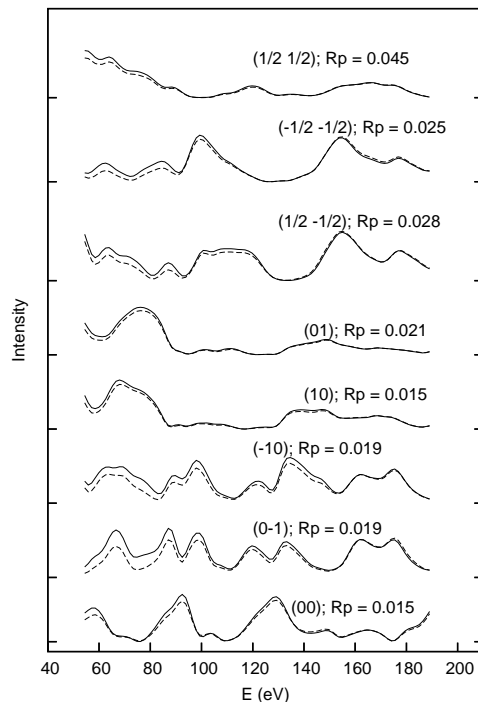


Figure 4.5: Tilted CO/Cu(100)- $c(2 \times 2)$, $\theta = 30^\circ$, $\phi = 60^\circ$. Solid line: standard approach, dashed line: T-matrix approach.

experimental data set if the LEED pattern is not dense enough [143, 35, 120] or to develop a tomographic approach to the problem (Chapter 7).

Fig. 4.6 shows $I(\theta)$ curves for the same $c(2 \times 2)$ -CO geometry as described in section 4.5.1. The calculations were performed for constant values of the azimuthal angle ($\phi = 45^\circ$) and the energy ($E = 109$ eV). For both integer and fractional order beams Fig. 4.6 shows the same level of agreement, as we have seen before in the IV curves, between the conventional layer-type LEED calculation and the approach based on a non-diagonal T-matrix.

4.5.2 Strong Scatterers: $p(1 \times 1)$ upright Cu_2 on hollow

In the previous cases we have dealt with a molecule consisting of weak atomic scatterers. Therefore, MS between the molecules, in the plane parallel to the surface, is negligible, even in the relatively densely packed $c(2 \times 2)$ -CO overlayer. In the following example we focus on the other extreme, relatively strong atomic scatterers gathered into 'pseudo-molecules' which are densely packed. The 'pseudo-molecules' in this case are Cu_2 dimers placed upright on hollow sites of a Cu(100) surface with a $p(1 \times 1)$ periodicity. The Cu-Cu distance for the dimers is assumed to be 1.6 \AA . The vertical position in the hollow sites is chosen to be identical to the position of the next layer of Cu atoms, when the bulk-stacking is continued. Therefore only the top-most layer of Cu atoms deviates from the bulk-periodicity by being placed on atop sites of its underlying layer. MS contributions are important in this close

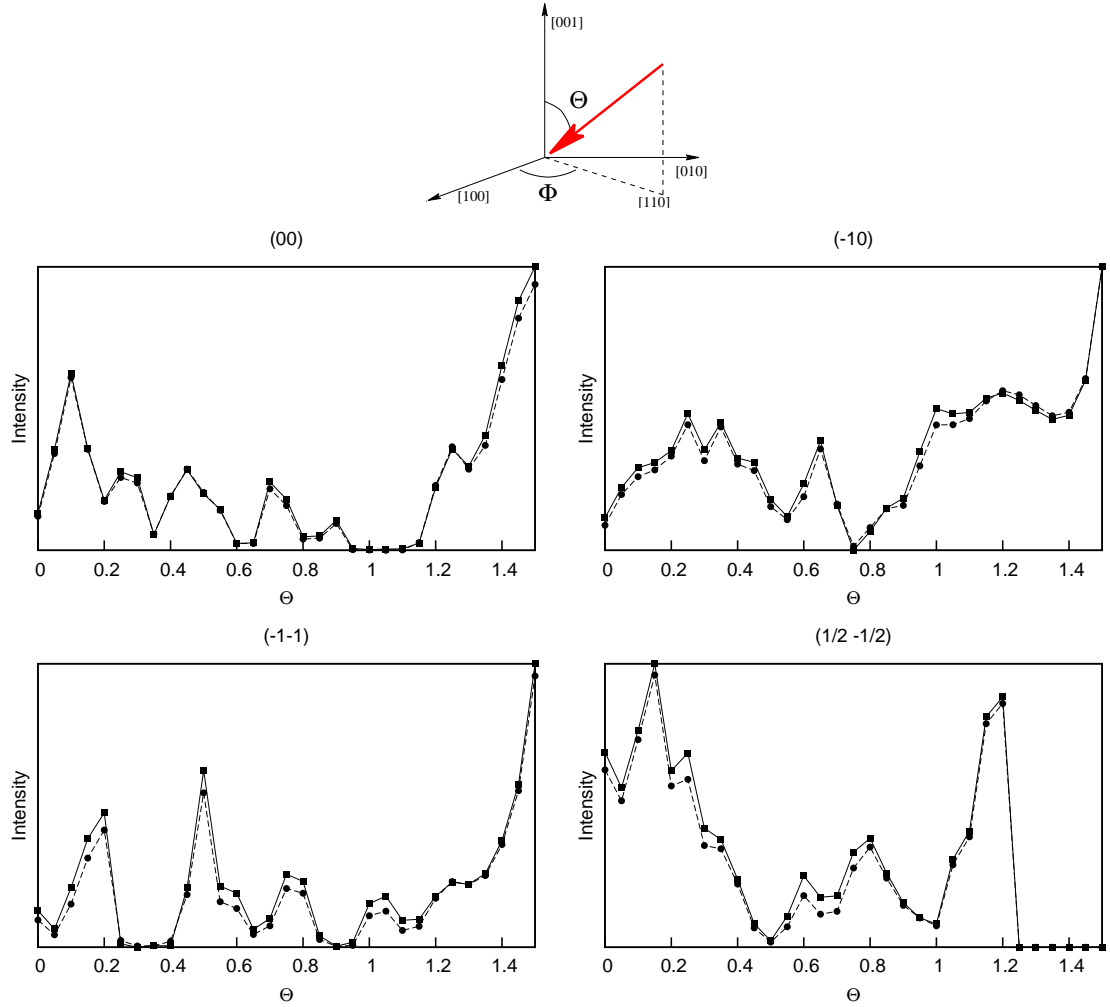


Figure 4.6: LEED Intensities as a function of the primary beam polar angle for a $c(2 \times 2)$ ordered layer of CO adsorbed on top sites at Cu(100). Parameters relevant for the calculation are kept to the same values as in previous cases. The azimuthal angle is fixed at $\phi = 45^\circ$. Continuous line: reference LEED calculation, dashed line: non-diagonal T-matrix formalism.

packed arrangement of Cu_2 dimers, both in the plane parallel to the surface and perpendicular to it. The latter contributions are shared between the T-matrix and the conventional part of the program. The angle of incidence is arbitrarily fixed at $\theta = 28^\circ$, $\phi = 17^\circ$. Other parameters, like V_{0i} , energy range, etc, are kept to the same values as in the previous examples. $l_{T,\max}$ had to be increased to at least 10 in order to get good agreement with the conventional LEED calculation, while l_{\max} was kept at the value of 7 at the substrate. Results are shown in Fig. 4.7, where again both visual comparison and the low R_P factors show that the two methods are equivalent. The quality of the agreement is the same as for molecules consisting of weak atomic scatterers.

A similar calculation has been made with a plane of Cu_2 tilted molecules, which reproduce two bulk planes. Here, the quality of the reconstructed clean surface IV curves was poorer than expected. It is observed that shortcomings at scattering in a molecular plane w.r.t. a double atomic plane (accomplished by layer doubling) are reflected in the backscattered intensities as a lack of the 4-fold symmetry in the molecular case. The agreement is only recovered when using higher $l_{T,\max}$ values.

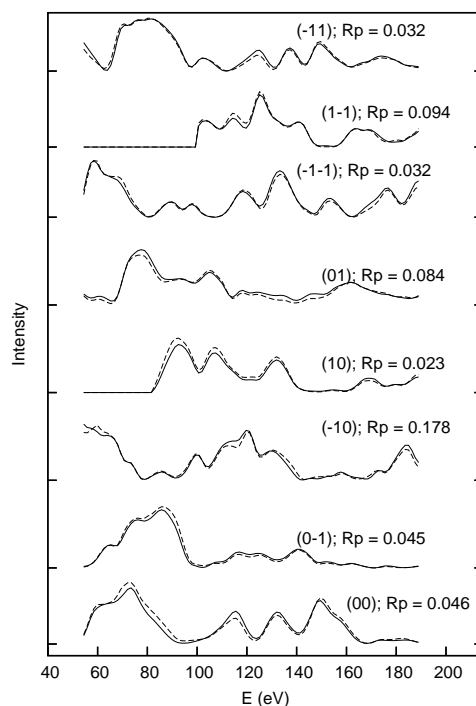


Figure 4.7: IV curves for a hypothetical Cu_2 dimer adsorbed on hollow forming a $p(1 \times 1)$ overlayer on $\text{Cu}(100)$. The primary beam is at non-normal incidence ($\theta = 28^\circ, \phi = 17^\circ$), the Cu-Cu distance in the Cu_2 dimer is arbitrarily fixed to 1.6 \AA , and $l_{T,\max} = 10$ has been used to obtain convergent results. Solid line: standard methods. Dashed line: T-matrix has been used to describe the pseudo-molecule.

4.5.3 Larger molecules: benzene on Ni(111)

In the final example we investigate the accuracy of the T-matrix approach for larger molecules, namely benzene. Eq. (4.17) indicates that if the type of scatterers in the molecule does not change, $l_{T,\max}$ should grow linearly with the size of the molecule. Since the increase in size between CO and benzene is about a factor 1.6, a significantly larger value of $l_{T,\max}$ is expected to be necessary to achieve good agreement with the conventional calculation, as we have discussed before.

In Fig. 4.9 we show IV curves for a $\sqrt{7} \times \sqrt{7} \text{R}19^\circ\text{-(C}_6\text{H}_6\text{)}$ overlayer with flat lying benzene molecules adsorbed on fcc hollow sites of Ni(111), depicted at Fig. 4.8. The parameters have been chosen to represent the real system, which is described in detail in Ref. [142], with the height of the C_6 ring above the surface of 2.03 Å and significant buckling of up to 0.14 Å. For the sake of simplicity, in our calculations we use an undistorted ring with a distance of 1.39 Å between the carbon atoms. Due to the low scattering strength of hydrogen atoms at the energies under consideration, they are ignored in the calculations as it has been common use in LEED structure analyzes. The imaginary part of the optical potential, $V_{0i} = 4.0$ eV, was set to the same value as before. Results are properly converged for $l_{T,\max} = 12$. Indeed, visual agreement between the conventional LEED calculation (solid lines in Fig. 4.9) and the molecular T-matrix approach (dashed lines), and the corresponding Pendry R-factors, clearly indicate very good agreement for both integer and non-integer beams.

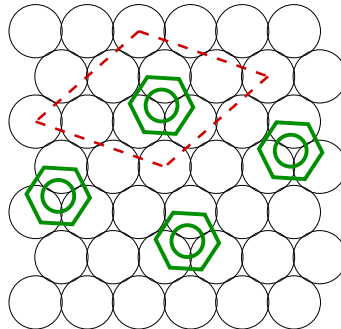


Figure 4.8: C_6H_6 / $\text{Ni(111)}\text{-(}\sqrt{7} \times \sqrt{7}\text{)R}19^\circ$ model structure.

4.6 Conclusions

The excellent agreement generally found in the above examples between the conventional LEED approach and the one based on a non-diagonal T-matrix shows that the two methods are equivalently suited for structural analysis of LEED IV-curves. Differences at compared LEED IV-curves appear mainly at low energies as intensity differences, where the molecule approach provides slightly smaller intensities. This is due to the fact that in the LEED calculation electrons travel an additional distance, namely those existing between the lowest atom of the molecule and the molecule

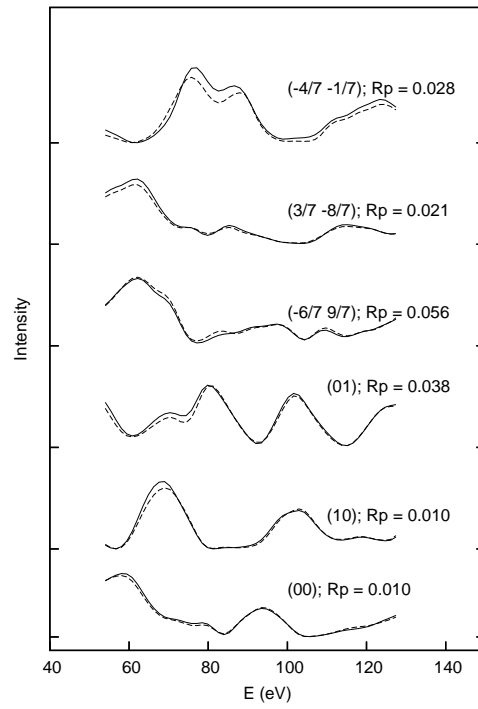


Figure 4.9: IV curves for benzene adsorbed on Ni(111), at fcc site. Conventional LEED calculation (solid line) and T-matrix approach (dashed line) are compared for $l_{T,\max} = 12$ (see text for other parameters).

origin plus the distance between the origin and the upper atom of the molecule, under the effect of electron damping. Agreement is quantified by Pendry's R_P values well under 0.1 for all the examined model cases.

There are several advantages of the T-matrix method that can be foreseen for structural searches. Probably the biggest is the possibility of preserving molecules as complete entities in the search. For large molecules with more than 2 atoms this reduces the number of search parameters significantly to 3 translations of the centre of mass and 2 or 3 rotations for linear and non-linear molecules, respectively. Especially when different adsorption sites and molecular orientations have to be tested, T-matrices of undistorted molecules in their gas-phase configuration can be used to eliminate a large number of possible adsorption geometries. It is a common experience with many LEED structure analyses of adsorbed molecules that their gas-phase geometry is not changed upon adsorption. Even substantial intra-molecular distortions of around 0.1 Å usually affect the R-factor much less than changes in the adsorption site, molecular orientation, or relaxations/reconstructions of the upper substrate layers (see e.g. [142, 144]). Not only is the number of search parameters reduced, but with the T-matrix approach computer time is saved in each search step since the matrix needs to be calculated only once for each energy and can be stored for repeated use. Typical savings are between 20% and 30% for most of the examples shown in this work. For example, Fig. 4.3 shows the CPU times for the atop $c(2 \times 2)$ -CO/Cu(100) normal incidence case. Scaling with $l_{T,\max}$ is the same, but the prefactor is smaller for the molecular calculation. Greater savings can be expected for larger molecules.

The T-matrix for a distorted molecule can be computed efficiently using a linear expansion scheme similar to Tensor-LEED [23]; this is, however, only possible for small distortions and a section of next Chapter explores this implementation. For larger distortions, a new T-matrix needs to be computed and no savings are achieved.

The computer time needed for calculating the T-matrices for the electron energy range of the LEED IV-curves is comparable to a conventional LEED calculation, provided the same $l_{T,\max}$ is used. The storage space requirements are less than 200 kbytes per energy. Considering the fact that the T-matrices used in the IV calculations can be interpolated from calculated matrices about 10 eV apart without significant loss of accuracy, this leads to a total storage space of 2 to 3 Mbytes needed for T-matrices involved in a typical search. Storage space can be saved by choosing a symmetry orientation for the molecule, where its T-matrix is more sparse. Obviously, the fact that $l_{T,\max}$ for the T-matrix part of the IV calculation is normally larger than for the conventional part will cost some extra computer time, which is, however, much less than calculating the full MS for the molecule each time. At least for molecules involving weak scatterers, such as e.g. hydrocarbons, the increase of $l_{T,\max}$ with the diameter of the molecule seems to be smaller than the one predicted by Eq. (4.17). This is probably due to the fact that for such molecules only MS paths between nearest or next nearest neighbours play a significant role and therefore $l_{T,\max}$ scales with these distance rather than with the size of the entire molecule. Similarly to a conventional LEED calculation, the convergence needs to be tested by monitoring the change in the intensities, as Eq. (4.17) should only be taken as a rough guide.

A further advantage of the T-matrix approach is that it opens the possibility to include, within a MS formalism, anisotropic and anharmonic vibrations of the entire molecule in a straightforward way [50]. This should be a good and simple approach to describe modes related to frustrated translations and rotations, which have been found to be important in some systems, like CO adsorption on Ir(100) [137]. These modes are associated with very low frequencies and large vibrational amplitudes, which make them more relevant for the LEED analysis than intra-molecular modes. In current conventional LEED codes they are incorporated through isotropic uncorrelated vibrations of each single atom, which is a poor description for these modes, and can result in false static distortions (e.g., a tilt for the example above) mimicking the real dynamics of the adsorbed molecule.

The next step of refinement would be using non-spherical muffin-tin potentials for creating the molecular T-matrix [45, 145]. Especially in cases like CO or benzene, where a significant fraction of electrons resides in regions outside the muffin-tin spheres surrounding the atoms, this should improve the agreement between theory and experimental data significantly. Because this refinement improves directly on the non-diagonal T-matrix, we notice that it remains fully compatible with a refined treatment of vibrations of the entire molecule as commented above, and it does not imply any extra amount of work for the LEED code.

Finally, we recall on the advantage of having implemented both TMOL and LEED90 codes in a modern language (FORTRAN-90/95) from scratch. They are open and modular codes that should be useful in the future to benchmark new developments. The drawback of not being symmetry optimized is compensated by their clearness and modularity. In particular, T-matrices produced by TMOL have been successfully fed into other “mature” LEED codes, after the necessary changes have been made, for other applications:

- Inside CLEED vibrations of the molecule as a whole, by cumulant expansion treatment has been tried.
- Inside TensErLEED the first steps towards structure searches with entire molecules within TLEED formalism have been made, as we will see in the next Chapter.

Besides, molecular T-matrices should work inside DLEED code and even inside other diffraction techniques calculations, such as PD, NEXAFS, etc.

Chapter 5

Perturbative approximations involving the molecular T-matrix

5.1 Introduction

In the present Chapter two techniques are presented that make use of the molecular T-matrix. Both are based in the Tensor LEED formalism, i.e. they are approximations that involve a perturbative scheme. As we have already seen, the molecular T-matrix formalism is such that the matrix is computed once at a *fixed geometry* for each energy, and stored for subsequent usage in a conventional LEED program. This implies that any calculation done with this matrix does not offer the possibility of distorting the molecule. This would be highly desirable if one wishes to make a structural search including intramolecular bond lengths and/or bond angles as parameters to fit. For example, small distortions of the molecule can be interesting when investigating the effect of molecular vibration modes on the spectra, or when searching for feasible distortions induced on the adsorbed molecule by the underlying substrate reconstruction. A procedure for computing the changes in a molecular T-matrix due to small distortions is introduced in section 5.2.

Alternatively, one may like to perform structure searches at constant molecule geometry, for example, when studying situations where the adsorbed molecule structure does not change w.r.t. the structure at its gas phase. However, if molecules are big, a large $l_{T,\max}$ value is required to reproduce correctly the molecule scattering properties. This implies that the molecular overlayer matrix calculation inside the LEED code will be computationally demanding. In section 5.3 an approximation is presented to make this task faster. As we have already seen, the molecular T-matrix can be translated and rotated without loss of accuracy. Also vibrations of the molecule as a whole can be applied to the T-matrix to describe modes related to frustrated translations or rotations. These movements of the molecule can be implemented within the Tensor LEED approximation to speed up searches, and this is another application that is to be seen at section 5.3.

Thus, the aim of this Chapter is to offer the possibility of extending the use of the molecular T-matrix beyond a plain computation of diffracted intensities for a given surface configuration to an scenario where the molecules are “flexible”, in the sense that the user of the LEED code can efficiently manage a small range of

distortions affecting the molecule, with or without changing intramolecular bonds.

5.2 Perturbative approach to small distortions of intra-molecular bonds

As stated in the introduction, molecular t-matrices are computed once for a fixed geometry to be used inside a typical LEED code. However, there are several situations where we can be interested in exploring configurations where the intramolecular bonds are distorted. This would require to compute a new molecular T-matrix from scratch for the distorted molecule. If the molecule is big, this can result a time consuming task, since a matrix inversion would be needed for each newly computed T-matrix. The time needed by such inversions scales as $l_{T,\max}^6$.

However, when distortions are weak, it is possible that a TLEED-like approximation remains valid. Thus, the distorted molecule can be thought of being computed in three steps taking (i) the undistorted molecular T-matrix as a reference, (ii) writing the distorted molecular T-matrix as an expansion in the new atomic t-matrices (updated by translation operators) and (iii) retaining only the linear terms in those new atomic t-matrices of the moved atoms.

5.2.1 Formalism

We will take, as starting point for this formalism, the T-matrix of the reference molecule written by blocks, which is a Dyson-like expression already seen at Chapter 4:

$$\tilde{\tau}^{vv''} = \tilde{t}^v \delta_{vv''} + \tilde{t}^v \cdot \sum_{v'} \tilde{G}_{OI}^{vv'} \cdot \tilde{\tau}^{v'v''} \quad (5.1)$$

where

$$\delta_{vv'} = \begin{cases} 1 & \text{if } v' \neq v \\ 0 & \text{if } v' = v \end{cases} \quad (5.2)$$

$\tilde{G}_{OI}^{vv'}$ is a Green propagator (see Appendix A) and \tilde{t}^v is the diagonal atomic t-matrix of atom v -th. Notice that this is not the finally derived molecular T-matrix. There, additional propagations were applied so that all scattering paths started and ended at a common origin \vec{r}_0 . In Eq. (5.1) all the possible scattering paths inside the molecule can be found, which start and end at all pairs of atoms vv'' in the molecule.

We will derive the expression for the distorted molecule T-matrix, $\tilde{\tau}_{\text{dist}}^{vv''}$, produced by a small movement in the n -th atom described by a vector $\delta\vec{r}_n$. Taking the original position of this atom at the reference molecule, the n -th atom t-matrix change after the displacement is

$$\begin{aligned} \tilde{t}_{\text{dist}}^n &= \tilde{t}^n + \delta\tilde{t}^n \\ \delta\tilde{t}^n &= \tilde{G}_{II}(\delta\vec{r}_n) \cdot \tilde{t}^n \cdot \tilde{G}_{II}(-\delta\vec{r}_n) - \tilde{t}^n \end{aligned} \quad (5.3)$$

The distorted molecular T-matrix at first order in perturbation theory¹ is found by substituting this expression in Eq. (5.1) and neglecting terms of higher order

¹Actually, this derivation corresponds to the “second level of sophistication” if the original convention of Rous’ *et al* [23] is used.

$\mathcal{O}((\delta\tilde{t}^n)^k)$ with $k \geq 2$. This reduces the calculation to evaluating the following equation:

$$\begin{aligned}\tilde{\tau}_{\text{dist}}^{vv''} &\simeq \tilde{\tau}^{vv''} + \delta\tilde{\tau}^{vv''}(\delta\vec{r}_n) \\ \delta\tilde{\tau}^{vv''}(\delta\vec{r}_n) &= \left(\sum_{x \neq n} \tilde{\tau}^{vx} \cdot \tilde{G}_{IO}^{xn} \right) \cdot \delta\tilde{t}^n \cdot \left(\sum_{x \neq n} \tilde{G}_{IO}^{nx} \cdot \tilde{\tau}^{xv''} \right) \\ &\quad + \left(\sum_{x \neq n} \tilde{\tau}^{vx} \cdot \tilde{G}_{IO}^{xn} \right) \cdot \delta\tilde{t}^n \delta_{nv''} + \delta_{nv} \delta\tilde{t}^n \cdot \left(\sum_{x \neq n} \tilde{G}_{IO}^{nx} \cdot \tilde{\tau}^{xv''} \right) \quad (5.4)\end{aligned}$$

Four terms can be distinguished in these equations, depending on the vv'' atom pair block that is to be corrected: (i) the reference molecule T-matrix, (ii) perturbative terms that correspond to new scattering paths where scattering at the displaced n -th atom is intermediate, (iii) perturbative terms that start with a scattering event at n and (iv) perturbative terms that end with a scattering event at n . Notice that \tilde{G}_{IO}^{xn} and \tilde{G}_{IO}^{nx} start and end, respectively, at the original position of the n -th atom, since additional paths undergone by the electron due to the displacement $\delta\vec{r}_n$ are already accounted for inside the operator $\delta\tilde{t}^n$. If more atoms are involved in the distortion, their corresponding contribution terms are summed up at Eq. (5.4).

The final step for making the new molecular T-matrix usable by the LEED code is to refer all blocks $\tilde{\tau}_{\text{dist}}^{vv''}$ to a common origin \vec{r}_0 , in the same way as it is done in section 4.3.1.

5.2.2 Example: the CO/Cu(100)-c(2×2) surface

To check the range of applicability of this formalism, we have applied it to the case of CO/Cu(100)-c(2×2) surface at normal incidence, which has been already used in the previous Chapter. For the sake of simplicity, we take upright adsorbed CO molecules at atop sites. The test calculations have been done using our TMOL and LEED90 programs, and consist in a theory-theory comparison of the following calculations:

- On one hand, we compute IV curves for CO molecules of elongated bonds using the exactly computed molecular T-matrices, starting from $d = 1.2 \text{ \AA}$ and taking different longitudes $d + \delta$.
- On the other hand, we compute the same IV curves but using the molecular t-matrices calculated with the perturbative scheme.

For the molecule sizes to be considered here, the semi-classical approach yields that values $l_{T,\text{max}} = 9 - 13$ are enough to ensure convergence of the T-matrix approach versus the atomic calculation, as discussed in section 4.5.1. The other parameters in this calculations are fixed to the same values used at section 4.5.1.

Fig. 5.1 shows two panels with the IV curves (at three integer and two half-integer beams) for the cases $\delta = 0.08 \text{ \AA}$ ($l_{T,\text{max}} = 9$) and $\delta = 0.40 \text{ \AA}$ ($l_{T,\text{max}} = 12$) respectively. The difference between using the exact T-matrix and the perturbed one is almost negligible at the first case ($R_P = 0.0027 \pm 0.0005$) and quite acceptable at the second one ($R_P = 0.039 \pm 0.007$ if done with $l_{T,\text{max}} = 9$ and $R_P = 0.049 \pm 0.009$ if

done with the correct $l_{T,\max} = 12$). Notice that $\delta = 0.40 \text{ \AA}$ is the value usually taken by TLEED theory as the upper limit for applicability, beyond which the perturbation theory is not valid. The same panels contain an additional IV curve: the one calculated for the reference molecule of length 1.2 \AA . For the smaller distortion, the change in the molecule length does not induce a noticeable change in the IV curves, but, when increasing the bond length in 0.40 \AA , the change in the curves is strong. Thus, the use of the linear perturbation in the t-matrices to compute the elongated molecule T-matrix is proved to be enough even at this length.

Fig. 5.2 shows the evolution of R_P with the elongation, comparing the exact and approximated calculations. All values up to $\delta = 0.40$ remain with $R_P \leq 0.05$, similarly to typical results from conventional TLEED. For bigger elongations, fluctuations in the R_P appear, and, although values are still acceptable at levels around $R_P \simeq 0.1$, the validity of the perturbative approximation should be taken with caution.

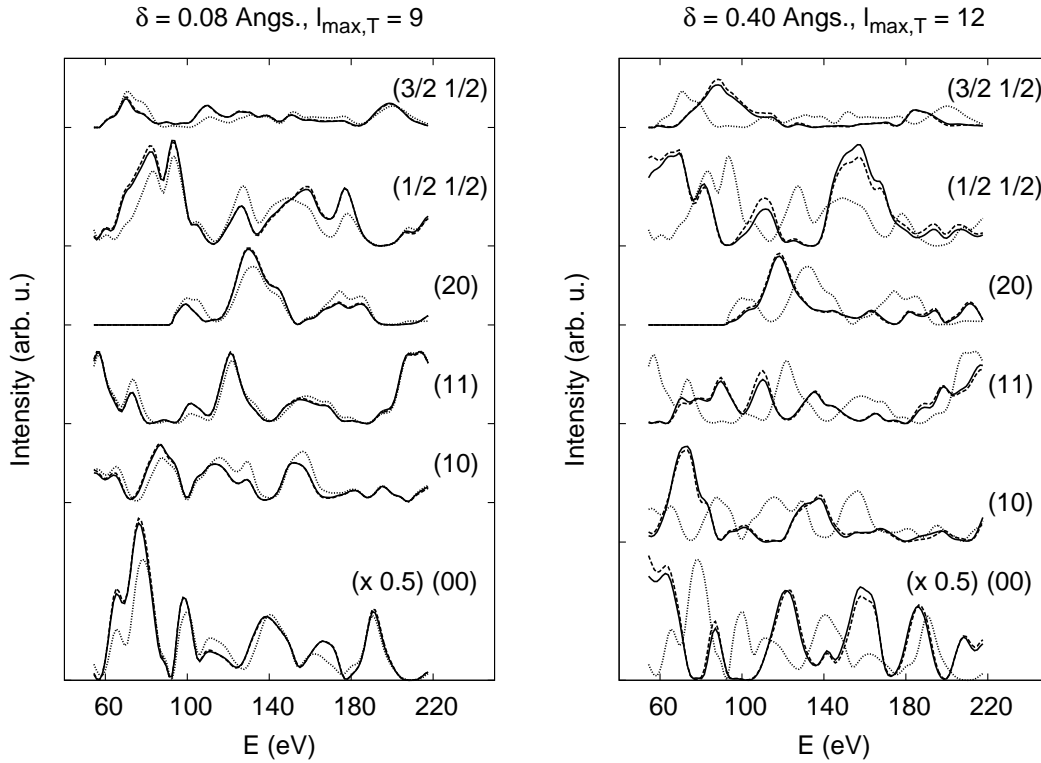


Figure 5.1: IV curves for the CO/Cu(100)-c(2×2) surface at normal incidence with upright molecules. Left hand panel shows the IV curves for an elongation $\delta = 0.08 \text{ \AA}$ (taking $l_{T,\max} = 9$). The right hand panel is for an elongation $\delta = 0.40 \text{ \AA}$ (taking $l_{T,\max} = 12$). In both panels, the dotted curves correspond to the IV curves for the undistorted CO, where the molecule length is 1.2 \AA . Solid and dashed lines are the IV curves for elongated molecules, solid line for exact T-matrix calculation and dashed line for approximated T-matrix calculation.

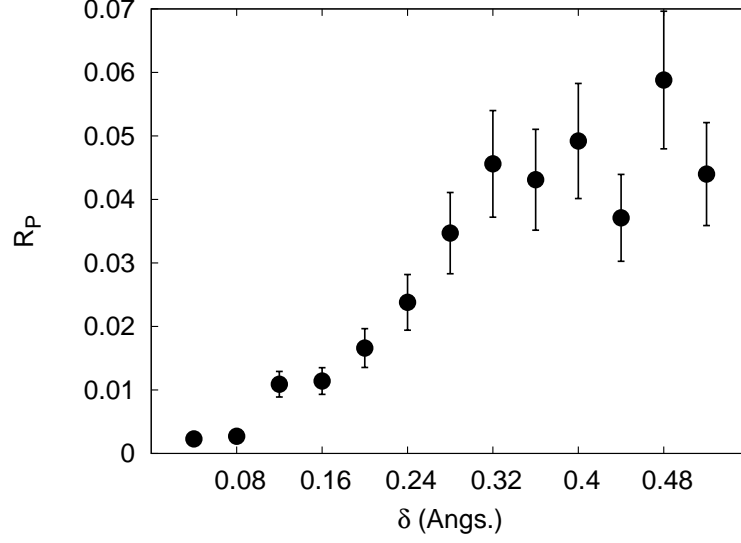


Figure 5.2: R_P IV curves in the CO/Cu(100)-c(2×2) example comparing the calculation with the exact and approximated molecular t-matrices as a function of the distortion length, δ in Å, i.e. R_P comparing solid and dashed lines of Fig. 5.1. Circles represent calculations made with the adequate $l_{T,\max}$ value for each elongated molecule size. These values are: 9 for $\delta = 0.04, 0.08$, 10 for $\delta = 0.12 - 0.20$, 11 for $\delta = 0.24 - 0.32$, 12 for $\delta = 0.36 - 0.44$ and 13 for $\delta = 0.48, 0.52$.

The method presented here is able to compute the molecular T-matrix of a slightly distorted molecule if the T-matrix of the undistorted molecule is given, without any further matrix inversions. A considerable computational cost is saved, since computation time scales as $(N(l_{T,\max} + 1)^2)^3$, where N is the number of atoms, due to the matrix inversion. The magnitude of the distortion the method can safely handle has two limitations:

- $l_{T,\max}$: this parameter must be chosen according to the final size of the distorted molecule.
- As in the TLEED approach, applicability relies on the propagators $G_{II}(\pm\delta\vec{r}_n)$ and their ability to account for the $\delta\vec{r}_n$ displacement.

5.2.3 Description of molecular normal modes of vibration

We have already seen that a distortion applied at the intramolecular bonds produces a change at the molecular T-matrix, which can be described within a linear perturbative approximation as long as the distortion is small. But we might be interested in bond distortions that are not fixed in time, for example, those due to thermal vibrations. In particular, the method discussed above can help to describe the coordinated motion of the molecule atoms when normal modes of vibration are excited in the molecule, such as bond stretching or bending, breathing modes, etc. This section deals with a formalism to describe those features.

This is interesting because thermally driven molecule dynamics upon a surface will, in general, be different from that of the gas phase. In the previous Chapter we have described how to treat vibrations and movements (rotations and translations) of the molecules that keep the bonds unchanged. These coordinated motion of the molecule's atoms will strongly affect the multiple scattering (MS). However, LEED will not be sensitive to the molecule vibrational normal modes in many cases, since their frequencies are too high and usually lie in the IR regime. For these situations, electron energy-loss spectroscopies (EELS) and IR absorption spectroscopy (IRAS) are used to access vibrational properties. However, there are some other cases where the bonds can be soft enough to affect LEED intensities. For example, vibrations when the dissociation of the molecule is about to happen [146].

De Andrés *et al* developed a method to account for background intensities due to phonons by using the TLEED first level of sophistication [147]. The authors compute amplitude changes, which are linear in the displacements along the principal axes of the vibration. This reduces the calculations to making changes on the intensities. In this work, our aim is to give a step forward, accounting for changes at the T-matrix using the second level of sophistication.

We propose approximating the T-matrix by its thermal average, using a probability distribution function (PDF) that accounts for all the molecule's atomic positions simultaneously. Let the set of vectors $\{\vec{r}_n\}_{n=1,\dots,N}$ be a generic instantaneous distortion of the molecule. Then, the PDF at temperature T for the N atoms is given by a Boltzmann distribution:

$$\text{PDF}(\{\vec{r}_n\}_{n=1,\dots,N}; T) \sim e^{-\frac{1}{k_B T} E(\{\vec{r}_n\}_{n=1,\dots,N})} \quad (5.5)$$

where E is the energy change associated to the distortion and k_B is the Boltzmann constant. The effect of the distortion at the molecular T-matrix blocks, according to Eq. (5.4), can be approximated by the following thermal average:

$$\langle \delta \tilde{\tau}^{vv''}(\{\vec{r}_n\}_{n=1,\dots,N}) \rangle_T = \frac{\int \left(\sum_{n=1}^N \delta \tilde{\tau}_n^{vv''}(\{\vec{r}_n\}) \right) \text{PDF}(\{\vec{r}_n\}_{n=1,\dots,N}; T) d^3 \vec{r}_1 \dots d^3 \vec{r}_N}{\int \text{PDF}(\{\vec{r}_n\}_{n=1,\dots,N}; T) d^3 \vec{r}_1 \dots d^3 \vec{r}_N} \quad (5.6)$$

Now, consider that the distortion is produced by the excitation of the j -th normal vibration mode of the molecule. In the gas phase, from symmetry considerations, the molecule has $3N - 6$ non-degenerate normal vibration frequencies ($2N - 3$ if it is a diatomic molecule). When the molecule adsorbed on the surface, the number of non-degenerate vibration frequencies is usually reduced. Following the harmonic analysis for vibrations, let ω_j be the j -th mode frequency and let $\{u_{ni}^{(j)}\}$ be the corresponding eigenvector, where the index $n = 1, \dots, N$ labels the atom and $i = x, y, z$ the Cartesian coordinates. When a normal mode is excited, the molecule atoms suffer a collective displacement proportional to the eigenvector. Let α be that proportionality constant. Then, the elastic energy associated to the excitation of the j -th mode is:

$$E^{(j)} = \frac{1}{2} \mu \omega_j^2 \sum_{n=1}^N |\alpha \vec{u}_n^{(j)}|^2 \quad (5.7)$$

where μ is the reduced mass of the molecule. The PDF corresponding to the excitation of the j -th mode is just a function of α , since the direction is fixed by the

eigenvectors of the j -th normal mode:

$$\text{PDF}(\{\vec{r}_n\}_{n=1,\dots,N}; T) \sim e^{-\frac{1}{2k_B T} \mu \omega_j^2 \sum_{n=1}^N |\alpha \vec{u}_n^{(j)}|^2} \prod_{n=1}^N \delta(\hat{r}_n - \widehat{u}_n^{(j)}) \quad (5.8)$$

This description of displacements in terms of normal modes, allows a splitting of the thermal average into the following separate atom terms:

$$\langle \delta \tilde{\tau}_{(j)}^{vv''} \rangle_T = \sum_{n=1}^N \frac{\int \delta \tilde{\tau}^{vv''}(\vec{r}_n) e^{-\frac{1}{2k_B T} \mu \omega_j^2 \sum_{n=1}^N |\alpha \vec{u}_n^{(j)}|^2} \delta(\hat{r}_n - \widehat{u}_n^{(j)}) d^3 \vec{r}_n}{\int e^{-\frac{1}{2k_B T} \mu \omega_j^2 \sum_{n=1}^N |\alpha \vec{u}_n^{(j)}|^2} \delta(\hat{r}_n - \widehat{u}_n^{(j)}) d^3 \vec{r}_n} \quad (5.9)$$

In this equation, the dependence in the distortion will appear through terms of type $G_{II}(\vec{r}_n) \cdot \tilde{t}^n \cdot G_{II}(-\vec{r}_n)$ (see Eqs. (5.3) and (5.4)). We write down the explicit form of the matrix element $(LL'') \equiv (lm, l''m'')$ of such product using the Green operators from Appendix A: $\hat{r}_n = \widehat{u}_n^{(j)}$:

$$\begin{aligned} (G_{II}(\vec{r}_n) \cdot \tilde{t}^n \cdot G_{II}(-\vec{r}_n))_{LL''} &= \sum_{L'} G_{LL'}^{II}(\vec{r}_n) \cdot t_{L'}^n \cdot G_{L'L''}^{II}(-\vec{r}_n) \\ &= \sum_{L'} t_{L'}^n \sum_{L_1, L_2} 4\pi i^{l-l'-l_1} (-1)^{m'+m_1} j_{l_1}(\kappa|\vec{r}_n|) Y_{l_1-m_1}(\Omega(\vec{r}_n)) \int Y_{lm} Y_{l_1 m_1} Y_{l'-m'} \\ &\quad \times 4\pi i^{l'-l''-l_2} (-1)^{m_2+m''} j_{l_2}(\kappa|\vec{u}_n|) (-1)^{l_2} Y_{l_2-m_2}(\Omega(\vec{r}_n)) \int Y_{l'm'} Y_{l_2 m_2} Y_{l''-m''} \quad (5.10) \end{aligned}$$

From substitution of this equation in Eq. (5.9), integrals of the following type appear at the numerator:

$$\int Y_{l_1 m_1}(\hat{r}_n) Y_{l_2 m_2}(\hat{r}_n) j_{l_1}(\kappa|\vec{r}_n|) j_{l_2}(\kappa|\vec{r}_n|) e^{-\frac{1}{2k_B T} \mu \omega_j^2 \alpha^2 \sum_{n=1}^N |\vec{u}_n^{(j)}|^2} \delta(\hat{r}_n - \widehat{u}_n^{(j)}) d^3 \vec{r}_n \quad (5.11)$$

In this integral, we can separate angular and radial parts. The angular part is:

$$\int Y_{l_1 m_1}(\hat{r}_n) Y_{l_2 m_2}(\hat{r}_n) \delta(\hat{r}_n - \widehat{u}_n^{(j)}) d^2 \hat{r}_n = Y_{l_1 m_1}(\widehat{u}_n^{(j)}) Y_{l_2 m_2}(\widehat{u}_n^{(j)}) \quad (5.12)$$

and the radial integral is made with the change $d|\vec{r}_n| = |\vec{u}_n^{(j)}| d\alpha$ and noticing that κ is a complex constant, with $\Re(\kappa) > 0$ and $\Im(\kappa) > 0$:

$$\begin{aligned} &\int_0^\infty j_{l_1}(\kappa \alpha |\vec{u}_n^{(j)}|) j_{l_2}(\kappa \alpha |\vec{u}_n^{(j)}|) \alpha^2 |\vec{u}_n^{(j)}|^2 e^{-\frac{1}{2k_B T} \mu \omega_j^2 \alpha^2 \sum_{n=1}^N |\vec{u}_n^{(j)}|^2} d\alpha \\ &= \frac{1}{2} |\vec{u}_n^{(j)}|^2 i 2^{-2-l_1-l_2} b a^{-2} e^{-i\pi(l_1+l_2)/2} \left(-\frac{b^2}{a} \right)^{(-1+l_1+l_2)/2} \\ &\quad \times \pi \Gamma(2+l_1+l_2) \Gamma\left(\frac{3+l_1+l_2}{2}\right) \frac{{}_3F_3(a_1, a_2, a_3; b_1, b_2, b_3; -\frac{b^2}{a})}{\Gamma(b_1) \Gamma(b_2) \Gamma(b_3)} \quad (5.13) \end{aligned}$$

where ${}_3F_3$ is a generalized hypergeometric function [148] and

$$a_1 = \frac{2+l_1+l_2}{2}; \quad a_2 = \frac{3+l_1+l_2}{2}; \quad a_3 = \frac{3+l_1+l_2}{2}$$

$$\begin{aligned}
b_1 &= \frac{3}{2} + l_1; \quad b_2 = \frac{3}{2} + l_2; \quad b_3 = 2 + l_1 + l_2 \\
a &= \frac{1}{2k_B T} \mu \omega_j^2 \sum_{n=1}^N |\vec{u}_n^{(j)}|^2 \\
b &= \kappa |\vec{u}_n^{(j)}|
\end{aligned} \tag{5.14}$$

The last step is to divide by the denominator integral of Eq. (5.9). The angular part of that integral is equal to one. The radial part is:

$$\int_0^\infty \alpha^2 |\vec{u}_n^{(j)}|^2 e^{-a\alpha^2} d\alpha = |\vec{u}_n^{(j)}|^2 \frac{1}{a^3} \tag{5.15}$$

where the expression for the coefficient a can be found at Eq. (5.14).

Our approach to molecular vibrations is harmonic, and for each excited normal mode, it is isotropic w.r.t. the eigenvectors. Notice that this does not mean that the atoms vibrate isotropically: it is the normal mode what is isotropically oscillating, while individual atoms oscillate in directions given by the eigenvector. Besides, atoms do not move regardless of other atoms, but their movements are coupled by the normal mode.

In a realistic situation, it is probable that several modes are thermally excited at the same time, so that their contributions are superimposed. On the other hand, if we are willing to study soft modes of the molecule, we must consider that such modes usually involve large vibration amplitudes. Thus, we must check that the distortions are kept within the limits of the approach, $\lesssim 0.4$ Å. Again, a suitable value of $l_{T,\max}$ must be chosen according to the maximum molecule size.

5.3 Use of the molecular T-matrix in a Tensor LEED program

In section 2.10 we described the TLEED approach. It is based in the principle that small displacements from a reference structure will only cause small changes in the diffracted amplitudes. We shall remind briefly that the most widely used approximation level, the second as described by Rous *et al* [23], consists of taking perturbative terms at the amplitudes that are linear in the matrix elements of the change in the atomic t-matrices. Thus, the change in the amplitude of beam \vec{g} due to a displacement \vec{R}_w of the w -th atom of the surface can be written as:

$$\delta A_{\vec{g}w} = \langle \vec{k} + \vec{g}; \text{out} | \delta \tilde{t}^w(\delta \vec{R}_w) | \vec{k}; \text{in} \rangle = \tilde{M}_{\vec{g}w} f(\delta \vec{R}_w) \tag{5.16}$$

where $f(\delta \vec{R}_w)$ is a function of the displacement and $\tilde{M}_{\vec{g}w}$ is the *tensor*, which depends on the reference structure only. If more than one atom is varied, perturbation terms $\delta A_{\vec{g}w}$ are added. At the reference calculation, which must be done full-dynamically, the required tensors are computed and stored. Then, the amplitudes diffracted by structures that differ from the reference structure by small displacements only, can be calculated straightforward using the tensors and Eq. (5.16), with no need of

further matrix inversions. The matrix accounting for the change in the w -th atom t-matrix is:

$$\delta \tilde{t}^w(\delta \vec{R}_w) = \tilde{G}_{II}(\delta \vec{r}_w) \cdot \tilde{t}^w \cdot \tilde{G}_{II}(-\delta \vec{r}_w) - \tilde{t}^w \quad (5.17)$$

where \tilde{G}_{II} is a translation operator described at Appendix A. The $\delta \tilde{t}^w$ matrix computed in this way, is non-diagonal, since the displacement can be seen as a symmetry breaking w.r.t. the position that the w -th atom occupied in the reference structure. Thus, a certain parallelism can be established between the treatment of the atomic displacements by TLEED and the use of a non-diagonal molecular T-matrix.

We have already shown in Chapter 4 that the required $l_{T,\max}$ to describe the molecule accurately is proportional to its size. In general, large $l_{T,\max}$ values will be needed for overlayers at full-dynamical spectra evaluations. We have to consider also that matrix multiplication scales in general like N^3 , while diagonal matrix multiplication scales like N . Therefore, working with large molecules can be computationally demanding in some cases. In order to overcome these drawbacks, we will introduce in this section a method to handle molecular T-matrices taking advantage of the TLEED formalism described before.

Let the site w -th of the overlayer be occupied by a molecule, described by a T-matrix \tilde{T}^w . Our approach to the surface IVs consists of the following steps:

1. At the reference structure, use at the w -th site a diagonal matrix containing the molecular T-matrix diagonal elements only:

$$t_{lm}^w = T_{lm,l'm'}^w \delta_{ll'} \delta_{mm'} \quad (5.18)$$

Compute the tensors using this “pseudo-atom” described by the diagonal t-matrix \tilde{t}^w .

2. At the perturbative step, i.e. Eq. (5.16), use the extradiagonal terms of the molecular T-matrix in place of $\delta \tilde{t}^w$:

$$\delta t_{lm,l'm'}^w = T_{lm,l'm'}^w \cdot (1 - \delta_{ll'} \delta_{mm'}) \quad (5.19)$$

We are willing to retrieve the exact spectra, i.e. the one that would be obtained using full-dynamically the entire T-matrix. There are several reasons for which this method might fail. The most evident one is that, quantitatively, for typical molecules, extra-diagonal terms of typical molecular T-matrix have similar magnitudes as the diagonal ones, i.e we are applying a strong perturbation in step 2. Another reason lies in step 1, which is more subtle: the reference calculation itself has been made with an unrealistic “pseudo-atom”. For this scatterer, t_{lm}^w values are different for the same l , due to the symmetry breaking and the mixing of phase shifts from different atomic species that can occur sometimes. By themselves, these spectra taken from such a reference calculation are meaningless. The features of the reference IV curves have little in common with the actual spectra arising from substrate plus adsorbed molecule. In addition, we must consider the inaccuracies brought by the use of the T-matrix formalism instead of the conventional atomic layer calculation.

Nevertheless, this method has been implemented at TensErLEED code [70] to check its feasibility. We have found that it works well, despite the apparent shortcomings we have just discussed. Notice that the R_P comparing this method and the full-dynamical atomic conventional calculations will have a lower bound, which is given by the use of a molecular T-matrix.

Example 1

The structure chosen for this test has been again CO/Cu(100)-c(2×2), with the upright CO molecule at atop sites (of length 1.2 Å and with Cu-C distance equal to 1.8 Å), at normal incidence with $l_{T,\max} = 9$ (other parameters are fixed as in section 4.5.1). Fig. 5.3 shows some IV curves from three different types of calculation:

1. Conventional full-dynamical atomic calculation, which splits the CO adlayer into two planes.
2. Curves for the approach presented here, combining TMOL and TensErLEED codes. Compared to the previous set of curves, we have $R_P = 0.049 \pm 0.003$. Notice that the lowest bound to this R_P is given by the R_P between the molecular T-matrix approximation and the conventional atomic calculation, which has the value $R_P = 0.044 \pm 0.003$ shown in the previous Chapter.
3. The meaningless curves of the reference calculation used for the approach, i.e. using the diagonal elements only of the CO T-matrix. It can be observed that, as expected, these curves do not have many features in common with the actual spectra of CO/Cu(100)-c(2×2). They differ by a factor $R_P = 0.55 \pm 0.04$.

However, when adding the extra-diagonal terms of the molecular T-matrix as a perturbation, the spectra of the actual structure is retrieved, in spite of the striking differences with the reference spectra. This result is surprising, due to the shortcomings we had predicted. It is remarkable that the addition of this perturbation produces a stronger change than a simple movement of an atom, a change that is applicable only for movements of $\lesssim 0.40$ Å, while the CO molecule is 1.2 Å long.

Example 2

Another test has been made in order to check the performance of this method under less symmetrical conditions. To do this, we have chosen the same CO/Cu(100)-c(2×2) surface, but with a tilt at CO of $\theta = 30^\circ$ and $\phi = 45^\circ$ (this azimuthal ϕ angle corresponds to the in-plane direction [011]) about the molecule centre. This tilting has been achieved by applying Wigner's matrices. In this case, the T-matrix is less sparse than the more symmetric upright CO. Therefore, we expect to obtain a poorer R_P value, since more extradiagonal terms take part at the perturbative correction. Fig. 5.4 shows some IV corresponding to this surface at normal incidence using the three types of calculation mentioned above. A factor $R_P = 0.078 \pm 0.004$ is obtained between IV curves calculated from this method and IV curves calculated full-dynamically, as expected. This R_P value is in fact larger than that obtained for the upright CO. The starting discrepancy between the reference IVs and the full-dynamical calculation is also larger, $R_P = 0.63 \pm 0.03$.

Example 3

In the two examples shown above, we have seen that our method has the ability to speed up spectra evaluations involving large molecules, i.e. molecular T-matrices with high $l_{T,\max}$ values. Another interesting application is found by pushing forward the method to describe movements of the entire molecule, keeping intramolecular bonds fixed. In the present example, we check the implications of tilting the molecule through a small angle. As the molecule T-matrix can be rotated without any significative loss of accuracy, we have studied the applicability range of the following method: let \tilde{T}_R^w be the T-matrix of the tilted molecule, obtained from \tilde{T}^w by applying Eq. (4.10), for example. Then:

1. As the reference calculation use the diagonal of the *upright* molecule:

$$t_{lm}^w = T_{lm,l'm'}^w \delta_{ll'} \delta_{mm'} \quad (5.20)$$

2. Take all the matrix elements of the *rotated* molecule as the perturbation:

$$\delta t_{lm,l'm'}^w = T_{R,lm,l'm'}^w \quad (5.21)$$

This method has been applied to the CO/Cu(100)-c(2×2) system with tilted CO. The tilt azimuthal angle is $\phi = 45^\circ$, and the polar angle is θ . The CO is rotated about its centre, i.e. the molecule centre remains at its original atop position in the upright configuration. We have obtained the IV curves of this structure from four different types of calculation, and computed the R_P between them as a function of θ . These R_P are summarized at Fig. 5.5. The four calculations, two full-dynamical and two TLEED-like, are the following:

- (i) Conventional full-dynamical atomic calculation, labelled “atoms” at Fig. 5.5.
- (ii) Full-dynamical calculation using the molecular T-matrix of the rotated molecule, labelled “Tmol” at Fig. 5.5.
- (iii) Conventional TLEED calculation, taking the upright molecule configuration as reference structure. This is labelled “Tensor+atoms”
- (iv) The method presented in this subsection, taking the upright molecule T-matrix diagonal elements at the reference calculation, and adding the rotated T-matrix as a perturbation. This is labelled “Tensor+Tmol”.

The applicability range of our method is given by the R-factor comparing calculation types (i) and (iv), which yields values $R_P(\text{atoms}, \text{Tensor} + \text{Tmol}) \lesssim 0.1$ for tilt angles $\theta \lesssim 15^\circ$, as shown in Fig. 5.5. At $\theta \sim 15^\circ$, C and O atoms are vertically displaced by distances $\sim 0.02 \text{ \AA}$ and displacements parallel to the surface are $\sim 0.15 \text{ \AA}$. These values are in good agreement with the conventional TLEED applicability range. This range is shown in Fig. 5.5, too, labelled by $R_P(\text{atoms}, \text{Tensor} + \text{atoms})$. We remind that the lower bound for our method applicability is given by the use of the molecular T-matrix, i.e.

$$R_P(\text{atoms}, \text{Tensor} + \text{Tmol}) \geq R_P(\text{atoms}, \text{Tmol}) \quad (5.22)$$

This limit is kept at constant value of $R_P(\text{atoms}, \text{Tmol}) \sim 0.4$ for the studied tilt angles. In particular, Fig. 5.6 shows the IV curves calculated following methods “atoms” and “Tensor+Tmol”, at tilt angles $\theta = 8^\circ$ and $\theta = 20^\circ$, which yield $R_P = 0.071 \pm 0.004$ and $R_P = 0.113 \pm 0.006$ respectively.

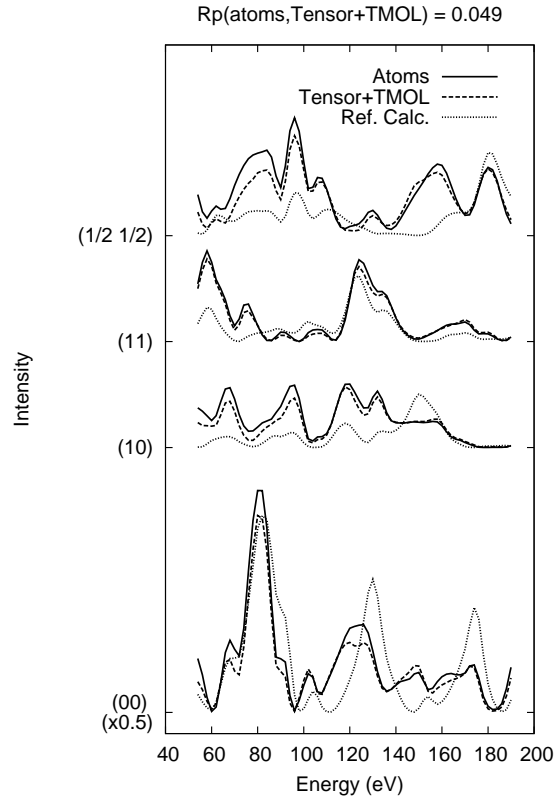


Figure 5.3: In the example of atop CO/Cu(100)-c(2×2) with upright CO, this figure shows the effect of adding the extradiagonal terms of the CO T-matrix as a perturbation, in the TLEED sense, calculated with the TensorLEED code. The dotted lines are the IV curves of the reference calculation using only the diagonal terms of the T-matrix, the dashed curves are obtained adding the extradiagonal terms as a perturbation and the solid line are obtained from the exact full-dynamical calculation, with the CO molecules split into two atomic layers.

5.4 Conclusions

In this Chapter two different usages of the molecular T-matrix inspired in the TLEED approximation have been developed. The first one consists of computing efficiently, for a given molecule, the T-matrix of the slightly distorted molecule. The validity range of this method, checked in the CO/Cu(100)-c(2×2) system, is of the same order as the applicability range of the TLEED approach. However, the $l_{T,\max}$ value must be carefully chosen according to the molecule size in order to be correctly handled inside any LEED program.

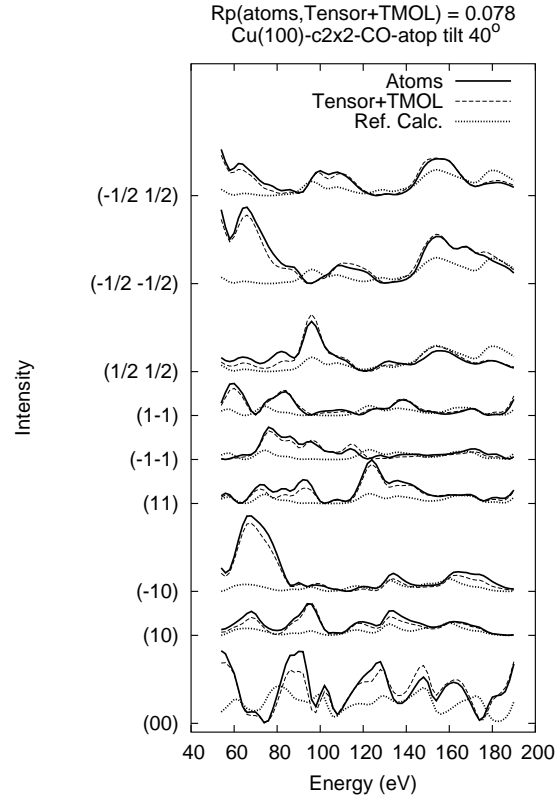


Figure 5.4: IV curves for the case CO/Cu(100)-c(2×2) with tilted CO molecule by angles $\theta = 30^\circ$ and $\phi = 45^\circ$. The used line types are the same as in Fig. 5.3.

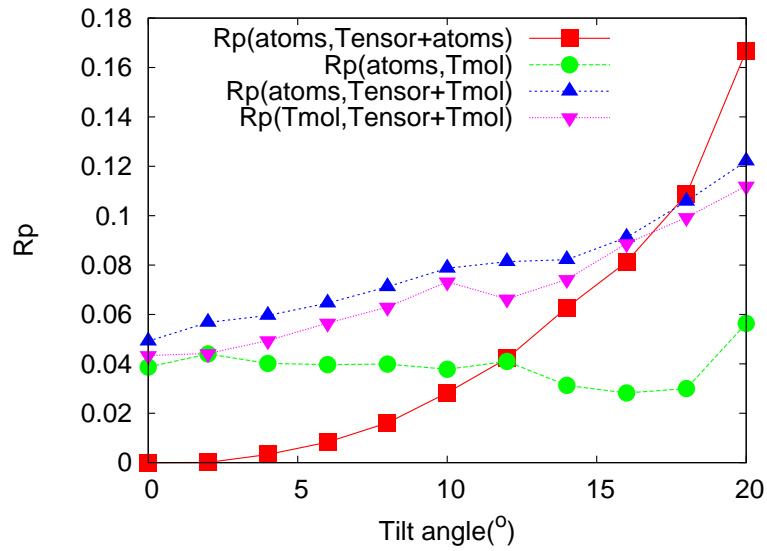


Figure 5.5: R_P comparing several approaches to calculating IV curves in Cu(100)-c(2×2) with tilted CO. The label details can be found in the text.

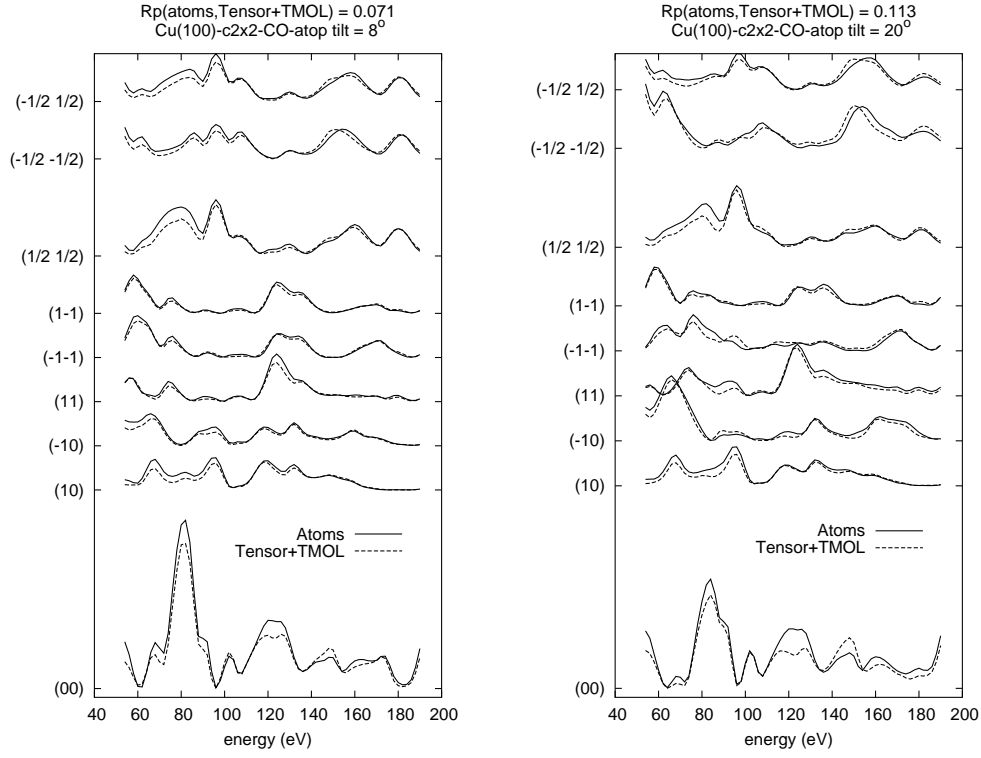


Figure 5.6: IV curves for the case CO/Cu(100)-c(2×2) with tilted CO molecule by angles $\theta = 8^\circ$ and $\theta = 20^\circ$ respectively, at $\phi = 45^\circ$. Solid line corresponds to the conventional calculation (“atoms”) and dashed line to the approach “Tensor+Tmol” (see the text for the details).

The perturbative approach to molecular distortions allows a description of molecular vibrations in terms of normal modes, which can be relevant at LEED experiments on molecules having soft vibrations.

The second usage can be applied when working with fixed structure molecular adsorbates. The TensErLEED package has been modified to use the diagonal terms of the molecular T-matrix in the reference structure calculation and to use the extradiagonal terms as a perturbation during the amplitude change evaluation. This saves a number of multiplications with non-diagonal matrices. The diffracted intensities obtained from the reference calculation are meaningless, but the intensities of the complete structure are retrieved at the perturbative step of the calculation. The accuracy of this approach has been studied in the CO/Cu(100)-c(2×2) system, and found to be $R_P \lesssim 0.1$. This is quite an acceptable result, since we must consider that the method is limited by molecular T-matrix approach itself and by the fact that extradiagonal terms constitute a much harder perturbation than simply displacing an atom or changing a chemical species.

This method can be generalized by using all the matrix elements of the slightly tilted molecule w.r.t. its original orientation at the perturbative step. For the same model structure, this method has been found to be valid up to a tilt angle of $\sim 15^\circ$. This method has a straightforward implementation in structural search involving tilt angles. The same formalism can be implemented to account for molecule translations or vibrations in a search. Furthermore, the two techniques presented in this Chapter for both distorted and undistorted molecule can be combined, and use the T-matrix of the slightly distorted molecule as a perturbation to speed up spectra calculation.

Chapter 6

Surface Diffraction Structure Determination from Combinatorial Simultaneous Optimization

6.1 Introduction

To understand physical and chemistry processes on surfaces a detailed knowledge of atomic positions and/or atomic trajectories is required. A popular way to obtain this information is the analysis of diffracted spectra from different techniques, such as: Low-Energy Electron Diffraction (LEED) [14, 1, 15], Photoelectron Diffraction (PD) [17], Surface X-ray Diffraction (SXRD), [149, 150], Near-Edge X-ray Absorption Fine Structure (NEXAFS), [18] etc. [14, 1, 3, 4]. This is a typical inverse problem where the database, \mathcal{S} , is a function of the structure, \mathcal{X} : $\mathcal{S} = f(\mathcal{X})$. Formally, the problem could be solved by inverting the algorithm relating the structure and the experimental database $\mathcal{X} = f^{-1}(\mathcal{S})$. In practice, basic problems forbid such a simple procedure, as the lack of information on the phase of the diffracted waves, or the requirement of self-consistency. Therefore, it has been necessary to apply a trial and error procedure that compares experimental and calculated spectra for different proposed models.

The quality of the fit for each trial structure is measured by means of a reliability R-factor, playing the role of a cost function which must be minimized. The R-factor, as a function of a given structure described by a set of N structural parameters, is a hypersurface of complex topography, often showing several minima, and our task will be to make a multidimensional minimization of such a scalar function, $R : \mathbb{R}^N \rightarrow \mathbb{R}$.

If we intend to find out the R-factor minimum by simple brute force search, i.e., evaluating the R-factor for every point of a grid in structural parameters, we find that the number of trial structures, t , scales exponentially with N . In the case of a grid where the number of pixels in each of the N dimensions is equal to n_p , then $t = n_p^N$ structures should be tried. For this reason, optimization theory classifies this as a non-polynomial NP-complete problem, as pointed out by Kirkpatrick *et al* [151] and by Pendry *et al* [152]. Particularly, if we carry out an exhaustive search on a continuous interval of length L for each parameter, making sure that the solution

is at the worst case at a maximum distance ϵ from the true solution, we obtain:

$$t \simeq \left(\frac{L\sqrt{N}}{\epsilon} \right)^N \quad (6.1)$$

This scaling law ¹, $t \sim N^{N/2}$, for high N values is even slower than the exponential law that appears in the grid case. This is due to the constraint imposed by the distance ϵ , since distances scale as \sqrt{N} in the \mathbb{R}^N space.

We analyze how to build an optimum strategy in the context of two problems central to scattering theory: phase retrieval and multiple scattering, which are considered the two basic difficulties for direct methods. Both effects will be analyzed in the framework of single atom scattering and LEED structure determination respectively.

Single atom scattering

The simple case of electron scattering by a single atom illustrates the implications of the lack of information on diffracted wave phases [153, 154]. Given an incident plane wave of momentum κ , the scattered amplitude in the far field as a function of the polar angle θ is

$$A(\theta; \kappa) = \frac{1}{2i\kappa} \sum_l (e^{2i\delta_l(\kappa)} - 1) P_l(\cos\theta) \quad (6.2)$$

where $P_l(\cos\theta)$ are Legendre polynomials. If the phase could be measured, the atomic phase shifts $\vec{x} = \{\delta_l(\kappa)\}$ would be found from Legendre polynomials orthonormal properties. As experiments can only provide the intensities, $I(\theta; \kappa) = |A(\theta; \kappa)|^2$, this is not possible, and we turn to a ‘trial and error’ algorithm. We shall retrieve the \vec{x} by minimizing a cost function such as

$$R(\vec{x}) = \sum_{\theta} (I_{\text{th}}(\vec{x}, \theta; \kappa) - I_{\text{exp}}(\theta; \kappa))^2 \quad (6.3)$$

where I_{th} and I_{exp} are the calculated and experimental intensities, respectively. We notice that this is a highly nonlinear function of \vec{x} , and a slightly more complicated problem than the standard phase retrieval, where only one phase is needed, not a set of phases.

The ability to retrieve phase shifts from the intensities is the first step to try to recover the potential behind.

¹The Eq. 6.1 can be derived in the following way: if the absolute minimum of R lies in $\vec{x}^0 \in \mathbb{R}^N$, then the N -dimensional distance from a point $\vec{x} \in \mathbb{R}^N$ to the solution is given by $d = \sqrt{\sum_{i=1}^N (x_i - x_i^0)^2}$. Nearby the solution, where $d \leq \epsilon$, we can define a one-dimensional distance δ such that $\epsilon \simeq \delta\sqrt{N}$. Thus, an exhaustive search to achieve the solution with a precision ϵ would require to evaluate R on the points of a grid, where pixel size is given by δ . That would imply making $t = (L/\delta)^N \simeq (L\sqrt{N}/\epsilon)^N$ evaluations.

LEED

Multiple scattering (MS) is common in surface structural techniques where a strong interaction increases sensitivity to the surface region. The price to pay are even harder non-linear conditions on the equations. As an example, let us consider a LEED experiment, which has become the main technique for structure determination in surface crystallography. In general, the experimental database for an ordered surface consists of a set of intensity vs. incident electron energy spectra for the diffracted beams (IV curves), taken at a fixed incidence direction. It is possible to obtain accurate spectra within a self-consistent theory framework that describes MS inside the surface, but it is computationally expensive [14, 1]. Therefore, a great effort has been done so far in order to implement strategies that reduce the amount of computational effort in several stages of the optimization calculations. Recent improvements include:

- Reduction of the number of trial structures by means of an efficient sampling of the R-factor hypersurface.
- Reduction of the number of intensity evaluations, by the use of novel R-factors based on a reduced database [155].
- Faster single intensity calculations applying approaches like Tensor LEED instead of full dynamical calculations near the real structure [23].

Recent attempts have been focused on developing *global* rather than local search strategies, since all the existing R-factors hypersurfaces are known to show a complicated structure of local minima. So far, there is a great variety of descent methods, mostly based in the use of derivatives, that find the minimum in a local well of a surface [44], with a promising N^2 scaling law. But, if one wishes to find a global minimum using these methods, an additional multiple launch strategy is necessary, which makes the problem NP-like again, due to the exponential scaling of the number of possible starting points. Most of the global methods are based on a Monte Carlo-like strategy, that occasionally allows aleatory uphill moves.

6.2 R-factor topography

In Chapter 2, at section 2.8, the expressions for calculating Pendry R-factor R_P [41] are given. As we commented there, intensities are affected by background contributions of temperature effects and electron damping, so R-factors that make use of IV derivatives are, in general, more reliable. In particular, R_P treats "equally" all maxima, minima and zeros at the IV's, since all of them are likely to contain information about the structure, even the smallest peaks. Pendry uses the Y -functions, based on logarithmic derivatives, to highlight all the extrema found in the spectra, and R_P quantifies the agreement between experimental and calculated Y -functions.

Due to correlations among surface parameters, both structural and non-structural, a number of shallow local minima will appear in the R-factor hypersurface. These fluctuations make local methods unlikely to succeed, since they act as traps for the solutions when only one search from one starting point is launched. Thus, the final

solution is not guaranteed to be the most likely structure, since it may correspond to a local well.

The R_P local minima probability distribution is found to have two main peaks [156, 157]:

- One smaller sharp peak at low R_P values, due to diffraction coincidences in the Bragg condition, $\vec{k} \cdot \vec{r} = 2\pi n$, for each diffracted beam. For typical LEED values of the perpendicular momentum transfer, this would yield low R-factors every $\sim 0.5 \text{ \AA}$.
- One broad peak at high R_P values, due to shallow local wells arising from fluctuations. Rous' model assumes that these fluctuations appear as a consequence of random correlations between experimental and theoretical spectra. The width of this peak depends on the energy overlap between theory and experiment and the IV curve peak width, intimately related to the imaginary part of the inner potential. As these quantities do not depend on the surface, fluctuations in R_P are a generic property.

The possible chaotic nature of wavefunctions, due to the complexity introduced by MS, influences the R_P factor. Following de Andr s and Verg s [58], three regions can be distinguished in the parameter space:

- I. A perturbative region, characterized by a polynomial dependence in the surface parameter values, $R_P(p) \propto p^n$. This polynomial law can be explained by perturbation theories, e.g. TLEED discussed at section 2.10.
- II. An exponential region, $R_P(p) \propto e^p$, where small changes in the structure produce large variations in R_P .
- III. A fully chaotic region where R_P saturates to values ~ 1 , corresponding to completely uncorrelated structures.

For typical LEED experimental intensities, the region II is limited by parameters values $0.1\text{--}0.2 \text{ \AA}$, that correspond approximately to $R_P = 0.2\text{--}0.4$. Thus, structures having $R_P \gtrsim 0.4$ should not be taken as reliable.

6.3 Previous work overview

To date, many attempts have been done in order to make quantitative LEED-IV analysis less computationally expensive. Most of the studied methods are inspired by other applications of function minimization. Lately, there is a tendency to implement global algorithms. Besides, directed searches are designed in order to reduce the number of calls to the R-factor function, since spectra calculation is complex in LEED.

We shall comment on some algorithms used to date in LEED optimization, both local and global methods. The former will be briefly described and the latter will be described in greater detail, since the new algorithm introduced in this Chapter corresponds to the family of global methods.

6.3.1 Local methods

In general, local methods based in R-factor derivatives are faster in optimization problems. As we have mentioned above, scaling law of these kind of methods is fast, but they have the drawback of being able to explore only a single attraction basin of the R-factor hypersurface [158]. The most simple way of using gradients is the so-called steepest descent method, that consists in moving from \vec{x}_i to \vec{x}_{i+1} by minimizing along the line in the direction of the local gradient, $-\nabla R(\vec{x}_i)$.

Conjugate gradients is, to date, considered the most successful gradient method. Rather than using the local gradient, it follows a direction that is *conjugate* to the previous gradient, and, if possible, to all the previous directions traversed.

Other authors have worked with more sophisticated gradient methods including second derivatives [159] or steepest descent methods that do not need derivatives [156].

Though it is also local, the method developed by Kleinle *et al* [160, 155] deserves some attention, since some of the features of the algorithm that will be introduced in this work bear some resemblance with it. These authors introduce two levels of improvement:

1. They propose a novel R-factor, R_{DE} , where DE denotes “discrete energies”. It is partially inspired by methods developed for SXRD [149], where several beam intensities are usually recorded for a single energy. R_{DE} , which yields similar results as Pendry’s and Zanazzi-Jona’s R-factor with small energy steps (~ 3 eV), has the property of remaining nearly unchanged when increasing the energy step up to ~ 15 eV. This reduction of data is justified by the fact that some values of the curve can be regarded as redundant.
2. In addition to introducing the R_{DE} , the authors propose using the Levenberg-Marquardt method [44]. This method has the ability to adapt to the topography at the current surface point, using steepest descent far for the minimum region and a linear expansion near the minimum, where the gradients are close to zero and steepest descent method converges slowly.

There are a few comments I would like to make about some claims of the papers referenced above. Kleinle *et al* justify a reduction in the database by the fact that some values of the curve can be regarded as redundant, since the IV curves can be interpreted as a superposition of Lorentzian-shaped peaks, but this is just a phenomenological argument. In fact, the $I(E)$ datapoints are not independent, since the underlying link of the surface structure exists among them. Thus, any N datapoints should be needed to retrieve the N structure parameters.

Regarding the significance of peak positions, they say: ‘also the positions of the IV maxima with respect to each other are correlated. For this reason there is no particular significance of the maxima positions, as often believed’. I slightly disagree with those authors’ statement, as long as a Bragg picture is taken to describe reflections. While it is true that one could infer the structure from any N points in an exact picture, the peak positions give additional hints about the phases of the wavefields arriving from individual atoms at the detector, namely that almost all those phases are of comparable magnitude.

The simplex is another type of local algorithm that has been applied to LEED [22]. A simplex for N dimensions is a polyhedra of $N + 1$ vertices. Theoretically, it is based in the fact that if the function to be optimized were linear, the minimal maxima must be in one of the vertices of that polyhedra (then the name of linear programming). Briefly, the minimum finding is done by moving the vertex of the simplex where the function takes the largest value. Typical moves are expansions, contractions, reflections along one dimension.

6.3.2 Global methods

Pendry *et al* [152, 161, 162] suggested a non-local method based in heavy atom methods from X-ray diffraction. In this procedure, computed intensities are derived w.r.t. the structural parameters $\vec{x} = (x_1, \dots, x_N)$ to obtain a system of nonlinear equations:

$$\frac{\partial}{\partial x_i} \sum_{E,g} (I_g^{\text{exp}}(E) - I_g^{\text{th}}(E; \vec{x}))^2 = 0 \quad (6.4)$$

where E is the energy and g labels beams. Then, provided that the parameter search space is a small area around a well known reference geometry, the system is linearized in the atomic displacements by application of Tensor LEED in its simplest level of sophistication [23]. Finally, the system is solved iteratively. The main drawback of this method is that it uses intensity comparison, so the equations are in fact quadratic in displacements, not linear. The same authors have reported an extension to this method [163], consisting in:

1. Use of the Tensor LEED approach in the second level of sophistication.
2. Compare Pendry's Y-functions rather than intensities. This has the advantage of eliminating errors arising from direct intensity comparison, such as temperature effects or electron damping.

Recent investigations on global methods deal mainly with simulated annealing (SA) and other methods based on the construction of a Markov chain to explore the parameter space (GA and RSA). The common feature of these methods is that trial structures are proposed at random and accepted according to a certain probability distribution.

Simulated annealing

Simulated annealing (SA) was proposed by Kirkpatrick *et al* [151] for NP-complete problem study, in analogy with the description that Statistical Mechanics makes of the behaviour of a physical system undergoing an adiabatical cooling down. This is the case of, for example, liquid freezing or recrystallization in a metal by annealing. If the temperature is slowly decreased, the system will access the ground state at zero temperature. If the cooling is not slow enough, i.e. if the system does not reach thermal equilibrium at every temperature, the final state can be metastable, as it would be the case of quenching in a crystal. In such a scenario, (i) the possible microscopic configurations play the role of the parameter space points, (ii) the energy,

E , would be the scalar function to be minimized, and (iii) the temperature, T , acts as a control parameter. Metastable states are local minima of the energy. Each visited configuration is described by N parameters $\vec{x} = (x_1, \dots, x_N)$ and the goal of SA is to find the \vec{x} vector that describes the ground state. Fig. 6.1 shows a flow diagram for the entire algorithm. In each step, each component x_i is given a small random displacement δx_i which produces a change ΔE in the energy. Following the Metropolis criterion, this move will be accepted with this probability:

$$P_{\text{accept}} = \begin{cases} 1 & \text{if } \Delta E < 0 \\ e^{-\Delta E/k_B T} & \text{if } \Delta E > 0 \end{cases} \quad (6.5)$$

This will ensure that thermal fluctuation can occasionally take the system out of a local well, making the algorithm global. The set of the configurations visited by the system during the cooling process is a so-called *Markov chain*.

Rous has thoroughly investigated the application of SA to LEED structure determination on the Ir(110)-p(2×1) surface [157]. Particularly, he has found that the proper starting temperature and the cooling scheme can be derived from the mean and standard deviation of the random fluctuations in the R_P hypersurface. As stated above, these are generic features for every surface, and thus the best temperature schedule election can be transported to other systems. Tuning the temperature, the best reported scaling law for SA is $t \propto N^6$.

Nascimento *et al* [164] have checked the fast SA implementation in LEED, which improves standard SA in the following way:

- New trial structures are generated according to a Cauchy-Lorentz shaped probability distribution:

$$P(\delta x_i; T) = \frac{T}{T^2 + (\delta x_i)^2} \quad (6.6)$$

As a consequence, the chance of jumping from one local well to another is higher, since the “tail” of this distribution is greater than that of the widely used gaussian.

- A fast cooling scheme is used. It consists in a reduction of T in every \vec{x} update event, rejected or not. Therefore, the visited points in the Markov chain do not correspond to equilibrium states in the Statistical Mechanics image, so that this method would not guarantee a non metastable final state.

These authors apply fast SA to the CdTe(100) surface optimization, and report a linear scaling law, $t \propto N$. In a more recent work, they have shown that slightly faster searches can be achieved by using other visiting probability distributions [165], but with a considerable reduction of minimum finding. However, we do not expect these results to be transferable to other cases. From a theoretical point of view, a linear scaling can only be achieved, in general, for a linear function. The next fastest method would be steepest descent at a single attraction basin of the R-factor hypersurface, which scales as $t \propto N^2$. Globalizing that search would make the scaling even slower.

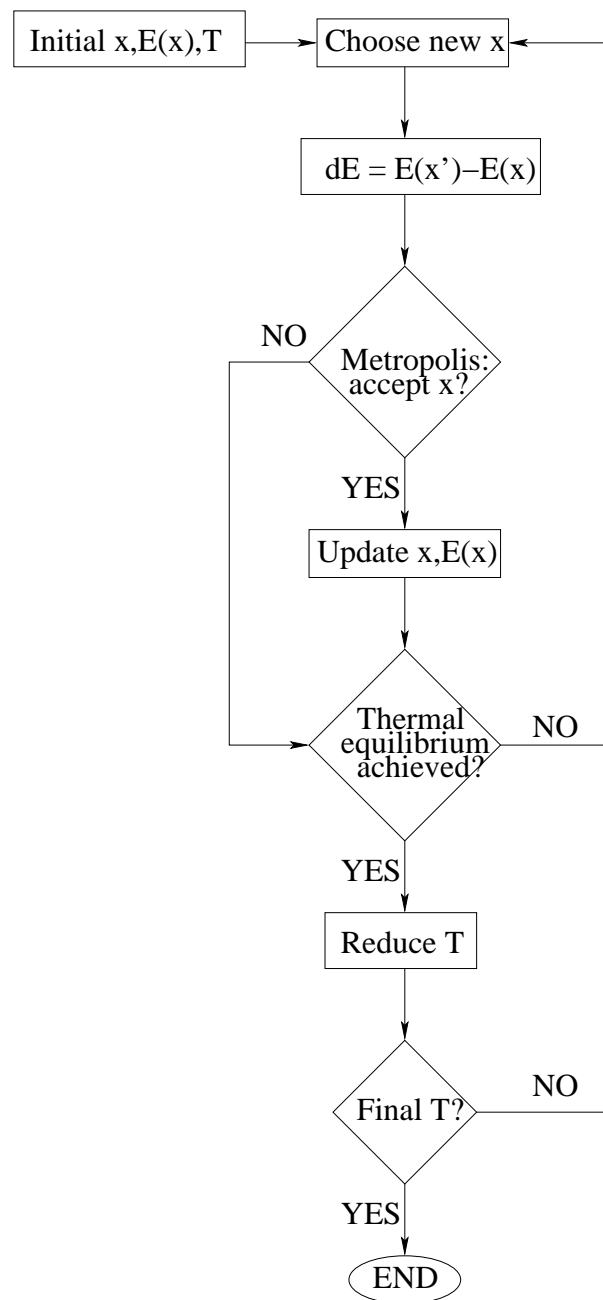


Figure 6.1: Flow diagram for simulated annealing algorithm

Random sampling algorithm

Kottcke and Heinz have implemented the so-called random sampling algorithm (RSA) [118]. It differs from conventional SA in the Metropolis criterion, since RSA rejects every non-descendant move. Apparently, this would increase the risk of being trapped in a local minimum. To ensure a non-zero scape probability, the next move is selected with a gaussian probability of a width related to the current R_P and available parameters. Thus, this algorithm performs a global search at high R_P values and becomes progressively “less global” as R_P decreases, i.e. the size of the sampled region in the parameters space becomes progressively smaller as R_P decreases.

Furthermore, this process is combined with a multiple launch strategy, that makes it possible to detect multiple local minima, and Tensor LEED approach for spectra evaluation. The whole procedure is embedded in TensErLEED package [70]. The overall scaling law is $N^{2.5}$.

Genetic algorithms

Döll and Van Hove have been the first authors to introduce genetic algorithms (GA) in LEED [166]. Genetic algorithms mimic the natural selection rules in living organisms. Each value of the unknown structural parameters is codified into a bit string, that will play the role of a chromosome. A community of a certain population of chromosomes is allowed to evolve according to life evolution laws. The goal of the evolution procedure is to get chromosomes that produce a R-factor as low as possible. In each step of the search procedure, a new generation of chromosomes is created from genetic information exchange between parent chromosomes. Children chromosomes inherit chromosome portions from their parents. Mutations, as aleatory bit changes, are allowed. No scaling law has been reported for LEED with GA.

6.4 The simultaneous optimization strategy

In this work we introduce a new method that achieves both a considerable reduction in the number of visited structures and in the number of intensity evaluations. The algorithm is made of two shells: in the inner one, good candidate structures are quickly determined by solving a simplified set of non-linear equations and/or back and forward tracking promising directions. In the external shell the ergodic principle is used to make sure that the solution is not trapped on local minima. Its success rate to locate the global solution for the examples considered here has been found close to 100%. The inner shell takes advantage from the fact that the experimental database provides a number of independent intensities, N_D , much larger than the number of parameters to be determined, N . Therefore, the formal equation $\mathcal{S} = f(\mathcal{X})$ forms an overdetermined nonlinear system of N_D equations and N unknowns. From this point of view, the standard way of minimizing a given R-factor (e.g., Pendry R_P) becomes a particular mapping of the N_D zeroed individual equations of the system into a single scalar master function. Alternatively, we can construct independent determined systems by choosing subsets $\mathcal{S}' \in \mathcal{S}$ among the $\binom{N_D}{N}$ total number of

available subsets. The actual solution must be invariant w.r.t. the subspace selected. Therefore, the algorithm visits partial solutions until an stationary minimum is found. This simultaneous optimization (SO) algorithm [167] will be described in detail in the following subsections.

SO strategy gathers some of the advantages of the methods implemented so far and presented above:

- It is global, since a change in the subset \mathcal{S}' can eventually bring the solution to a different well of the R-factor.
- Computation effort is reduced in a twofold scheme: the number of trial structures is smaller because of the use of an efficient sampling. Only a few points of the IV curves are required for each partial system study.
- It can be easily embedded in a LEED optimization package.

The method we introduce here follows the standard procedure in LEED, that is, to find a minimum in a reliability factor that measures the agreement between experimental and calculated IV curves. We use Pendry's R-factor R_P , which has the advantage of being sensitive to peak positions, more than to absolute intensities, by means of the Y-function.

6.4.1 The partial problem

The database subspace $\mathcal{S}' = \{d_1, \dots, d_N\}$ is chosen at random, and each of its elements yields one equation in the nonlinear system,

$$\vec{f}(\vec{x}, \mathcal{S}') = (f_1(\vec{x}, d_1), \dots, f_N(\vec{x}, d_N)) = 0 \quad (6.7)$$

To deal with the problem of solving the nonlinear system we will use Broyden method [168, 44]. It is a globally convergent method that combines a Newton-like method with a descent strategy that ensures some progress towards the solution at each iteration. Smoothness is an important feature, since this method needs \vec{f} to be continuous and differentiable w.r.t. \vec{x} . Fig. 6.2 shows a flow diagram of the algorithm described in detail below.

The i -th Newton step $\vec{x}^{(i)}$ is

$$\tilde{J}^{(i)} \cdot \delta \vec{x}^{(i)} = -\vec{f}^{(i)} \quad (6.8)$$

where $\tilde{J}^{(i)}$ is the jacobian matrix of $\vec{f}^{(i)}$ at $\vec{x}^{(i)}$,

$$J_{jk}^{(i)} = \frac{\partial f_j^{(i)}}{\partial x_k^{(i)}} \quad (6.9)$$

and $\delta \vec{x}^{(i)} = \vec{x}^{(i+1)} - \vec{x}^{(i)}$. The secant condition is that $\tilde{J}^{(i+1)}$ satisfy:

$$\tilde{J}^{(i+1)} \cdot \delta \vec{x}^{(i)} = \delta \vec{f}^{(i)} \quad (6.10)$$

where $\delta \vec{f}^{(i)} = \vec{f}^{(i+1)} - \vec{f}^{(i)}$.

Up to here, we have described a conventional multidimensional secant method. In order to save derivative evaluations, we use Broyden's approximate jacobian matrix [168], \tilde{B} : $\tilde{B}^{(i+1)}$ is chosen so that the change in $\vec{f}^{(i)}$ predicted by $\tilde{B}^{(i+1)}$ in a direction orthogonal to $\delta\vec{x}^{(i)}$ is the same as it would be if predicted by $\tilde{B}^{(i)}$. It can be demonstrated that such a jacobian must be:

$$\tilde{B}^{(i+1)} = \tilde{B}^{(i)} + \frac{(\delta\vec{f}^{(i)} - \tilde{B}^{(i)} \cdot \delta\vec{x}^{(i)}) \otimes \delta\vec{x}^{(i)}}{\delta\vec{f}^{(i)} \cdot \delta\vec{f}^{(i)}} \quad (6.11)$$

Finally,

$$\delta\vec{x}^{(i)} = - \left[\tilde{B}^{(i)} \right]^{-1} \cdot \vec{f}^{(i)} \quad (6.12)$$

is determined by QR decomposition. We need an starting point and an initial jacobian, namely the exact one.

However, Newton's method tends to wander around the parameter space if the starting point is not close enough to the solution. This can be avoided by embedding the Newton step in a globally convergent strategy that tries to minimize the scalar function

$$F = \frac{1}{2} \vec{f} \cdot \vec{f} \quad (6.13)$$

Every solution to (6.7) minimizes (6.13), but there might be local minima at the surface (6.13) that are not solutions to (6.7). A good choice is that every step $\delta\vec{x}^{(i)}$ decreases F . If we use the exact jacobian \tilde{J} , $\delta\vec{x}^{(i)}$ yields already a descent direction for F , but the whole step may not make F smaller. For this reason, we perform a line search along this vector,

$$\vec{x}^{(i+1)} = \vec{x}^{(i)} + \lambda \delta\vec{x}^{(i)} \quad (6.14)$$

for five values $\lambda = 1, 0.8, \dots, 0.2$, taking the λ that gives the smallest value of F . More sophisticated line searches could be made at this stage [44], but this five point line sampling is found to be enough for our purposes. This method is non-local, because, even if the line search takes place along a descent direction of F , a longer step can overcome a hypersurface barrier.

We must remember that we are trying to locate the geometrical parameters \vec{x} inside a well defined interval. It may happen that the step $\delta\vec{x}^{(i)}$ drives the solution out of the interval for several reasons, such as:

- The search is taking place at a region where the function F has decreasing values when \vec{x} moves towards the limits of the interval.
- The point $\vec{x}^{(i)}$ lays on a local maxima of F , with zero slope, so that the step (6.12) causes an infinite move.

For these reasons, the longest $\delta\vec{x}^{(i)}$ allowed ends at the wall of the search interval. If consecutive iterations try to push \vec{x} out of the limits, the partial problem ends up and the obtained \vec{x} is dismissed.

We must have into account also that, since \tilde{B} is just an approximate jacobian, it may not produce a true descent direction. In this case, we must rectify this step and reinitialize the algorithm with the true jacobian, \tilde{J} , at the current point.

Further unsuccessful steps can arise when the sampling of the points in the line (6.14) is too coarse to find a suitable descent move in F . In this case, in addition to Broyden's jacobian and the exact jacobian, a direction $\delta\vec{x}^{(i)}$ given by the exact numerical gradient, ∇F , can be tested.

At the end of each iteration, the exiting criterion is checked. We use convergence in the modulus of \vec{x} as exiting condition in this way:

$$|\vec{x}^{(i+1)} - \vec{x}^{(i)}| < x_{\min} \quad (6.15)$$

6.4.2 The global problem

We have already seen that the minimization of F is a complex problem itself, so the Broyden method described in Section 6.4.1 can fail to find a global solution for the system. Even if it gave the global solution for the system, it may happen that this solution did not correspond to the global minimum in the R-factor. Thus, solutions \vec{x}_B provided by Broyden need to be validated against the whole database.

Because computing the global R-factor is time consuming, it is convenient to check that \vec{x}_B remains a solution for a different subspace \mathcal{S}'' before attempting to compute R_P itself. Thus, another set of N energies is chosen at random from \mathcal{S} , and the corresponding system is solved with a starting point at the final point of the previous iteration. This procedure is repeated $N_{PC} \approx N$ times and then the final resulting solution $\vec{x}^{(i)}$ is validated by calculation of its R_P . In this way, many R_P calculations are saved. The whole procedure is described at the diagram in Fig. 6.3.

The next step consists of choosing a new structure $\vec{x}^{(i+1)}$ at random, which would correspond to the Metropolis step in SA. The difference is that here the random move is always accepted. Following the RSA idea [118], $\vec{x}^{(i+1)}$ is selected with a gaussian probability function centered in $\vec{x}^{(i)}$, of a width σ depending on the current R_P . These gaussian deviates are generated by means of the Box-Muller algorithm [44].

In this way, uphill moves are guaranteed and the search space size is quickly reduced at small values of R_P . We remark that whenever the algorithm is driven into the global minimum attraction basin, convergence should be fast, since that region is a solution for every subsystem. If R_P is low but not close to the global minimum, different \mathcal{S}'' choices will probably drive the solution away from that point, ensuring jumps out of deep wells. That can occur if the corresponding system has several equations and the algorithm finds a spurious one. However, it may happen that the new \mathcal{S}'' spoils a promising \vec{x} solution, making the search wander away from a deep R_P region, because it fails to solve the system. This kind of situation is likely to occur when noise is present in the measured data, so that some choices of partial problems have a solution slightly different from the global one. Actually, this will happen when managing real experimental data, where the minimum R-factor does not tend to a zero value.

Finally, the global procedure ends up when a structure with an R-factor smaller than a given threshold, $R_P < R_{P\min}$, is found.

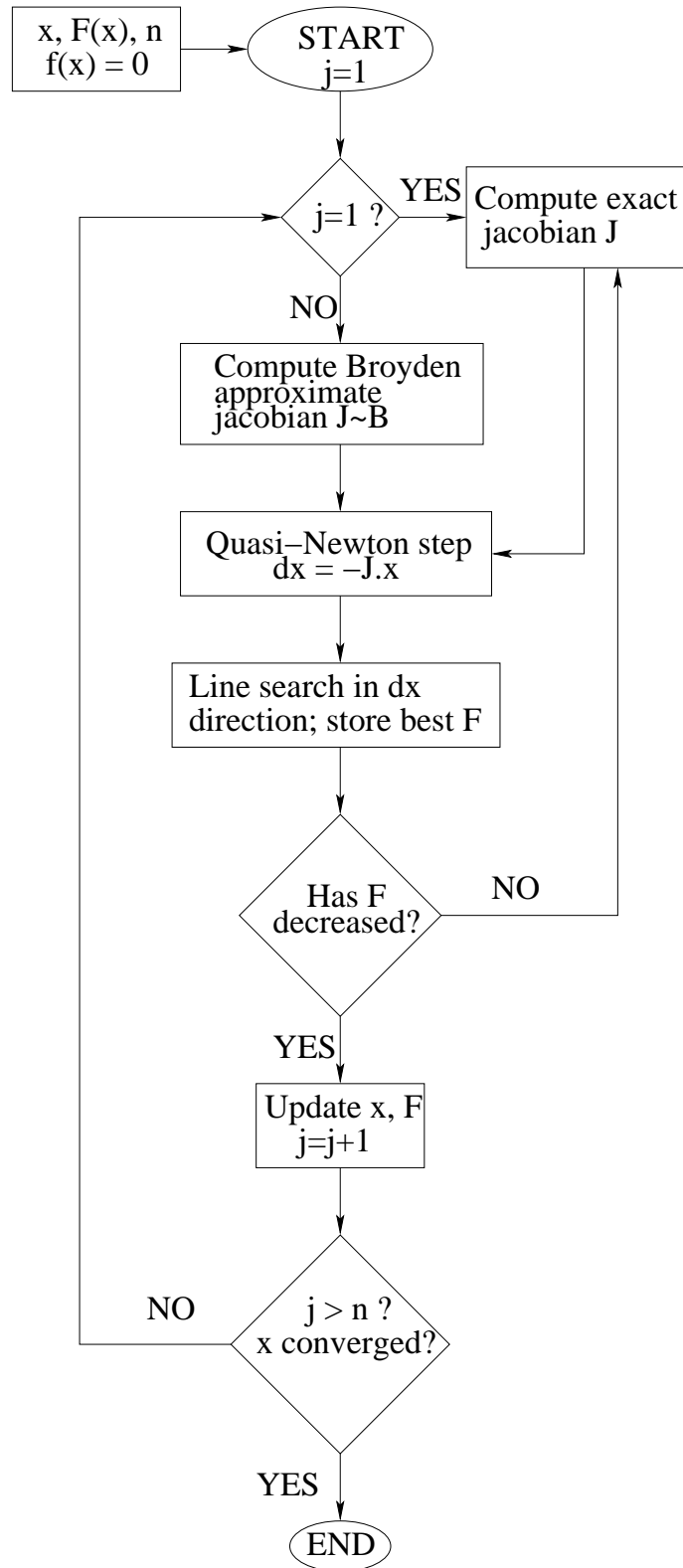


Figure 6.2: Flow diagram for partial problem in simultaneous optimization algorithm. Starting point is \vec{x} . The iterative process continues until convergence is found or a maximum number n of iterations is reached.

Scaling law estimate

The scaling law of Broyden's system solver should be, by construction, $\mathcal{O}(N^3)$. This law is due to the $\mathcal{O}(N^2)$ scaling of the quasi-Newton step and the $\mathcal{O}(N)$ line search part. As we are evaluating R_P every $N_{PC} \sim N$ partial problem calls, the total scaling exponent for the inner shell of the algorithm should be $\beta \sim 4$. On the other hand, we can expect the outer shell to have a maximum scaling similar to RSA algorithm, which has an exponent $\beta = 2.5$. Thus, this analysis allows us to establish a maximum value of the scale exponent for SO $\beta \lesssim 6.5$ (with noiseless data).

However, we will see in the results sections that SO yields a much better exponent $\beta \sim 4$, since

- the partial part of the algorithm provides promising structures, diminishing the number of R-factor evaluations.
- At late stages of the search, the starting point is always close to the solution.

6.5 Electronic parameter retrieval: single atom scattering

In order to evaluate the behaviour and optimum conditions for applicability of the algorithm shown above, we have used it in the simple problem of the scattering of a plane wave by an atom [154, 153]. The formalism used to describe the scattering process expands the incident plane wave in a superposition of partial waves. The scatterer introduces a phase shift in each partial wave. For a given incident electron momentum κ , the scattered amplitude in the far field as a function of the polar angle θ is given by Eq. (6.2). A hypothetical experiment would provide the intensities only, i.e. the squared modulus of the diffracted amplitudes. Thus, our approach to find the unique set $\vec{x} = \{\delta_l(\kappa)\}$ is to find the global minimum of the R-factor Eq. (6.3). This R-factor uses equal intensity conditions for simplicity. It ensures the overall agreement between experimental and calculated intensities. To establish a model closer to a surface diffraction experiment, the experimental database should be further reduced by considering only a forward or backscattering hemisphere.

This function measures the overall agreement between experimental and calculated intensities. Each partial problem is constructed from the same intensity condition at N scattering angles $\{\theta_i\}$,

$$\begin{aligned} f_1(\vec{x}, \theta_1) &= I_{\text{th}}(\vec{x}, \theta_1; \kappa) - I_{\text{exp}}(\theta_1; \kappa) = 0 \\ &\dots \\ f_N(\vec{x}, \theta_N) &= I_{\text{th}}(\vec{x}, \theta_N; \kappa) - I_{\text{exp}}(\theta_N; \kappa) = 0 \end{aligned} \quad (6.16)$$

Within this framework, we have analyzed the influence that some parameters may have in the search procedure, such as the amount of experimental data and the degree of accuracy. In order to avoid phase redundancies, we restrict the search space to the interval $[0 : \pi/2]$. Besides, instead of not letting the solution to cross

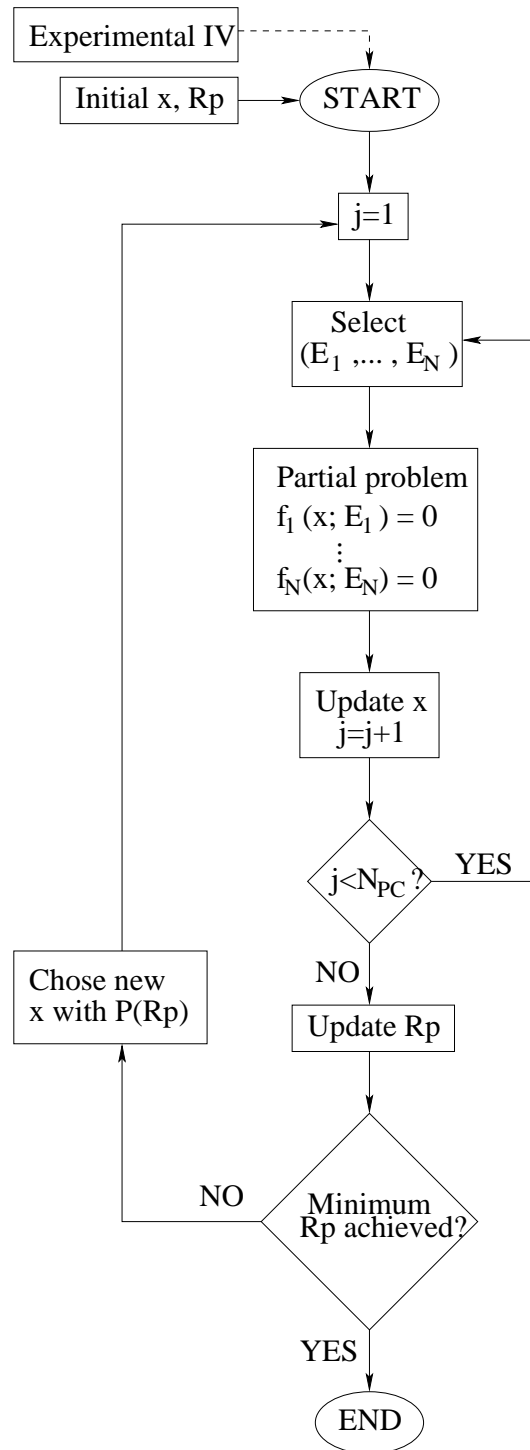


Figure 6.3: Flow diagram for the complete simultaneous optimization algorithm.

the interval borders, we remap the phase shifts onto the restricted search space. The search achieves convergence when the distance to the solution is smaller than 0.03. Other parameters for the global part are $N_{PC} = 2N$ calls to the partial problem before evaluating global R (provided by Eq. (6.3)) and a width $\sigma = \pi R/4$ for choosing new points at the global problem.

6.5.1 Results for phase shifts retrieval

First, we investigate the phase shifts retrieval problem over $N_{\text{stat}} = 500$ simulated random experiments where noise-free backscattered intensities are available over a database of $N_\theta = 250$ angles. Exiting condition for the searches is $x_{\min} = 0.03$.

We shall examine the statistical behaviour of the computation effort taking the quantity $t = N_{\text{call}}/N_\theta$, where N_{call} is the number of single-angle intensity evaluations for different N values (Eq. (6.2)). The probability distribution function (PDF) effort displays a sharp peak at low t values and is exponentially decreasing. Fig. 6.4 shows the normalized histogram for the particular case $N = 6$ as an example. The PDF is fitted reasonably well by a 1-event Poisson-like form (see Appendix C for derivation of this PDF):

$$p_1(t) = w^2 t e^{-wt} \quad (6.17)$$

This “event” corresponds to finding one global solution during the search. By integrating the PDF up to a certain t value, we obtain the global probability success rate of the algorithm:

$$P_1(t) = \int_0^t p_1(t') dt' = 1 - (1 + wt) e^{-wt} \quad (6.18)$$

Fig. 6.5 represents several average values of t as a function of N . The length of the search was such that success was 100% within the accuracy of the analysis. The simple statistical average $\langle t \rangle$ over the 500 model searches displays a polynomial scaling law for $N \geq 5$, $\langle t \rangle \propto N^\beta$ with $(\beta = 3.5 \pm 0.2)$. The slower scaling showing at low N values is related to the absence of many minima for small N , and the good performance of the system solver on that region. For a general case, the optimum scaling law expected comes from the partial solver, and should be proportional to N^3 at best. More advantageous scaling laws must arise from *particular* conditions alone (e.g., starting the random search inside the basin of attraction would result on a N^2 law, while searching on a linear region could even render a scaling proportional to N).

Fig. 6.5 contains two more averages of the computing effort, calculated in alternative ways:

- The expectation value $\langle t \rangle_E = \int_0^\infty t p_1(t) dt = 2/w$, where w is obtained from histogram fitting to Eq. (6.17).
- The effort needed to achieve a confidence rate of 99%, $\langle t \rangle_{0.99}$, which is obtained by making Eq. (6.18) equal to 0.99, substituting the w value obtained from histogram fitting and solving the resulting equation in t .

It is observed that these two quantities and the statistical average, $\langle t \rangle$, hold the same scaling law with $\beta \sim 3.5$.

For such a simple problem, it is instructive to compare with other methods. We have used standard routines [44] to test performance against a number of methods like SA, simplex, conjugated gradients, quasi-Newton, etc. In addition, different SA flavours have been tried (e.g., standard Metropolis and fast SA). All these methods have performed at least two order of magnitude worse in number of evaluations, but the most interesting feature observed has been the ability of SO to stay close to a 100% success rate, while all the other methods show a notoriously much faster deterioration with increasing N .

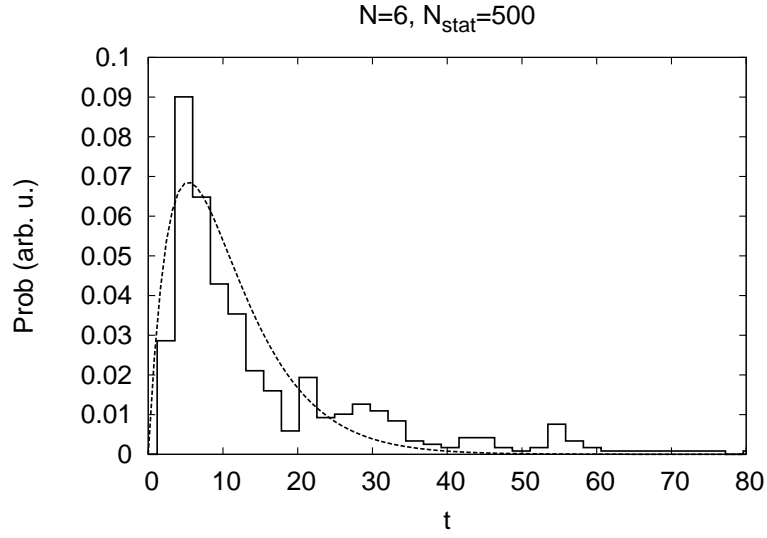


Figure 6.4: Histogram for the 500 search runs using SO for $N = 6$ phase shifts retrieval problem. The least-squares fit to a 1-event Poisson law, $P(t) = w^2 t e^{-wt}$, yielding $w = 0.186 \pm 0.006$ and a expected value $\langle t \rangle \pm \sigma = 11 \pm 7$.

6.5.2 Data-base size effect

The database size, N_θ , do not seem to be a determinant parameter for the search statistics, as long as $N_\theta \gg N$. Fig. 6.6 shows the effect of increasing or decreasing N_θ for a search of $N = 6$, keeping the other search parameters fixed at the same values as in previous searches. Apparently, the number of explored points, t seems smaller for bigger data sizes. However, this effect is just due to our definition $t = N_{\text{call}}/N_\theta$. N_θ must be such that the number of available systems of equations, $\binom{N_\theta}{N}$, is much larger than the number of inner loops invoked during the search. In Fig. 6.6, $\binom{N_\theta}{N}$ is $\sim 10^9$ for $N_\theta = 100$, 10^{11} for 250 and 10^{13} for 500, in all cases far beyond the inner loop requirements.

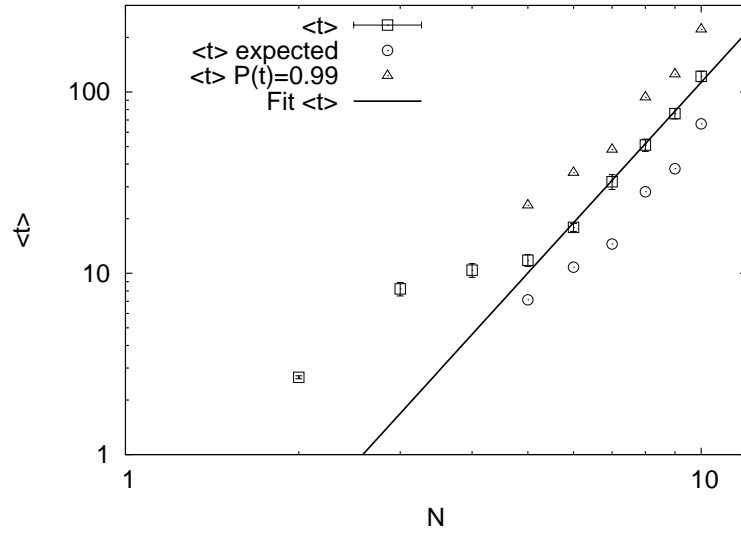


Figure 6.5: Log-log plot of some average computing efforts for phase shift retrieval vs. the number of parameters to be determined, N : squares are statistical averages $\langle t \rangle$ computed directly from search results, circles are the expectation values $\langle t \rangle_E = 2/w$ and triangles represent the average effort needed to achieve 99% of success rate, $\langle t \rangle_{0.99}$. A linear fit for $\langle t \rangle$ with $N \geq 5$ shows a scaling law $\propto N^\beta$ ($\beta = 3.5 \pm 0.2$).

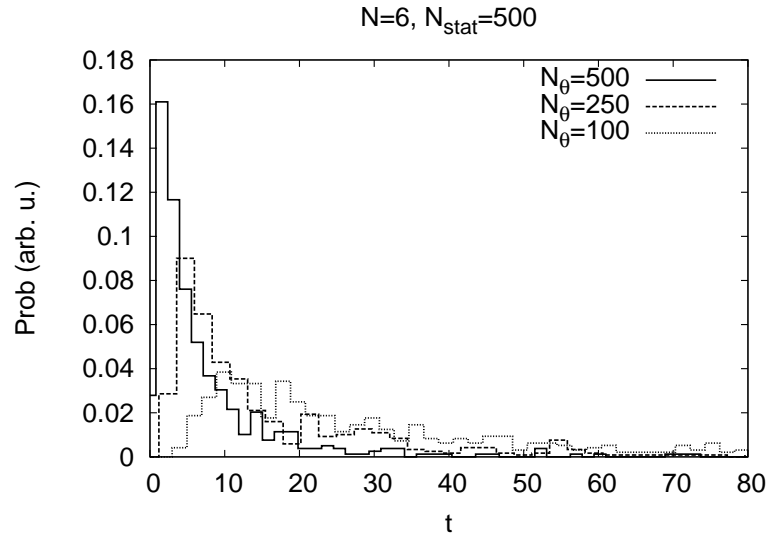


Figure 6.6: Histograms for the 500 search runs using SO for $N = 6$ phase shifts retrieval problem with different data-base sizes, N_θ . Solid line corresponds to $N_\theta = 500$, dashed line to $N_\theta = 250$ and dotted line to $N_\theta = 100$.

6.5.3 Noise effect

We have examined the effect of blurring the simulated diffracted spectrum with random noise, $\tilde{I}(\theta; \kappa) = (1 + nr)I(\theta; \kappa)$, where r is a uniform random deviate taking values in the $[-0.5 : 0.5]$ interval and n is the noise rate.

The SO fails to achieve the solution in many cases for noisy data. We have tried two different ways of tackling this problem, the second one being the one that works:

1. Making the database bigger: this does not work, since the noise is homogeneously distributed among the data-base. As we have seen in the examples above, the SO search procedure success rate is mainly dominated by the partial problem part, which is independent of N_θ . When noise is present, the success probability is highly dependent in the slow ergodic global part of the algorithm. Therefore, this method is not efficient.
2. Using a bigger subset of data in the partial problem step: Eq. (6.16) becomes an overdetermined system. The partial scalar function F is thus constructed from a larger number of intensity conditions and the noise effect on the partial map is diminished, and the effect of the solution oscillating around the true value is damped.

N_{ov} will be the oversampling factor, such that the partial problem is made of $N \times N_{ov}$ equations and N unknowns. In this framework, QR decomposition is no longer a valid method to solve the system of equations. Instead, we use a least-squares method, which provides the most likely solution for the system in the least-squares sense.

To illustrate the applicability of the second proposal, we have repeated the 500 statistical searches for $N = 6$ under the same convergence conditions shown in the previous subsection, i.e. $N_\theta = 250$ and $x_{\min} = 0.03$, with a noise ratio $n = 0.05$ (5%) and oversampling factors $N_{ov} = 1, 2, 4$. Fig. 6.7 gathers the corresponding PDFs. The sharp peak feature is lost if conventional $N_{ov} = 1$ method is used, whereas the Poisson-like exponential decay is recovered for bigger N_{ov} values. However, efficiency is much slower than in the noiseless case.

In Fig. 6.8 the scaling laws for searches with noisy data are summarized. With noise rate of 5% and 10%, N_{ov} has been selected to ensure a success rate above 90%. We find that $N_{ov} = 2$ for $N < 6$ and $N_{ov} = 4$ for $N \geq 6$ is enough. The scale exponent suffers only a slight increase w.r.t the noiseless exponent, by a factor ≈ 1.3 , the main difference being the prefactor of the scaling law, that increases by a factor $\approx 8 - 10$.

6.6 Structure determination from LEED simulated data: the Ir(110)-p(2×1) surface

To test the performance of SO in LEED, we have studied the behaviour of the proposed simultaneous optimization method in the Ir(110)-p(2×1) surface. The 1×1 surface is rectangular, with largest lattice parameter $a_0 = 3.84 \text{ \AA}$. This structure has been studied by Van Hove's group. A detailed quantitative analysis of the

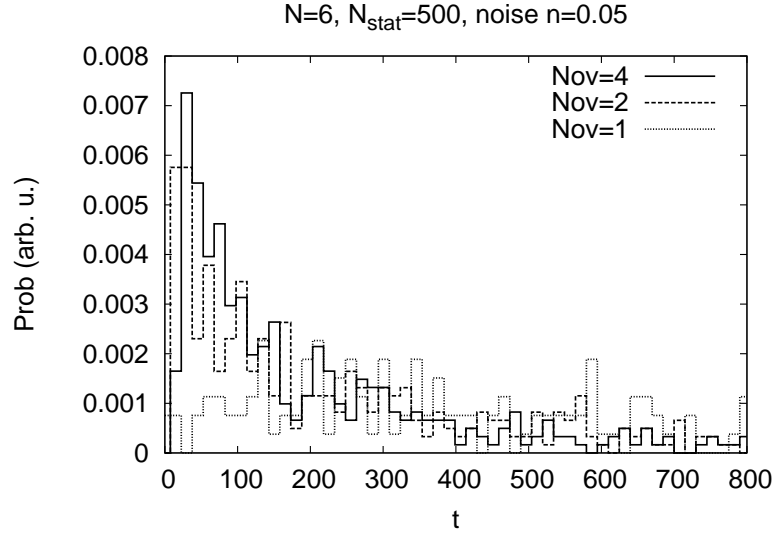


Figure 6.7: Histograms for the 500 search runs using SO for $N = 6$ phase shifts retrieval problem with a noise ratio $n = 0.05$. Dotted line ($N_{ov} = 1$) corresponds to conventional system construction of $N = 6$ equations, dashed line to systems of $N \times N_{ov} = 12$ equations and solid line to systems of 24 equations.

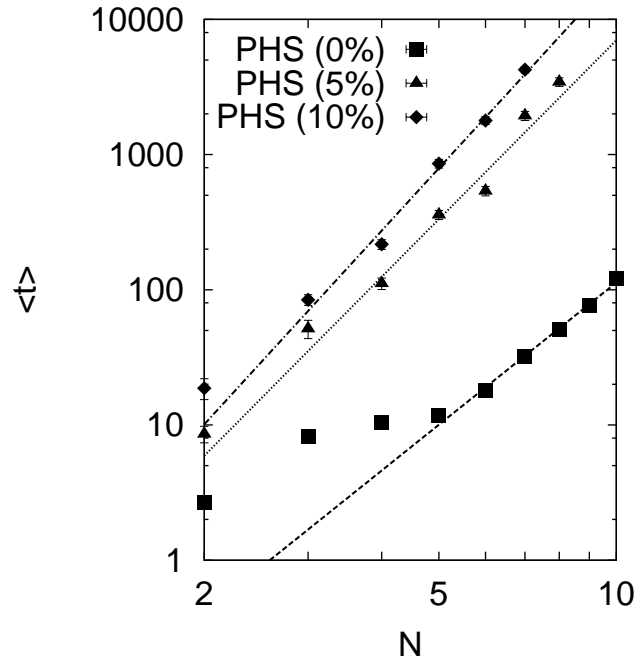


Figure 6.8: Scale law for phase shifts retrieval problem with several noise ratios: square corresponds to noiseless calculation, triangles to 5% gaussian noise at the theoretical experiment intensities and diamonds to 10% noise. See text for oversampling factors details for these calculations.

experimental IV curves yields the best R_P for the missing row model [1], which is depicted in Fig. 6.9. Optimum structure has $R_P = 0.24$ and the first interlayer spacing is contracted to 1.16 \AA from its bulk value, $d_b = 1.36 \text{ \AA}$.

We use this surface in the test because it has been previously used in the literature as a benchmark for other algorithms [157, 166, 118]. Therefore, a direct comparison is possible.

We have performed statistical averages over several “simulated” experiments with target geometries chosen at random, at normal incidence and zero temperature. Optimization has been carried out for geometrical parameters only. These parameters are the topmost interlayer spacings, shown on Fig. 6.9, taking values in an interval 1 \AA^N .

We must point out that some of these simulated geometries may be unphysical (e.g. implying strong deviations from the bulk structure at deep layers). However, the unphysical geometries do not interfere with the optimization problem and we do this to generate enough statistic cases for the scaling law.

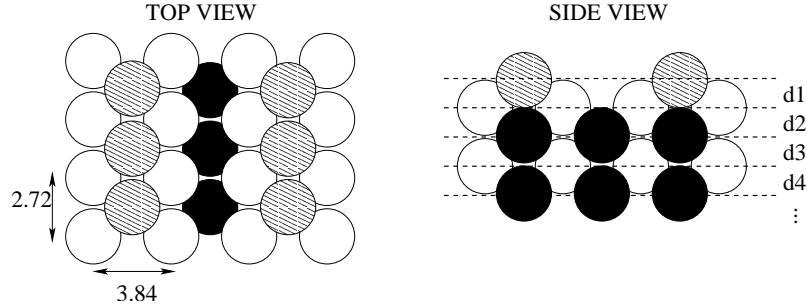


Figure 6.9: Hard sphere model for missing row Ir(110)-p(2 \times 1) reconstruction. Distances are in \AA . The side view shows the geometrical parameters that will be included in the search. The bulk interlayer distance is $d_b = 1.36 \text{ \AA}$.

The search space consists of a 1 \AA^N hypercube, taking values between 1 and 2 \AA . The simulated experimental data-base contains the following beams: (10), (01), (11), $(\frac{1}{2}0)$, $(\frac{3}{2}0)$ and $(\frac{1}{2}1)$. in the energy range $54.4 - 160.5 \text{ eV}$ ($N_e = 50$ points per IV curve). Experimental data is assumed to be noise-free, though it would be interesting to see how noise affects the global search. The imaginary part of the inner potential is set to $V_{0i} = 4 \text{ eV}$. For this preliminary statistical study, the real part V_{0r} is set to zero. Considering a shift in V_{0r} as another parameter in the search is delicate in this algorithm. This subject will be discussed on section 6.6.4.

Having in mind that our goal is to find the global minimum in R_P , our first step will be to reduce the amount of experimental data by selecting those energies that produce maxima, minima and shoulders in any of the experimental IV curves, because these highlight the coincidences between peak positions more than similarities in intensity values. This is arbitrary, but a well defined procedure. With such a database, denoted by $\hat{\mathcal{S}}$, we ensure a good description of the problem. Following this criterion, we will use the following vectorial function $\vec{f} = (f_1, \dots, f_N)$ for our

systems:

$$\begin{aligned}
 f_1(E_1; \vec{x}) &= \sum_g |Y_g^{\text{th}}(E_1; \vec{x}) - Y_g^{\text{exp}}(E_1; \vec{x})| = 0 \\
 &\dots \\
 f_N(E_N; \vec{x}) &= \sum_g |Y_g^{\text{th}}(E_N; \vec{x}) - Y_g^{\text{exp}}(E_N; \vec{x})| = 0
 \end{aligned} \tag{6.19}$$

where $\vec{x} = (x_1, \dots, x_N)$ are the N unknown structural parameters, (E_1, \dots, E_N) is a set of N different energies taken from $\tilde{\mathcal{S}}$ at random, that we will denote \mathcal{S}' , and the index g runs over the available beams. The reason for the sum over beams is to gather as much information as possible (from the practical point of view, no extra computing information is needed). Additionally, we get a smoother function than the one corresponding to the g value associated to the extreme in the curve.

$N_{PC} = 2N$ partial problem calls are made before using the whole data base to compute the global R_P . Random updates in the structure are drawn from a probability distribution of width $\sigma = R_P^2$, and $R_P < 0.1$ is used as threshold to end the search. With these criteria, all the found structures are closer than 0.02 Å to the real one in any geometrical parameter. All IV calculations have been computed with our full-dynamical code LEED90 [54].

6.6.1 Topography of the $N = 2$ case

For $N = 2$, we have examined the surfaces of both R_P and some partial functions F in order to illustrate some features of the simultaneous optimization algorithm. In the model structure Ir(110)-p(2×1), the two topmost interlayer distances for this example have been set to $d_1 = 0.48 a_0$ and $d_2 = 0.33 a_0$ respectively, where $a_0 = 3.84$ Å is the lattice parameter. This surface has a $\tilde{\mathcal{S}}$ set formed by 73 energies giving maxima and minima in the six selected beam spectra. Fig. 6.10 shows the R_P in this case, which has a deep minimum for the correct structure and several secondary minima with high R_P values. The same Figure shows the F function surface for three sets $\mathcal{S}'' \in \tilde{\mathcal{S}}$ of energies. The absolute minimum in all of them coincides with that of R_P . However, in one case a secondary minima with low R_P is observed, which means that this system has a “ghost” solution. Depending on the selected energies, partial functions strongly differ. This justifies our previous assumption that a change in \mathcal{S}'' will allow us to explore a large region of the parameter space.

On Fig. 6.11, three search paths for three different starting points are shown upon the R_P surface, where it is clearly seen that the procedure can easily overcome barriers.

6.6.2 Statistical interpretation

To study the scaling law of SO algorithm as a function of N , we have performed a number N_{stat} of independent model searches with $N = 2, 3, 4, 5$, namely, $N_{\text{stat}} = 200$ for $N = 2, 3$; $N_{\text{stat}} = 100$ for $N = 4$ and $N_{\text{stat}} = 30$ for $N = 5$. The different numbers for N_{stat} are imposed by computing power limitations. We must point out that all these searches arrive at the right solution.

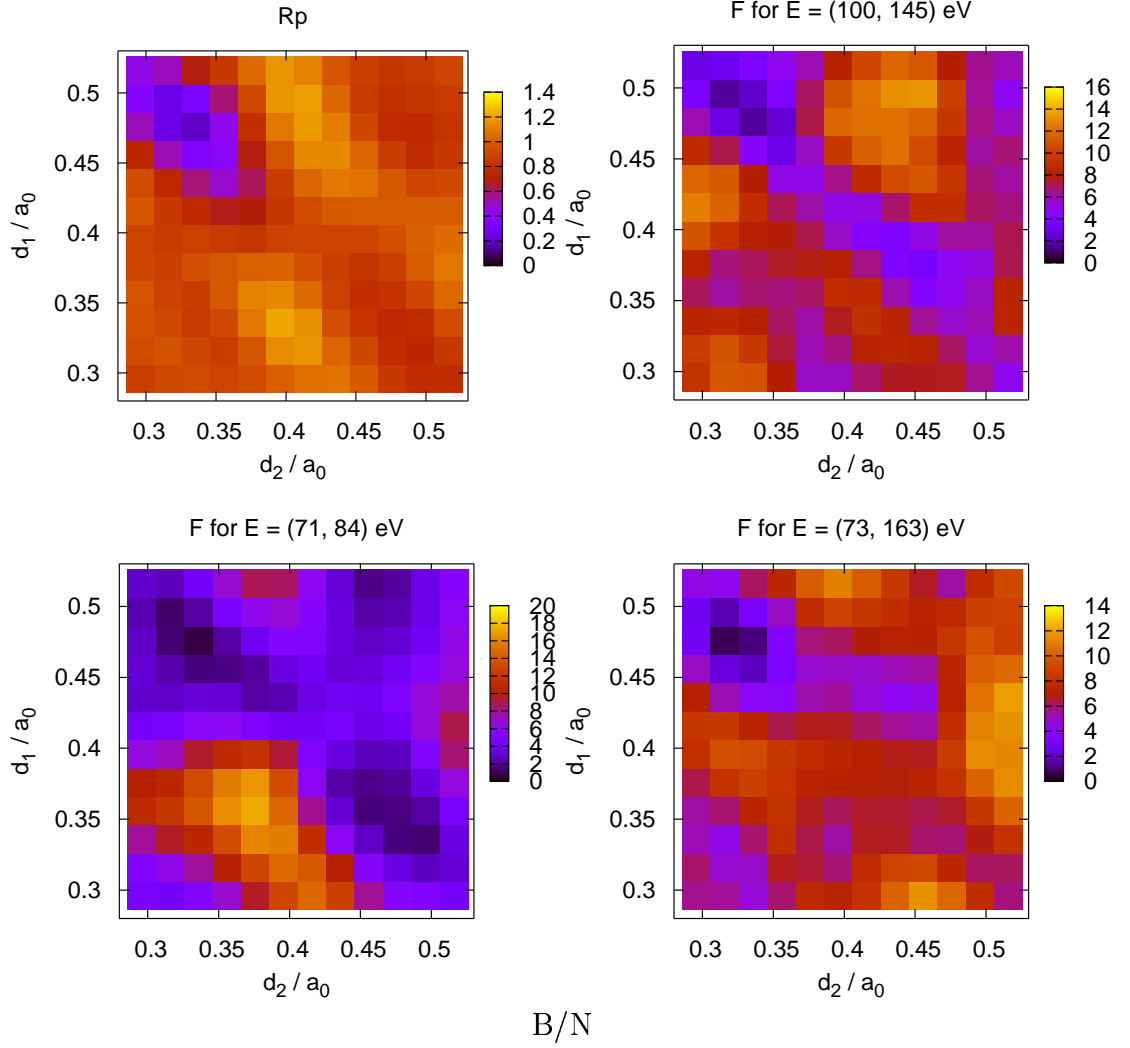


Figure 6.10: The top left panel shows the R_P map plotted for a simulated experiment with parameters $d_1 = 0.48 a_0$ and $d_2 = 0.33 a_0$ ($a_0 = 3.84 \text{ \AA}$). In the map, blue (resp. red) regions correspond to nice (resp. poor) correlation. The other three panels are F partial function maps for different selected sets of two energies from data set $\tilde{\mathcal{S}}$. We can observe that the minimization of F (which is equivalent to solving the system $\vec{f} = 0$) is a difficult task, too. These surfaces show a complex topography, with a clear minimum at the global minimum of R_P . The bottom left panel shows a case with multiple solutions.

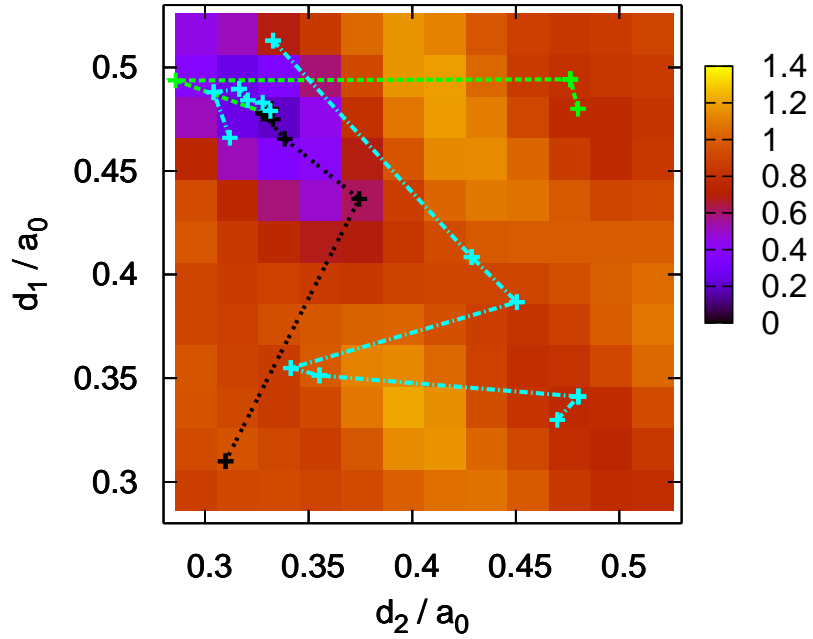


Figure 6.11: Paths or trajectories for three different starting points on the simulated experiment of Fig. 6.10. Each starting point has a colour assigned to it. Solid line of the same colour represent the path followed during the resolution of a N -equation system. The discontinuity at on of the paths (dashed-dotted) indicates that a random move is made after global R_P calculation. In another path (dashed), we can observe that the step before this move drives the solution outside the search interval.

The four panels in Fig. 6.12 show the corresponding histograms of $t = N_{\text{call}}/N_e$, normalized to the same area. In this expression, N_{call} is the number of calls to the LEED routine for a single energy. Other authors count the number of trial structures, but SO method uses different number of energies at different stages of the search: N_e at each structure in the R_P calculation, and $2N$ at each visited structure during the system solving Eq. (6.7). Therefore, a fair comparison between our results and others in the literature imply we must divide the number of intensity evaluations by N_e to get a quantity that accounts faithfully for the number of trial structures. Qualitatively, the probability density function (PDF) of cases $N = 2, 3, 4$ is non-symmetric and displays a sharp peak at low t values. The maximum number of necessary structures happens with a exponentially small probability. Similarly to the phase shift retrieval problem, the PDF can be satisfactory fitted by a 1-event Poisson-like form, Eq. (6.17). We notice that for $N = 5$, N_{stat} is low and the fit is poor.

$N = 3$ gives us easy access to published results on the same system with SA and GA, and we compare performances in Table 6.1. Integrating the PDF up to a 99.98% success rate goal (Eq. (6.18)), we locate the global minimum on 300 calls, improving by a factor from 8 to 3 results obtained on same conditions from SA or GA. The expected value and deviation extracted from the fit are $\langle t \rangle \pm \sigma = 54 \pm 38$, to be compared with 314 ± 137 for GA. Authors of Ref. [166] obtain the latter result for GA by fitting their histogram to a gaussian PDF:

$$p_g(t) = \frac{1}{\sigma\sqrt{2\pi}} e^{-\frac{1}{2}\frac{(t-n)^2}{\sigma^2}} \quad (6.20)$$

that yields the following global probability:

$$P_g(t) = \int_{-\infty}^t p_g(t') dt' = \frac{1}{2} + \frac{1}{2} \text{Erf} \left(\frac{t-n}{\sigma\sqrt{2}} \right) \quad (6.21)$$

Both $p_1(t)$ (given by Eq. (6.17)) and $p_g(t)$ are represented in Fig. 6.13 for the fit parameters obtained from $N = 3$ statistics in Ir(110)-p(2×1). The corresponding global probabilities are shown on the left hand panel of Fig. 6.14. The right hand panel of this Fig. shows the global probability obtained by Rous using SA taken from Ref. [157]. Those plots demonstrate that the solutions are achieved by SO much faster than with the other two global methods.

Our results also outperform RSA working on a reduced domain. However, both results should not be directly compared. The use of TLEED requires RSA to work in a smaller search space, of size 0.4 \AA^3 . The criterion used at Ref. [118] for success probability is also different from ours, due to the multiple launch strategy used in RSA. They use as global probability the the fraction of trajectories that end up in the global minimum well.

We have also checked the performance of the Downhill Simplex method [44, 169] in Ir(110)-p(2×1) structure with $N = 3$ unknown parameters in a 1 \AA^3 hypervolume. This has been done by means of the CLEED code [22], where it has been used widely, taking average values over $N_{\text{stat}} = 100$ simulated structures. The simplex method is not a global one and only requires function evaluations, not derivatives. We have checked that only a 7% of the searches finish successfully at the global minimum,

Method	N_{stat}	$\langle t \rangle_{0.9998}$	$\langle t \rangle_{0.97}$	$\langle t \rangle_{0.90}$	Scaling law
SA [157]	1000	2500		800	N^6
GA [166]	100	800	570	490	Not reported
SO	200	300(46)	145(22)	105(16)	$N^{4.1}(N^{2.8})$
RSA [118]	700		330		$N^{2.5}$

Table 6.1: For three free parameters ($N = 3$), average number of structures explored to find the global minimum of R_P with a probability P , $\langle t \rangle_P$ Ir(110)-p(2×1) missing row surface has been taken as a benchmark system, and compared with results derived from other optimization strategies. For SA, GA and SO, the domain for the search is a hypercube of 1 \AA^3 , and the solution has been located with a precision of $\lesssim 0.02 \text{ \AA}$. For RSA the domain has been reduced to 0.4 \AA^3 to allow the use of TLEED, and the solution has been located with a precision of ($\lesssim 0.05 \text{ \AA}$ for RSA). N_{stat} is the number of independent simulations used to calculate statistical average values. The number of full R_P evaluations required by SO (i.e. iterations spent in the outer loop) is given in parenthesis.

while others are trapped in local minima. Interestingly, the average number of R-factor calls to achieve a converged simplex for $N = 3$ is $\langle t \rangle \sim 70$.

6.6.3 Scale law

Table 6.2 summarizes the scaling behaviour of the SO algorithm. In this table, notice that $\langle t \rangle$ is the average number of trial structures over the N_{stat} independent searches. $\langle N_{\text{brd}} \rangle$ is the average number of partial problems needed in each search. Figs. 6.15 and 6.16 show a log-log plot scaling of these two averages and the least-squares fit to a polynomial law, N^β . In these fits, each point has been weighted with the squared inverse of its own error bar [44]. The exponent found for $\langle t \rangle$ is $\beta = 4.1 \pm 0.1$, that implies significant improvement from the reported SA result, $\beta = 6.0 \pm 0.3$ [157]. This β value is in good agreement with the predicted scale law, $\mathcal{O}(N^4)$.

The exponent for $\langle N_{\text{brd}} \rangle$ scaling law is $\beta_{\text{brd}} = 3.3 \pm 0.1$. Dividing $\langle N_{\text{brd}} \rangle$ by $N_{PC} = 2N$, we find the average number of complete R_P evaluations. This quantity scales with exponent $\beta_{R_P} = 2.6 \pm 0.2$. Such a behaviour can be interpreted in this way: the larger N , the more global character is found for SO, i.e., a smaller number of outer loops (full R_P calls) is needed.

In the statistical searches, it can be observed that side effects grow with N , in the sense of search paths that try to cross the borders of the search space. This is due to the increase in the complexity of F partial maps topography.

6.6.4 Fitting V_{0r}

Commonly, the quantity V_{0r} is fitted by taking the value of an energy shift Δ in the theoretical curves from a discrete list that gives the optimum value at the R_P calculation. Therefore, the number of trial structures remains unchanged.

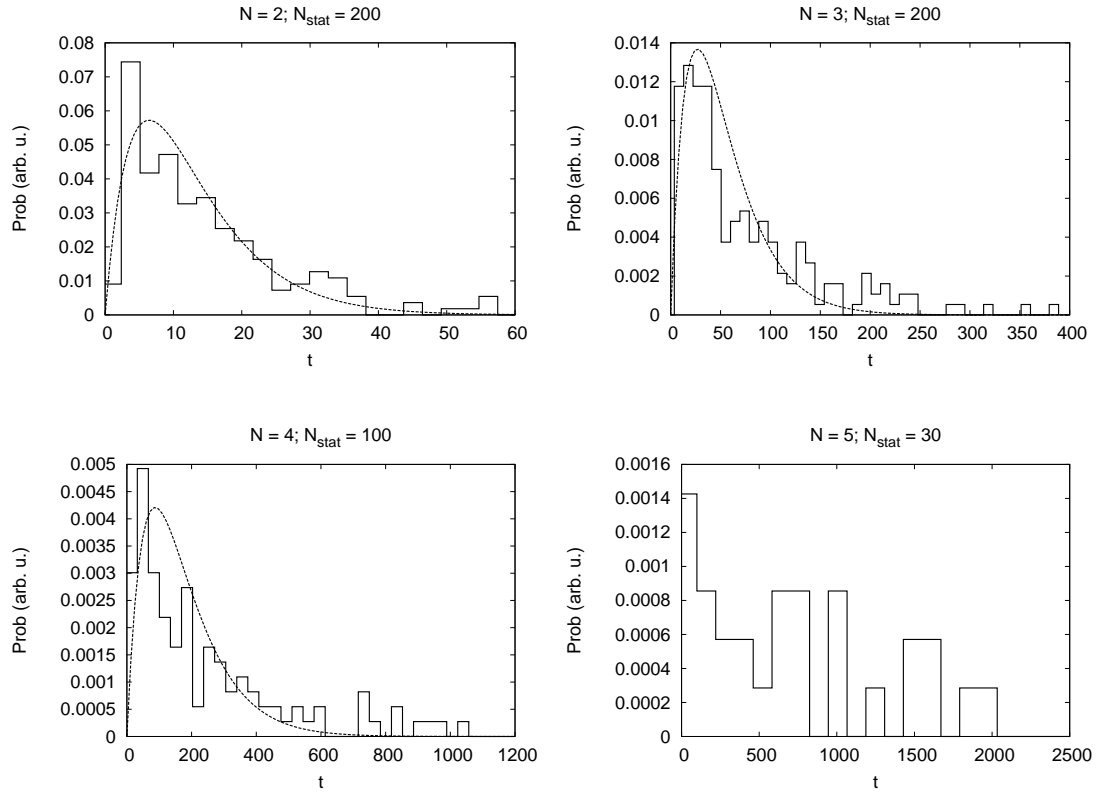


Figure 6.12: The panels in this figure show the histograms for the number of calls in $N = 2, 3, 4, 5$ LEED parameter determination of Ir(110)-p(2×1) missing row surface. The dashed line is the least-squares fit to a Poisson law with $P(t) = w^2 t e^{-wt}$. The fit for $N = 5$ is not shown, since the amount of data is not enough.

N	N_{stat}	$\langle t \rangle$	$\langle N_{\text{brd}} \rangle$	$\langle N_{R_P} \rangle$
2	200	16 ± 1	9.5 ± 0.5	2
3	200	81 ± 5	34 ± 2	6
4	100	273 ± 26	93 ± 9	12
5	30	836 ± 122	234 ± 33	23

Table 6.2: Average values obtained from N_{stat} independent simulated searches of N parameters (notice that these averages are not the expected values from fitted PDFs). $\langle t \rangle$ is the average number of trial structures and $\langle N_{\text{brd}} \rangle$ is the average number of partial problem loops iterated in each search. In the last column, the approximate number of full R_P evaluations is shown.

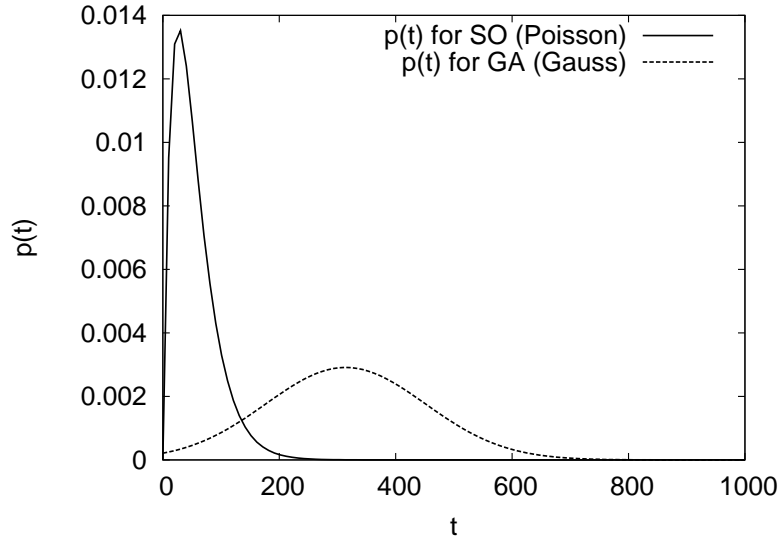


Figure 6.13: Fitted PDFs for the $N = 3$ LEED parameter determination of Ir(110)-p(2 \times 1) surface in (i) SO (solid line), where the PDF is 1-even Poisson-like shaped, given by Eq. (6.17), and (ii) GA (dashed line), where the PDF is gaussian shaped, given by Eq. (6.20) taken from Ref. [166].

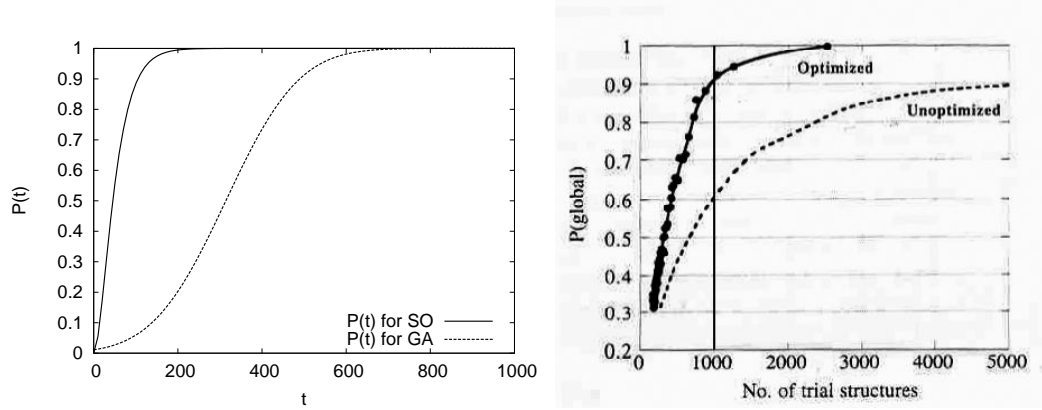


Figure 6.14: The left hand panel shows the SO (solid line) and GA (dashed line) integrated global probabilities from Fig. 6.13, given by Eqs. (6.18) and (6.21), respectively. The right hand panel is the integrated global probability function in the SA method, with optimized (solid line) and unoptimized (dashed line) cooling scheme. This figure is taken from reference [157].

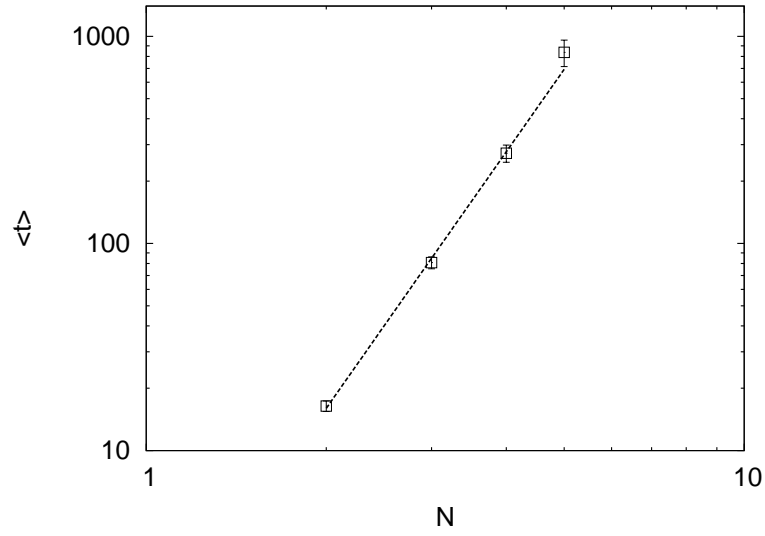


Figure 6.15: Log-log plot giving the scaling law for $\langle t \rangle$ in the LEED optimization of the Ir(110)-p(2 \times 1) missing row surface. The least-squares fit to a polynomial law results in a scale exponent $\beta = 4.1 \pm 0.1$. Averages have been determined using 200 model searches for $N = 2, 3, 100$ for $N = 4$ and 30 for $N = 5$.

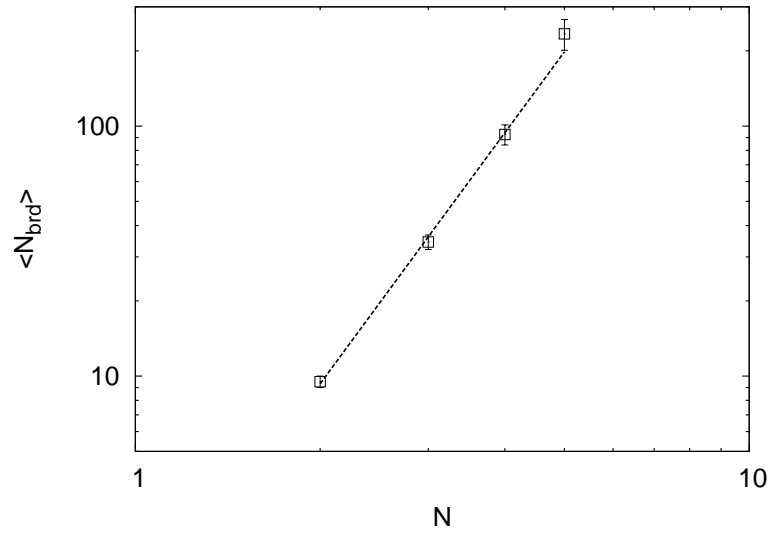


Figure 6.16: Log-log plot giving the scaling law for $\langle N_{\text{brd}} \rangle$, the average number of partial problem calls, in the LEED optimization of the Ir(110)-p(2 \times 1) missing row surface. The least-squares fit to a polynomial law results in a scale exponent 3.3 ± 0.1 .

However, within the SO framework, this procedure is not robust enough. In general, when the search is wandering away from the solution, the value of Δ will be far from its correct value too. Thus, if we enter the partial problem loop with this Δ , the system of equations will bear little resemblance with the actual R_P . In other words, many solutions to the systems will not correspond to partial solutions of the global problem.

A better strategy consists in including the Δ energy shift as another unknown in the systems, by adding another equation built from another point in the $\tilde{\mathcal{S}}$ set. The initial value of Δ at each partial loop is the value that produced the best R_P in the previous global step.

We have carried out further model searches of the Ir(110)-p(1×2) surface adding V_{0r} , taking values between 9.25 and 12.5 eV, to the N geometrical search parameters. In this case, we have taken a less demanding, but still realistic, exit condition: $R_P < 0.15$. Table 6.3 contains the statistical results for these calculations. Each time R_P is computed, the best V_{0r} is chosen from a list of values $\Delta = (9.248, 9.384, 9.520 \dots, 12.512)$ eV. It can be observed that the increase of calls w.r.t. the fixed V_{0r} case is, in fact, smaller than that one would expect from an additional parameter fitting. In particular, the number of R_P evaluations is of the same order in both cases.

N	N_{stat}	$\langle t \rangle$	$\langle N_{\text{brd}} \rangle$	$\langle N_{R_P} \rangle$
2	122	52 ± 4	21 ± 2	4
3	87	157 ± 15	53 ± 5	7
4	19	710 ± 15	217 ± 50	22

Table 6.3: Statistics including the V_{0r} fit in the LEED optimization of the Ir(110)-p(2×1) missing row surface. The first column indicates the number N of geometrical parameters only. The last column indicates the approximated number of full R_P evaluations needed. Search parameters are the same as for previous searches, excluding the exiting condition, which has been changed to $R_P < 0.15$.

6.7 Structure determination from LEED experimental data: the Cu(100) surface

The real challenge is to deal with experimental data, where the match between measured and theoretical spectra can not be perfect. In this situation, not all the extrema in the experimental IV curves are expected to coincide with those of the calculated spectra at the R_P global minimum structure. Thus, some of the nonlinear systems of N equations might result in structures wandering away far from the true global minimum. We have already examined a similar scenario, namely the phase shifts retrieval from intensities scattered by a single atom when a random noise is present at the data. A good strategy to deal with this problem was to use overdetermined systems, which have the ability of gathering more features of R_P . These systems have N variables and $N_{ov} \times N$ equations, where N_{ov} is the oversampling factor.

We have applied SO to experimental IV curves from the Cu(100) surface, which have been provided by Prof. K. Heinz (University of Erlangen-Nürnberg) [170, 46]. The database consists of four beams, (10), (11), (20) and (21) in the energy range 55-400 eV, measured at normal incidence. Total energy overlap of the database is 1300 eV, containing 57 extrema. This database has been used to find the two topmost interlayer distances, d_1 and d_2 . Lattice parameter of Cu(100) is $a_0 = 2.53$, and our parameter search space is $[0.5a_0 : 0.9a_0]$, i.e. $\sim 1 \text{ \AA}^2$. We have fixed the third and deeper interlayer distances to their bulk values. Other non-structural parameters have been set to the reported fit values [170]. These are: $V_{0i} = 4.68 \text{ eV}$ for the imaginary part of the inner potential, and Debye temperatures $\Theta_D^b = 443 \text{ K}$ for bulk atoms and $\Theta_D^o = 235 \text{ K}$ for atoms at the two topmost layers. The experiment was done at 90 K. We have used our code LEED90 for the full-dynamical calculations, with 8 layer doubling steps and $l_{\max} = 10$. For the reported best distances, $(d_1, d_2)_{\text{best}} = (0.69a_0, 0.72a_0)$, we find $R_P = 0.23 \pm 0.04$ for a constant value $V_{0r} = 6.67 \text{ eV}$ for the real part of the inner potential. For the sake of simplicity, we have taken a constant value V_{0r} . Actually, it has been shown that the best agreement with experimental data is found when considering an energy dependent V_{0r} [46]. By working under these conditions, namely fitting two structural parameters only and taking a constant V_{0r} , we can not achieve the degree of accuracy found at Refs. [170] and [46]. Fig. 6.17 shows the global Pendry's R_P map upon the $\sim 1 \text{ \AA}^2$ search space. It has a narrow global minimum near $(d_1, d_2) = (0.7a_0, 0.7a_0)$ with $R_P \sim 0.2$ and another narrow secondary minimum near $(d_1, d_2) = (0.55a_0, 0.85a_0)$ with $R_P \sim 0.5$. The rest of the map shows the usual corrugated topography of height $R_P \sim 0.8$, due to random correlations in the database.

We have performed three searches starting from different points in the parameter space, with the plain SO method (i.e. $N_{ov} = 1$) and with an oversampling factor $N_{ov} = 2$ (i.e. using systems of 4 equations and 2 unknowns). Fig. 6.18 shows some maps of the partial scalar function, F , at $N_{ov} = 1, 2, 3$. We can observe that, as expected, the minima in F will not coincide with the global minimum of R_P . In particular, these F maps for $N_{ov} = 1, 2, 3$ show a strong strip-shaped corrugation. That strip pattern is observed at the global R_P map, too, proving that the partial problems contain the main topographic features of the global R_P . In all the chosen subspaces, the point $(d_1, d_2)_{\text{best}}$ is a local minima of F , but many other regions of low F value are present in the maps. In these examples, it seems that taking an oversampling factor $N_{ov} > 1$ reduces the extent of the low F map regions w.r.t. $N_{ov} = 1$.

We have studied the trajectories or paths undergone by these searches on the R_P map. Table 6.4 shows the starting and ending points of these searches, together with the final R_P value achieved and the computational effort needed, $t = N_{\text{call}}/Ne$. We have observed that path no. 2 with $N_{ov} = 1$, that uses $t \sim 140$ structures, visits the secondary minima, too. The other two shorter paths are depicted on the R_P map at left hand panel of Fig. 6.19. Right hand panel of Fig. 6.19 shows the three paths undergone by the three searches with $N_{ov} = 2$. In this case, the search is also brought near the secondary minimum. Unfortunately, the number of studied paths is too small to obtain accurate statistical averages. A larger number of starting points and calculations with other N_{ov} would be needed to get accurate values of

$\langle t \rangle$.

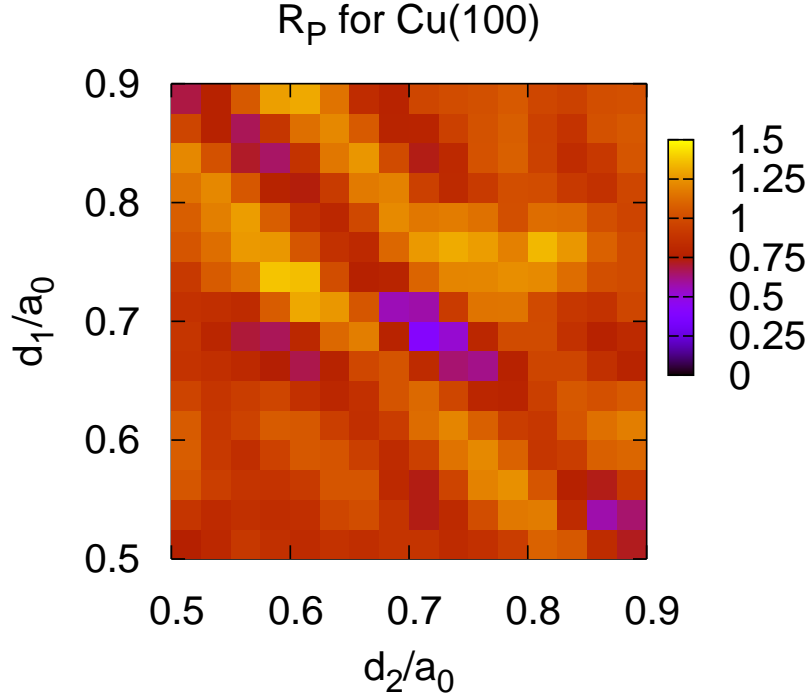


Figure 6.17: Pendry's R_P for two topmost interlayer spacings (d_1, d_2) of Cu(100) surface. Lattice parameter is $a_0 = 2.53 \text{ \AA}$. Experimental database is taken from Ref. [170], and consists of four beams and 1300 eV of energy overlap. Best structure (global minimum) corresponds to the point $(0.69a_0, 0.72a_0)$. Blue (resp. red) regions correspond to nice (resp. poor) correlation.

$N_{ov} = 1$	PATH	Start	End	R_P	t
	1	$(0.64a_0, 0.77a_0)$	$(0.69a_0, 0.72a_0)$	0.23	20
	2	$(0.81a_0, 0.84a_0)$	$(0.68a_0, 0.72a_0)$	0.26	140
	3	$(0.52a_0, 0.72a_0)$	$(0.70a_0, 0.69a_0)$	0.30	30
$N_{ov} = 2$	PATH	Start	End	R_P	t
	1	$(0.80a_0, 0.60a_0)$	$(0.69a_0, 0.72a_0)$	0.23	50
	2	$(0.62a_0, 0.60a_0)$	$(0.70a_0, 0.71a_0)$	0.26	15
	3	$(0.51a_0, 0.57a_0)$	$(0.70a_0, 0.71a_0)$	0.25	50

Table 6.4: Parameters of the six searches performed on the two topmost interlayer spacings of Cu(100). Starting and ending points of each search are shown, together with the corresponding final R_P achieved and the number t of trial structures needed. Top panel corresponds to plain SO searches, i.e. no oversampling. Bottom panel corresponds to an oversampling factor $N_{ov} = 2$.

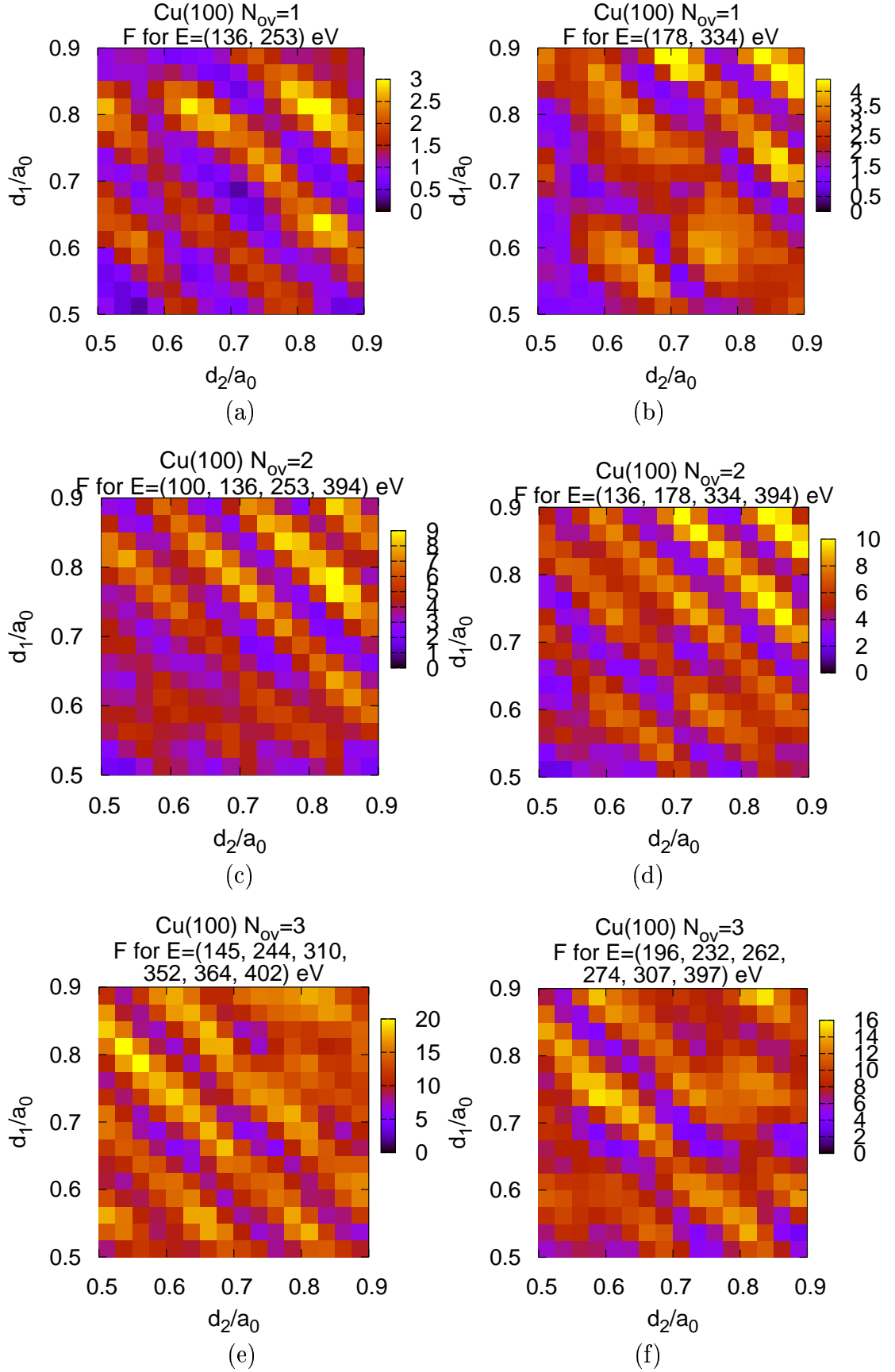


Figure 6.18: Maps of the partial scalar function, F , as a function of the two topmost interlayer spacings of Cu(100) for some selected data subspaces. For panels (a) and (b), subspaces are made of two datapoints, panels (c) and (d) correspond to four datapoints (oversampling factor $N_{ov} = 2$), and panels (e) and (f) to six datapoints (oversampling factor $N_{ov} = 3$). Lattice parameter is $a_0 = 2.53$ Å.

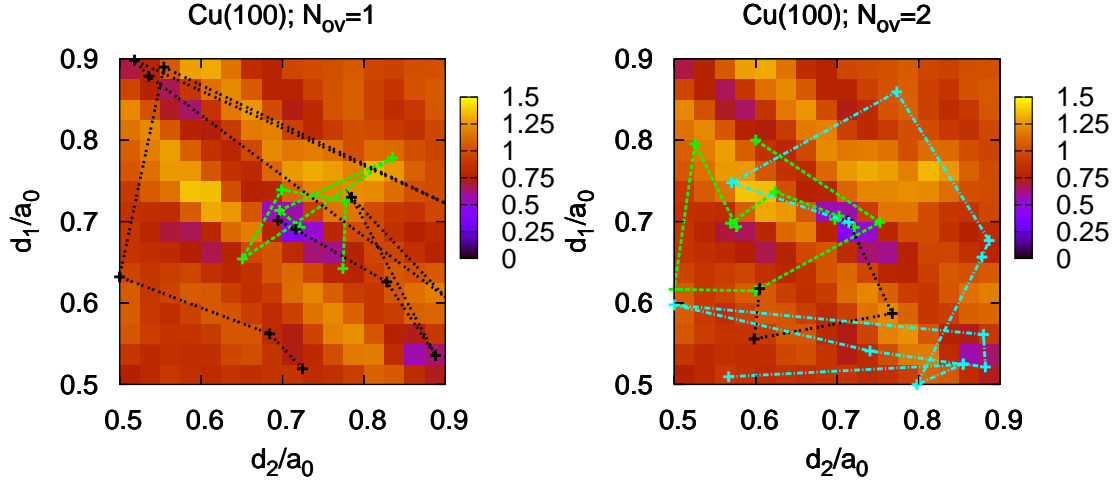


Figure 6.19: Paths undergone by the six searches for Cu(100) surface depicted on the global R_P map. The corresponding starting and ending points can be found at Table 6.4. Lattice parameter is $a_0 = 2.53$ Å. Marked points correspond to visited structures in the outer loop of SO, i.e. they indicate solutions provided after $N_{PC} = 4$ partial problem iterations. Left hand panel shows paths no. 1 and no. 3 of the $N_{ov} = 1$ case only. Right hand panel shows all three paths of the $N_{ov} = 2$ case.

6.8 Conclusions

We have introduced a method for multi-dimensional optimization in structural search techniques that is very efficient both from the point of view of the number of structures to be explored, and the scaling law with increasing number of parameters. The algorithm is organized at two levels: an internal one providing solutions for a partial problem, and an external one helping to avoid local traps and instabilities inherent to non-linear problems. The reason for the efficiency of SO can be understood by realizing that the partial problem corresponds to project R_P on a restricted database. Because this contains many relevant features of R_P , these solutions make a better strategy than simple blind random search. In addition, this is a fast problem because the sampling of \vec{f} needs only $2N$ intensity evaluations per structure (function evaluation plus derivative). For LEED, we notice that whenever the search is stabilized below a reasonable value of R_P , the partial solving problem can take advantage of TLEED, because regions involved on this part are always inside its convergence limits. We have benchmarked SO on simulated noiseless IV curves for the Ir(110)-p(2×1) missing row surface. For $N = 3$ parameters retrieval, SO needs 300 trial structures to find the solution with success probability near to 100%, which is a strongly competitive result if compared to similar search algorithms: working under the same conditions, GA needs 800 structures and SA 2500. Scaling law exponent for SO is $\beta = 4$, much efficient than $\beta = 6$ from SA.

However, dealing with experimental data deserves some special treatment, since the match between calculated and measured spectra can not be perfect. We have simulated this by (i) introducing up to a 10% of gaussian noise on the theoretical

experiment used as reference to retrieve phase-shifts, and (ii) introducing real LEED data for Cu(100)[170]. The main effect of noise on phase-shifts retrieval is to increase the prefactor of the scaling law by $\approx 8 - 10$ and the exponent by ≈ 1.3 . This is related to the solution oscillating around the true value; these oscillations can be damped by constructing overdetermined systems of $N_{ov} \times N$ non-linear equations. For real LEED structure determination, we have recovered values for relaxations of the two topmost layers on Cu(100). Similarly to the phase-shifts case, different sets of redundant equations ($N_{ov} = 1, 2$) have been used, and the effort has been higher than for the ideal case by about a factor of $\approx 4 - 5$. More experience on different structures and better statistics will be needed, but important savings for the expensive LEED multiple scattering calculations seem to be at hand.

Chapter 7

Direct structure determination in electron diffraction from tomography and error-reduction

7.1 Introduction

As we have commented in Chapter 6, if we are willing to extract information (structural and/or non-structural) by direct inversion of the experimental database, we must face two related problems: (i) inability to measure the phase of the diffracted wavefield and (ii) self-consistency driven by multiple scattering (MS). The former, phase retrieval, is a traditional problem of imaging techniques, that affects a number of apparently different fields ranging from diffraction crystallography and microscopy to astronomy, geophysical survey or medical diagnosis. In low-energy electron techniques, this lack of phase information is added to the complexity introduced by MS.

Our aim in the present Chapter is to solve the following problem: from the diffracted intensities and having *a priori* partial knowledge of the geometry of the surface structure (the geometry of the known part will be labelled by $X^{(\text{kn})}$ in the following), we want to determine the unknown part of the structure (labelled by $X^{(\text{unk})}$). This is a subject belonging to the family of structure completion problems. Structure completion is a popular topic in X-ray crystallography, motivated by the interest in modelling of macromolecules (mainly proteins), complex structured crystals and, more recently, surfaces.

Two different interpretations can be made of this problem. On one hand, it can be interpreted in terms of conditional probabilities, i.e. $P(X^{(\text{unk})}|X^{(\text{kn})}, I)$ is the probability of the geometry in the unknown part being $X^{(\text{unk})}$ on the conditions the known part is $X^{(\text{kn})}$ and the intensities diffracted by the whole structure are the measured ones, labelled by I . Maximization of this probability, also called exponential modelling, constitutes a solution to the structure completion problem [36]. Bayes' theorem can be applied to determine the conditional probability. This theorem statement is:

$$P(X^{(\text{unk})}|X^{(\text{kn})}, I) = \frac{P(X^{(\text{kn})}|X^{(\text{unk})}, I) \times P(X^{(\text{unk})}|I)}{P(X^{(\text{kn})}|I)} \quad (7.1)$$

Maximum entropy method is an exponential modelling method that has been successfully applied in X-ray crystallography [171, 172, 173, 174, 175] and also in LEED [37, 176].

On the other hand, the measured intensity pattern can be interpreted as a hologram [177], which is the result of the interference of an unknown wave (object wave) and a known wave (reference wave). The hologram codifies the information needed to reconstruct the object wave, which can be retrieved by illuminating the hologram with a suitable reference wave. PD spectra have been interpreted in this way, as well as DLEED patterns. We shall comment on this method in section 7.2.1.

In this work, we will restrict ourselves to considering that the substrate is the known part of the structure, and that the adsorbate positions are to be found from the intensities diffracted by the surface. We recall on the holographic interpretation to establish a parallelism, and take $\psi^{(\text{kn})}$ (the wave diffracted by $X^{(\text{kn})}$) as the reference wave, and $\psi^{(\text{unk})}$ (the wave diffracted by $X^{(\text{unk})}$) as the object wave. Notice that $\psi^{(\text{unk})}$ and $\psi^{(\text{kn})}$ are not exactly the object and reference waves used in electron diffraction holography, as we will see in section 7.2.1. In the latter, the wave outgoing from the adsorbate is taken as reference and the wave outgoing from the substrate after an encounter with the adsorbate is the object. In our case, substrate and adsorbate roles are exchanged w.r.t. holography, and we will not consider scattering paths relating substrate and adsorbate. Approximately, the total wave diffracted by the surface can be formulated as:

$$\psi = \psi^{(\text{kn})} + \psi^{(\text{unk})} = \sqrt{I}e^{i\phi} \quad (7.2)$$

where ϕ is the total wave phase. Regarding this equation as valid, our aim is to use the wave

$$\psi^{(\text{unk})} = \sqrt{I}e^{i\phi} - \psi^{(\text{kn})} \quad (7.3)$$

to extract the atomic positions in the unknown region. The first handicap to do this is obvious:

Problem 1: impossibility of measuring the diffracted wavefield phase.

Knowledge of the phase is crucial to determine the structure, since scattering paths undergone by the electrons are codified in the diffracted wave phase. The phase problem has attracted the attention of several fields, and many techniques have been developed in order to solve it. Pendry was the first to tackle the phase retrieval problem specifically for LEED [178] by using Kramers-Kronig dispersion relations between modulus and phase of the diffracted wavefield, as it is used in optics [179]. This method has a drawback: the position of the zeros of the reflected amplitude must be known beforehand, and this is not possible in LEED. As an alternative, in this work we will use phase retrieval techniques imported from optics, that will be described in section 7.3.

Notice that, for the sake of simplicity, Eq. (7.2) has been written under the assumptions that MS between substrate and adsorbate is weak. Thus, Eq. (7.2), which considers scattering of $X^{(\text{unk})}$ uncoupled from scattering of $X^{(\text{kn})}$, is not accurate, in general, since bond lengths between substrate and adsorbate atoms tend to be short. Thus, the second drawback appears:

Problem 2: multiple scattering paths between atoms in the known and the unknown region exist, which are not negligible.

We can put forward a situation where *Problem 2* is not that critic: a situation where we know the amplitudes diffracted by a structure $X^{(\text{kn})}$, and measure the intensities diffracted by another structure that differs slightly from $X^{(\text{kn})}$. If so, Eq. (7.2) can be interpreted in a Tensor LEED sense, with $\psi = \psi^{(\text{kn})} + \delta\psi^{(\text{kn})}$. In this case, $\delta\psi^{(\text{kn})}$ causes a small perturbation on the already existing scattering paths: no further propagators between surface atoms are introduced, but the existing ones are modified. Within the TLEED second level of sophistication (see section 2.10), which is expected to be valid in a range of geometric distortions $0.2 - 0.4 \text{ \AA}$, no MS exists between the surface atoms and the displaced atom t-matrix update,

$$\delta\tilde{t}^w = \tilde{G}_{II}(\delta\vec{r}_w) \cdot \tilde{t}^w \cdot \tilde{G}_{II}(-\delta\vec{r}_w) - \tilde{t}^w, \quad (7.4)$$

Thus, if we considered $\psi^{(\text{unk})}$ as a small distortion of $\psi^{(\text{kn})}$ within the TLEED applicability range, *Problem 2* could be ruled out. On the other hand, in a non-perturbative case, where a term $\psi^{(\text{unk})}$ associated to the appearance of a completely new atom(s) upon $X^{(\text{kn})}$ is taken, the perturbation is too strong for Eq. (7.2) to be accurate.

Nevertheless, we imagine that we can access the phase and that Eq. (7.2) is correct even in the non-perturbative situation, and continue with our intention of extracting atomic positions from $\psi^{(\text{unk})}$. In many cases, MS inside the unknown part is weak, specially when the adsorbate is a dilute lattice gas-like layer, or an ordered layer with large superstructure unit cell. Therefore, we can apply Born approximation to describe scattering inside the unknown region. When adsorbates are molecules, this approximation should not, in principle, be valid, but we will make the following derivation for a generic non-monoatomic adsorbate, obviating this fact. Back to general MS theory (see section 2.5), the Born approximation consists in substituting the total scattered wavefield by the incident wavefield at the integral in the Lippman-Schwinger equation (Eq. (2.14)). For an incident plane wave, this yields the following expression for the scattered wave:

$$\psi^{(\text{unk})}(\vec{r}) = \int d^3\vec{r}' V(\vec{r}') G_0(k_0; \vec{r}' - \vec{r}) e^{i\vec{k}_0 \cdot \vec{r}'} \quad (7.5)$$

where G_0 is the free space Green propagator, $V(\vec{r})$ is the adsorbate scattering potential, $\vec{k}_0 = k_0 \hat{s}_0$ is the incident electron momentum and $\vec{r} = r \hat{s}$ is the position where the scattered wavefield is to be measured, which is, in our case, located at a hemispherical detector. Here, we can apply the far field condition, which means that the detector is placed at a much longer distance than the potential range of influence. Thus, the Green propagator is:

$$G_0(k_0; \vec{r}' - \vec{r}) = -\frac{1}{4\pi} \frac{e^{ik_0|\vec{r}' - \vec{r}|}}{|\vec{r}' - \vec{r}|} \simeq -\frac{1}{4\pi r} e^{ik_0 r} e^{-ik_0 \hat{s} \cdot \vec{r}'} \quad (7.6)$$

Substituting this expression in the Eq. (7.5), we obtain:

$$\psi^{(\text{unk})}(r\hat{s}) = -\frac{1}{4\pi r} e^{ik_0 r} \tilde{V}(\vec{K}); \quad \vec{K} = k_0(\hat{s} - \hat{s}_0) \quad (7.7)$$

where \vec{K} is the diffraction vector and \tilde{V} is the Fourier transform of the potential V . Thus, the scattering factor in the Born and far field approximations is

$$F^{(\text{unk})}(k_0\hat{s}_0, \hat{s}) = -\frac{1}{4\pi}\tilde{V}(\vec{K}) \quad (7.8)$$

From Eq. (7.7) we can see that the solution to the inverse problem (i.e., retrieving the scattering potential from diffracted wavefield), in the case we could measure both phase and modulus of the scattered wave, consists of simply inverse Fourier transforming the measured wavefield. We will see next that this is not an easy task, even if we could access the phase.

Both for an extended ordered adlayer and for a localized finite cluster of a single atomic species, the scattering potential is the convolution product $V(\vec{r}) = V_1(\vec{r}) * P(\vec{r})$, where V_1 is the scattering potential of a single atom and P is a set of delta functions peaking at atomic sites. In the Born approximation the scattering factor is $F^{(\text{unk})}(k\hat{s}_0, \hat{s}) = f_1(k\hat{s}_0, \hat{s})\tilde{P}(\vec{K})$, where f_1 is the atomic scattering factor and \tilde{P} is the Fourier transform of the distribution P . Thus, the atomic positions can be retrieved by inverse Fourier transforming the scattered field and a convolution with f_1 , which plays the role of a point spread function. If several atomic species are present, this deconvolution is not possible. Without deconvolution, we would retrieve a phase object, since the action of f_1 is to insert a phase shift at the partial components of the incident plane wave.

Using the Born approximation, if the scattering factor $F^{(\text{unk})}$ is known for all values $(k_0\hat{s}_0, k_0\hat{s})$, then the corresponding scattering potential can be uniquely determined formally [180]. In a situation closer to the experimental case, where only a finite number of data points $(k_0\hat{s}_0, k_0\hat{s})$ exist (in fact, the use of a cutoff value for k_0 already implies a low band passed reconstruction), then it can be shown that there exists an infinite number of potentials that can produce such data points. The only exception to this theorem are spherically symmetric potentials [181]. We must emphasize that this would happen even if the phases were known. This result may lead to think that, even if the potential is not uniquely retrieved, better quality can be achieved at the reconstruction if a larger number of incidences are used, since the Fourier space datapoint coverage is more dense. Resolution will be better if high k_0 values are used, since the pixel size at the reconstruction is $\propto 1/k_0$.

Taking that theorem into account, we find that a third problem must be overcome in addition to the two ones stated already this introduction:

Problem 3: to reconstruct the structure of a three-dimensional object from a finite set of measurements of the field scattered by that object.

Diffraction Tomography (DT) is a set of widely used methods to solve this problem [182]. Some of them will be described in section 7.4.

Summarizing, the outline for the theoretical description of the method presented in this Chapter for direct inversion structure determination is the following:

- We shall comment on the existing direct methods at electron diffraction techniques, such as HLEED and Patterson function. They are examples of structure retrieval based in an inverse Fourier transform of the diffracted intensities. A brief description of the maximum entropy method will be given, too.

- Our goal for structure retrieval consists of inverse Fourier transforming the diffracted amplitudes, rather than the intensities, i.e. we are willing to make an inverse Fourier transform of Eq. (7.7). For our method to work, we need two main ingredients imported from optics:
 1. As we can not access the phase at the experiment, we use error-reduction iterative methods to retrieve it. We will give a description of such algorithms.
 2. We will use large databases obtained from intensities recorded at different incident energy and direction conditions. Previous work on tomography methods to manage diffracted data will be shown.
- In LEED, we have to deal with the problem of MS. An approach to account for MS, at least at a first order approximation, will be given.

7.2 Overview of previous work on direct methods in electron diffraction

7.2.1 Holography

Gabor discovered the holography principle in 1948, and proposed its application to electron microscopy. This principle can be stated as follows: if an unknown wave (called object wave) and a known wave (called reference wave) interfere, the intensity of the resulting pattern measured at the detector is a hologram, which contains all the information needed to reconstruct the unknown wave. If we illuminate this hologram with an appropriate reference wave, the object wave is reproduced by the modulation caused at that reference by the hologram. The hologram has the ability of codifying three-dimensional information about an object on a two-dimensional screen, according to the Helmholtz-Kirchhoff theorem [183]. Fig. 7.1 shows schematically the geometry needed for holography at surfaces. Ideally, it consists of an adsorbate, which acts as a beam-splitter for the incident wave. The wave scattered by the adsorbate is the reference wave, and the wave scattered by the adsorbate and by the substrate afterwards constitutes the object wave. The intensity measured at the detector is thus:

$$I(\vec{k}) = |R(\vec{k}) + O(\vec{k})|^2 = |R(\vec{k})|^2 + |O(\vec{k})|^2 + R^*(\vec{k})O(\vec{k}) + R(\vec{k})O^*(\vec{k}) \quad (7.9)$$

where R and O are the reference and object waves respectively, which depend on the outgoing momentum, \vec{k} . Two assumptions are usually made for holography: (i) Only first order MS terms between adsorbate and substrate are retained, and (ii) $|O(\vec{k})|^2$ terms are negligible w.r.t. $|R(\vec{k})|^2$.

The LEED case must be considered carefully, since some first order scattering paths exist which contribute to the reflected amplitudes with terms of the same magnitude as the O wave, but are not holographic. These contributions are depicted in Fig. 7.1, and appear from scattering at the substrate prior to the encounter with the adatom, and are usually included at R , which is usually modelled as a spherical wave.

Sometimes it is useful to define a normalized modulation function for the measured intensities to eliminate background contributions and keep only the interference terms of the intensity:

$$\chi(\vec{k}) = \frac{I(\vec{k}) - I_0(\vec{k})}{I_0(\vec{k})}; \quad I_0(\vec{k}) \equiv |R(\vec{k})|^2 \quad (7.10)$$

We record this on a hemispherical screen, \mathcal{D} , and illuminate it with a convergent spherical wave, such that the centre of the sphere lies at the photoemitting source. By applying the Helmholtz-Kirchhoff theorem, we obtain that the wavefield inside the sphere is (at points $r \ll R$):

$$U(\vec{r}) \propto \int \int_{\mathcal{D}} \chi(\hat{k}) e^{-ik_0 \hat{k} \cdot \vec{r}} d^2 \hat{k} \quad (7.11)$$

where \mathcal{D} is used to denote integration over the detector surface. On the other hand, we can write the diffracted reference and object waves as:

$$\begin{aligned} R &= f_0(\vec{k}) e^{i\vec{k} \cdot \vec{r}} \\ O &= \sum_{j \neq 0} f_j(\vec{k}) e^{i\vec{k} \cdot (\vec{r} - \vec{r}_j)} \end{aligned} \quad (7.12)$$

where f_0 is the adsorbate scattering factor and f_j are the generalized substrate atomic factors, which occupy the positions \vec{r}_j . Substituting these expressions at the Helmholtz-Kirchhoff equation, stationary phase conditions yield peaks at positions $\vec{r} = \pm \vec{r}_j$. One of these signs corresponds to the twin image. If the hologram were recorded on the whole sphere, there would be no doubling of the image and the resolution would be $\sim 1/k_0$ in all three directions.

After making this short introduction about the principles of electron diffraction holography, it is interesting to show chronologically the origins of this direct method and the contributions made afterwards to improve reconstruction quality, both at LEED and PD.

- **Szöke (1986)** [28]: the first proposal was to expand $I(\vec{k})$ in terms of spherical harmonics, I_{lm} , in order to build a system of equations where the coefficients of the O expansion, O_{lm} , are the unknowns. This system is highly nonlinear and its solution would require a powerful minimization tool. To the author's knowledge, this proposal has never been applied to experimental neither to simulated data.
- **Barton (1988)** [29]: this was the first interpretation of a O/Ni(100) PD pattern as an hologram, in the Helmholtz-Kirchhoff sense discussed above.
- **Saldin and de Andrés (1990)** [30]: the holographic interpretation was extended to DLEED patterns and benchmarked upon experiments on the O/Ni(100) surface [67]. MS was incorporated in the substrate by using modified generalized factors f_j . No intensity smoothing was applied.

- **Barton (1991)** [184]: the negative effects of twin images and MS in PD were diminished by Fourier filtering the $U(\vec{r})$ functions through several incident momenta values, k_0 . Poor resolution in the perpendicular direction was still a problem.
- **Tong *et al* (1992)** [185, 27]: alternatively, rather than integrating over k_0 , these authors proposed filtering through outgoing \vec{k} vectors. Reconstructions are satisfactory in both radial and angular components. The same idea was applied to DLEED patterns [186].
- **Wei *et al* (1994)** [187]: it was suggested that the summation of reconstructions over several incidence angles lead to the elimination of artifacts due to MS.
- **Saldin *et al* (1995)** [188]: since taking experimental data at different conditions has some practical drawbacks, these authors proposed a reconstruction algorithm (CORRECT) that uses a kernel in the Fourier transform of Eq. (7.11), constructed from a model of the reference wave anisotropy. This allows better quality reconstructions.
- **Seubert *et al* (2000)** [189, 32]: the method was extended to ordered or partially ordered adsorbates by taking superstructure spots as a grid sampling of the DLEED pattern. In addition, a more accurate kernel than CORRECT was constructed iteratively, which eliminates artifacts.

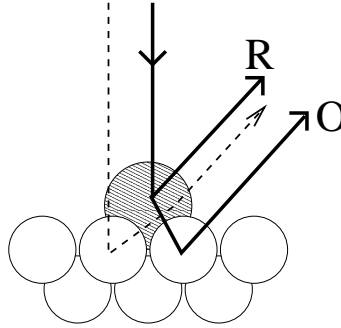


Figure 7.1: Reference (R) and object (O) waves for hologram formation in DLEED, represented by solid lines. Dashed line represents a scattering event of first order (leaving the adsorbate after being scattered by a substrate atom nearby), that produces terms of the same magnitude as the object wave and are included in R .

7.2.2 Patterson Function

The Patterson function [33] is defined as the Fourier transform of the diffracted intensity pattern. It was first proposed for X-ray crystallography, where the diffracted intensities are

$$I(hkl) \propto |f_1(hkl) \times S(hkl)|^2 \quad (7.13)$$

where (hkl) are the Miller indices labelling each intensity spot, f_1 is a single atom scattering factor and S is the crystal structure factor (notice that this corresponds to the simple case of a crystal containing a single atomic species). Thus, the intensities contain the interatomic vectors of the crystal, so that a Fourier transform produces peaks at the positions corresponding to such vectors, i.e. the Patterson function is related to the autoconvolution of the atomic positions. This technique is widely used in X-ray and in neutron diffraction also [149]. Tong *et al* have shown that, in common with holography, this technique filters out higher scattering orders, i.e. Patterson function retains first order scattering paths contributions and filters out higher orders¹. The difference is that it does not make use of any reference wave and yields the interatomic vectors only, not the atomic positions.

The Patterson function realization in LEED is more complicated, since low-energy electrons interaction with the crystal atoms is stronger than interaction with X-rays, making high order scattering paths contributions non-negligible. Furthermore, atomic scattering factors have a complex angular dependence. These two effects yield fuzzy Patterson functions and also artifacts, the later caused by repetition of scattering paths in the MS events. For example, if \vec{R} is the interatomic vector of a diatomic molecule, the Patterson function from LEED data will have peaks at positions $\pm\vec{R}, \pm 2\vec{R}, \pm 3\vec{R}, \dots$ with peak heights decreasing as $\sim R^{-2n}$, where n is the order of the scattering event, since the interatomic propagator is an spherical wave proportional to $\frac{e^{ikR}}{kR}$.

Early implementations of Patterson function in LEED made use of the *transform deconvolution method* [190]. Since Patterson function for LEED intensities within a single scattering framework are a convolution product of structural and non-structural terms (atomic scattering factors), the effect of the later can be swept out via a deconvolution process. MS blurring effect can be also diminished by considering a noise component at the deconvolution. Recently, a simpler technique was proposed, which consisted in adding, in phase, the Patterson functions of experimental data from several incidence directions [34, 120]. The expression for such a Patterson function is:

$$P(\vec{r}) = \left| \sum_{\vec{k}_{in}} \sum_{\vec{g}} \int I(\vec{k}_{in}, \vec{q}) e^{i\vec{K} \cdot \vec{r}} dK_{\perp} \right|^2 \quad (7.14)$$

where \vec{r} is the position inside the direct space unit cell, \vec{g} is the label for each diffraction spot, \vec{k}_{in} is the incident electron momentum and $\vec{K} = \vec{k}_{out, \vec{g}} - \vec{k}_{in}$ is the diffraction vector. Using this function, first order scattering contribution sum grows more rapidly than higher order scattering terms, so that the later terms are filtered out and many artifacts associated to those orders disappear.

7.2.3 Maximum entropy method

Holographic methods have the disadvantage of being restricted to small clusters around the reference wave source, since this wave decays as $1/r$. A method has

¹This does not mean that X-rays undergo non-negligible first order MS paths inside the crystal. What we mean is that phase terms of type $e^{i\vec{K} \cdot (\vec{r}_j - \vec{r}_{j'})}$ appear at the intensity, connecting atom pairs jj' , which give stationary phase conditions at the Fourier transform.

been recently developed for direct determination of ordered adlayers from measured LEED-IV curves, that picks up some ideas from holography and uses exponential modelling to retrieve the phases [175, 176]. However, it aims to retrieve the atomic positions PDF at the adlayer unit cell, rather than substrate atoms. This method considers waves diffracted from the bulk as reference waves and waves scattered at least once at the adlayer as object waves. The diffracted beam amplitudes are retrieved from maximum entropy method [44]. We shall comment briefly on the importance of maximum entropy in many fields in the next section.

7.3 Phase retrieval methods

It is remarkable that the phase of the wave diffracted by an object carries more information about the object than the intensities. A nice example of this effect is shown at Ref. [174]. The authors swap the phases of the Fourier transforms of two photographs (real objects). The inverse Fourier transform closely resembles the photograph from which the phase was taken. In crystallography we find a similar situation, since scattering paths undergone by electrons are accounted for in the phase through terms of type $e^{i\vec{K}\cdot\vec{r}_j}$. Therefore, when inverse Fourier transforming, stationary phase conditions, and thus peak features in the reconstruction, appear at positions $\vec{r} = \vec{r}_j$.

Error-Reduction algorithms

Gerchberg-Saxton and similar algorithms, referred to as error-reduction algorithms (ER), are a popular way of solving the phase problem [181, 191]. They are able to find the direct space object that yields the best agreement with the measured intensities, as long as object and diffracted amplitudes are related by a Fourier transform operation, which is equivalent to having Fraunhofer conditions at optics. Both direct and Fourier spaces are pixelated, i.e., a rectangular grid is used, so that Fast Fourier Transform (FFT) methods can be applied. Let x and q be the labels for the pixels at those spaces respectively. Each n -th iteration of the ER algorithm consists of four steps:

1. Fourier transform an estimate, $g_n(x)$, of the object:

$$G_n(q) = \mathcal{F}[g_n(x)] = |G_n(q)|e^{i\text{Arg}(G_n(q))} \quad (7.15)$$

2. Replace the modulus of that transform with the square root of the measured intensity:

$$G'_n(q) = \sqrt{I(q)}e^{i\text{Arg}(G_n(q))} \quad (7.16)$$

Thus, an estimate of the diffracted wave is achieved, in both modulus and phase.

3. Inverse Fourier transform the estimated wave.

$$g'_n(x) = \mathcal{F}^{-1}[G'_n(q)] \quad (7.17)$$

4. Impose known information about the object, for example, object modulus, support, etc. (impose object domain constraints).

$$g_{n+1}(x) = f(g'_n(x)) \quad (7.18)$$

In many cases the object is known to be contained inside a known support region, \mathcal{S} . Depending on the way the constraints defined by f are imposed at the object domain, different prescriptions for the ER algorithm can be proposed. The most popular are:

- Basic ER:

$$g_{n+1}(x) = \begin{cases} g'_n(x) & \text{if } x \in \mathcal{S} \\ 0 & \text{if } x \notin \mathcal{S} \end{cases} \quad (7.19)$$

- Hybrid input-output (HIO):

$$g_{n+1}(x) = \begin{cases} g'_n(x) & \text{if } x \in \mathcal{S} \\ g_n(x) - \beta g'_n(x) & \text{if } x \notin \mathcal{S} \end{cases} \quad (7.20)$$

We can define an error function at each iteration at the Fourier space:

$$E_n = \frac{1}{N} \sum_q |G_n(q) - G'_n(q)|^2 = \frac{1}{N} \sum_q ||G_n(q)| - \sqrt{I(q)}|^2 = \sum_x |g_n(x) - g'_n(x)|^2 \quad (7.21)$$

This error function plays the role of a cost function, or in the LEED crystallographic language, an R-factor. Here N is the number of pixels considered in the calculations (remember that FFT is performed numerically on a homogeneous rectangular grid). The last equality uses Parseval theorem. Since both $G'_n(q)$ and $G'_{n+1}(q)$ satisfy the intensity condition at any point q and by definition $G'_{n+1}(q)$ is the nearest value to $G_{n+1}(q)$ that satisfies Fourier space conditions,

$$|G_{n+1}(q) - G'_{n+1}(q)| \leq |G_{n+1}(q) - G'_n(q)| \quad (7.22)$$

This proves that ER is a convergent algorithm. However, it sometimes converges slowly or even stagnates. When that happens, alternative use of the different prescriptions shown above can take the algorithm out of the stagnation point. Stability and convergence are guaranteed for small values of β . Increasing the value of β makes convergence faster, but the risk of instability arises.

The method can be accelerated using extrapolation to predict subsequent points based on values from previous iterations [192]. Many other special features have been developed in optics to increase phase retrieval quality, such as the use of different support shapes and different starting configurations [193]. In particular, the support can be updated *dynamically* at every iteration by making equal to zero the smaller valued pixels of $\{g_{n+1}(x)\}$ [194, 195]. The blind deconvolution algorithm is used to filter out noise during phase retrieval in imaging [196], by adding a *kernel* or filter function at the third step of the ER algorithm.

Bayesian algorithms

The decreasing condition of the error described above (Eq. (7.21)) can lead to another way of dealing with phase retrieval: considering the error function or any similar cost function as a hypersurface in the direct or Fourier space which is to be minimized. This connects the phase retrieval problem with the algorithms discussed in Chapter 6.

Derivative methods and conjugate gradients in particular can be defined specifically for Eq. (7.21) [191]. SA and similar methods have been used in optics and astronomy imaging problems, too [197, 198].

However, the most popular methods for dealing with problems involving incomplete and noisy data are the Bayesian-like (or exponential modelling) methods, and in particular, the maximum entropy method. It is based in the following principle: the most likely distribution $\{g(x)\}$ is the one that maximizes the entropy and is constrained by a cost function consistent with the experimental data. Thus, the problem is reduced to maximizing the functional

$$Q[\{g(x)\}] = S[\{g(x)\}] - \lambda \chi^2[\{g(x)\}] \quad (7.23)$$

where χ^2 represents the cost function and λ is a Lagrange multiplier. The entropy term, using a simple statistical mechanics analogy, can be formulated as:

$$S[\{g(x)\}] = - \sum_x g(x) \log(g(x)) \quad (7.24)$$

The solution to the problem consists of solving an iterative equation for the $\{g(x)\}$ distribution, which arises from maximization of Eq. (7.23). More details about the actual meaning of the entropy term can be found at Refs. [36, 44]. Applications of maximum entropy range from astronomy [199] to protein crystallography [171, 172] and SXRD [173].

7.4 Diffraction Tomography

The main practical problem concerning DT is that Fourier space is sampled on an inhomogeneous grid during the data acquisition process, whereas it would be desirable to have samples over a rectangular lattice, so that we could use FFT to perform Fourier transforms. The two preferred strategies for reconstructing the object from measurements of the scattered field are (i) filtered backpropagation [200], and (ii) interpolation in the Fourier space, in particular the so-called unified frequency domain interpolation [182].

Filtered Backpropagation

This method uses each set of data, i.e. amplitudes measured at the (two-dimensional) detector for each incident plane wave, separately. It performs a sequence of two-dimensional inverse Fourier transforms on the amplitudes, each of them filtered by a function depending on the depth in the direction parallel to the incidence. Thus, each transform *backpropagates* the amplitudes to a certain depth. This process is

similar to the case of HLEED, where the filter $e^{-iz\sqrt{k_0^2 - k_x^2 - k_y^2}}$ appears at each transform to obtain the reconstruction section at plane z when calculating Eq. (7.11). Afterwards, reconstructions corresponding to all the incidences are superimposed (or better interpolated) in the direct space. However, this last step produces, in general, enhancement of noise at the reconstruction.

Unified frequency domain interpolation (UFR)

This approach interpolates data in the Fourier space by assuming that the reconstruction in the direct space is spatially limited by a support, \mathcal{S} , or window function:

$$i(\vec{r}) = \begin{cases} 1 & \text{if } \vec{r} \in \mathcal{S} \\ 0 & \text{if } \vec{r} \notin \mathcal{S} \end{cases} \quad (7.25)$$

Thus, if $I(\vec{q})$ is the Fourier transform of the window function, and $G(\vec{q})$ are the diffracted amplitudes, the object can be reconstructed by Fourier inverting the convolution product of $G(\vec{q})$ and $I(\vec{q})$:

$$\begin{aligned} g(\vec{r}) &= \mathcal{F}^{-1} [\tilde{G}(\vec{q})] \\ \tilde{G}(\vec{q}) &= I(\vec{q}) * G(\vec{q}) = \int I(\vec{q} - \vec{q}') G(\vec{q}') d^3 \vec{q}' \end{aligned} \quad (7.26)$$

To perform the Fourier transform above by FFT, the sampling $\{\vec{q}\}$ must be rectangular.

We need a variable change between the rectangular grid coordinates of the Fourier space $\{\vec{q}\}$ and variables used in the geometry of our experimental setup for data acquisition. In two-dimensions, the most common choice is to keep k_0 fixed and vary incoming and outgoing angles. In three dimensions, the choice is not so clear. Let $\vec{\omega} = (\omega_1, \omega_2, \omega_3)$ be three generic parameters of data collection and $\vec{q} = (q_x, q_y, q_z)$ a point in the three-dimensional rectangular grid, so that the convolution product can be written

$$\tilde{G}(\vec{q}) = \int I(\vec{q} - \vec{q}'(\vec{\omega})) J(\vec{\omega}) G(\vec{\omega}) d^3 \vec{\omega} \quad (7.27)$$

where the jacobian of the transformation is

$$J(\vec{\omega}) = \left| \frac{\partial(q'_x, q'_y, q'_z)}{\partial(\omega_1, \omega_2, \omega_3)} \right| \quad (7.28)$$

For each pixel \vec{q} of the Fourier space, we must calculate the integral (7.27). Integration variables are now the parameters of the experimental setup, typically angles. The last step to retrieve the object is to invert Fourier $\tilde{G}(\vec{q})$ using FFT.

7.5 Structure and phase retrieval from diffracted intensities by small clusters of atoms

Our aim in this section is to develop a structure determination algorithm using an iterative procedure for phase retrieval. We will benchmark it on a small cluster of

atoms, which can be considered as a reduced model of a disordered (lattice gas-like) surface. Our final purpose is to get a phase retrieval method that works for DLEED or PD patterns. We will assume that some information about the structure is known *a priori*. We assume that some atomic positions of the cluster are known, e.g. the substrate atoms, and we shall try to retrieve the PDF of the other atomic positions restricted to a support region, e.g. the adsorbed atoms or molecules. Thus, we are trying to solve a problem which is the inverse of the one proposed at holography with DLEED data (see section 7.2.1). The method introduced here follows closely, apart from the limitations introduced by MS, already developed methods for surface structure [174, 175, 201] and nanoparticle imaging [194, 202, 195] using X-ray crystallography methods. We will regard also as known the atomic species in the cluster, to obtain more clear reconstructions through a deconvolution process. Our simulated experiments consist in illuminating the cluster using electron plane waves of several energies and incidence directions, and measuring the backscattered intensities.

The tomographic reconstruction method should be chosen according to the geometry at the intensity data acquisition process. Since the intensities are to be measured at different energy and/or incidence direction conditions, the optimum algorithm for the tomographic approach will be different for each case. As we have mentioned in section 7.4, DT methods deal with the problem of making inverse Fourier transforms on non-homogeneous distributed data at the reciprocal space. On the other hand, the experimental database lacks in information about the diffracted wavefield phase. Thus, the final efficiency of the algorithm will depend on our ability to insert the tomographic approach inside a phase retrieval algorithm. In optics, it is a common practice to use two measurement planes, so that the phase can be obtained similarly to interferometry [183, 203, 204]. Unfortunately, in crystallography, such experimental setups are not possible.

As we have seen at section 7.2, multiple incidences and energies are used in HLEED to filter out MS terms of orders higher than second, retaining first order ones. These contain the phase terms corresponding to the interatomic vectors defining the structure. On the contrary, in the method proposed here our aim is to invert the amplitudes scattered by the unknown adsorbate, $F^{(\text{unk})}$, according to Eq. (7.7), rather than the intensities. Iteratively, we can make estimates of such amplitudes using the ER phase retrieval algorithms shown before. A higher number of incident electron energies and directions will not have that filtering effect explicitly. They will only produce a more dense sampling of the Fourier space, so that DT methods should provide a less fuzzy reconstruction. But notice that this has nothing to do with MS, since at both ER and DT we are assuming that the diffraction process takes place under Fraunhofer conditions in the unknown region, i.e. spectra and structure are related by a Fourier transform, that is, we are assuming that scattering is kinematic at the unknown positions. In section 7.6 we will present an approach to account for, at least, first order MS events during the iterative phase retrieval procedure.

However, in the perturbative scenario, where $F^{(\text{unk})}$ differs slightly from the reference wave, the Fraunhofer condition assumption would more accurate, since no new scattering paths would be introduced (a distortion of the reference structure

introduces variations of the already existing paths).

7.5.1 The algorithm

Next, the basic algorithm used at the cluster problem is described. In the following, this notation convention is taken: $K = k_0(\hat{s} - \hat{s}_0)$ are the inhomogeneous sampling points at the Fourier space, corresponding to the exact diffraction vectors of the simulated experiment. \vec{q} and \vec{r} are the Cartesian coordinates of Fourier and direct spaces respectively. As information known *a priori*, we provide the algorithm with: (i) the intensities $I(\vec{K})$, (ii) the atomic scattering factors of the atomic species at the unknown part of the cluster $f^{(\text{unk})}(\vec{K})$, (iii) the amplitudes backscattered by the known part $F^{(\text{kn})}(\vec{K})$, and (iv) the support region constraining the unknown positions $\mathcal{S}(\vec{r})$. To begin with, an initial random PDF of the unknown positions $P_0^{(\text{unk})}(\vec{r})$ is fed into the algorithm. The next steps constitute the n -th iteration of the algorithm:

1. A Fourier transform (FFT) is applied on the tentative PDF:

$$G_n^{(\text{unk})}(\vec{q}) = \mathcal{F}[P_n^{(\text{unk})}(\vec{r})](\vec{q}) \quad (7.29)$$

As a technical remark, we recall that, as long as the amount of pixels in use is kept within sensible limits, Fourier transforms should be made padding the P_n data array with zeros to prevent aliasing effects [44].

2. Using UFR inversely, i.e. given a set of rectangular $\{\vec{q}\}$ get the amplitudes at points $\{\vec{K} = k_0(\hat{s} - \hat{s}_0)\}$ by convolution using the inverse variable change at Eq. (7.27), $\tilde{G}_n^{(\text{unk})}(\vec{K})$ values are obtained.
3. At this step, the atomic scattering factors $f^{(\text{unk})}(\vec{K})$ are considered. We do this by simply multiplying the scattering factor by the transform obtained at the previous step (which is equivalent to a convolution of scattering potential and PDF at the direct space), following the average atom concept used at X-rays (Eq. (7.13)). This means that we are neglecting MS inside the unknown part of the cluster (or the perturbed reference structure in the Tensor LEED sense), which is not a bad approximation as long as atoms in that region are well separated from each other. If we want to reconstruct a small molecule from scratch, it is probable that this approach will give us unreliable or fuzzy reconstructions.

At this step, we introduce a trick to reduce noise at the $P_n^{(\text{unk})}(\vec{r})$ reconstruction. We make a convolution with a point spread function, namely a small circular slit. In the Fourier space, the transform of the slit is an Airy function, $A(K)$. By doing this, the PDF obtained by inverse Fourier transformation is smoothed, since the contribution of high $|\vec{K}|$ values to the transform are diminished [44]. However, this must be carefully done, because the larger the slit radius, the less atomic resolution at the PDF.

Summarizing, this step corresponds to doing:

$$F_n^{(\text{unk})}(\vec{K}) = \tilde{G}_n^{(\text{unk})}(\vec{K}) \frac{f^{(\text{unk})}(\vec{K})}{A(K)} \quad (7.30)$$

4. The total reflected amplitude by the cluster is:

$$F_n(\vec{K}) = F^{(\text{kn})}(\vec{K}) + F_n^{(\text{unk})}(\vec{K}) \quad (7.31)$$

Here, we are neglecting scattering paths involving atoms of the known and unknown parts. In subsequent sections, we will derive an approach to account for first order MS between these components [176, 37].

5. Apply the Fourier space constraints (measured intensities):

$$F_n^{(\text{unk})'}(\vec{K}) = w_n \sqrt{I(\vec{K})} e^{i\text{Arg}(F_n(\vec{K}))} - F^{(\text{kn})}(\vec{K}) \quad (7.32)$$

where w_n is a real constant that scales the measured intensities to match its calculated counterpart at the n -th iteration. w_n is another parameter to be fitted during the procedure. To estimate it, we observe that the global aim of this iterative procedure is to minimize the following cost function:

$$\chi^2 \propto \sum_{\vec{K}} \left| F_n(\vec{K}) - w_{n-1} \sqrt{I(\vec{K})} e^{i\text{Arg}(F_{n-1}(\vec{K}))} \right|^2 \quad (7.33)$$

i.e. near the stagnation point, the successive calculated amplitudes should approach the same value and hold the Fourier space constraint on the modulus [176]. The value of w_{n-1} that minimizes such a cost function must hold:

$$\frac{\partial \chi^2}{\partial w_{n-1}} = 0 \quad (7.34)$$

which yields:

$$w_{n-1} = \frac{\sum_{\vec{K}} \sqrt{I(\vec{K})} \Re[F_n(\vec{K}) e^{-i\text{Arg}(F_{n-1}(\vec{K}))}]}{\sum_{\vec{K}} I(\vec{K})} \quad (7.35)$$

Actually, the value w_{n-1} is used at the n -th iteration, since it depends on the amplitude calculated at the n -th step.

6. Make a deconvolution with the scattering factor and a convolution with slit to prepare the inverse Fourier transform:

$$\tilde{G}_n^{(\text{unk})'}(\vec{K}) = F_n^{(\text{unk})'}(\vec{K}) \frac{A(K)}{f^{(\text{unk})}(\vec{K})} \quad (7.36)$$

7. Use UFR (Eq. (7.27)) to get values at rectangular grid points: $G_n^{(\text{unk})'}(\vec{q})$.

8. Inverse Fourier transform using FFT:

$$P_n^{(\text{unk})'}(\vec{r}) = \mathcal{F}^{-1}[G_n^{(\text{unk})'}(\vec{q})](\vec{r}) \quad (7.37)$$

As we will see afterwards, when working with surfaces and regardless of the chosen data collection geometry, we can sample points only at the $q_z < 0$ half of the Fourier space (remember that the OZ axis points inwards the solid). We will extract the points at the $q_z > 0$ half by imposing the symmetry condition

$$G_n^{(\text{unk})'}(\vec{q}) = [G_n^{(\text{unk})'}(-\vec{q})]^* \quad (7.38)$$

which allows us to ensure that $P_n^{(\text{unk})'}(\vec{r})$ is real valued, as it must be.

9. Apply direct space constraints, which are (i) positivity and (ii) support of the PDF. Thus, $P_{n+1}^{(\text{unk})}(\vec{r})$ is zero outside the support or where $P_n^{(\text{unk})}(\vec{r}) < 0$. This corresponds to simple ER procedure, but HIO or any other flavour can be used [191]. Optionally, if we know the exact number of atoms contained at $P^{(\text{unk})}$, we can use this information to normalize the estimated PDF. Sometimes, if this is not done, the algorithm may become unstable.

One more simple algorithm would consist in interpolating intensities, atomic scattering factors and amplitudes from the known part into a rectangular grid prior to the iterative phase retrieval procedure, so that no interpolations would have to be made at every iteration. We have checked out this possibility, and it results in very inaccurate reconstructions. Thus, we conclude that it seems that the structure recovery is highly sensitive to the accuracy of the *a priori* information. On the other hand, interpolating the estimates made during the procedure introduces a smaller amount of noise. Therefore, we will focus on the implementation of the algorithm presented above.

In usual LEED or PD experiments, intensities are collected on a hemispherical screen. Changing the incident electron beam energy or direction, we get a rich three-dimensional sampling of data points $\vec{K} = k_0(\hat{s} - \hat{s}_0)$. However, the algorithm above has the drawback of being time and memory consuming, mainly at the UFR steps of the procedure. One way of overcoming this drawback is to find situations where the three-dimensional Fourier transforms can be changed into two-dimensional ones, so that UFR steps can be restricted to planes. This approach is presented at the next subsection.

7.5.2 Reconstruction from two-dimensional scans

In general, our database is formed by the set of intensities recorded at the hemispherical detector (i.e. two-dimensional data) for each incident direction and energy of the electron beam. By varying the incidence conditions, we obtain a complicated sampling in three dimensions of the Fourier space. Making UFR interpolation of such a big set of data into a three-dimensional rectangular grid is computationally demanding. We propose a simple approach, where only two-dimensional UFR is required, by reducing the experimental data acquisition procedure to scanning at a fixed azimuthal angle, ϕ . In the plane so defined, called ϕ -plane in the following, we vary polar incident and outgoing angles, as it is shown at Fig. 7.2. Thus, we are using only a transversal cut at ϕ of the whole hemispherical detector. For each incidence sampled, Fourier space points form an arch, shown at Fig. 7.3. We will restrict ourselves to reflected intensities from the object, so that the maximum spatial frequency we achieve is $2k_0$. Thus, we expect a resolution $\frac{\pi}{2k_0}$ at the reconstructed object.

For a given ϕ -plane, at the n -th iteration of the phase retrieval process, we can make an estimate of a projection of the total PDF, $P_{n,\phi}^{(\text{unk})}(\eta, z)$, where η is the abscissa at the ϕ -plane. If we have a number N_ϕ of ϕ -planes available, at the end of the ER iteration the set of projections can be combined to give a three-dimensional

estimate by doing:

$$\begin{pmatrix} \xi \\ \eta \end{pmatrix} = \begin{pmatrix} \sin \phi & -\cos \phi \\ \cos \phi & \sin \phi \end{pmatrix} \begin{pmatrix} x \\ y \end{pmatrix} \quad (7.39)$$

$$P_n^{(\text{unk})}(x, y; z) = \sum_{\phi} P_{n, \phi}^{(\text{unk})}(\eta(x, y), z) \quad (7.40)$$

This simple combination of projections by superposition is called Radon transform, and it is a widely used technique at non-diffracting tomography [182].

The algorithm presented here is summarized in the flowchart of Fig. 7.5. If no MS corrections are to be used, a faster and less space consuming procedure would consist in retrieving the phase for each projection separately and doing the Radon superposition only once at the end.

In our model calculations, we have used two types of two-dimensional samplings according to different orientations of sample, incident beam and detector:

Type I

The electron beam and the detector are kept fixed, with the beamline perpendicular to the hemispherical detector basement, and the sample is rotated through an incident angle θ_0 . Thus, we are collecting data at the reflection semicircle arches of Fig. 7.3. We must notice that \hat{s} outgoing directions having a positive z component can not be accessed when working with a surface, so that we dismiss the corresponding \vec{K} points. Thus, for a single energy, the Fourier space sampling is a circular wreath, with outer radius $2k_0$ and inner radius $k_0\sqrt{2}$ (see left panel of Fig. 7.4). The new variables in the convolution integral 7.26 are the incident and outgoing polar angles θ and θ' as defined at Fig. 7.3, which are taken to be equispaced. The variable change from (θ, θ') to the Cartesian grid defined by the coordinates q_η, q_z is:

$$\begin{aligned} \begin{pmatrix} q_\eta(\theta, \theta'; k_0) \\ q_z(\theta, \theta'; k_0) \end{pmatrix} &= \begin{pmatrix} \cos \theta & -\sin \theta \\ \sin \theta & \cos \theta \end{pmatrix} \begin{pmatrix} \pm k_0 \sin \theta' - k_0 \\ k_0 \cos \theta' \end{pmatrix} \\ &= \begin{pmatrix} \pm k_0 \sin(\theta' \mp \theta) - k_0 \cos \theta \\ k_0 \cos(\theta' \mp \theta) - k_0 \sin \theta \end{pmatrix} \end{aligned} \quad (7.41)$$

where the upper sign corresponds to transmission mode and the lower sign to reflection mode. The variable change jacobian is $J(\theta, \theta'; k_0) = k_0 |\cos \theta'|$.

The sampled area by reflection in the Fourier space using this method is reduced and leaves a big hole at small $|\vec{K}|$ values. Usage of several energies, E_i , can help to fill out this empty space. If values are chosen such that $E_i = 2E_{i-1}$, then the wreaths do not overlap, so that the variable change explained above for the integral is maintained within each of the wreaths. Therefore, the UFR integral for this type of sampling is:

$$\tilde{G}(q_\eta, q_z) = \sum_{k_0} \int \int I(q_\eta - q'_\eta(\theta, \theta'; k_0), q_z - q'_z(\theta, \theta'; k_0)) J(\theta, \theta'; k_0) G(\theta, \theta'; k_0) d\theta d\theta' \quad (7.42)$$

where the expressions derived above must be substituted. For a finite number of equispaced (θ, θ') angles, the integral above is transformed into a finite sum.

Type II

Both surface and detector are kept fixed, and the incident beam is moved. In this situation, parts of the reflection and transmission arches are used. The arches follow Eqs. (7.41), as above. The coverage obtained by changing θ at a single energy is shown at the right panel of Fig. 7.4. In this case, the region of small frequencies is accessed. The drawback is that areas sampled by different energies overlap.

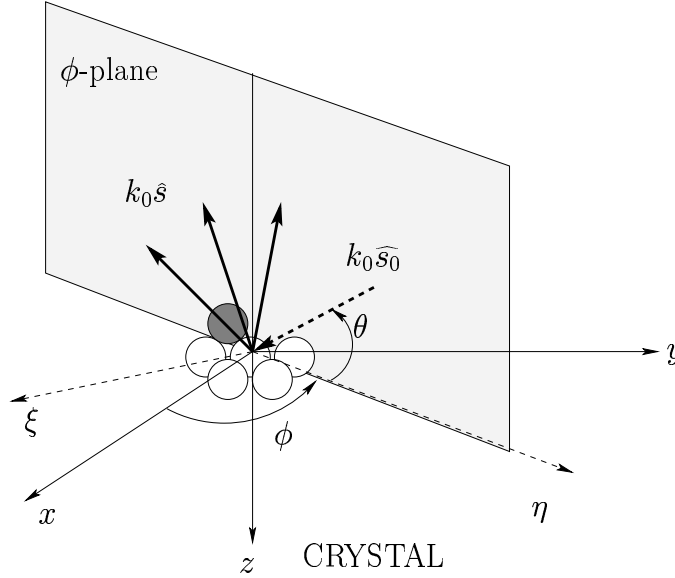


Figure 7.2: Geometry for data collection using two-dimensional scans at a single azimuthal ϕ angle. Polar incident and outgoing angles lie on the plane defined by ϕ .

7.5.3 Position retrieval from measured amplitudes: results for a flat molecule

Prior to showing the behaviour of the phase retrieval algorithm explained above, we will examine a more simple case. In this subsection, we will try to recover the atomic coordinates of a flat molecule from measured reflected *amplitudes*, by simple Fourier inversion of Eq. (7.7). The simulated experiment consists in illuminating the molecule with plane waves of wavevectors $k_0 \hat{s}_0$ lying on the molecule plane, and measuring the diffracted amplitudes at directions \hat{s} lying on the plane, too. We choose a sampling of type I at the Fourier space, similarly to the one shown at left panel of Fig. 7.4.

In this simple situation, we can benchmark some basic features of our method, for example:

- The behaviour of UFR when we are dealing with atomic scatterers. In fact, atoms are *phase objects*, that insert phase shifts at the incident plane wave partial components.

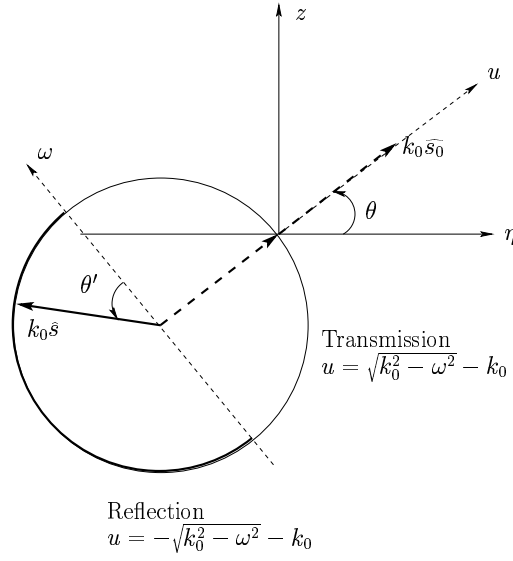


Figure 7.3: The collected data for a single incidence at the ϕ -plane are arch-shaped. This picture shows both smirches, corresponding to transmission and reflection.

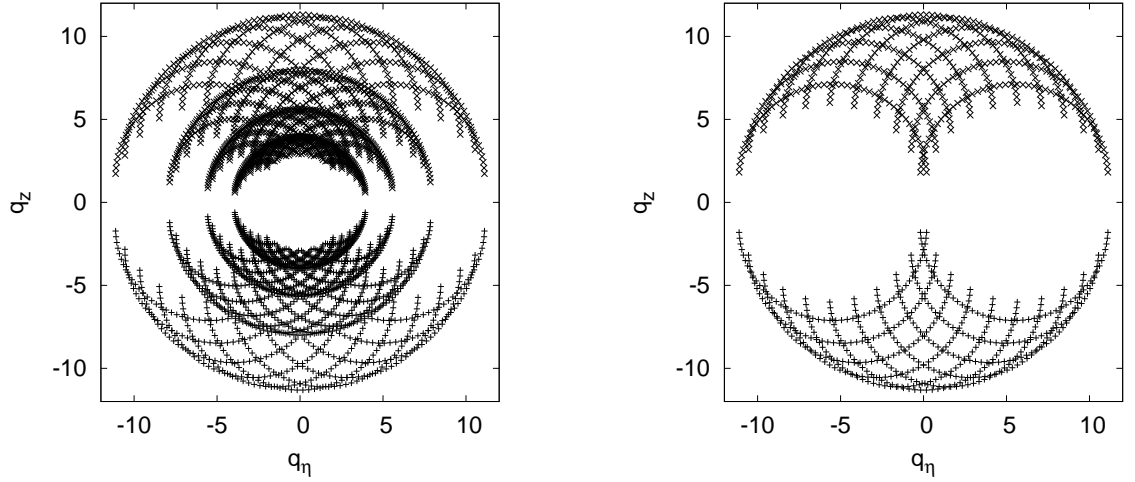


Figure 7.4: Samplings in reflection mode tomography in two-dimensions for a scan in polar angles θ at fixed azimuthal angle ϕ . In both panels a number of incident $N_\theta = 10$ and outgoing $N_{\theta'} = 50$ angles have been used, and points at the $q_z < 0$ region are sampled by the symmetry condition Eq. (7.38). (i) Left panel: four energies (2, 4, 8 and 16 H) and rotating sample. Notice that for the energy sequence $E_n = 2E_{n-1}$ sampled areas of different energies do not overlap, and (ii) Right panel: one energy only (16 H), fixed hemispherical detector and movable electron emitter.

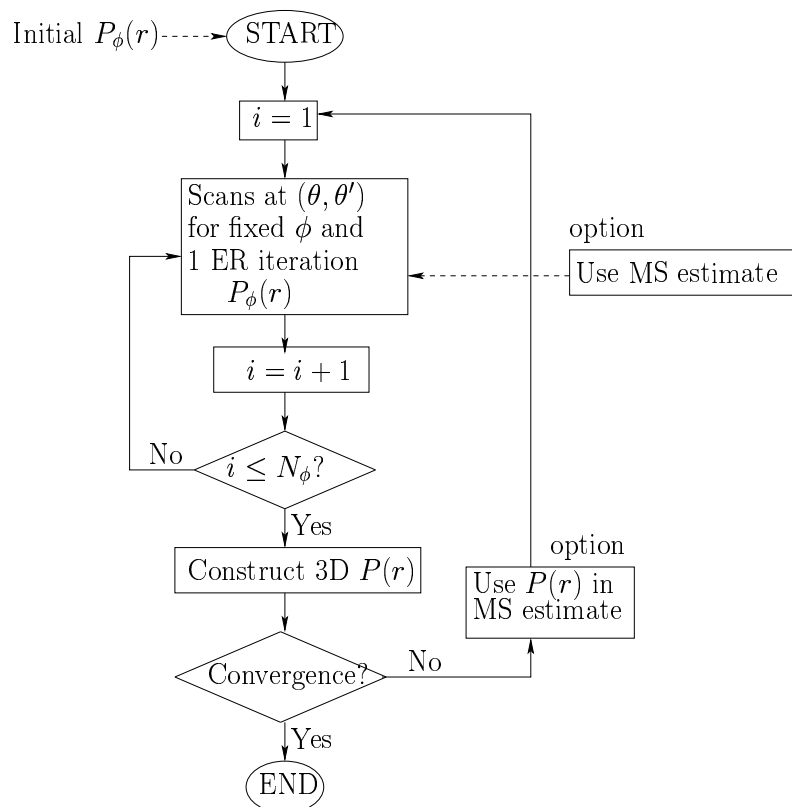


Figure 7.5: Flowchart of the reconstruction algorithm that uses a scanning of two-dimensional azimuthal sections of the object.

- We will observe the effect of the intramolecular MS on the quality of the reconstruction.

In practice, we are not able to measure the diffracted wavefield phase. However, since our algorithm consists of estimating such phase in an iterative procedure, the example examined at the present subsection can be regarded as a test on the effectiveness of the reconstruction procedure at each ER iteration of the entire algorithm. Since we are using the exact phases, the present example would correspond to checking the reconstruction quality in the ideal case.

We have chosen a flat O_3 molecule, where the oxygen atoms lie at positions $(0.0 - 2.0)$ Bohr, $(3.0, 1.0)$ Bohr and $(-2.5, 1.5)$ Bohr². Top panel of Fig. 7.6 shows the molecule geometry. Our database consists of $N_\theta = 15$ incident angles ranging in $[0 : \pi]$ and $N_{\theta'} = 128$ outgoing angles per incident plane wave, i.e. the semiarch-shaped detector is divided into 128 pixels. We will use four different incident energies, 2, 4, 8 and 16 H. The energies hold the relation $E_i = 2E_{i-1}$, so that each of them will sample non-overlapping regions at the Fourier space.

The rectangular grid at the Fourier space has 128×128 pixels $\vec{q} = (q_x, q_y)$, where $\tilde{G}(\vec{q})$ values are to be evaluated by UFR convolution method. As we are using only incident angles in the interval $[0 : \pi]$, we can only measure amplitudes at diffraction vectors holding $K_y < 0$. Thus, by UFR we get $\tilde{G}(q_x, q_y < 0)$, and $\tilde{G}(q_x, q_y > 0)$ are obtained by applying the symmetry condition $\tilde{G}(-\vec{q}) = [\tilde{G}(\vec{q})]^*$, which ensures that its inverse transform, $g(\vec{r})$, is real valued. The expected resolution from the maximum energy used is $\pi/2k_{0,\text{max}} = 0.28$ Bohr. However, this resolution increases by a factor of two if we pad the $\tilde{G}(\vec{q})$ with zeros, increasing the number of pixels to 256×256 . By doing this, we avoid aliasing effects in the numerical FFT [44]. Thus, we obtain that our final resolution is 0.14 Bohr.

The diffracted amplitudes have been computed using the routines of our code TMOL [54]. The molecule scattering factor in the far field approach is:

$$f(k_0 \hat{s}_0, \hat{s}) = \frac{4\pi}{ik_0} \sum_{vv'=1}^3 e^{ik_0 \hat{s}_0 \cdot \vec{r}_{v'}} e^{-ik_0 \hat{s} \cdot \vec{r}_v} \sum_{lm, l'm'} i^{l'} (-1)^{m'} Y_{l'-m'}(\hat{s}) \tau_{l'm', lm}^{v'v} i^{-l} Y_{lm}(\hat{s}_0) \quad (7.43)$$

where v index labels O atoms and $\tilde{\tau}^{v'v}$ matrix elements are given by Eq. (4.8). For this O_3 molecule, we need $l_{\text{max}, T} = 11$. To account for absorption during MS, we use $V_{0i} = -0.147$ H.

Bottom left panel of Fig. 7.6 shows the reconstructed O_3 from this parameters in the case of single scattering at $\tilde{\tau}^{v'v}$ matrix, i.e. \tilde{X} is set to zero at Eq. (4.8). Actually, that picture shows the absolute value $|g(\vec{r})|$. The bright features correspond to the actual atomic positions, shown at the top panel. Quality of the reconstruction is good. The observed noise does not disappear when increasing the number of datapoints, so it is possibly due to the band-pass character of the algorithm (large frequencies, which are not sampled, correspond to short distance features at the reconstruction) and the inhomogeneity of the Fourier space sampling. Bottom right panel of the same figure shows the same reconstruction in the case MS is present

²In the examples shown throughout this Chapter we use atomic units: 1 Bohr = 0.529 Å and 1 Hartree = 27.2 eV.

at $\tilde{\tau}^{v'v}$ matrix. MS causes “artifacts” or a certain splitting of the peaks at $|g(\vec{r})|$. However, the effect in this case is not strong enough to introduce strong uncertainties in the atomic positions.

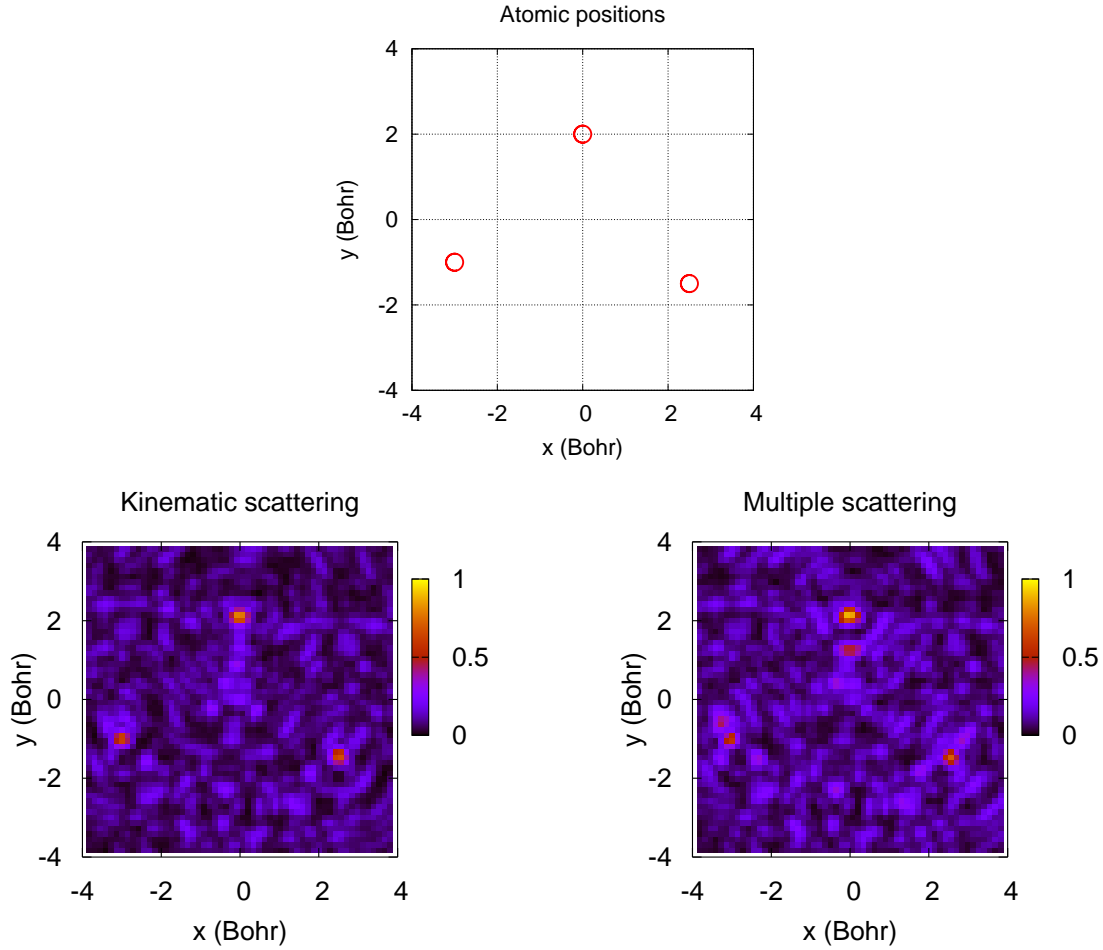


Figure 7.6: Position retrieval from measured backscattered amplitudes on a single plane for a flat lying O_3 molecule. Top panel indicates the O atom actual positions. Bottom left (resp. right) hand panel shows the reconstructed molecule when scattering among O atoms is kinematic (resp. multiple). Bright features coincide with the actual positions. A kind of position splitting is observed in the MS case, though.

7.5.4 Position retrieval from measured intensities: results for localized clusters

In this subsection we benchmark the performance of the complete algorithm adding error-reduction and scanning at ϕ angles. We will retrieve atomic positions from a three-dimensional cluster of atoms from backscattered *intensities*, applying the two-dimensional scanning scheme. For the model calculations, we chose a cluster, as it is a reduced version of a surface with a lattice gas-like adsorbate.

We take, as known positions of the clusters, a square of Ni atoms, at coordinates $(2.35, 2.35, 0.5)$, $(-2.35, 2.35, 0.5)$, $(-2.35, -2.35, 0.5)$ and $(2.35, -2.35, 0.5)$ Bohr (the positive OZ axis points inwards the crystal, as usual). We will study some cases with the O atom placed at different places w.r.t. the Ni atoms. For the reconstructions, we use a hemispherical support for the O atom PDF of radius 3 Bohr. This cluster geometry is represented at the top panel of Fig. 7.7.

Convolution with the oxygen atom scattering factor (steps 3 and 6 of the algorithm) use an Airy function of radius 0.7 Bohr, as point spread function. Regarding the database size, we use samplings of type I, taking four energies: 2, 4, 8 and 16 H. This provides, as in the O_3 case, a resolution of 0.14 Bohr in the reconstruction. We use $N_\phi = 7$ azimuthal scans. At each constant ϕ value, we use $N_\theta = 11$ incident plane waves and measure $N_{\theta'} = 25$ outgoing intensities at the detector per incident plane wave. Using UFR at each two-dimensional scan, data are interpolated into a rectangular grid of 64×64 points. Those values are large enough for our requirements. Our starting PDF for the whole procedure is random and constrained to the support region.

Next, we shall comment on the reconstruction quality using the parameters above for different cluster geometries.

Example 1

The example of Fig. 7.7 corresponds to locating the O atom at the hollow site at 1.7 Bohr above the Ni atoms, thus the O atom is at $(0, 0, -1.2)$ Bohr coordinates. After seven ER iterations, the procedure is observed to stagnate. No change to other algorithm, like HIO, is found to improve the reconstruction. The bottom panels of Fig. 7.7 show the reconstructed PDF of the O atom at two plane cuts of the support region: $x = y$ plane and $z = -1.2$ Bohr plane, respectively. The bright peak feature positions are in perfect agreement with the O atom coordinates.

Left hand panel of Fig. 7.8 shows the evolution of the average error in the intensities as a function of the ER iterations. This error accounts for the difference between the actual “experimental” intensities and the intensities estimated at the n -th iteration, which is given by:

$$E_n^I = \frac{\sum_{\vec{K}} |\sqrt{I(\vec{K})} - |F_n(\vec{K})||^2}{\sum_{\vec{K}} I(\vec{K})} \quad (7.44)$$

This quantity is observed to decrease rapidly at the first iteration, and stagnates at the first iterations. However, this error is not expected to be monotonously decaying as discussed in section 7.3, since our object does not hold the property of being the exact inverse Fourier transform of the diffracted amplitudes. A similar behaviour can be observed at the error in the estimated phases, shown at the right hand panel of Fig. 7.8. This error is

$$E_n^\phi = \frac{1}{N_{\vec{K}}} \sum_{\vec{K}} |\phi(\vec{K}) - \text{Arg}(F_n(\vec{K}))|^2 \quad (7.45)$$

where $N_{\vec{K}} = 4N_\phi N_\theta N_{\theta'}$ is the number of datapoints and $\{\phi(\vec{K})\}$ are the actual backscattered wavefield phases. This error stagnates at the first iterations, too. Its

final value is close to 9° , which is quite low. It has been observed in other phase retrieval works, for both SXRD and LEED [174, 176], that the atomic positions are correctly retrieved even at larger error values in the phase, of the order of tens of degrees, in the average phase.

Example 2

Our next example consists of placing the O atom at a less symmetrical position, $(-0.5, 1.0, -1.2)$ Bohr, as shown at top panel of Fig. 7.9. The other reconstruction parameters are kept at the same values as in Example 1. Panels (a) and (b) of Fig. 7.9 show the reconstructed PDF of the O atom, at plane cuts $y = 1$ and $z = -1.2$ Bohr, respectively. The bright peak features are in agreement with the O atom coordinate, $(-0.5, 1.0, -1.2)$ Bohr. However, the peaks are less intense than the ones obtained in Example 1.

Panels (c) and (d) of Fig. 7.9 show the reconstructed PDF if a sampling of type II is used, instead. The number of incidences are kept at their original values ($N_\phi = 7$, $N_\theta = 11$ and $N_{\theta'} = 25$), but now a single energy $E = 16$ H is used. In this case, reconstruction quality at the OZ axis is poor. This is due to the important lack of datapoints at the $q_z = 0$ region in the Fourier space, ∞ -shaped (see right panel at Fig. 7.4).

Example 3

This example shows that the algorithm is able to retrieve the PDF of more than one atom, at a low symmetry configuration. Back to type I sampling, we have tried retrieving the positions of a O_2 molecule parallel to the Ni atoms, with O atoms placed at coordinates $(\pm 1.5, 1.0, -2.0)$ Bohr. Top panel Fig. 7.10 shows the top view of this cluster. In this example, we have placed the O atoms at a larger vertical distance over the Ni atoms ($z = -2$ Å) so that the MS between them does not spoil the reconstruction. However, the final PDF is fairly fuzzy. The squared PDF at plane cuts $y = 1$ and $z = -2$ Bohr is shown at the bottom panels of Fig. 7.10. By squaring the PDF, the peak features appear enhanced. These peaks are in good agreement with the O atom coordinates, despite the reconstruction being noisy.

7.6 Approach for MS in clusters

In the model calculations above, we have seen that reconstructions lose accuracy when bond lengths are small, i.e. when MS becomes important. Our approach will be similar to the one already used at ordered surfaces recovered by maximum entropy [176], which consists in including first order MS between known and unknown parts of the cluster. However, the case we are dealing with is more difficult, since propagation operators are not plane waves, as it is the case of ordered surfaces.

We shall include the correction at the phase used in the second step of the ER procedure:

$$\text{Arg}(F^{(\text{unk})}(\vec{K}) + F^{(\text{kn})}(\vec{K}) + F^{(\text{ms1})}(\vec{K})) \quad (7.46)$$

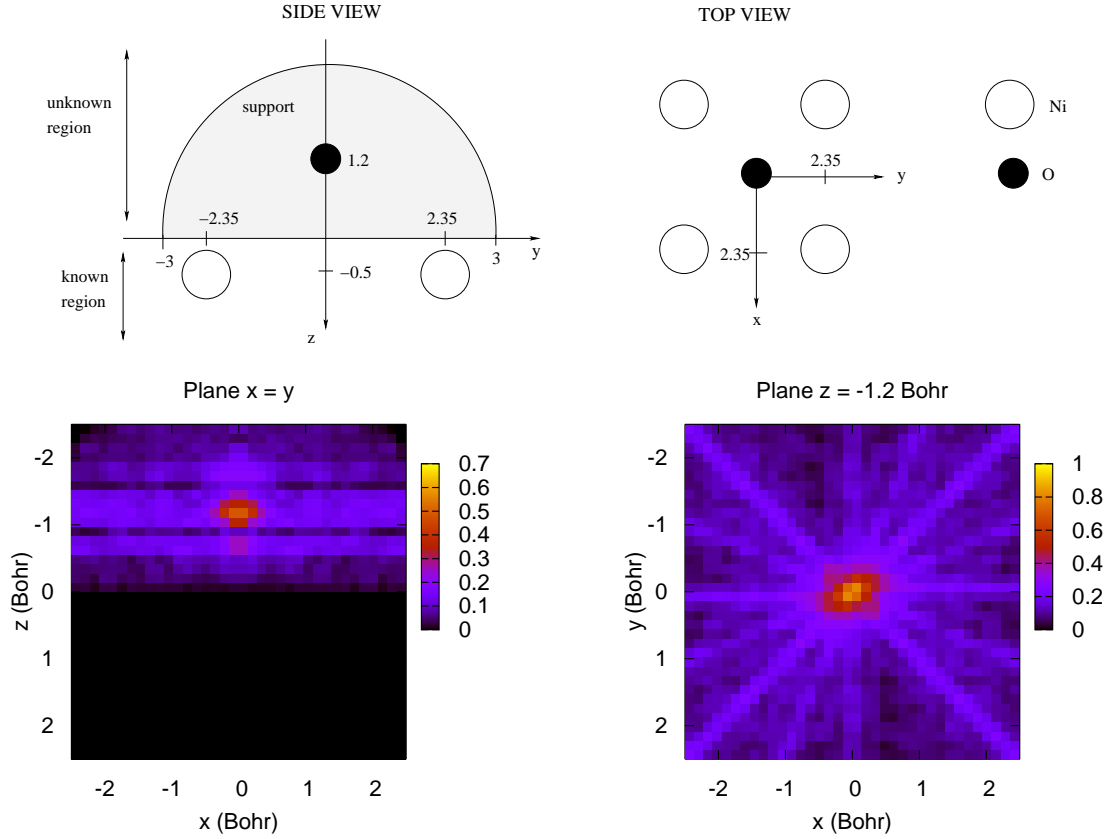


Figure 7.7: Reconstructed PDF for the case of the O atom at hollow position, $(0, 0, -1.2)$ Bohr, over four Ni atoms at $(\pm 2.35, \pm 2.35, 0.5)$ Bohr coordinates. Top panels show schematically the cluster structure. The bottom left panel shows the PDF cut at the $x = y$ plane and the bottom right panel shows the cut at $z = -1.2$ Bohr. Bright features in the plane cuts agree with the O atom actual position.

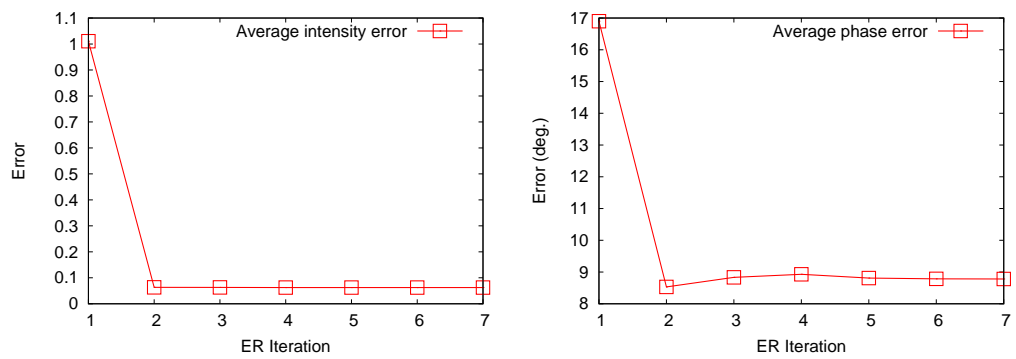


Figure 7.8: Error evolution as a function of ER iterations for the reconstruction of the cluster in Example 1 (see text and Fig. 7.7). Left hand panel represents the average error in the intensities retrieved by ER, and right hand panel represents the average error in the retrieved phase.

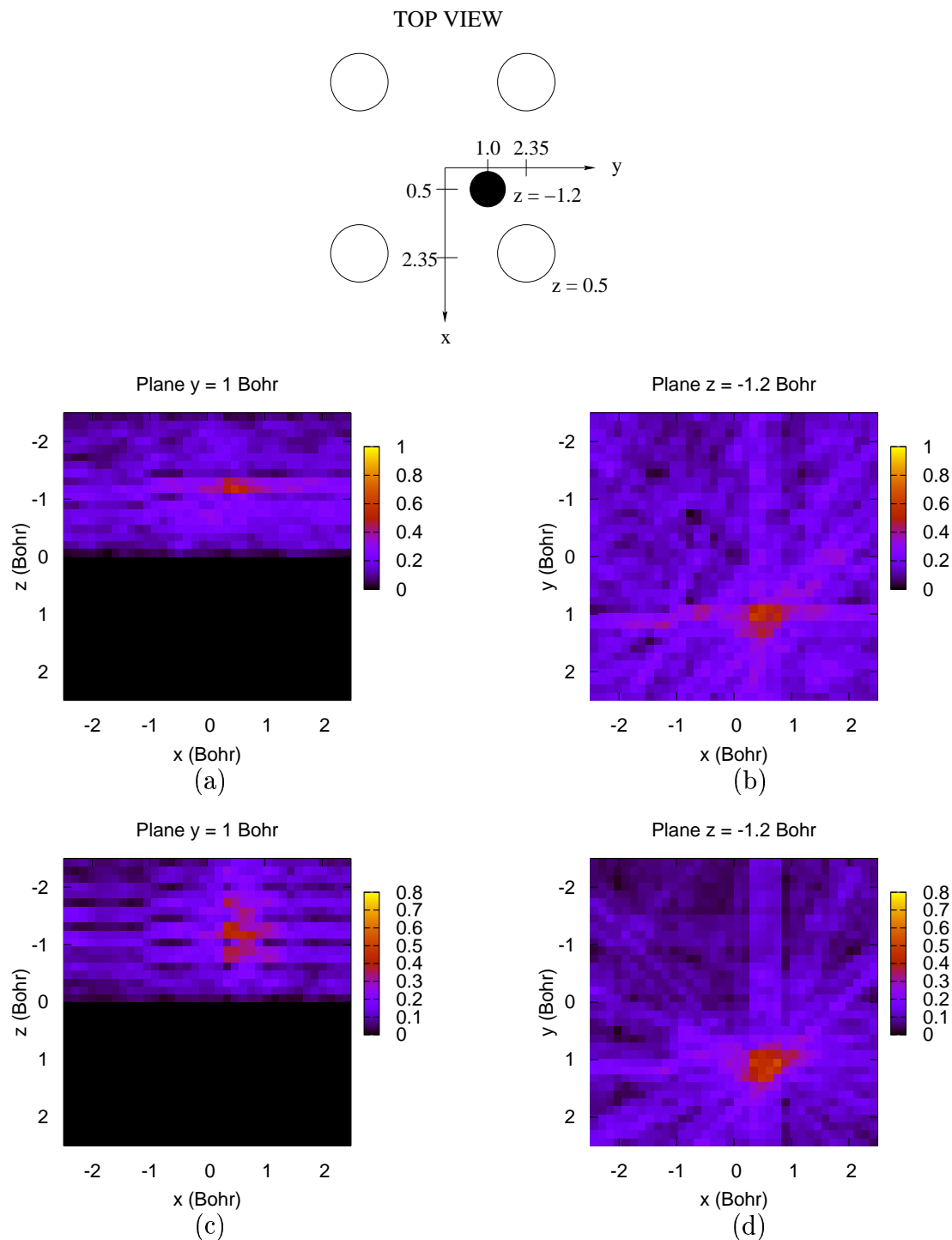


Figure 7.9: Top panel shows the cluster geometry of Example 2, where the O atom occupies a less symmetric position w.r.t. the Ni atoms: $(0.5, 1.0, -1.2)$ Bohr. The other panels show the reconstructed PDF at different plane cuts and for different sampling types. Panels (a) and (b) are $y = 1$ and $z = -1.2$ Bohr plane cuts for the reconstruction obtained from a sampling of type I using four energies (2, 4, 8 and 16 H). Panels (c) and (d) are $y = 1$ and $z = -1.2$ Bohr plane cuts after using a sampling of type II for a single energy of 16 H.

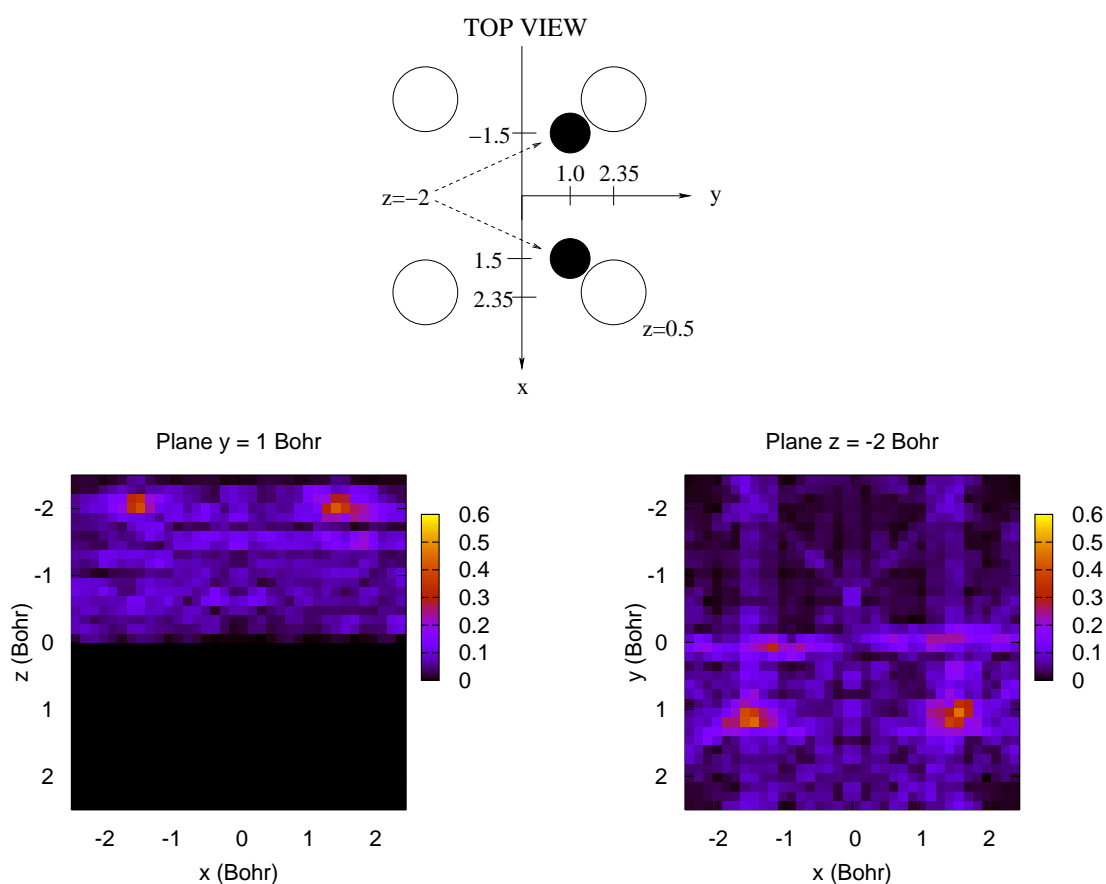


Figure 7.10: Top panels shows the cluster geometry for Example 3, where a O_2 molecule is parallel to the Ni atoms. O atoms occupy positions $(\pm 1.5, 1.0, -2.0)$ Bohr. Bottom panels represent the squared reconstructed PDF of the O atom positions. Left hand panel shows the cut at $y = 1$ and right hand panel at $z = -2$.

where $F^{(\text{ms1})}$ is the term accounting for first order terms of MS between known and unknown parts of the cluster. Actually, we should subtract such a term together with $F^{(\text{kn})}$ from the whole diffracted amplitudes, too, but this approximation should be valid because it is the phase what carries most of the structural information. Removing that term from the amplitude, since it is small, would be similar to invert Fourier using a conventional Wiener filter for noise [44]. In practice, it can be observed that adding such a filter does not improve significantly the reconstruction.

$F^{(\text{ms1})}$ consists of two terms of equal magnitude, travelling these two paths:

1. Emitter \rightarrow Unknown part \rightarrow Known part \rightarrow Detector
2. Emitter \rightarrow Known part \rightarrow Unknown part \rightarrow Detector

where the simplification of considering propagation carried by spherical waves is done. In the case of conventional holography, the second term is not considered, as long as kernels for anisotropy correction are not considered. Thus, the correction is constructed as follows:

$$F^{(\text{ms1})}(k_0\hat{s}_0, \hat{s}) = \int_S d^3\vec{r}_u P(\vec{r}_u) \sum_{j=1}^{N_{unk}} \left\{ e^{-ik_0\hat{s}\cdot\vec{r}_j} f_j^{(\text{kn})}(k_0\hat{s}, \widehat{\vec{r}_u - \vec{r}_j}) \frac{e^{ik_0|\vec{r}_u - \vec{r}_j|}}{|\vec{r}_u - \vec{r}_j|} f^{(\text{unk})}(k_0\widehat{\vec{r}_u - \vec{r}_j}, \hat{s}_0) e^{ik_0\hat{s}_0\cdot\vec{r}_u} + e^{-ik_0\hat{s}\cdot\vec{r}_u} f^{(\text{unk})}(k_0\hat{s}, \widehat{\vec{r}_j - \vec{r}_u}) \frac{e^{ik_0|\vec{r}_j - \vec{r}_u|}}{|\vec{r}_j - \vec{r}_u|} f_j^{(\text{kn})}(k_0\widehat{\vec{r}_j - \vec{r}_u}, \hat{s}_0) e^{ik_0\hat{s}_0\cdot\vec{r}_j} \right\} \quad (7.47)$$

where scattering paths should be read from right to left. The integral is made over positions in the support of the unknown part of the object, and P is an estimate of the sought probability distribution at the current ER iteration. The summation runs over the known atomic positions. Notice that by taking such a spherical wave in the propagation we are neglecting absorption. Such integral is complicated, and we do not need to be very accurate, since the distribution P itself is just an estimation. Thus, we make the following approximation: we neglect angular dependence at the atomic scattering factors, which can be done by substituting the $f^{(\text{unk})}$ factors by their angular average values. Doing so, we obtain:

$$F^{(\text{ms1})}(k_0\hat{s}_0, \hat{s}) = f^{(\text{unk})}(k_0) \sum_{j=1}^{N_{unk}} f_j^{(\text{kn})}(k_0) \left\{ e^{-ik_0\hat{s}\cdot\vec{r}_j} I(-k_0\hat{s}_0, \vec{r}_j) + e^{ik_0\hat{s}_0\cdot\vec{r}_j} I(k_0\hat{s}, \vec{r}_j) \right\}$$

$$I(k_0\hat{s}, \vec{r}_j) = \int_S d^3\vec{r}_u P(\vec{r}_u) e^{-ik_0\hat{s}\cdot\vec{r}_j} \frac{e^{ik_0|\vec{r}_j - \vec{r}_u|}}{|\vec{r}_j - \vec{r}_u|} \quad (7.48)$$

There are two ways of calculating this integral: (i) directly, by summation inside the support and (ii) doing some transformations to get residual integrals. In this second approach, we use

$$\frac{e^{ik_0|\vec{r} - \vec{r}_j|}}{|\vec{r} - \vec{r}_j|} = -\frac{1}{2\pi^2} \int d^3\vec{k} \frac{e^{i\vec{k}\cdot(\vec{r} - \vec{r}_j)}}{k_0^2 - |\vec{k}|^2 + i\delta} \quad (7.49)$$

Substituting in the I integrals, we get

$$I(k_0\hat{s}, \vec{r}_j) = -4\pi \int d^3\vec{k} \frac{e^{i\vec{k}\cdot\vec{r}_j} \tilde{P}(\vec{k} + k_0\hat{s})}{k_0^2 - |\vec{k}|^2 + i\delta} \quad (7.50)$$

(resp. $I(-k_0\hat{s}_0, \vec{r}_j)$), where \tilde{P} is the Fourier transform of the three-dimensional PDF of the unknown region. Making a variable change to bring $-k_0\hat{s}$ to the OZ axis direction,

$$\begin{aligned} I(k_0\hat{s}, \vec{r}_j) &= -4\pi \int \int du dv e^{i(ur_{jx} + vr_{jy})} \int dk_z \frac{e^{ik_z r_{jz}} \tilde{P}(u, v, k_z - k_0)}{k_0^2 - |\vec{k}|^2 + i\delta} \\ &= i4\pi^2 \int \int du dv e^{i(ur_{jx} + vr_{jy})} \frac{e^{(\gamma - k_0)r_{jz}}}{\gamma} \tilde{P}(u, v, \gamma - k_0) \\ \gamma &= \sqrt{k_0^2 - u^2 - v^2} \end{aligned} \quad (7.51)$$

Thus, this way of calculating the integral involves two-dimensional FFTs for each q_z coordinate. The $(u, v, \gamma - k_0)$ coordinates, needed at the evaluation of Eq. (7.51), correspond to points on a hemispherical shell perpendicular to the $-k_0\hat{s}$ direction (resp. the $k_0\hat{s}_0$ direction). However, by the algorithm construction, \tilde{P} takes values on a rectangular grid of the Fourier space. Therefore, to evaluate each of the two-dimensional FFTs of Eq. (7.51), we must calculate the \tilde{P} values at the hemispherical shell points. A convolution method, like UFR, seems to be the most accurate method for this task. As it is computationally expensive, we choose a simple linear interpolation of the rectangular grid points. This choice is justified by the fact that $F^{(\text{ms1})}$ is a term that accounts roughly for all the MS events between the atoms at the known and the unknown regions of the cluster, so that we do not need to be very accurate when estimating it.

7.6.1 Results

We have used the formulas above to improve the reconstruction quality. We have chosen an extreme cluster, though unrealistic, where Ni atoms coordinates are $(1.35, 1.35, 0.5)$, $(1.35, -1.35, 0.5)$, $(-1.35, -1.35, 0.5)$ and $(-1.35, 1.35, 0.5)$ Bohr, and the O atom is adsorbed at hollow position, at $(0.0, 0.0, -1.2)$ Bohr. This geometry is similar to the one examined at Example 1 of previous section, but where the Ni-Ni distances have been contracted. In the present example, O atom is too close to the Ni atoms for the plain algorithm to work, since MS is high. Thus, we will introduce the first order correction shown above. Reconstruction parameters are the same as the ones used at Example 1 of previous section. To calculate the I integrals, we have used Eq. (7.51) rather than explicit sum upon the window function, and we point out that $F^{(\text{ms1})}$ is considered at the phase estimation only, not at total wave and neither at the intensity normalization constant w_n .

The three left hand panels of Fig. 7.11 show the resulting squared PDF of the O atom after seven ER iterations without MS correction. Right hand panels show the resulting squared PDF after performing seven additional ER iterations adding the MS corrective term, $F^{(\text{ms1})}$, in the phase at the fifth step of the algorithm. The PDF

needs to be squared to stress the reconstruction peak features, since the resulting distribution in this case is fuzzy.

If no corrections are made, many artifacts appear in the reconstruction in addition to the peak corresponding to the actual O atom position, $(0, 0, -1.2)$ Bohr. The most striking of the artifacts arises at $(0, 0, -1.2)$ Bohr coordinates. This artifact, which is visible at panels (a) and (b) of Fig. 7.11, is significantly filtered out when introducing the $F^{(\text{msl})}$ term, as it is shown at panels (d) and (e) of the same figure. The peak corresponding to the actual position of the O atom is highlighted by the correction. We can see this by comparing the brightness of the central peaks of panels (c) and (d) of Fig. 7.11.

On the other hand, a set of symmetry related artifacts appear at the $z = -1.2$ Bohr plane cut of the O atom PDF (see panel (c)) and another set is visible at $z = -0.5$ Bohr (see panel (b)). The MS correction is not able to filter out these artifacts.

7.7 Error reduction at ordered surface structure retrieval from LEED-IV

In this section we apply the method shown above to the case of an ordered surface. Our problem will consist in extracting the atomic positions inside the overlayer unit cell from IV curves, when the *a priori* known information about the surface is the substrate structure and the overlayer atoms atomic species. This problem has been studied by Saldin *et al* [175, 176], who solved it using maximum entropy method.

As we have shown in Chapter 2, at section 2.6, due to the translational symmetry, in an ordered surface the electrons are only backscattered in discrete directions, whose parallel components are the reciprocal lattice vectors of the surface, labelled $\{\vec{g}\}$. Thus, in a LEED experiment with incident electron energy E and incident parallel momentum $\vec{k}_{0||}$, the diffraction vectors are

$$\begin{aligned}\vec{K}_{||}(\vec{g}; \vec{k}_{0||}) &= \vec{g} \\ K_z(\vec{g}; \vec{k}_{0||}) &= K_{\vec{g},z}^-(\vec{k}_{0||}) - K_{0,z}^+(\vec{k}_{0||}) \\ &= -\sqrt{2E - |\vec{k}_{0||} + \vec{g}|^2} - \sqrt{2E - |\vec{k}_{0||}|^2}\end{aligned}\quad (7.52)$$

where the subindex 0 indicates the specular beam, $\vec{g} = (00)$. Therefore, the Fourier space sampling in the parallel direction is discrete, at points \vec{g} , and independent from the incidence conditions, while the sampling in the OZ axis for each \vec{g} point can be made continuous by increasing the number of incidences, both in energies E and incidence angles (θ, ϕ) . This sampling is similar to the crystal truncation rods in SXRD. Each point in the database is a function of $(\vec{g}; \vec{k}_{0||}) \equiv (\vec{g}; E, \theta, \phi)$, and the $K_z(\vec{g}; \vec{k}_{0||})$ points in the OZ axis do not constitute a homogeneous sampling.

The parallelism between the ordered surface problem with the cluster problem is clear: $F^{(\text{kn})}$ is the wavefield backscattered from the substrate and $F^{(\text{unk})}$ the wavefield backscattered from the overlayer. Parallel to the substrate, the adsorbate support region is a the surface unit cell, and in the perpendicular direction, the

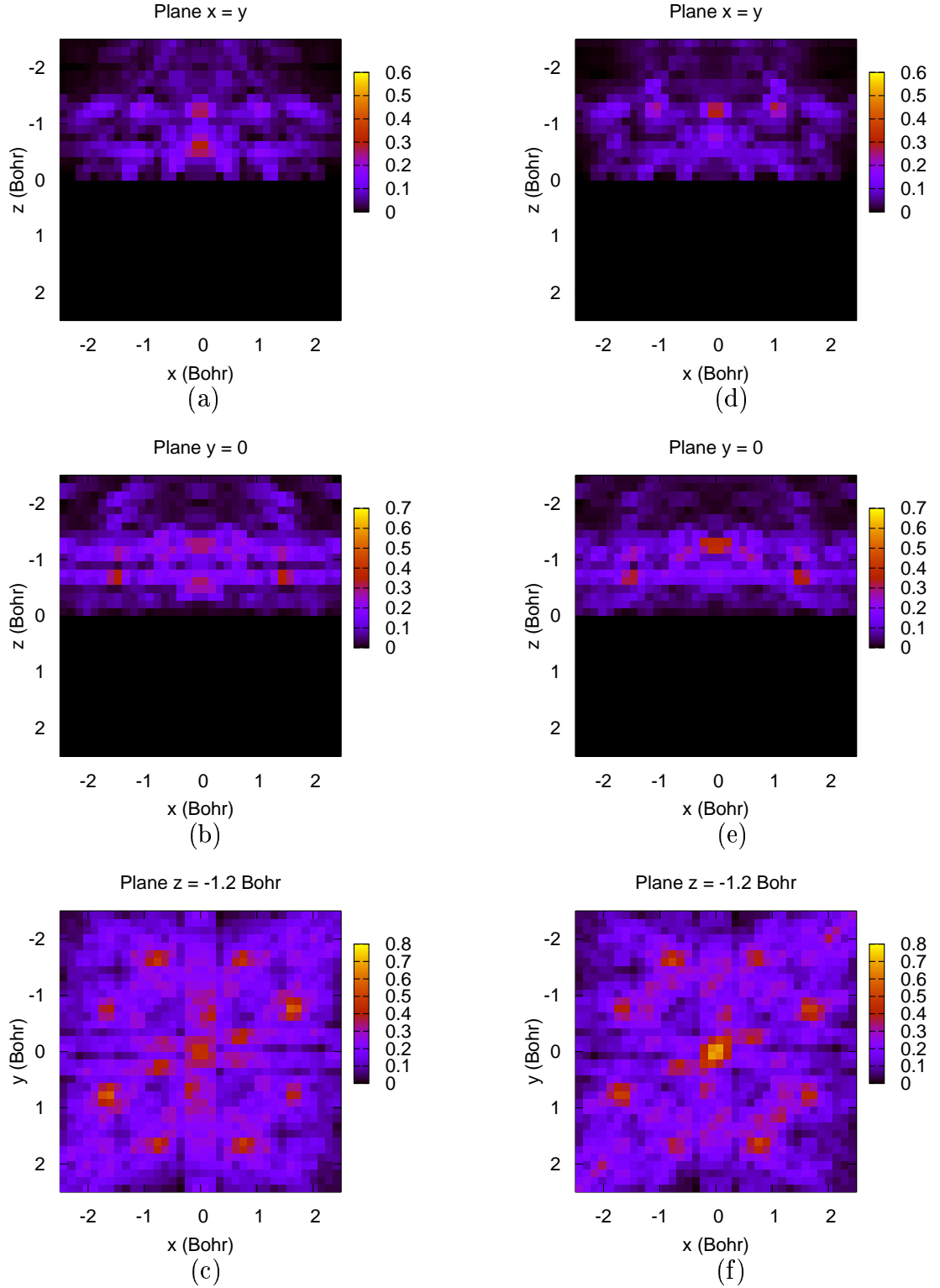


Figure 7.11: Panels (a), (b) and (c) show several plane cuts of the squared reconstructed PDF, using the conventional (Fraunhofer-like) approach, of an example where the O atom is at a hollow site, at $(0, 0, -1.2)$ Bohr but the four underlying Ni atoms are at $(\pm 1.35, \pm 1.35, 0.5)$ Bohr coordinates. Panels (d), (e) and (f) correspond to the squared reconstructed PDF after seven more iterations including a first order MS correction.

support range is the interval $[z_{min} : z_{max}]$ of height values above the substrate. This geometry of this problem is shown on Fig. 7.12. As in LEED calculations, we assume that intensities are to be measured on a plane above the surface, at an origin O . Positions will be referred to that origin in the following. Let B be the label for the substrate slab origin and j the label of each pixel of the adsorbate support region. The corresponding position vectors are shown on Fig. 7.12. At the n -th iteration of the ER process, we have an estimate of the PDF of the adsorbate layer unit cell available, $p_n(\vec{r}_{j0})$, where $\{\vec{r}_{j0}\}$ are position vectors corresponding to a rectangular homogeneous grid inside the support region.

Now, we turn to construct the estimated wavefield at the n -th iteration of the ER process. Let $B_{\vec{g},\vec{g}'}^{-+}(\vec{k}_{0||})$ be the substrate reflection matrix elements, which is known *a priori*, and $A_{\vec{g},\vec{g}'}^{-+}(\vec{k}_{0||})$ and $A_{\vec{g},\vec{g}'}^{++}(\vec{k}_{0||})$ be the adlayer reflection and transmission matrix elements, respectively, for each incident wavevector $\vec{k}_{0||}$. As *a priori* information about the adlayer, we have also the atomic scattering factors and the superstructure symmetry. In general, we will not have a single atom per unit cell. Thus, we can not compute A^{-+} and A^{++} exactly. However, if the adatoms are separated enough from each other, at incidences near the normal, it is a good approximation to neglect the intralayer MS when computing these matrices [175, 176]. Therefore, their matrix elements are just the scattering factors for electron momentum vectors $\vec{K}_{\vec{g}}^{\pm}(\vec{k}_{0||})$. The components of the total reflected wave contributed by the substrate and the adlayer, at the n -th ER iteration, are:

$$\begin{aligned} F^{(kn)}(\vec{K}(\vec{g}; \vec{k}_{0||})) &= P_{\vec{g}}^{OB}(\vec{k}_{0||}) B_{\vec{g},0}^{-+}(\vec{k}_{0||}) P_{\vec{g}}^{BO}(\vec{k}_{0||}) \\ F_n^{(unk)}(\vec{K}(\vec{g}; \vec{k}_{0||})) &= \sum_j p_n(\vec{r}_{j0}) P_{\vec{g}}^{Oj}(\vec{k}_{0||}) A_{\vec{g},0}^{-+}(\vec{k}_{0||}) P_{\vec{g}}^{jO}(\vec{k}_{0||}) \end{aligned} \quad (7.53)$$

where P^{BA} are the plane wave propagation operators from point Q to point Q' , already defined at Chapter 2:

$$P_{\vec{g}}^{Q'Q}(\vec{k}_{0||}) = e^{i\vec{K}_{\vec{g}}^{\pm}(\vec{k}_{0||}) \cdot \vec{r}_{Q'Q}} \quad (7.54)$$

where $\vec{r}_{Q'Q}$ is a vector pointing from Q to Q' . Here, $F_n^{(unk)}$ is constructed with the approximation of considering that the adsorbate is at position \vec{r}_{j0} with probability $p_n(\vec{r}_{j0})$ (*average surface atom approximation* [175, 176]).

First order MS corrective term, $F_n^{(ms1)}$, consists again of the sum of two terms of equal magnitude, travelling these two paths:

1. Emitter \rightarrow Unknown part (adsorbate) \rightarrow Known part (substrate) \rightarrow Detector:

$$F_n^{(ms1,BA)}(\vec{K}(\vec{g}; \vec{k}_{0||})) = \sum_{j,\vec{g}'} P_{\vec{g}}^{OB}(\vec{k}_{0||}) B_{\vec{g},\vec{g}'}^{-+}(\vec{k}_{0||}) p_n(\vec{r}_{j0}) P_{\vec{g}'}^{Bj}(\vec{k}_{0||}) A_{\vec{g}',0}^{++}(\vec{k}_{0||}) P_{\vec{g}'}^{jO}(\vec{k}_{0||}) \quad (7.55)$$

2. Emitter \rightarrow Known part (substrate) \rightarrow Unknown part (adsorbate) \rightarrow Detector:

$$F_n^{(ms1,AB)}(\vec{K}(\vec{g}; \vec{k}_{0||})) = \sum_{j,\vec{g}'} p_n(\vec{r}_{j0}) P_{\vec{g}}^{j0}(\vec{k}_{0||}) A_{\vec{g},\vec{g}'}^{++}(\vec{k}_{0||}) P_{\vec{g}'}^{jB}(\vec{k}_{0||}) B_{\vec{g}',0}^{-+}(\vec{k}_{0||}) P_{\vec{g}}^{BO}(\vec{k}_{0||}) \quad (7.56)$$

Again, we will use $F_n^{(\text{ms1})} = F_n^{(\text{ms1},BA)} + F_n^{(\text{ms1},AB)}$ as a correction in the phase only, not in the total wave.

Reconstruction algorithm steps can be applied here in the same way as in the cluster problem, the only difference being the geometry of sampled points in the Fourier space. The Fourier space constraints are given by the measured IV curves, which constitute the intensity database $\{I(\vec{g}; \vec{k}_{0||})\}$. Thus, the estimate of the amplitude diffracted by the adsorbate unit cell at the n -th iteration is:

$$\begin{aligned} F_n &= F_n^{(\text{unk})} + F^{(\text{kn})} + F_n^{(\text{ms1})} \\ F_n^{(\text{unk})'}(\vec{K}(\vec{g}; \vec{k}_{0||})) &= w_n \sqrt{I(\vec{g}; \vec{k}_{0||})} e^{i \text{Arg}(F_n(\vec{K}(\vec{g}; \vec{k}_{0||})))} - F^{(\text{kn})}(\vec{K}(\vec{g}; \vec{k}_{0||})) \end{aligned} \quad (7.57)$$

where we are using the weight for the IV curves given by Eq. (7.35), as we did in the cluster problem.

Since $\{\vec{g}\}$ form a uniform grid in the parallel direction, the inhomogeneous sampling of the Fourier space occurs in the perpendicular direction, only. Thus, the UFR method is no longer required. Instead, interpolation of datapoints $K_z(\vec{g}; \vec{k}_{0||})$ to an equispaced grid q_z is made in the OZ axis only for each \vec{g} by using, for example, cubic spline. Using a notation equivalent to the one used for the cluster, the inhomogeneous set of $F_n^{(\text{unk})'}(K_z(\vec{g}; \vec{k}_{0||}))$ points for each \vec{g} is interpolated into an equispaced set $G_n^{(\text{unk})'}(\vec{g}; q_z)$. To obtain a real object, and sample the region $q_z > 0$, we apply the symmetry condition $G_n^{(\text{unk})'}(\vec{g}; -q_z) = [G_n^{(\text{unk})'}(-\vec{g}; q_z)]^*$.

Finally, the inverse Fourier transform at the n -th ER iteration is:

$$p_n(\vec{r}_{jO}) = \sum_{\vec{g}} e^{i\vec{g} \cdot \vec{r}_{jO,||}} \sum_{q_z} G_n^{(\text{unk})'}(\vec{g}; q_z) e^{iq_z r_{jO,z}} \quad (7.58)$$

If only one incidence parameter is varied, e.g. if the database consists of a set of IV curves measured at a single incidence direction, a variable change can be made using the Eq. (7.52) to calculate the inverse Fourier transform in the OZ axis directly by integration over equispaced energies, instead of interpolating data at each \vec{g} .

Example

We have applied this procedure at the reconstruction of the overlayer in the O/Ni(100)-c(2×2) surface, with the O atom at a bridge site, from theoretical IV curves at normal incidence. The geometry of this surface is shown schematically at the top panel of Fig. 7.13. The 1×1 surface lattice parameter is $a_0 = 4.705$ Bohr (2.49 Å) and the O atom is at a bridge site, laterally displaced by $0.4a_0$ from the atop position, and at height $0.6a_0$ over the Ni substrate. The support, corresponding to the shaded regions of the figure, has $z_{\min} = 0.3a_0$ and $z_{\max} = a_0$. The vertical gap between the support and the substrate is necessary, since plane wave propagators (Eq. (7.54)) are no longer valid if the distance between atomic planes is small. We take a rectangular grid at the support of $30 \times 30 \times 30$ pixels. Since we know that there is one atom at the c(2×2) unit cell, we can further restrict the support to have the area of the 1×1 substrate unit cell, i.e. to reduced it to one half of the superstructure unit cell. This reduced support corresponds to the dark shaded regions of the figure. Apart from this, no further symmetry considerations are made at the

calculations. The starting PDF for the ER iterations is an uniform distribution in the reduced support.

The database will consist of only 15 energies, $E = 2.0, 2.4, 2.8, \dots 8.0$ H, and the following family of beams (10), (11), (20), (21), (22), and the family $(1/2 \ 1/2)$, $(3/2 \ 1/2)$, $(3/2 \ 3/2)$, $(5/2 \ 1/2)$, $(5/2 \ 3/2)$. Thus, a total number of 57 \vec{g} vectors are used. After performing ten ER iterations, we find that the procedure stagnates. The obtained PDF for the O adlayer, shown at the bottom panels of Fig. 7.13, has acceptable quality, and no artifacts are present. Regarding lateral resolution, the peak corresponding to the O atom position is at the correct xy coordinates, although it is wide. The peak width observed in the corresponding profile ~ 1.9 Bohr (~ 1 Å), to be compared to the STM resolution for oxygen, of several Å. Vertical resolution is good, despite the database being quite small. However, artifact peaks can be observed in the profile. We observe that no significant quality improvement is achieved by adding intensity data taken at off-normal incidences.

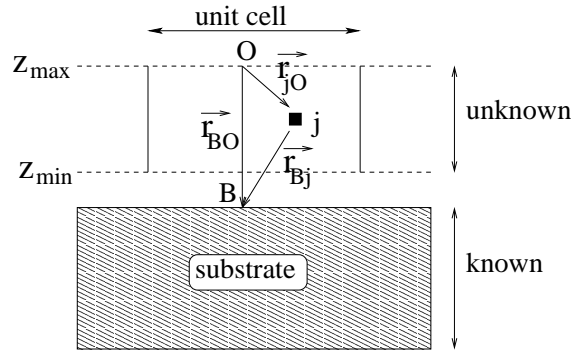


Figure 7.12: Notation for the problem of structure retrieval from intensities in ordered surfaces.

7.8 Conclusions

In the present Chapter we have proposed a direct method for structure determination from diffracted intensities in surface electron diffraction techniques. Our method tries to invert directly the Lippman-Schwinger equation in the Born approximation, by Fourier transform inversion of diffracted amplitudes. The reconstruction problem involves three different problems, that we have solved using imaging techniques and direct techniques previously developed for LEED and PD:

1. Lack of phase information: ER algorithm is used to retrieve it in an iterative procedure.
2. Geometry of collected data: by changing incidence conditions, the Fourier space is covered. However, the sampling is inhomogeneous, so we interpolate the available data into a rectangular grid, where FFT can be easily applied.

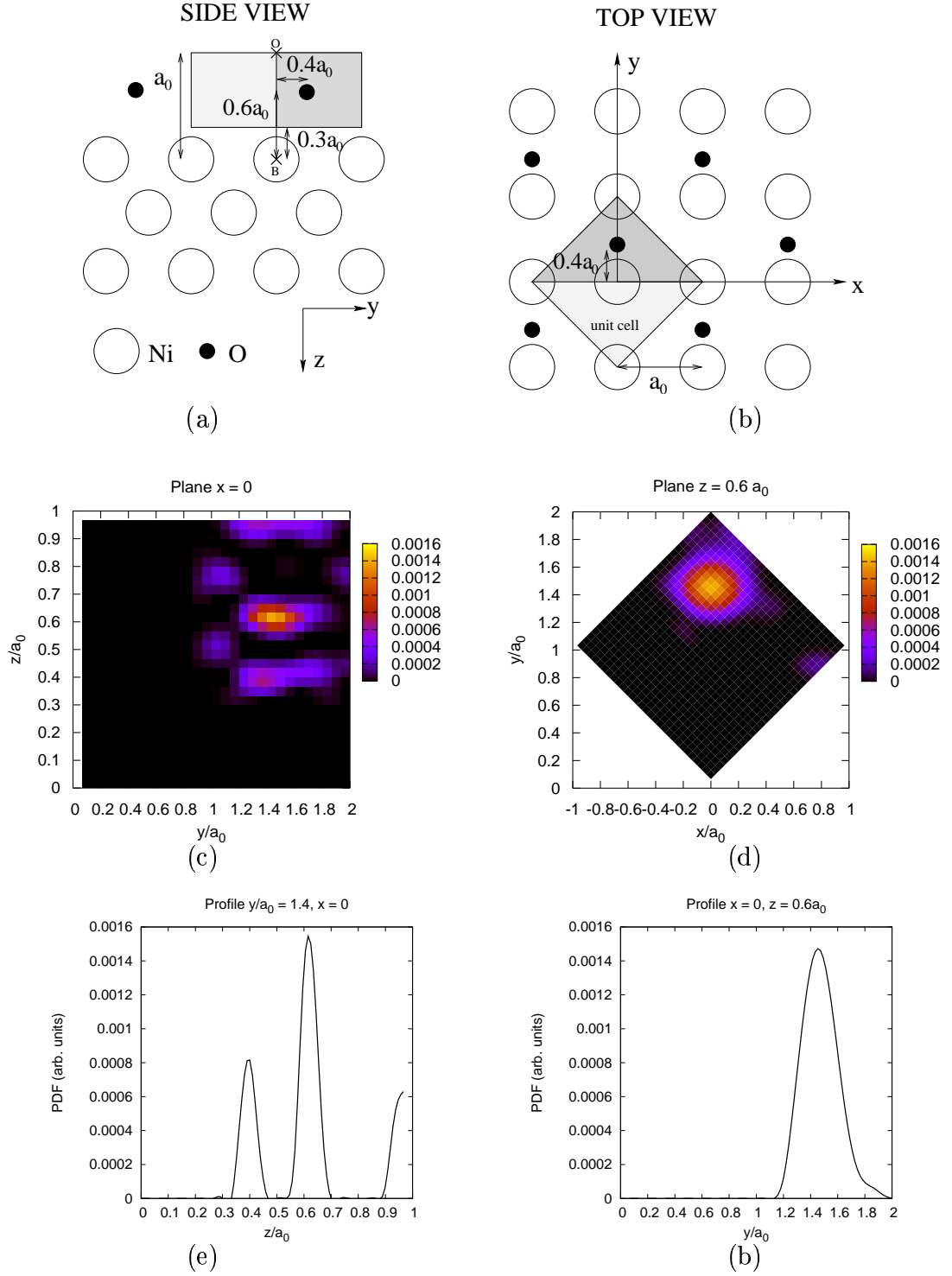


Figure 7.13: Panels (a) and (b): structure of the O/Ni(100)-c(2 × 2) with the O atom at bridge sites. Lattice parameter is $a_0 = 4.705$ Bohr (2.49 Å). Shaded regions correspond to the support used in the calculations. The darker shaded regions are the reduced support obtained from considering a single O atom per c(2 × 2) unit cell. Panels (c) and (d) show two plane cuts of the reconstructed PDF for the overlayer unit cell. Panel (c) corresponds to the $x = 0$ plane cut of the overlayer unit cell, showing a bright peak feature at the correct O atom position, indicated in the “side view” panel above. Panel (d) corresponds to the $z = 0.6a_0$ plane cut, showing a bright peak feature at the correct position, indicated above. Panel (e) corresponds to the profile $y/a_0 = 1.4$ of panel (c), and panel (f) corresponds to the profile $x = 0$ of panel (d).

3. Multiple scattering: using a correcting term of first order, the phase can be improved at each iteration of the error-reduction procedure.

We have applied this methodology to the reconstruction of parts of small clusters of atoms. In particular, we have observed that a fully three-dimensional analysis is not necessary: the structure can be retrieved from two dimensional scans, by reconstructing several projections that are superimposed, as long as enough incidences are used. The number of ER iterations required is very small, compared to other phase retrieval problems. The same methodology can be applied to IV curves from ordered surfaces for retrieving atomic positions in the overlayer, as long as MS between adatoms is weak.

One advantage of this method is that its spatial resolution is double w.r.t. the resolution achieved by HLEED, since we work with Fourier space coverages ranging in values $[-2k_0 : 2k_0]$, whereas HLEED inverts data from an interval $[-k_0 : k_0]$. Twin images are not expected, since we are Fourier inverting amplitudes. When inverting intensities, as in the Patterson function method, we obtain the autoconvolution of the object, so artifacts corresponding to all interatomic vectors may appear. Using our phase retrieval method, eventual artifacts can only be due to uncorrected MS effects. We are working in this direction by inverting the applicability of perturbation theories like TLEED. Finding the unknown adsorbate positions from scratch seems unlikely, since additional scattering paths introduced on the reference structure (the substrate) yield the already mentioned artifacts. On the contrary, in the case we were trying to recover the positions from intensities measured on a structure that differs slightly from the reference structure, no further scattering would be introduced. The existing ones would be modified, but this should not introduce artifacts.

Reconstruction quality is found to be poor in some of the presented case studies on atom clusters, mainly when symmetry is reduced. A more dense grid of ϕ angles can solve this shortcoming. However, in practice, such kind of data acquisition geometries are not efficient. Typical LEED experimental setups use hemispherical detector screens. For example, in a DLEED experiment, for each incidence, our method would make use of a single line cut of the two dimensional detector, and all the other measured intensities would be dismissed. If we want to use the complete data measured at the detector, UFR interpolation must be done in three dimensions, consuming large amounts of computation time. In that case, we would need an alternative tomography technique, such as backpropagation.

Despite the achieved cluster reconstructions being noisy, our method is relevant by itself, since it involves an approach to direct methods in electron diffraction which is completely different from the ones existing in the literature.

Regarding the application to ordered structures, our method presents a feature which is common to maximum entropy, namely that the computer effort needed is independent of the complexity of the adsorbate geometry, since the number of matrix products in the calculations scales as the number of pixels in the support. For the case presented here, our method seems to produce reliable structures with a smaller number of iterations than maximum entropy, where ~ 100 iterations are needed to retrieve the structure [176]. However, trials with more complex adsorbates (e.g. biatomic molecules) show that our method produces a high number of artifacts and stagnates at early stages of the iterative procedure. Nor a larger number of

off-normal incidence datapoints, neither other specialized ER-like phase retrieval algorithms are able to improve the reconstruction. On the other hand, maximum entropy on the same structures has a satisfactory performance, though it converges fairly slow. Using maximum entropy to restore a reconstruction obtained by our method might be a good strategy.

Maximum entropy method can be classified as a “descent method”, since consecutive PDF estimations make the Q functional (Eq. (7.23)) bigger by construction. Thus, it is not guaranteed that the final reconstructed PDF is the global maximum of Q . Our method would be descent-like in case Fraunhofer condition were held between the object and the amplitudes, but this is not true in the case of LEED, except in a perturbative sense.

Chapter 8

Conclusiones / Conclusions

LEED ha sido una de las primeras técnicas empleadas en investigación cuantitativa en ciencia de superficies, y aún hoy sigue siendo una de las principales herramientas para determinar estructuras. Se requiere un grado de precisión alto a la hora de determinar la estructura de una superficie, ya que esto tiene importantes consecuencias en el estudio de procesos químicos en superficies, como catálisis heterogénea, propiedades electrónicas, etc. A pesar del desarrollo de otras técnicas para superficies, en muchos laboratorios se sigue empleando LEED por la sencillez de los equipos experimentales requeridos, en comparación con otros métodos, y su alta sensibilidad a los parámetros de la superficie. La principal característica teórica de LEED es que necesita un formalismo de dispersión múltiple para describir los espectros de difracción con suficiente precisión. Este formalismo se propuso para LEED en los años sesenta, y desde entonces han sido varias las mejoras y técnicas desarrolladas.

El principal inconveniente de los cálculos de LEED es la eficiencia computacional, ya que la dispersión múltiple los convierte en cálculos muy costosos. Además, los espectros no se pueden invertir, en principio, para obtener directamente la estructura, que debe ser determinada a partir de un procedimiento de prueba y error. Las razones son la dispersión múltiple junto con la imposibilidad de medir fases experimentalmente. Por ello, los algoritmos de búsqueda y los métodos directos son importantes líneas de investigación en teoría de LEED. En resumen, podemos distinguir tres puntos principales donde la teoría de LEED puede mejorarse: (i) evaluación eficiente de los espectros de difracción para un modelo de superficie dado, (ii) procedimientos de búsqueda optimizados para disminuir el número de estructuras visitadas, y (iii) desarrollo de métodos directos para recuperar información acerca de la estructura mediante inversión directa del espectro.

El objetivo global de esta Tesis ha sido introducir nuevas mejoras en la metodología en estos tres puntos. En cuanto a los cálculos de espectros, se ha hecho un amplio estudio para mejorar la descripción de adsorbatos moleculares en los cálculos. En cuanto a los algoritmos de búsqueda, hemos propuesto uno novedoso. Además, hemos trabajado en métodos directos, reuniendo técnicas que van desde LEED holográfico hasta tomografía de difracción y métodos típicos de óptica para recuperación de fases.

Hemos desarrollado y probado en varias superficies modelo el método propuesto por Andersson y Pendry [38] para manejar moléculas como si fueran entidades rígidas dentro de los códigos de LEED. Este método empieza por calcular una matriz-T para

la molécula, que contenga toda la información acerca de la dispersión múltiple, de tal forma que se pueda emplear dentro de un código convencional de LEED como una matriz-t genérica (no diagonal). Esta técnica permite aplicar a la molécula movimientos rígidos que no la distorsionen, como vibraciones, rotaciones y traslaciones. Su eficacia, desde el punto de vista computacional, se basa en el hecho de que esta matriz-T se calcula una vez para cada energía y se almacena. El tiempo de cálculo se reduce, ya que no es necesario separar el adsorbato molecular en varios planos atómicos. Hemos comprobado que los factores-R entre el cálculo convencional y este método se encuentra siempre por debajo de 0.1. Además, se puede utilizar una orientación de alta simetría de la molécula a la hora de calcular su matriz-T, ya que la matriz contiene un mayor número de ceros en esa configuración, reduciéndose, por tanto, la memoria requerida para almacenarla. Una vez calculada, la matriz se puede rotar rápidamente sin pérdidas significativas de precisión.

La flexibilidad de la matriz-T molecular para describir los movimientos rígidos de la molécula se puede extender utilizando el método Tensor LEED. En primer lugar, se hace un cálculo de referencia utilizando, en lugar de la molécula, un pseudo-átomo caracterizado por una matriz-t que contiene sólo los elementos diagonales de la matriz-T de la molécula. Después, los términos extradiagonales se añaden en forma de perturbación. A pesar de que teóricamente no está garantizado que este procedimiento introduzca una perturbación pequeña, el espectro obtenido finalmente guarda un acuerdo aceptable con el calculado dinámicamente. El cálculo realizado de este modo es rápido. Este procedimiento se puede incluir en una búsqueda estructural de parámetros que afecten a la molécula rígida, tales como su sitio de adsorción o su ángulo de inclinación. Esto se puede hacer fácilmente añadiendo no los términos extradiagonales de la molécula, sino todos los términos de la matriz-T de la molécula girada o desplazada. Para el caso examinado en este trabajo, CO/Cu(100)-c(2×2), este formalismo da cuenta de ángulos de inclinación de hasta 15° , manteniendo el factor-R de comparación con el método habitual por debajo de 0.1.

Por otra parte, uno puede querer utilizar configuraciones de la molécula que suponen una pequeña distorsión respecto de su configuración original. En esta Tesis, hemos desarrollado un método basado en la aproximación Tensor LEED que calcula la matriz-T de moléculas con vectores interatómicos ligeramente distorsionados. Es un procedimiento rápido ya que no necesita invertir matrices, y su precisión está asegurada si los desplazamientos son pequeños, dentro del mismo rango de validez de Tensor LEED, $\sim 0.4 \text{ \AA}$. Este formalismo se puede emplear para describir modos de vibración de la molécula.

La conclusión general de esta parte de la Tesis es que las moléculas pueden ser descritas adecuadamente dentro de la teoría de LEED como entidades rígidas, contrariamente al método convencional, donde las capas moleculares se dividen en planos atómicos, perdiendo la identidad química molecular. El método mostrado en este trabajo presenta ventajas tanto desde el punto de vista computacional como desde el punto de vista de la descripción física o química de las moléculas, permitiendo una mejor descripción del comportamiento térmico o de la geometría de adsorción. Esto tiene implicaciones importantes, ya que gran parte del trabajo en ciencia de superficies concierne a los adsorbatos moleculares, que en muchos casos

varían poco su estructura respecto de la que tienen en su fase gaseosa.

Hemos desarrollado un nuevo algoritmo de búsqueda global más eficiente que otros algoritmos similares existentes. Se ha llamado algoritmo de *Optimización Simultánea* (SO), y está organizado en dos niveles. SO construye proyecciones del factor-R sobre bases de datos reducidas, donde se pueden hacer búsquedas rápidas. Las estructuras resultantes se verifican posteriormente utilizando la base de datos completa. Como los mapas parciales del factor-R contienen características comunes con el mapa global, las soluciones obtenidas a partir de ellos consituyen una estrategia mejor que las búsquedas aleatorias usuales sobre la hipersuperficie del factor-R global, ya que dentro del primer nivel el algoritmo realiza un menor número de evaluaciones de intensidad. Las estadísticas de las búsquedas realizadas con SO muestran una gran eficacia tanto desde el punto de vista del número de estructuras visitadas como de la ley de escala del algoritmo con el número de parámetros presentes en la búsqueda. Los histogramas del número de estructuras pueden explicarse mediante la distribución de Poisson de un suceso aleatorio, suceso que correspondería a encontrar la estructura solución. Para curvas IV de la superficie Ir(110)-p(2 × 1) *missing row* simuladas sin ruido, las ley de escala obtenida para SO tiene un exponente $\beta = 4$, que debe compararse con $\beta = 6$ obtenido mediante SA, trabajando en las mismas condiciones. SO necesita 300 estructuras para recuperar tres parámetros con una probabilidad de éxito próxima al 100%, mientras que SA necesita 2500 y GA necesita 800 en condiciones similares.

Los efectos de trabajar con datos experimentales reales se pueden modelizar añadiendo un ruido aleatorio a las intensidades simuladas, Nuestra propuesta para esta situación consiste en añadir varios datos más al construir los mapas parciales del factor-R. Haciendo esto, los mínimos espúreos debidos a fluctuaciones por ruido se pueden filtrar.

Hemos hecho una contribución novedosa a los métodos directos en LEED, alternativa a las que se encuentran en la literatura, como LEED holográfico o función de Patterson. Estos métodos hacen un análisis de Fourier de las intensidades difractadas, mientras que nuestra aproximación consiste en invertir Fourier las amplitudes. Como los experimentos no pueden proporcionarnos la fase de la onda difractada, hemos utilizado métodos de recuperación de fase comunes en óptica, que son habituales en monitorización y que han tenido éxito en muchos trabajos de cristalografía de rayos-X. Al igual que en las últimas implementaciones de HLEED y función de Patterson, hemos analizado bases de datos grandes, construidas con espectros tomados para distintas energías y direcciones de incidencia. Esto ayuda a disminuir el efecto de reconstrucción borrosa que la dispersión múltiple produce en los métodos mencionados, ya que permiten retener la dispersión de primer orden y filtrar la de órdenes más altos. En nuestro caso, en principio, esta clase de bases de datos no reducen el efecto de la dispersión múltiple, ya que nuestro método trabaja sobre la base de dispersión simple, es decir, cuando objeto y espectro se relacionan mediante transformada de Fourier (equivalente a las condiciones de Fraunhofer en óptica). Es necesario utilizar varias condiciones de incidencia para obtener un muestreo mas denso del espacio de Fourier, de forma que la transformada inversa sea más precisa utilizando técnicas de tomografía. Hemos introducido dispersión múltiple en primer orden de aproximación para construir términos de corrección, calculados

explícitamente, durante las iteraciones de recuperación de fase.

En resumen, hemos desarrollado un procedimiento de reconstrucción a partir de intensidades difractadas que contiene ingredientes de métodos directos de LEED, tomografía y recuperación de fase convencional. Los modelos empleados para chequear este método han sido pequeños *clusters* de átomos, que pueden considerarse modelos reducidos de una superficie con un adsorbato de tipo red gaseosa. En varias geometrías se muestra el efecto borroso que la dispersión múltiple produce en la calidad de la reconstrucción cuando las longitudes de enlace son pequeñas ($\lesssim 1$ Å) y cómo las correcciones de primer orden pueden ayudar a reducir el ruido.

Todo este trabajo metodológico ha producido un notable número de códigos. Dos de los programas desarrollados durante esta Tesis han sido publicados y están disponibles en la CPC Library en las referencias [54] y [141]. Sus nombres son TMOL y LEED90 respectivamente, ambos escritos en FORTRAN-90/95. El primero es un código que calcula matrices-T moleculares y el segundo es un código convencional de LEED-IV. LEED90 tiene la particularidad de ser el primer código de LEED que puede manejar adsorbatos de matrices-t no diagonales, y ha sido empleado para chequear la aplicabilidad del método de matrices-T moleculares. A pesar de que otros códigos de LEED han sido implementados con vistas a la optimización de recursos computacionales, LEED90 se ha escrito con el objetivo de ser simple y modular, para uso académico y para probar los métodos propuestos durante esta Tesis. Además de estos dos, se han escrito otros códigos que no se han publicado. Por ejemplo, DeltaTMOL para calcular las matrices-T de moléculas distorsionadas y BRYLEED para búsquedas estructurales combinando el algoritmo SO con las rutinas de LEED90. Además, el paquete TensErLEED [70] se ha modificado para que pueda manejar matrices-T moleculares. Asimismo, se han hecho diferentes implementaciones de inversión directa de intensidades difractadas.

Finalmente, en paralelo al trabajo metodológico y computacional en teoría de LEED, se ha llevado a cabo una determinación estructural a partir de datos experimentales de LEED-IV. La superficie estudiada ha sido el rutilo $\text{TiO}_2(110)\text{-}1 \times 2$. Las superficies de TiO_2 son un importante objeto de estudio en ciencia de superficies, debido a sus aplicaciones en catálisis heterogénea, fotocatalisis y como sensor de gases. Este trabajo ha supuesto el primer estudio cuantitativo de LEED-IV de la reconstrucción 1×2 . Hemos obtenido un factor-R de Pendry $R_P = 0.28$, que es muy razonable y similar al conseguido en un análisis previo de LEED-IV de la superficie 1×1 [87]. El trabajo de LEED presentado en esta Tesis es parte de un estudio más amplio, completado por resultados de STM y DFT. Tras unas pruebas preliminares sobre varios modelos de la literatura, encontramos que es el modelo de Onishi y colaboradores el que produce el factor-R más pequeño [91]. Este modelo consiste en filas añadidas de estequiometría Ti_2O_3 . Durante el análisis se han incluido tanto parámetros estructurales como vibracionales. Hemos encontrado que las vibraciones térmicas de las últimas capas son importantes a la hora de determinar la estructura relajada, y que sus valores en los grupos Ti_2O_3 están fuertemente acentuados respecto a los valores de las amplitudes de vibración de los átomos dentro del sólido. Por medio de LEED solamente, se hallan dos estructuras con relajaciones diferentes que producen mínimos en el factor-R, siendo la diferente altura del oxígeno más externo el parámetro más relevante que las distingue. Una de estas dos estructuras

se puede descartar mediante comparación con la estructura proporcionada por los cálculos DFT. La otra guarda un acuerdo aceptable con las posiciones atómicas proporcionadas por DFT. Como hallazgo interesante, la configuración de mínima energía muestra una característica electrónica curiosa: la superficie es conductora en la dirección de las filas Ti_2O_3 , pero es aislante en la dirección perpendicular a aquéllas.

LEED has been one of the first techniques used for quantitative surface science research, and it remains nowadays as one of the main tools for structure determination. A high degree of precision is required when determining surface structures, since it has important consequences in the study of chemistry processes at surfaces, such as heterogeneous catalysis, electronic properties, etc. In spite of the development of other surface techniques, LEED is still widely used at many laboratories for the simplicity of the experimental setup needed, in comparison with other methods, and its high sensitivity to surface parameters. The main theoretical feature of LEED is that it needs a multiple scattering formalism to describe spectra with enough accuracy. This formalism was first proposed for LEED in the sixties, and a number of improvements and related techniques have been developed since then.

The main drawback of LEED calculations has always been the computational efficiency, since multiple scattering makes them very demanding. Besides, the spectra can not be inverted, in principle, to directly obtain the structure, which must be determined from a trial and error procedure. The reasons are the multiple scattering together with the impossibility of measuring the phase experimentally. Therefore, important lines of investigation in LEED theory are search algorithms and direct methods. Thus, we can distinguish three main points where LEED theory still needs to be improved: (i) efficient spectra evaluation for a given surface model, (ii) optimized search procedures to diminish the number of trial structures, and (iii) development of direct methods to retrieve structural information from direct inversion of spectral data.

The global aim of this thesis has been to introduce new methodological improvements at all these three parts. Regarding spectral calculation, a thorough study of a method to improve management of molecular adsorbates at spectra evaluation has been done. Regarding search algorithms, a new one has been proposed. Besides, some work on direct methods has been carried out, gathering techniques ranging from Holographic LEED to diffraction tomography and phase retrieval methods, typical from optics.

The method proposed by Andersson and Pendry [38] to handle molecules as rigid entities inside LEED codes has been developed and benchmarked in a number of model surfaces. It starts by calculating a T-matrix for the molecule, containing all the intramolecular multiple scattering information, so that it can be used in a conventional LEED code as a generic (non-diagonal) t-matrix. This technique allows to perform rigid movements of the molecule as a whole, for example, vibrations, rota-

tions and translation. Its efficiency from the computational point of view is based in the fact that this T-matrix is computed once for each energy and stored, reducing spectra evaluation time, since no further splitting of the molecular adsorbate by atomic planes is needed. We have checked that the R-factors between conventional methods and this one are always below 0.1. Besides, a symmetric orientation for the molecule can be used to compute its T-matrix, since the T-matrix in such a configuration should be a sparse matrix, reducing storage space requirements. Once computed, it can be quickly rotated with no significant loss of accuracy.

This flexibility of the molecular T-matrix when describing rigid movements of the molecule as a whole can be further exploited using the Tensor LEED approach. A reference calculation is carried out using a pseudo-atom characterized by only the diagonal terms of the molecular T-matrix. Then, the extra-diagonal terms are added as a perturbation. Even if theoretically it is not guaranteed that this procedure introduces a small perturbation, the final spectra are in acceptable agreement with the full-dynamically calculated one. The spectra evaluation is fast using this approach. We can introduce this procedure in a structure search for parameters affecting the whole molecule, such as its adsorption site or tilt angle. This can be done easily by adding not the original molecule extradiagonal terms, but those of a displaced or rotated molecule. For the examined case, CO/Cu(100)-c(2×2), tilt angles of up to 15° can be accounted for with this formalism, keeping the R-factor with the conventional method under 0.1.

However, one may wish to use slightly distorted configurations of the molecule. In this Thesis, we have developed a method, based on the Tensor LEED approach, that computes the T-matrix of the molecules with slightly different interatomic vectors. It is a fast procedure, since it does not need matrix inversion, and its accuracy is ensured if atomic displacements are small, belonging to the same validity range as the Tensor LEED approach, ~ 0.4 Å. This formalism can be used to describe molecule vibrations.

The general conclusion from this part of the Thesis is that molecules are better described in LEED if they are considered as individual entities, contrary to the common method, that splits molecular layers into atomic planes, losing their chemical identity. Advantages of this method are both from the point of view of the computational efficiency and of the physical or chemical description of the molecules, allowing a better description of thermal dynamics or adsorption geometry. This has important implications, since a great deal of work in surface science concerns systems with molecular adsorbates, where the molecule structure is fairly similar to that of its gas phase.

A new global directed search algorithm has been introduced that outperforms similar existing ones. The algorithm has been called *Simultaneous Optimization* (SO), and it is organized in two levels. It constructs projections of the R-factor on reduced databases, where fast searches can be made. The resulting structures are afterwards verified using the complete database. Since the partial R-factor maps contain many features in common with the global one, those solutions make a better strategy than usual random blind searches on the global R-factor hypersurface, since it performs a smaller number of intensity evaluations at the first level. The statistics of the searches show a very efficient performance from both the point of view of

the number of visited structures and the scaling law with the number of search parameters. Histograms of the number of structures can be explained by a Poisson distribution of one random event, an event that corresponds to the structure solution finding. For simulated noiseless IV curves from Ir(110)-p(2 × 1) missing row surface, the obtained scale law exponent for SO is $\beta = 4$, to be compared to $\beta = 6$ of SA, working under the same conditions. SO needs 300 trial structures to retrieve three parameters with a success probability close to 100%, whereas SA needs 2500 and GA needs 800 under similar conditions.

The effect of working with real experimental data can be modelled by adding random noise to the simulated intensities. Our proposal to deal with this situation is to add a few more datapoints when constructing the partial R-factor map. By doing this, spurious minima due to noise fluctuations are filtered out.

We have made a novel contribution to direct methods in LEED, alternative to those already put forward in the literature, such as Holographic LEED and Patterson function. These methods make a Fourier analysis of the diffracted intensities, whereas our approach consists of directly Fourier inverting the diffracted amplitudes. As the experiments are unable to provide the diffracted wavefield phase, we have used typical iterative phase retrieval techniques imported from optics, which are usual at imaging methods and have been successful in many X-ray crystallography works. As in the later implementations of HLEED and Patterson function, we have analyzed enlarged databases, made of spectra taken at different energies and incidence directions. This helps to diminish the blurring effect on the reconstruction that multiple scattering produces in the mentioned methods, since they are implemented in such a way that they retain first order multiple scattering, while higher order components are filtered out by addition of data. In our case, these kind of databases do not, in principle, reduce the multiple scattering, since our phase retrieval methodology works only in the case of single scattering diffraction, i.e., when object and spectra are related by Fourier transform (equivalently to Fraunhofer conditions in optics). Using several incidence conditions is necessary to obtain more dense samplings of the Fourier space, so that inversion is more accurate, using tomography techniques. We have introduced first order multiple scattering events to construct corrective terms, explicitly calculated, during the phase retrieval iterations.

Summarizing, we have developed a procedure for reconstruction from diffracted intensities containing ingredients from conventional LEED direct methods, tomography and conventional phase retrieval. The model systems used to benchmark this approach have been small clusters of atoms, that can be seen as a reduced models of a surface with a lattice gas adsorbate. Several geometries show the blurring effect of the multiple scattering in the reconstruction quality when bond lengths are small ($\lesssim 1 \text{ \AA}$) and how the first order corrections help to reduce the noise.

Our methodological work has produced a number of computer codes. Two of the programs developed during this Thesis have been published and are available from the CPC Library at references [54] and [141]. Their names are TMOL and LEED90 respectively, both of them written in FORTRAN-90/95. The former is a code that computes molecular T-matrices and the later is a conventional LEED-IV code. LEED90 has the particularity that it can handle adsorbate layers of non-diagonal t-matrices, and it has been used to check the applicability of the molecular

T-matrix method. Despite other LEED codes having special computer saving features, LEED90 has been written with the aim of simplicity and modularity, for academic use and testing of the methods proposed throughout the Thesis. Apart from these two published codes, a number of other unpublished codes have been written. For example, the DeltaTMOL code for calculating the T-matrix of distorted molecules, and BRYLEED for structural searches combining SO algorithm and LEED90 routines. Besides, the TensErLEED package [70] has been modified to handle molecular T-matrices. Different implementations for direct inversion of spectral data have been made, too.

Finally, apart from the methodological and the computational work on LEED theory, a structure determination from experimental LEED-IV data has been made. The surface under study has been rutile $\text{TiO}_2(110)\text{-}2 \times 1$. TiO_2 surfaces are important subjects of study in surface science due to its applicability on heterogeneous catalysis, photocatalysis and gas sensing. The present work has been the first quantitative LEED-IV study of the 2×1 reconstruction. We have achieved a Pendry R-factor $R_P = 0.28$, which is very reasonable and similar to the one achieved on a previous LEED-IV analysis for the 1×1 surface [87]. The LEED work presented in this Thesis is part of a more comprehensive analysis, completed by STM and DFT results. After a preliminary test of a number of model surfaces proposed in the literature, we find that Onishi and co-workers' model is the one that yields the smaller R-factor [91]. This model consists of added rows of Ti_2O_3 stoichiometry. During the analysis, both structural and vibrational parameters have been included. We have found that thermal vibrations of the overlayer atoms are important when determining the relaxed structures, and their values at the Ti_2O_3 groups are strongly enhanced w.r.t. bulk atoms vibration amplitudes. By LEED means only, two different relaxed structures can be found that produce a minimum at the R-factor, being the different height of the two topmost oxygen atoms its defining feature. One of the structures can be ruled out by comparison with DFT calculations. The other holds acceptable agreement with the atomic positions provided by DFT. Interestingly, the minimum energy configuration shows a curious electronic feature: the surface is a conductor in the Ti_2O_3 rows direction but it is an insulator in the perpendicular direction.

Appendix A

Green propagators in spherical wave basis

$\tilde{G}_{OI}^{vv'}$ is an operator that translates incoming spherical waves at $\vec{r}_{v'}$ position into outgoing spherical waves at \vec{r}_v . Its matrix elements, $G_{lm,l''m''}^{OI}(\vec{r}_{v'} - \vec{r}_v)$, are defined by

$$h_l^{(1)}(\kappa|\vec{r} - \vec{r}_v|)Y_{lm}(\vec{r} - \vec{r}_v) = \sum_{l''m''} G_{lm,l''m''}^{OI}(\vec{r}_{v'} - \vec{r}_v)j_{l''}(\kappa|\vec{r} - \vec{r}_{v'}|)Y_{l''m''}(\vec{r} - \vec{r}_{v'}) \quad (\text{A.1})$$

with the following explicit expression:

$$G_{lm,l''m''}^{OI}(\vec{R}) = \sum_{l'm'} 4\pi i^{l-l'-l''} (-1)^{m'+m''} h_{l'}^{(1)}(\kappa R) Y_{l'-m'}(\vec{R}) \int Y_{lm} Y_{l'm'} Y_{l''-m''} \quad (\text{A.2})$$

The validity range of this operator is: $|\vec{r} - \vec{r}_{v'}| \leq |\vec{r}_v - \vec{r}_{v'}|$. Similarly, $\tilde{G}_{II}^{vv'}$ is an operator that translates incoming spherical waves at $\vec{r}_{v'}$ position into incoming spherical waves at \vec{r}_v . Its matrix elements, $G_{lm,l''m''}^{II}(\vec{r}_{v'} - \vec{r}_v)$, are defined by

$$j_l(\kappa|\vec{r} - \vec{r}_v|)Y_{lm}(\vec{r} - \vec{r}_v) = \sum_{l''m''} G_{lm,l''m''}^{II}(\vec{r}_{v'} - \vec{r}_v)j_{l''}(\kappa|\vec{r} - \vec{r}_{v'}|)Y_{l''m''}(\vec{r} - \vec{r}_{v'}) \quad (\text{A.3})$$

$$G_{lm,l''m''}^{II}(\vec{R}) = \sum_{l'm'} 4\pi i^{l-l'-l''} (-1)^{m'+m''} j_{l'}(\kappa R) Y_{l'-m'}(\vec{R}) \int Y_{lm} Y_{l'm'} Y_{l''-m''} \quad (\text{A.4})$$

Due to the triangular property of Gaunt coefficients (the integral of three spherical harmonics) [136], the summations are done for $l' = 0 \dots 2l_{\max}$.

Appendix B

Gaunt coefficients

In quantum mechanics, the integral of three spherical harmonics appears in calculations involving addition of angular momentum. It is called Gaunt's integral [136, 148]:

$$\begin{aligned} g_{l_1 m_1 \ l_2 m_2 \ l_3 m_3} &= \int_0^\pi d(\cos\theta) \int_0^{2\pi} d\phi Y_{l_1 m_1}(\theta, \phi) Y_{l_2 m_2}(\theta, \phi) Y_{l_3 m_3}(\theta, \phi) \\ &= \sqrt{\frac{(2l_1 + 1)(2l_2 + 1)(2l_3 + 1)}{4\pi}} \\ &\quad \times \begin{pmatrix} l_1 & l_2 & l_3 \\ m_1 & m_2 & m_3 \end{pmatrix} \begin{pmatrix} l_1 & l_2 & l_3 \\ 0 & 0 & 0 \end{pmatrix} \end{aligned} \quad (\text{B.1})$$

The parenthesis are Wigner 3_{jm} symbols. These coefficients are non-zero only if:

1. $m_1 + m_2 + m_3 = 0$ (physical condition).
2. $|l_2 - l_3| \leq l_1 \leq l_2 + l_3$ (triangular condition).
3. $(-1)^{l_1 + l_2 + l_3} = 1$ ($l_1 + l_2 + l_3$ is even).

Appendix C

Poisson probability distribution derivation

The Probability Density Function (PDF) of a random event, $p(t)$, is the probability of occurrence of that event in a time interval between t and $t + dt$ [205, 206]. Mapping to structure finding algorithms, $p(t)$ is the probability of finding one solution when using a number of function calls between t and $t + dt$. The global (or cumulative) probability of an event happening in a period t , $P(t)$ is found by integrating the PDF:

$$P(t) = \int_{-\infty}^t p(t') dt' \quad (\text{C.1})$$

Poisson distribution model some discrete random variables. Typically, a Poisson random variable is a count of the number of events that occur in a certain time interval or spatial area. The events must hold the following conditions: they must be equivalent and equally probable, and the observation time must be fixed in advance. For example, the number of cars passing a fixed point in a given time interval or the number of persons arriving at an information desk during a time period [206]. Let us derive the functional form for the Poisson distribution from the latter example. In a time interval of one hour, $n = 0, 1, 2, \dots$ persons arrive at an information desk. Let f be the average time of person arrival during that hour. We divide this hour in θ time intervals, small enough for letting only one person arrives at the desk at each interval, in such a way that each person arrives with probability f/θ . The probability of no person arriving in each interval is $1 - f/\theta$. Therefore, the probability of no person arrival during the whole hour is $(1 - f/\theta)^\theta$. When $\theta \rightarrow \infty$, this probability tends to $p_0 = e^{-f}$. The probability of a single person arriving in an hour is

$$p_1 = \binom{1}{\theta} \frac{f}{\theta} \left(1 - \frac{f}{\theta}\right)^{\theta-1} \rightarrow f e^{-f} \quad (\text{C.2})$$

And only two persons arriving:

$$p_2 = \binom{2}{\theta} \frac{f^2}{\theta^2} \left(1 - \frac{f}{\theta}\right)^{\theta-2} \rightarrow \frac{1}{2} f^2 e^{-f} \quad (\text{C.3})$$

For n persons, by making the limit we obtain,

$$p_n = \frac{1}{n!} f^n e^{-f} \quad (\text{C.4})$$

Our interests are restricted to $n = 1$, because search algorithms usually stop when one global solution is found. The event would be the finding of that solution, and we can see that the necessary conditions are hold, since the N_{stat} statistical searches are independent and equally probable. Besides, a maximum number of function calls is fixed in advance. Our histograms represent the PDF of the waiting time for one solution finding, which has the expression

$$p_1(t) = w^2 t e^{-wt} \quad (\text{C.5})$$

where the definition of a frequency w related to a relaxation time has been introduced. This PDF has a peak at $1/w$. The probability of finding one solution after t function calls is

$$P_1(t) = \int_0^t p_1(t') dt' = 1 - (1 + wt)e^{-wt} \quad (\text{C.6})$$

From this equation, we can calculate the expectation value $\langle t \rangle$ and the deviation σ ,

$$\begin{aligned} \langle t \rangle &= \int_0^\infty t p_1(t) dt = \frac{2}{w} \\ \sigma^2 &= \langle t^2 \rangle - \langle t \rangle^2 = \frac{2}{w^2} \end{aligned} \quad (\text{C.7})$$

References

- [1] M. A. Van Hove, V. H. Weinberg, C.-M. Chan, Low-Energy Electron Diffraction, Springer, Berlin, 1986.
- [2] G. Ertl, J. Kupperts, Low Energy Electrons and Surface Chemistry, Wiley, 1986.
- [3] D. P. Woodruff, T. A. Delchar, Modern Techniques of Surface Science, Cambridge University Press, Cambridge, 1994.
- [4] A. Zangwill, Physics at Surfaces, Cambridge University Press, Cambridge, 1998.
- [5] C. J. Davisson, L. H. Germer, Nature 119 (1927) 558.
- [6] G. P. Thompson, A. Reid, Nature 119 (1927) 890.
- [7] E. G. McRae, Surf. Sci. 11 (1968) 479.
- [8] P. M. Marcus, D. W. Jepsen, Phys. Rev. Lett. 20 (1968) 925.
- [9] J. L. Beeby, J. Phys. C (Proc. Phys. Soc.) 1 (1968) 82.
- [10] J. B. Pendry, J. Phys. C: Solid St. Phys. 2 (1969) 1215,2273,2283.
- [11] J. B. Pendry, J. Phys. C: Solid St. Phys. 4 (1971) 2501,2514.
- [12] M. A. Van Hove, J. B. Pendry, J. Phys. C: Solid St. Phys. 8 (1975) 1362.
- [13] S. Y. Tong, Prog. Surf. Sci. 7 (1975) 1.
- [14] J. B. Pendry, Low-Energy Electron Diffraction, Academic, London, 1974.
- [15] M. A. Van Hove, S. Y. Tong, Surface crystallography by LEED, Springer, Berlin, 1979.
- [16] K. Heinz, Prog. Surf. Sci. 27 (1988) 293.
- [17] D. P. Woodruff, A. M. Bradshaw, Rep. Prog. Phys. 57 (1994) 1029.
- [18] D. Norman, J. Phys. C: Solid St. Phys. 19 (1986) 3273.
- [19] G. Hörmandinger, J. B. Pendry, Surf. Sci. 295 (1993) 34.

- [20] M. A. Van Hove, W. Moritz, H. Over, P. J. Rous, A. Wander, A. Barbieri, N. Materer, U. Starke, G. A. Somorjai, *Surf. Sci. Rep.* 19 (1993) 191.
- [21] A. Wander, *Comput. Phys. Commun.* 137 (2001) 4.
- [22] G. Held, W. Braun, CLEED manual, available from the authors, (University of Cambridge).
- [23] P. J. Rous, J. B. Pendry, D. K. Saldin, K. Heinz, K. Müller, N. Bickel, *Phys. Rev. Lett.* 57 (1986) 2951.
- [24] J. B. Pendry, *Surf. Sci. Rep.* 19 (1993) 87.
- [25] A. Wander, J. B. Pendry, M. A. Van Hove, *Phys. Rev. B* 46 (1992) 9897.
- [26] K. Heinz, *Rep. Prog. Phys.* 58 (1995) 637.
- [27] S. Y. Tong, *Adv. Phys.* 48 (1999) 135.
- [28] A. Szöke, Short wavelength coherent radiation: Generation and applications, in: D. J. Attwood, J. Boker (Eds.), *AIP Conference Proceedings No. 147*, AIP, New York, 1986.
- [29] J. J. Barton, *Phys. Rev. Lett.* 61 (1988) 1359.
- [30] D. K. Saldin, P. L. de Andrés, *Phys. Rev. Lett.* 64 (1990) 1270.
- [31] D. K. Saldin, X. Chen, J. A. Vamvakas, M. Ott, H. Wedler, K. Reuter, K. Heinz, P. L. de Andrés, *Surf. Rev. Lett.* 4 (1997) 991.
- [32] K. Heinz, A. Seubert, D. K. Saldin, *J. Phys.: Condens. Matter* 13 (2001) 10647.
- [33] A. L. Patterson, *Phys. Rev.* 46 (1934) 372.
- [34] H. Wu, S. Y. Tong, *Phys. Rev. Lett.* 87 (2001) 036101.
- [35] C. Rogero, C. Polop, L. Magaud, J. Sacedón, P. L. de Andrés, J. A. Martín-Gago, *Phys. Rev. B* 66 (2002) 235421.
- [36] C. J. Gilmore, *Acta Cryst. A* 52 (1996) 561.
- [37] D. K. Saldin, A. Seubert, K. Heinz, *Phys. Rev. Lett.* 88 (2002) 115507.
- [38] S. Andersson, J. B. Pendry, *J. Phys. C: Solid St. Phys.* 13 (1980) 3547.
- [39] U. Diebold, *Surf. Sci. Rep.* 48 (2003) 53.
- [40] <http://www.sitp.lbl.gov/graphs/plots/ssdtech.html>.
- [41] J. B. Pendry, *J. Phys. C: Solid St. Phys.* 13 (1980) 937.
- [42] N. C. Kothari, H. Over, D. K. Saldin, *Phys. Rev. B* 49 (1994) 11088.

- [43] <http://www-dak.ch.cam.ac.uk/LEED.html>.
- [44] W. H. Press, S. A. Teukolsky, W. T. Vetterling, Numerical Recipes, Cambridge University Press, Cambridge, 2002.
- [45] A. Gonis, W. H. Butler, Multiple Scattering in Solids, Springer, Berlin, 2000.
- [46] S. Walter, V. Blum, L. Hammer, S. Müller, K. Heinz, M. Giesen, Surf. Sci. 458 (2000) 155.
- [47] P. M. Echenique, J. Phys. C: Solid State Phys. 9 (1976) 3193.
- [48] F. Guinea, C. Tejedor, F. Flores, E. Louis, Phys. Rev. B 28 (1983) 4397.
- [49] U. Löffler, U. Muschiol, P. Bayer, K. Heinz, V. Fritzsche, J. B. Pendry, Surf. Sci. 331 (1995) 1435.
- [50] P. L. de Andrés, D. A. King, Comp. Phys. Commun. 138 (2001) 281.
- [51] W. Moritz, J. Landskron, Surf. Sci. 337 (1995) 278.
- [52] V. Fritzsche, Phys. Rev. B 50 (1994) 1922.
- [53] A. Barbieri, M. A. Van Hove, <http://electron.lbl.gov/leedpack>.
- [54] M. Blanco-Rey, P. L. de Andrés, G. Held, D. A. King, Comp. Phys. Comm. 161 (2004) 151.
- [55] M. Abramowitz, I. Stegun (editors), Handbook of Mathematical Functions, 9th ed., Dover Publications, New York, 1972.
- [56] I. Chivers, J. Sleightholme, Introducing Fortran, Springer, London, 1995.
- [57] V. Blum, L. Hammer, W. Meier, K. Heinz, Surf. Sci. 488 (2001) 219.
- [58] P. L. de Andrés, J. A. Vergés, Phys. Rev. B 59 (1999) 3086.
- [59] D. K. Saldin, J. B. Pendry, M. A. Van Hove, G. A. Somorjai, Phys. Rev. B 31 (1985) 1216.
- [60] D. K. Saldin, J. B. Pendry, Surf. Sci. 162 (1985) 941.
- [61] K. Heinz, U. Starke, M. A. Van Hove, G. A. Somorjai, Surf. Sci. 261 (1992) 57.
- [62] M. A. Van Hove, R. Lin, G. A. Somorjai, Phys. Rev. Lett. 51 (1983) 778.
- [63] J. B. Pendry, D. K. Saldin, Surf. Sci. 145 (1984) 33.
- [64] P. J. Durham, J. B. Pendry, C. H. Hodges, Comp. Phys. Commun. 25 (1982) 193.
- [65] J. B. Pendry, Surf. Sci. 57 (1976) 679.

- [66] D. K. Saldin, J. B. Pendry, *Comput. Phys. Commun.* 42 (1986) 399.
- [67] U. Starke, P. L. de Andrés, D. K. Saldin, K. Heinz, J. B. Pendry, *Phys. Rev. B* 38 (1988) 12277.
- [68] K. Heinz, *Vacuum* 41 (1990) 332.
- [69] P. J. Rous, *Prog. Surf. Sci.* 39 (1992) 3.
- [70] V. Blum, K. Heinz, *Comp. Phys. Commun.* 134 (2001) 392.
- [71] <http://www.sitp.lbl.gov/index.php?content=/leedpack/leedpack.html>.
- [72] U. Löffler, R. Döll, K. Heinz, *Surf. Sci.* 301 (1994) 346.
- [73] R. Döll, M. Kottcke, K. Heinz, *Phys. Rev. B* 48 (1993) 1973.
- [74] R. Baudoing, Y. Gauthier, M. Lundbergland, J. Rundgren, *J. Phys. C* 19 (1986) 2825.
- [75] V. Blum, PhD thesis, University of Erlangen-Nürnberg.
- [76] V. E. Henrich, P. A. Cox, *The surface science of metal oxides*, Cambridge University Press, Cambridge, 1994.
- [77] J. Abad, PhD thesis, Universidad Autónoma de Madrid.
- [78] M. A. Henderson, *Surf. Sci. Rep.* 46 (2002) 1.
- [79] P. J. D. Lindan, N. M. Harrison, M. J. Gillan, *Phys. Rev. Lett.* 80 (1998) 762.
- [80] M. Haruta, *Catal. Today* 36 (1997) 153.
- [81] M. Valden, X. Lai, D. W. Goodman, *Science* 281 (1998) 1647.
- [82] M. Ramamoorthy, D. Vanderbilt, R. D. King-Smith, *Phys. Rev. B* 49 (1994) 16721.
- [83] P. W. Tasker, *J. Phys. C* 12 (1979) 4977.
- [84] J. P. LaFemina, *Crit. Rev. Surf. Chem.* 3 (1994) 297.
- [85] V. E. Henrich, *Prog. Surf. Sci.* 14 (1983) 175.
- [86] G. Charlton, P. B. Howes, C. L. Nicklin, P. Steadman, J. S. G. Taylor, C. A. Muryn, S. P. Harte, J. Mercer, R. McGrath, D. Norman, T. S. Turner, G. Thornton, *Phys. Rev. Lett.* 78 (1997) 495.
- [87] R. Lindsay, A. Wander, A. Ernst, B. Montanari, G. Thornton, N. M. Harrison, *Phys. Rev. Lett.* 94 (2005) 246102.
- [88] N. M. Harrison, X. G. Wang, J. Muscat, M. Scheffler, *Faraday Discuss.* 114 (1999) 305.

- [89] V. Swamy, J. Muscat, J. D. Gale, N. M. Harrison, *Surf. Sci.* 504 (2002) 115.
- [90] P. W. Murray, N. G. Condon, G. Thornton, *Phys. Rev. B* 51 (1995) 10989.
- [91] H. Onishi, Y. Iwasawa, *Surf. Sci.* 313 (1994) L783.
- [92] C. L. Pang, S. A. Haycock, H. Raza, P. W. Murray, G. Thornton, O. Gulseren, R. James, D. W. Bullett, *Phys. Rev. B* 58 (1998) 1586.
- [93] R. A. Bennett, P. Stone, M. Bowker, *Faraday Discuss.* 114 (1999) 267.
- [94] R. A. Bennett, P. Stone, M. Bowker, *Phys. Rev. Lett.* 82 (1999) 3831.
- [95] J. Biener, J. Wang, R. J. Madix, *Surf. Sci.* 442 (1999) 47.
- [96] R. E. Tanner, M. R. Castell, G. A. D. Briggs, *Surf. Sci.* 412 (1998) 672.
- [97] M. Ashino, T. Uchihashi, K. Yokoyama, Y. Sugawara, S. Morita, M. Ishikawa, *Phys. Rev. B* 61 (2000) 13955.
- [98] M. Ashino, Y. Sugawara, S. Morita, M. Ishikawa, *Phys. Rev. Lett.* 86 (2001) 4334.
- [99] U. Diebold, J. F. Anderson, K. O. Ng, D. Vanderbilt, *Phys. Rev. Lett.* 77 (1996) 1322.
- [100] S. D. Elliott, S. P. Bates, *Phys. Chem. Chem. Phys.* 3 (2001) 1954.
- [101] S. D. Elliott, S. P. Bates, *Phys. Rev. B* 65 (2002) 245415.
- [102] S. D. Elliott, S. P. Bates, *Phys. Rev. B* 67 (2003) 035421.
- [103] P. J. Møller, M. C. Wu, *Surf. Sci.* 224 (1989) 265.
- [104] Q. Guo, I. Cocks, E. M. Williams, *Phys. Rev. Lett.* 77 (1996) 3851.
- [105] H. Onishi, Y. Iwasawa, *Phys. Rev. Lett.* 76 (1996) 791.
- [106] M. Blanco-Rey, J. Abad, C. Rogero, J. Mendez, M. F. Lopez, J. A. Martin-Gago, P. L. de Andres, *Phys. Rev. Lett.* 96 (2006) 055502.
- [107] K. O. Ng, D. Vanderbilt, *Phys. Rev. B* 56 (1997) 10544.
- [108] I. D. Cocks, Q. Guo, E. M. Williams, *Surf. Sci.* 390 (1997) 119.
- [109] M. Ashino, T. Uchihashi, K. Yokoyama, Y. Sugawara, S. Morita, M. Ishikawa, *Jpn. J. Appl. Phys.* 39 (2000) 3765.
- [110] E. Asari, R. Souda, *Phys. Rev. B* 60 (1999) 10719.
- [111] E. Asari, R. Souda, *Appl. Surf. Sci.* 167 (2000) 169.
- [112] I. P. Batra, *J. Phys. C: Solid St. Phys.* 15 (1982) 5399.

- [113] <http://www.icmm.csic.es/esisna/index1.htm>.
- [114] E. Prince, *Mathematical techniques in crystallography and material sciences*, Springer, Berlin, 1982.
- [115] M. Frisch, et al., Gaussian 03, revision b.05, <http://www.gaussian.com>.
- [116] R. Lindsay, Private Communication.
- [117] R. F. W. Bader, *Atoms in Molecules: a Quantum Theory*, Oxford University Press, Oxford, 1990.
- [118] M. Kottcke, K. Heinz, *Surf. Sci.* 376 (1977) 352.
- [119] C. Rogero, Private Communication.
- [120] C. Rogero, J. A. Martín-Gago, P. L. de Andrés, *Phys. Rev. B* 67 (2003) 073402.
- [121] Lindsay, X. Torrelles, G. Cabailh, S. Ferrero, G. Thornton, O. Bikondoa, A. Ernst, A. Wander, N. Harrison, *TiO₂(110): exploring surface structure*, in: ASEVA Summer School, Avila, 2005, to be published.
- [122] F. d'Acapito, S. Mobilio, P. Gastaldo, D. Barbier, L. F. Santos, O. Martins, R. M. Almeida, *J. Non-Cryst. Solids* 293–295 (2001) 118.
- [123] <http://www.bsc.es>.
- [124] M. D. Segall, P. L. D. Lindan, M. J. Robert, C. J. Pickard, P. J. Hasnip, S. J. Clark, M. C. Payne, *J. Phys.: Cond. Matt.* 14 (2002) 2717.
- [125] <http://www.accelrys.com>.
- [126] D. Vanderbilt, *Phys. Rev. B* 41 (1990) 7892.
- [127] J. P. Perdew, K. Burke, M. Ernzerhof, *Phys. Rev. Lett.* 77 (1996) 3865.
- [128] T. J. Beck, A. Klust, M. Batzill, U. Diebold, C. D. Valentin, A. Selloni, *Phys. Rev. Lett.* 93 (2004) 036104.
- [129] P. J. Lindan, N. M. Harrison, M. J. Gillan, J. A. White, *Phys. Rev. B* 55 (1997) 15919.
- [130] A. T. Paxton, L. Thiên-Nga, *Phys. Rev. B* 57 (1998) 1579.
- [131] J. Abad, C. Rogero, J. Méndez, M. F. López, J. A. Martín-Gago, E. Román, *Appl. Surf. Sci.* 234 (2004) 497.
- [132] D. K. Saldin, J. B. Pendry, *Comp. Phys. Commun.* 46 (1987) 129.
- [133] G. Illing, D. Eskett, E. W. Plummer, H. J. Freund, J. Somers, T. Lindner, A. M. Bradshaw, U. Buskotte, M. Neumann, U. Starke, K. Heinz, P. L. de Andrés, D. K. Saldin, J. B. Pendry, *Surf. Sci.* 206 (1988) 1.

- [134] D. D. Vvedensky, D. K. Saldin, J. B. Pendry, *Comp. Phys. Commun.* 40 (1986) 421.
- [135] P. Lloyd, P. V. Smith, *Adv. Phys.* 21 (1972) 62.
- [136] D. A. Varshalovich, A. N. Moskalev, V. K. Khersonskii, *Quantum Theory of Angular Momentum*, World Scientific, Singapore, 1988.
- [137] S. Titmuss, K. Johnson, Q. Ge, D. A. King, *J. Chem. Phys.* 116 (2002) 8097.
- [138] G. Held, W. Braun, H. Steinrück, S. Yamagishi, S. J. Jenkins, D. A. King, *Phys. Rev. Lett.* 87 (2001) 216102.
- [139] J. J. Sakurai, *Advanced Quantum Mechanics*, Addison-Wesley, London, 1967.
- [140] R. G. Newton, *Scattering theory of waves and particles*, McGraw Hill, New York.
- [141] M. Blanco-Rey, P. L. de Andrés, G. Held, D. A. King, *Comp. Phys. Comm.* 161 (2004) 166.
- [142] G. Held, M. P. Bessent, S. Titmuss, D. A. King, *J. Chem. Phys.* 105 (1996) 11305.
- [143] G. Held, A. Wander, D. A. King, *Phys. Rev. B* 51 (1995) 17856.
- [144] W. Braun, H. P. Steinrück, G. Held, *Surf. Sci.* 574 (2005) 193.
- [145] J. V. Peetz, W. Schattke, *J. of Electr. Spectr. and Rel. Phen.* 68 (1994) 167.
- [146] J. B. Pendry, *Phil. Trans. R. Soc. Lond. A* 334 (1991) 539.
- [147] P. L. de Andrés, P. Rous, J. B. Pendry, *Surf. Sci.* 193 (1988) 1.
- [148] S. Wolfram, *The Mathematica Book*, Cambridge University Press, Cambridge, 1996.
- [149] G. H. Stout, L. H. Jensen, *X-ray structure determination: a practical guide*, John Wiley and sons, New York, 1989.
- [150] K. Robinson, D. J. Tweet, *Rep. Prog. Phys* 55 (1992) 599.
- [151] S. Kirkpatrick, C. D. Gelatt, M. P. Vecchi, *Science* 220 (1983) 671.
- [152] J. B. Pendry, K. Heinz, W. Oed, *Phys. Rev. Lett.* 61 (1988) 2953.
- [153] T. Y. Wu, T. Ohmura, *Quantum Theory of Scattering*, Prentice Hall, London, 1962.
- [154] N. F. Mott, H. S. W. Massey, *The theory of atomic collisions*, Oxford, Oxford, 1965.

- [155] G. Kleinle, W. Moritz, G. Ertl, Surf. Sci. 238 (1990) 119.
- [156] P. J. Rous, M. A. Van Hove, G. A. Somorjai, Surf. Sci. 226 (1990) 15.
- [157] P. J. Rous, Surf. Sci. 296 (1993) 358.
- [158] P. G. Cowell, V. E. de Carvalho, Surf. Sci. 187 (1987) 175.
- [159] D. L. Adams, Surf. Sci. 519 (2002) 157.
- [160] G. Kleinle, W. Moritz, D. L. Adams, G. Ertl, Surf. Sci. 219 (1989) 175.
- [161] J. B. Pendry, K. Heinz, Surf. Sci. 230 (1990) 137.
- [162] J. B. Pendry, Vacuum 41 (1990) 340.
- [163] K. Heinz, W. Oed, J. B. Pendry, Phys. Rev. B 41 (1990) 10179.
- [164] V. B. Nascimento, V. E. de Carvalho, *et al*, Surf. Sci. 487 (2001) 15.
- [165] E. R. Correia, V. B. Nascimento, *et al*, J. Phys.: Condens. Matter 17 (2005) 1.
- [166] R. Döll, M. A. Van Hove, Surf. Sci. 355 (1996) L393.
- [167] M. Blanco-Rey, P. L. de Andrés, Surf. Sci. 600 (2006) L91.
- [168] C. G. Broyden, Mathematics of Computation 19 (1965) 577.
- [169] J. A. Nelder, R. Mead, Computer Journal 7 (1965) 308.
- [170] S. Müller, A. Kinne, M. Kottcke, R. Metzler, P. Bayer, L. Hammer, K. Heinz, Phys. Rev. Lett 75 (1995) 2859.
- [171] D. M. Collins, Nature 298 (1982) 49.
- [172] V. L. Shneerson, D. L. Wild, D. K. Saldin, Acta Cryst. A 57 (2001) 163.
- [173] D. K. Saldin, R. Harder, H. Vogler, W. Moritz, I. K. Robinsoin, Comp. Phys. Commun. 137 (2001) 12.
- [174] D. K. Saldin, R. J. Harder, V. L. Shneerson, W. Moritz, J. Phys.: Condens. Matter 13 (2001) 10689.
- [175] D. K. Saldin, V. L. Shneerson, R. Fung, Physica B 336 (2003) 16.
- [176] A. Seubert, K. Heinz, D. K. Saldin, Phys. Rev. B 67 (2003) 125417.
- [177] D. Gabor, Nature 161 (1948) 777.
- [178] C. G. Kinniburgh, J. B. Pendry, J. Phys. C: Solid State Phys. 11 (1977) 2415.
- [179] R. E. Burge, M. A. F. and A. H. Greenway, G. Ross, J. Phys. D: Applied Phys. 7 (1974) L65.

- [180] R. T. Prosser, *J. Math. Phys.* 10 (1968) 1819.
- [181] J. R. Fienup, *Opt. Lett.* 3 (1978) 27.
- [182] A. C. Kak, M. Slaney, *Principles of Computerized Tomographic Imaging*, IEEE Press, NY, 1988.
- [183] M. Born, E. Wolf, *Principles of optics: electromagnetic theory of propagation, interference and diffraction of light*, 7th (expanded edition), Cambridge University Press, Cambridge, 1999.
- [184] J. J. Barton, *Phys. Rev. Lett.* 67 (1991) 3106.
- [185] S. Y. Tong, H. Huang, C. M. Wei, *Phys. Rev. Lett.* 46 (1992) 2452.
- [186] C. Wei, S. Y. Tong, *Surf. Sci.* 274 (1992) L577.
- [187] C. Wei, S. Y. Tong, H. Wedler, M. A. Mendez, K. Heinz, *Phys. Rev. Lett.* 72 (1994) 2434.
- [188] D. K. Saldin, X. Chen, *Phys. Rev. B* 52 (1995) 2941.
- [189] A. Seubert, D. K. Saldin, J. Bernhardt, U. Starke, K. Heinz, *J. Phys.: Condens. Matter* 12 (2000) 5527.
- [190] D. L. Adams, U. Landman, *Phys. Rev. B* 15 (1977) 3775.
- [191] J. R. Fienup, *App. Opt.* 21 (1982) 2758.
- [192] D. S. C. Biggs, M. Andrews, *App. Opt.* 36 (1997) 1766.
- [193] J. R. Fienup, *J. Opt. Soc. Am. A* 4 (1987) 118.
- [194] J. S. Wu, J. C. H. Spence, *Acta Cryst. A* 61 (2004) 194.
- [195] J. S. Wu, U. Weierstall, J. C. H. Spence, *Nature Mat.* 4 (2005) 912.
- [196] J. H. Seldin, J. R. Fienup, *J. Opt. Soc. Am. A* 7 (1990) 428.
- [197] M. Nieto-Vesperinas, J. A. Méndez, *Opt. Commun.* 59 (1986) 249.
- [198] M. J. Pérez-Ilzarbe, M. Nieto-Vesperinas, R. Navarro, *J. Opt. Soc. Am. A* 7 (1990) 434.
- [199] S. F. Gull, G. J. Daniell, *Nature* 272 (1978) 686.
- [200] A. J. Devaney, *Ultrasonic Imag.* 4 (1982) 336.
- [201] P. F. Lyman, V. L. Shneerson, R. Fung, et al, *Phys. Rev. B* 71 (2005) 081402.
- [202] J. S. Wu, U. Weierstall, J. C. H. Spence, C. Koch, *Opt. Lett.* 29 (2004) 2737.
- [203] A. F. Fercher, H. Bartelt, H. Becker, E. Wiltchko, *Appl. Opt.* 14 (1979) 2427.

- [204] G. Gbur, W. Wolf, *Opt. Lett.* 27 (2002) 1890.
- [205] G. B. Wetherill, *Elementary Statistical Methods*, Chapman and Hall, New York, 1982.
- [206] M. Laboureur, M. Chossat, C. Cardot, *Course de Calcul Mathématique Moderne*, tome 1, Dunod, Paris, 1968.

Agradecimientos / Acknowledgements

Al Dr. Pedro de Andrés por el interés que ha puesto en la dirección de esta tesis. Sin su acierto a la hora de proponer temas y su orientación durante la resolución de éstos, esta tesis no habría sido posible. Tengo que agradecerle además el inmenso esfuerzo que ha realizado durante este último mes en las revisiones de la memoria, para conseguir que la tesis pudiera estar terminada a tiempo.

Al Prof. Fernando Flores por su tutela.

Al Ministerio de Educación y Ciencia por su financiación a través de una beca FPU durante el periodo 2003-2005.

Al CSIC y a la empresa Nanotec por la beca I3P-postgrado durante 2006.

Al ICMM, su director, el Prof. Federico Soria, y a todo su personal, por proporcionarme durante este tiempo un entorno de trabajo agradable.

A los miembros del grupo ESISNA del ICMM, con quienes he tenido el placer de trabajar: los doctores Jose Abad, Celia Rogero, José Angel Martín-Gago, Paqui López, Javier Méndez y Elisa Román. Sin este valioso contacto con el mundo experimental, la tesis habría quedado “coja”.

To Prof. Sir David A. King and all the members of his surface science group at the University of Cambridge, where I spent a pleasant stay. In particular, I acknowledge Prof. King and Dr. Georg Held for their collaboration and their interest in including the molecular T-matrix formalism in their CLEED code.

To Prof. Klaus Heinz and all the members of his group at the University of Erlangen, that hosted me for two months. It has been a privilege to be advised by an expert in LEED theory like him. He is also acknowledged for providing us with experimental IVs of Cu(100).

To Dr. Robert Lindsay and Prof. Geoffrey Thornton for many interesting discussions about TiO_2 and for providing us with their self-consistent phase shifts.

Al Prof. Manuel Nieto-Vesperinas por proporcionarme bibliografía y consejos en mis primeros cálculos sobre tomografía y recuperación de fase.

Al Barcelona Supercomputer Center por suministrarnos tiempo de cálculo.

A todos los miembros del Departamento de Teoría de la Materia Condensada del ICMM, y muy especialmente a aquéllos con quienes comparto mesa a diario.

A mis padres y mis abuelos, que nunca me han fallado cuando les he necesitado. Lamento no haber podido pasar más tiempo con ellos durante estos últimos años.

Y a Iván, por estar al pie del cañón todos los días, recordándome que “esto es una carrera de fondo”.

